Spectra and Large-scale Isotropy of the Cosmic X-ray Background from ASCA Observations

Yoshitaka Ishisaki

Abstract

We have studied the average spectra of the Cosmic X-ray Background (CXB) and the field-to-field difference of the CXB spectral parameters, mainly utilizing the ASCA GIS. We created the average CXB spectrum from the ASCA Large Sky Survey (LSS) observations, which was carried out at the region around $(l, b) = (75.4^\circ, 83.4^\circ)$ covering the large continuous sky of $\sim 1^\circ \times 5^\circ$ with 76 pointings and 515 ks exposure. In the 2–10 keV energy band, the spectrum is well fitted with the power-law model ($PL^{\rm hard}$) which is almost consistent with the HEAO-1 A2. However, there exists a clear soft-excess below ~ 1.2 keV, which can be fitted with the steep power-law ($PL^{\rm soft}$) of $\Gamma \sim 6$ or the 1-solar Raymod-Smith model of $kT \sim 0.3$ keV. Although this model appears to resembles the ROSAT measurements in the 0.5–1.5 keV energy band when unfolded, we cannot find the component of $\Gamma = 2.1$ which ROSAT reported. We also created the CXB spectra in 13 fields at high Galactic latitude with eliminating the discrete sources brighter than $\sim 2 \times 10^{-13}$ erg s^{-1} cm^{-2}, and fitted them with the $PL^{\rm hard} + PL^{\rm soft}$ model. The 2–10 keV fluxes of $PL^{\rm hard}$ are consistent with constant within the 90%-confidence upper-limit of 9%, while the 0.5–2 keV fluxes of $PL^{\rm soft}$, most part of which is probably the Galactic origin, vary from field to field.

CONTENTS

1 Introduction **1**

1.1 The Cosmic X-ray Background (CXB) 1

1.2 Problems with the CXB 2

1.3 CXB investigations with ASCA 3

1.4 Outline of the present thesis 3

2 Review of the Cosmic X-ray Background **5**

2.1 Spectral properties of the CXB 5

2.1.1 CXB spectrum above 2 keV 5

2.1.2 Lack of inerse-Compton effects 5

2.1.3 CXB spectrum below 2 keV 7

2.2 Brightness distribution of the CXB 9

2.2.1 Small-scale fluctuations 9

2.2.2 Global isotropy and dipole anisotropy 10

2.3 Contribution of known classes of discrete sources 11

2.3.1 Log$N$ - Log$S$ relations above 2 keV 11

2.3.2 Log$N$ - Log$S$ relations below 2 keV 11

2.3.3 The spectral paradox 13

3 Instrumentation **15**

3.1 The ASCA satellite 15

3.1.1 Launch of the ASCA satellite 15

3.1.2 Attitude control and attitude determination system 17

3.1.3 Satellite operation and data transfer 17

3.1.4 Early operations and observation program 18

3.2 X-ray telescope (XRT) 19

3.2.1 Principle of X-ray telescopes 19

3.2.2 Design and structure of the XRT 20

3.2.3 Alignments of four XRTs to each focal plane detector 22

3.3 Solid-state Imaging Spectrometer (SIS) 24

3.3.1 Design and structure of the SIS . . . 24
3.3.2 Data processing of the SIS . . . 26
3.4 Gas Imaging Spectrometer (GIS) . . . 28
3.4.1 Design and structure of the GIS . . . 28
3.4.2 Onboard data processing of the GIS . . . 32
3.4.3 Background rejection of the GIS . . . 33
3.4.4 Monitor counts and house keeping (HK) data of the GIS . . . 36
3.4.5 Basic event conversion for the GIS . . . 37

4 In Orbit Calibration of the GIS 43
4.1 Overview . . . 43
4.2 Response of the XRT+GIS system . . . 43
4.2.1 Formulation of the ASCA response and an ARF builder . . . 43
4.2.2 XRT part of ARF . . . 47
4.2.3 GIS part of ARF . . . 49
4.2.4 GIS part of RMF . . . 50
4.2.5 Verification of the XRT+GIS response for a point source . . . 53
4.3 Stray light effect to the CXB analysis . . . 56
4.3.1 What is stray light? . . . 56
4.3.2 Evaluation of stray light effects by ray-tracing . . . 57
4.3.3 Comparison of ray-tracing with Crab stray obserbations . . . 60
4.3.4 The ARF builder for the CXB spectrum . . . 62
4.4 Residual non X-ray background (RNXB) of the GIS . . . 64
4.4.1 Importance of RNXB in the CXB analyses . . . 64
4.4.2 Rough properties of RNXB . . . 64
4.4.3 Flare events and the GIS monitor counts . . . 68
4.4.4 RNXB reproducibility by H02-sorting method . . . 71

5 Observations 77
5.1 Selection of observed fields . . . 77
5.2 Description of Individual Fields . . . 78
5.2.1 LSS . . . 78
5.2.2 SA57 . . . 80
5.2.3 Draco Field . . . 80
5.2.4 NEP . . . 80
5.2.5 QSF3 . . . 81
5.2.6 z-system . . . 81

5.2.7 Braccesi Field 81
5.2.8 Jupiter, Arp 220, and 3C368 82
5.3 Data processing 82
5.3.1 Basic event selection 82
5.3.2 Handling of multiple pointings 83
5.3.3 Image smoothing 84

6 Average CXB spectrum in the LSS field 87
6.1 CXB data sampling and data analysis method 87
6.2 Ring-sorted CXB spectra 88
6.3 Spectral fits to the average CXB in the LSS field 90
6.3.1 Results in the 2–10 keV range 90
6.3.2 Results in the 0.6–10 keV range 92
6.4 Systematic error of the CXB spectrum 95
6.4.1 RNXB uncertainty 95
6.4.2 GIS low energy response uncertainty 96
6.4.3 XRT stray light uncertainty 97
6.4.4 XRT effective area uncertainty 98
6.4.5 Summary of the systematic errors 100

7 Field to field properties of the CXB 101
7.1 CXB spectra of individual fields including point sources 101
7.2 How to eliminate point sources 103
7.2.1 Outline of the source-finding 103
7.2.2 Determination of the CXB base level 105
7.2.3 Point-source images 107
7.2.4 Source-masking 110
7.3 Threshold flux of the source-masks 111
7.4 CXB properties of individual fields 113
7.4.1 Strategy to study individual fields 113
7.4.2 Field-to-field variation of the CXB base level 113
7.4.3 CXB spectra of individual fields excluding point sources 116
7.4.4 Field-to-field variation of $\Gamma^{\rm hard}$ 118
7.4.5 Field-to-field variation of $F_{\rm X}^{\rm hard}$ 119
7.4.6 Effects of the soft component 123
7.5 Average CXB spectra excluding point sources 125

8 Discussion and conclusion **129**

8.1 Average CXB spectrum 129

8.1.1 Summary of the observation 129

8.1.2 Comparison with previous observations 130

8.1.3 Effects of discrete sources 134

8.1.4 Constraints on the AGN mixture models of the CXB 136

8.2 Field to field fluctuation of the CXB 138

8.2.1 Summary of the observation 138

8.2.2 Comparison with previous measurements 138

A Log of the observed fields **143**

B Contour-map images of the observed fields **147**

C Flat field images and source-masks **155**

D Spectra of the CXB observations **163**

E Fitting results processed through source-masking at the threshold of 0.06 **169**

F Hardness-map images of the observed fields **173**

G All-sky maps of the X-ray observations **177**

H CXB fluctuation due to unresolved sources **181**

H.1 Formulation of the CXB fluctuation 181

H.2 Effective beam size for the XRT+GIS 182

List of Figures

2.1 The 3–50 keV CXB spectrum observed with HEAO-1 A2 6
2.2 The 0.1–2 keV CXB spectrum observed with ROSAT PSPC 8
2.3 The dipole anisotropy of the CXB with HEAO-1 A2 all-sky survey 10
2.4 The integral $\log N$-$\log S$ relation in 2–10 keV 12
2.5 The integral $\log N$-$\log S$ relation in 0.5–2 keV 13
2.6 Type 2 Seyfert galaxy Mkn3 spectrum observed with Ginga LAC 14

3.1 In orbit configration of the ASCA satellite 16
3.2 Onboard instruments of the ASCA satellite 16
3.3 Walter type I optics 19
3.4 One quadrant of the ASCA XRT 20
3.5 Effective area of the ASCA XRT compared with that in previous missions . 21
3.6 Alignment of the four focal plane detectors 23
3.7 Cross section view of the SIS camera 24
3.8 (a) Detection efficiency and (b) Energy resolutions of the SIS 26
3.9 Cross section view of the GIS sensor 29
3.10 Schematic view of the GIS sensor system 30
3.11 Data flow chart of the GIS electronics 32
3.12 (a) $RAWX$-$RAWY$ image and (b) PH-RT relation (no RT mask) 34
3.13 (a) $RAWX$-$RAWY$ image and (b) PH-RT relation (with RT mask) . . . 34
3.14 A scatter plot of squared radial distance in $RAWX$-$RAWY$ vs. SP 35
3.15 Sunlit earth images of GIS2 and GIS3 37
3.16 The position linearlization maps for GIS2 and GIS3 38
3.17 The gain maps for GIS2 and GIS3 39
3.18 (a) Temp. vs. calibration isotope PH, and (b) Long-term gain history . . . 39
3.19 Relative GIS gains plotted as a function of $LDHIT$ 40

4.1 Properties of the XRT effective area 48
4.2 Examples of the XRT PSF taken by GIS2 48
4.3 Energy dependences of the thermal shield and Be window transmission . . 51

4.4 (a) Be thickness map, and (b) support grid transmission map for GIS2 . . 51
4.5 Energy dependence of the position resolution of the GIS 51
4.6 Contour map and slices of the GIS RMF 52
4.7 Energy dependence of the energy resolution of the GIS 52
4.8 Pointing positions of the Crab nebula 53
4.9 The Crab nebula spectrum fitted with an absorbed power-law model 54
4.10 Offset angle dependences of the best fit parameters for the Crab spectra . . 55
4.11 Four examples of XRT light paths 56
4.12 Three of the Crab stray light images by GIS3 in 0.7–10 keV 58
4.13 Ray-tracing image of the stray light pattern at 1 keV for $\theta = 60'$ 58
4.14 (a) Calculated ratios of the CXB, and (b) averaged CXB/NXB spectra . . 59
4.15 Azimuthally averaged radial profiles of the CXB image 59
4.16 (a) Spectra of the Crab stray observations, and (b) simulated spectra . . . 61
4.17 Counting rates of the Crab stray observations and the simulations 62
4.18 Plot of the GIS2 and GIS3 ARFs for a point source and the CXB 63
4.19 Integrated spectra of the day-earth, the CXB, and the night-earth 65
4.20 Integrated GIS2 and GIS3 images for the entire night-earth observations . 66
4.21 Energy sorted radial profiles during the night-earth observations 67
4.22 Band profiles during the CXB and night-earth observations 67
4.23 *COR-LDHIT* correlation during the night-earth observations 68
4.24 Long term variations of the counting rate during the night-earth observations 68
4.25 Distribution map for three types of phenomena on the Earth surface 69
4.26 *COR-H*02 correlation during the night-earth observations 70
4.27 Correlations of (a) *H*02-*RNTE*, and (b) *COR-RNTE* 70
4.28 *RBMCNT* distribution for night-earth and during the soft-flares 71
4.29 Correlations of (a) *H*02-*RNTE*, and (b) *COR-RNTE* (with flare-cut) . . 72
4.30 *H*02 sorted spectra and radial profiles during the night-earth observations . 73
4.31 *H*02 distribution for the entire night-earth observations 74
4.32 Figures to check the RNXB reproducibility by H02-sorting method 75

5.1 Galactic positions of the observed fields in table 5.1 78
5.2 LSS pointing positions 79
5.3 Images of (a) M^{EXP} (b) M^{OBS} and (c) M^{CCF} in the Braccesi Field 86

6.1 Ring-sorted spectra of (a) CXB and (b) day-earth 88
6.2 (a) The ring-sorted CXB spectra, and (b) normalization for each spectrum 89
6.3 The average CXB spectrum fitted with (a) power-law and (b) brems. . . . 91

6.4 Changes of χ^2/d.o.f and the photon index when shifted fit lower boundary 92
6.5 The average CXB spectrum fitted with an abs. power-law + soft component 93
6.6 Confidence contours for abs. power-law + steep power-law fit 94
6.7 Confidence contours for abs. power-law + *RS* fit 94
6.8 Confidence contour of *RS* temperature vs. *RS* abundance 95
6.9 Changes of the best fit parameters when the RNXB level is scaled 95
6.10 Changes of the best fit parameters when additional Be thickness is applied 96
6.11 Changes of the best fit parameters when stray light level is scaled 97
6.12 (a) Flux and (b) photon index plotted versus the radius of each ring 99
6.13 Ratio of the observed Crab counts to that predicted by the ray-tracing . . 99

7.1 The NEP spectrum fitted with the $PL^{\rm hard} + PL^{\rm soft}$ model in 0.6–10 keV . . 103
7.2 Gray scale image of M^{RAW} for the entire LSS observations 106
7.3 Gray scale image of $M^{\overline{CXB}}$ for the entire LSS observations 107
7.4 Gray scale image of M^{RATIO} for the entire LSS observations 107
7.5 Distribution of pixel values in figure 7.4 108
7.6 Gray scale image of M^{FLAT} for the entire LSS observations 109
7.7 Distribution of pixel values in figure 7.6 109
7.8 Radial profile of 8′ offset Cyg X-1 image taken by GIS2 110
7.9 The source-mask for the entire LSS observations 111
7.10 Correlation between the source flux by Ueda (1996) and M^{FLAT} 112
7.11 CXB base levels (= α) in the 0.7–7.0 keV energy band 114
7.12 $\Gamma^{\rm hard}$, $F_{\rm X}^{\rm hard}$ (2–10 keV) and $F_{\rm X}^{\rm soft}$ (0.5–2 keV) plotted against the field ID . 117
7.13 Correlations of $\Gamma^{\rm hard}$ vs. $F_{\rm X}^{\rm hard}$ in each sample field 120
7.14 Confidence contours of $\Gamma^{\rm hard}$ vs. $F_{\rm X}^{\rm hard}$ after source-masking of 0.1 120
7.15 The remaining fraction (%) of $F_{\rm X}^{\rm hard}$ plotted against that of integration area 121
7.16 $\Gamma^{\rm hard}$, $F_{\rm X}^{\rm hard}$ (2–10 keV) and $F_{\rm X}^{\rm soft}$ (0.5–2 keV) when $\Gamma^{\rm hard}$ fixed to 1.44 . . . 122
7.17 The CXB base level α without the source-maskings plotted against $F_{\rm X}^{\rm hard}$. 123
7.18 $F_{\rm X}^{\rm hard}$ plotted against (a) $\Gamma^{\rm hard}$, $F_{\rm X}^{\rm hard}$ with (b) $\Gamma^{\rm hard}$ free, (c) fixed to 1.44 . 124
7.19 Average CXB spectra for (a) (b) (c) LSS and (d) ALL 126
7.20 Confidence contour of $\Gamma^{\rm hard}$ vs. $F_{\rm X}^{\rm hard}$ for the spectra shown in figure 7.19 . 127

8.1 Unfolded 0.6–10 keV spectra of the average CXB including point sources . 132
8.2 Unfolded 0.6–10 keV spectra of the average CXB after 0.10 source-masking 133
8.3 The $\log N$-$\log S$ relation in the 2–10 keV energy band 135
8.4 The fractional residuals of the total CXB spectrum in figure 7.19d to a power-law of $\Gamma = 1.4$ 136

8.5 The fractional residuals of various Seyfert 1 and Seyfert 2 mixture 2–10 keV CXB spectra to a power-law of $\Gamma = 1.4$ . . . 137
8.6 Positions of the HEAO-1 A2, Ginga LAC, and GIS on the Ω_e-S_c plane . . 140

B.1 LSS (Counting rate contour-map image of M^{CCF} in 0.7–7 keV) . . . 148
B.2 SA57 . . . 149
B.3 Draco Field . . . 149
B.4 NEP . . . 150
B.5 QSF3 . . . 150
B.6 z-system . . . 151
B.7 Braccesi Field . . . 152
B.8 Jupitar . . . 153
B.9 Arp 220 . . . 153
B.10 3C368 . . . 153

C.1 LSS (Flat field image and source-mask at the threshold of 0.10) . . . 156
C.2 SA57 . . . 157
C.3 Draco Field . . . 157
C.4 NEP . . . 158
C.5 QSF3 . . . 158
C.6 z-system . . . 159
C.7 Braccesi Field . . . 160
C.8 Jupiter . . . 161
C.9 Arp220 . . . 161
C.10 3C368 . . . 161

D.1 SA57 (Spectrum after source-masking of 0.1 fitted with $PL^{\rm hard} + PL^{\rm soft}$) . 163
D.2 a-LSS . . . 164
D.3 b-LSS . . . 164
D.4 c-LSS . . . 164
D.5 d-LSS . . . 165
D.6 Draco Field . . . 165
D.7 NEP . . . 165
D.8 QSF3 . . . 166
D.9 z-system . . . 166
D.10 Braccesi Field . . . 166
D.11 Jupiter . . . 167
D.12 Arp 220 . . . 167

D.13 3C368 167

E.1 LSS (Source-mask at the threshold of 0.06) 170
E.2 SA57 170
E.3 Draco Field 170
E.4 NEP 170
E.5 QSF3 171
E.6 z-system 171
E.7 Braccesi Field 172
E.8 Jupiter 172
E.9 Arp 220 172
E.10 3C368 172

F.1 LSS (Hardness-map gray-scale image of $M^{H/S}$) 174
F.2 SA57 174
F.3 Draco Field 174
F.4 NEP 174
F.5 QSF3 175
F.6 z-system 175
F.7 Braccesi Field 176
F.8 Jupiter 176
F.9 Arp 220 176
F.10 3C368 176

G.1 Map of the total number of hydrogen atoms on the sky 178
G.2 The X-ray sky from HEAO-1 A2 in Galactic coordinates at 3° resolution . 178
G.3 ROSAT PSPC all sky survey X-ray intensity Galactic coordinates maps . . 179
G.4 Brief descriptions of the main features seen in figure G.3 180
G.5 (a) C-band and (b) M-band maps from the Wisconsin sky survey 180

H.1 The observed Crab counting rate plotted against the offset angle 182
H.2 Calculation of Ω_e for the XRT+GIS. 183

List of Tables

3.1 Design parameters and performance of the ASCA XRT. 21
3.2 Design parameters and performance of the SIS 25
3.3 Design parameters and performance of the GIS 28
3.4 NXB count rate of the GIS in the 0.17–11 keV range under various rejection conditions 35
3.5 Summary of the GIS monitor counts 36

4.1 Summary of the coordinates 44
4.2 Summary of factors constituting the response function 45
4.3 Summary of the calibration files of XRT and GIS for jbldarf 46
4.4 An absorbed power-law fits to the 0.6–10 keV spectrum of the Crab nebula 54
4.5 Log of the Crab stray observations 60
4.6 Summary of the flare-cut conditions 72
4.7 Systematic errors of the RNXB counts in the 0.7–7.0 keV energy band . . . 75

5.1 Summary of the observed fields to be employed in this thesis. 77

6.1 Model fits to the 2–10 keV spectrum of the CXB 91
6.2 Model fits to the 0.6–10 keV spectrum of the average CXB 93
6.3 Summary of the systematic errors for the CXB spectrum in the LSS field . 100

7.1 ($PL^{\rm hard}$+$PL^{\rm soft}$) fits to the 0.6–10 keV spectrum of each field including point sources. All errors are 90% confidence level. $\Gamma^{\rm soft}$ is fixed to 6.0. . . 102
7.2 Fitting results of M^{RATIO} pixel values distribution for each sample field . 114
7.3 $PL^{\rm hard}$+$PL^{\rm soft}$ fits masking point sources at 0.1 on M^{FLAT}. 116
7.4 Mean values and standard deviations of $\Gamma^{\rm hard}$, $F_{\rm X}^{\rm hard}$, and $F_{\rm X}^{\rm soft}$. 118
7.5 ($PL^{\rm hard}$+$PL^{\rm soft}$) fits to the 0.6–10 keV spectrum of the total CXB (SA57+LSS+ Draco+NEP+QSF3+ZSYS+BF) and the whole LSS. All errors represent 90% confidence levels. 125

8.1 Summary of the previous results and the present work (ASCA XRT+GIS) 139

8.2 Rough estimations of the effective beam size Ω_e (deg^2) for each CXB observation 140

A.1 Pointing list of the LSS observations in GO-1 and GO-2 144
A.2 Pointing list of the LSS observations in GO-3 145
A.3 Pointing list of the observations 146

E.1 ($PL^{\rm hard}$+$PL^{\rm soft}$) fits to the 0.6–10 keV spectrum of each field with point sources being masked at the threshold of 0.06 on M^{FLAT}. All errors are the 90% confidence level. $\Gamma^{\rm soft}$ is fixed to 6.0. 169

G.1 Summary of the X-ray images in this chapter 177

Chapter 1

Introduction

1.1 The Cosmic X-ray Background (CXB)

It is not too much to say that the X-ray astronomy began with the cosmic X-ray background (CXB), a diffuse X-ray radiation coming from all directions of the sky (for reviews, see Boldt 1987; Fabian & Balcons 1992). Discovery of the CXB precedes that of cosmic microwave background (CMB) by Penzias and Wilson (1965), and goes back to the rocket experiment made in 1962 which was intended to study fluorescence X-rays from the Moon. The observers did not detect lunar X-rays, but instead they discovered the first extra-solar X-ray source which we call today Scorpius X-1, as well as the CXB (Giacconi et al. 1962).

The CXB dominates the energy density of the entire X-ray sky. Its spectrum has a canonical photon index $\Gamma = 1.4$ (photon number flux $\propto E^{-\Gamma}$ where E is the X-ray photon energy) in the 2–10 keV range, gradually steepening up to a few hundreds keV (see §2.2.1). The CXB brightness is highly isotropic, except for a small dipole anisotropy (§2.2) which arises from solar system's proper motion with respect to the Hubble flow. Only a week correlation ($13\pm5\%$) was detected with bright galaxy counts for the 2–10 keV CXB (Jahoda et al. 1991). These properties make us confident that the CXB undoubtedly has a cosmological origin, except in the energy range below ~ 2 keV where contributions from various Galactic components are significant. Indeed, this fact has been the prime motive force for the huge amount of effort spent in the CXB studies, for more than 30 years since its first discovery. Nevertheless, the exact origin of the CXB is still unclear.

So far, two categories of explanations were proposed for the CXB. One of them regard the CXB as a thermal radiation from hot diffuse plasmas permiating the universe, inspired by the apparently thermal shape of the CXB spectrum (see §2 for detail). However, this possibility has been ruled out (at most 0.01% of the total CXB brightness), because of the lack of the inverse-Compton effect expected in the CMB spectrum (§2). Therefore, presently we are left with only the other category of models, which regard the CXB as a

superposition of unresolved faint X-ray sources (mostly active galactic nuclei, or AGNs) distributed up to cosmological distances ($z \sim 1$–4).

As the cosmic X-ray observations made a rapid progress, a progressively larger farction of the CXB has been resolved into discrete X-ray sources (Boldt 1987). Particularly, deep observations with ROSAT have resolved ~ 70 % of the CXB below ~ 2 keV into discrete sources (Shanks et al. 1991; Hasinger et al. 1993). The faintest point sources thus resolved are by more than 8 orders of magnitude X-ray fainter than the first discovered Scorpius X-1, and most of them have subsequently been identified with dsitant AGNs. The ROSAT observations have also shown that the CXB spectrum steepens to $\Gamma \sim 2.1$ below 2 keV, and suggested that, in this energy band, the faint AGNs have similar spectral slopes.

1.2 Problems with the CXB

The ROSAT results on the CXB, though remarkable, are limited to the soft energy reange below ~ 2 keV where ordinary X-ray telescopes can work. This is a very minor portion of the vast energy region over which the CXB phenomenon is seen. Furthermore below ~ 2 keV, the CXB begins to be strongly affected by soft X-rays from Milky-Way plasmas and from local environment (Hot Bubbles) around the solar system (§2), both of which are diffuse but highly anisotropic. Below ~ 1 keV, photoelectric absorption of the CMB photons by our Galaxy's interstellar medium becomes significant, too. These facts urge us to carry on the CXB investigations in harder energy ranges.

In fact, when we turn our eyes to the energy region above 2 keV, the CXB mystery is far from being solved. Among several problems, the most serious one is so called "spectral paradox" (Boldt 1987); as described in §2.3.3, most known X-ray sources have too soft (steep) spectra to account for the observed CXB spectral slope of $\Gamma = 1.4$. Therefore, when a contribution of known objects is subtracted from the CXB spectrum, we are left with unusually hard spectral component. There is a possibility that highly absorbed AGNs, such as type 2 Seyfert galaxies, can provide the required hard spectral component (§2.3.4). However this view needs examinantion from X-ray observations above ~ 2 keV, where their spectral contribution is expected to be significant.

The CXB isotropy makes an outstanding contrast to the enormous inhomogeneities observed in the local universe, such as voids, great walls, and superclusters. The CXB isotropy provides a strong constraint on the lumpiness of spatial distributions of X-ray objects (mainly AGNs) contributing to the CXB, presumably in redshift ranges of $z \sim$ 0.5–3. At present, we do not know wheter the CXB isotropy can be reconciled with the inhomogeneities of the present-day universe, in terms of scenarios for the AGN luminosity evolution and for the evolution of large-scale structures.

1.3 CXB investigations with ASCA

With the ASCA observatory (Tanaka et al. 1994) launched on 20 February 1993, the CXB study is expected to make a big progress. ASCA is the first X-ray satellite covering an energy range of 0.5–10 keV, as realized by the four units of co-aligned X-ray Telescopes (XRTs; §3.2); importance of the sensitivity up to $\sim$ 10 keV in the CXB study may need no explanation. Furthermore, ASCA for the first time combines the *classical* energy range above $\sim$ 2 keV explored by non-imaging experiments, and the soft X-ray range below $\sim$ 2 keV where Einstein and ROSAT missions have made important contributions.

The XRT onboard ASCA provides several more advantages in the CXB study. It gives an imaging capability with a moderate angular resolution of order $\sim$ 3 arcmin. This enables us to detect and exclude point sources in the field of view, hence to study the genuine *unresolved* CXB for the first time above 2 keV. The ASCA field of view of $\sim 40'$ diameter is also ideal, because the large-scale structures seen in the present-day universe has a typical scale length of 100 Mpc, which translates to an angular scale of 0.5°–1° at redshift ranges of $z = 1$–3 where the CXB may originate. Yet another advantage is that the XRT has a very high throughput, achieving a photon collecting area three times that of ROSAT at 1 keV when the four modules are combined. Accordingly we can collect much larger number of CXB photons than ROSAT.

The XRT focal plane is equiped with two types of imaging X-ray detectors, the Solid-State Imaging Spectrometer (SIS; §3.3) and the Gas Imaging Spectrometer (GIS; §3.4). Both SIS and GIS have two particular advantages for the CXB study. One is their superior energy resolutions, which enable us to quantify the CXB spectrum with a high accuracy. The other is their extremely low level of non X-ray background, which is an essential feature when we investigate a diffuse emission with imaging optics.

1.4 Outline of the present thesis

In the present thesis, we attempt to derive the best estimates ever obtained for the spectrum and large-scale isotropy of the 0.7–10 keV CXB. Preliminary ASCA results on the CXB, using the SIS data, have already been published by Gendreau et al. (1995), in which the author of the present thesis is included as a co-author. In this thesis, on the contrary, we concentrate on the GIS data for the two reasons. One is that the GIS covers the entire XRT field of view of $\sim 40'$ diameter, whereas the SIS has a smaller field of view of $20' \times 20'$. The other reason is that the author belongs to the GIS team, and has deeply contributed to the development, pre-launch tests, in-orbit calibration, and software development for the GIS project. All these efforts provide a valuable basis for the CXB

investigation, and will constitute an important part of the present thesis.

The present thesis is arranged in the following way. In Chapter 2, we review essential properties of the CXB, and in Chapter 3 we describe the ASCA spacecraft and its instruments. Chapter 4 summarizes those efforts of instrumental calibrations that are relevant to the CXB study, and that have been contributed significantly by the auther himself. We give in Chaper 5 a brief description of how the 10 sample fields were observed. In Chapter 6 we carry out a pilot study of the average CXB spectrum for one of the sample fields called LSS, although the effect of point sources is still included. Chapter 7 is devoted to our main effort of removing point sources and quantifying the properties of the remaining CXB for all the sample fields. There, we show that the CXB spectrum in the 1.5–10 keV range can be described with a single power-law of $\Gamma = 1.44 \pm 0.06$, and the field-to-field brightness anisotropy is at most 9.2% (90% confidence level) after removing point sources with 2–10 keV fluxes above $\sim 2 \times 10^{-13}$ erg cm^{-2} s^{-1}. Finally, we discuss these results in Chapter 8.

In closing this chapter, we remark that two related thesis works are in progress using the ASCA data. These are the thesis work by Ueda (1996) who is studying the source number counts in the laregest continuous sky area (called LSS) covered with ASCA, and that of Ogasaka (1996) who analyzes source counts in the deepest sky region (caled SA57) observed with ASCA. The three thesis works utilize partially overlapping ASCA data base, but are fully independent of, and complementary to, one another.

Chapter 2

Review of the Cosmic X-ray Background

2.1 Spectral properties of the CXB

2.1.1 CXB spectrum above 2 keV

In early days of the X-ray astronomy, the CXB energy-flux specrum $I(E)$ was expressed with a broken power-law as (Schwartz and Gursky 1974)

$$I(E) = \begin{cases} 1.36 \times 10^{-8}\ E^{-0.40} & (1 \leq E \leq 21\ \mathrm{keV}) \\ 2.68 \times 10^{-7}\ E^{-1.38} & (21 < E\ \mathrm{keV}) \end{cases} \quad \mathrm{erg\ cm^{-2}\ s^{-2}\ str^{-1}\ keV^{-1}}, \quad (2.1)$$

where E is the X-ray photon energy in unit of keV. The energy index of 0.4 below 21 keV is equivalent to the photon index $\Gamma = 1.4$ mentioned in §1.1.

Later, observations with the HEAO-1 mission showed that the CXB spectrum in the 3–100 keV range can be expressed in a single form as

$$I(E) = 9.0 \times 10^{-9} \left(\frac{E}{3\ \mathrm{keV}}\right)^{-0.29} \exp\left(-\frac{E}{40\ \mathrm{keV}}\right) \quad \mathrm{erg\ cm^{-2}\ s^{-2}\ str^{-1}\ keV^{-1}} \quad (2.2)$$

(figure 2.1; Marshall et al. 1980; Rothschild et al. 1983; Boldt 1987) which is essentially identical to the thermal bremsstrahlung spectrum with temperature $kT = 40$ keV. In the 2–10 keV range, equation (2.1) and equation (2.2) are consistent within measurement errors.

By integrating these equations, the 2–10 keV CXB surface brightness becomes

$$F_{\mathrm{X}}^{2-10\,\mathrm{keV}} = 5.6 \times 10^{-8} \quad \mathrm{erg\ cm^{-2}\ s^{-1}\ str^{-1}}\ . \quad (2.3)$$

Therefore, by integrating over the whole sky, the 2–10 keV CXB energy flux becomes 7×10^{-7} erg cm^{-2} s^{-1}, a value quite close to that of Scorpius X-1 that is usually by far the brightest object on the X-ray sky.

2.1.2 Lack of inerse-Compton effects

As already mentioned in §1.1, the agreement of the CXB spectrum of equation (2.2) with the $kT = 40$ keV bremsstrahlung has naturally inspired a set of theoretical models

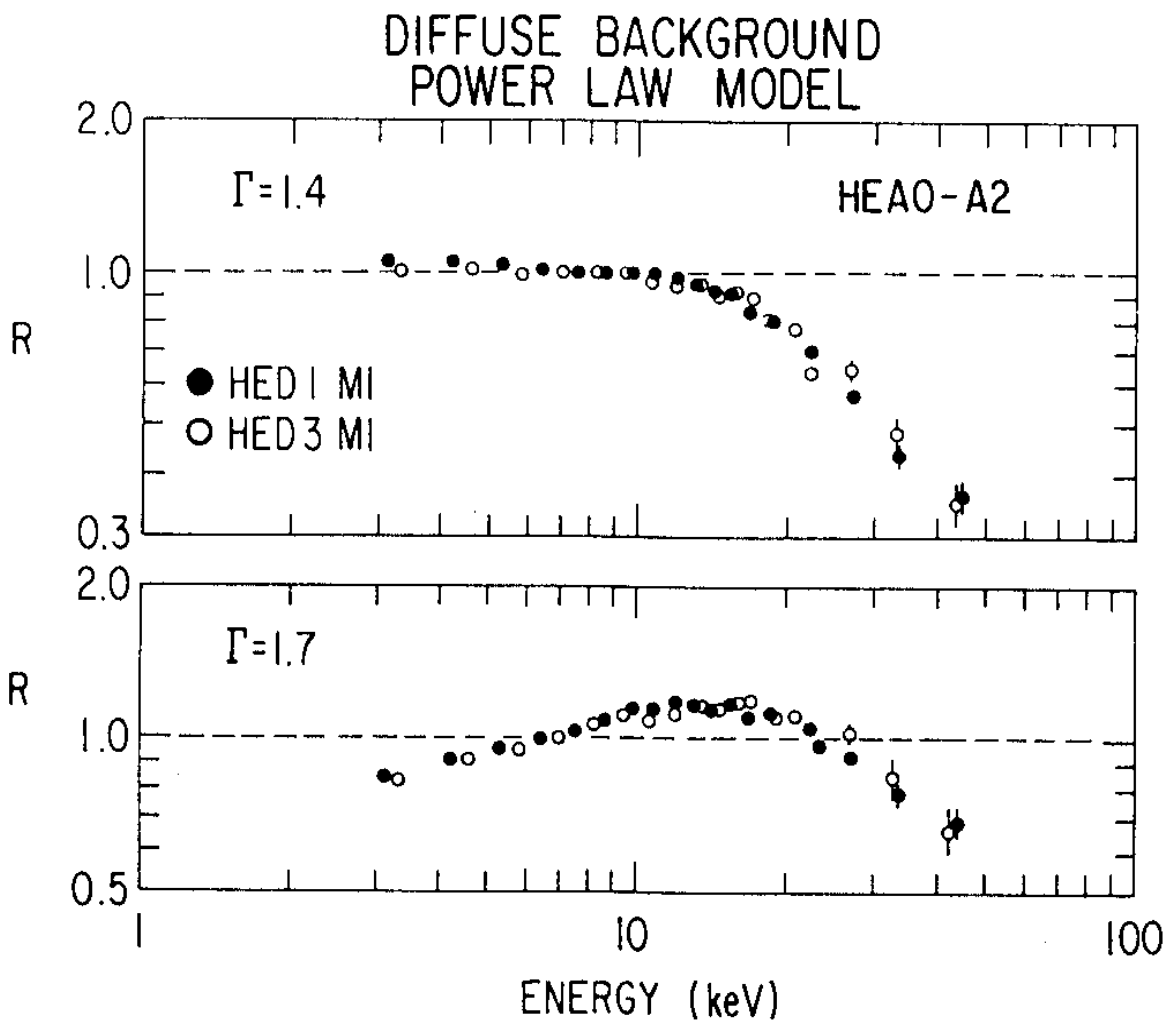

Figure 2.1: The 3–50 keV CXB spectrum observed with HEAO-1 A2, adopted from Boldt (1987). The ratio (R) of the observed CXB counts to that predicted by convolving, with the detector response, power-law spectra of photon indices $\Gamma = 1.4$ (upper panel) and $\Gamma = 1.7$ (lower panel) are plotted against energy.

which consider the CXB as thermal emission from hot diffuse plasmas of cosmological scales (Hoyle 1963; Cowsik & Kobetich 1972; Field & Perrenod 1977). Such hot plasmas, if distributed with a uniform density n_e which is high enough to account for the CXB brightness, would distort the CMB spectrum to a measurable degree. This occurs when the CMB photons, while traveling to us along a path lenght s, get inverse-Compton scattered off the high energy electrons in such plasmas (Zeldovich and Sunyaev 1969). The degree of this Zeldvich-Sunyaev effect can be parameterized by so-called Compton y-parameter, i.e., a dimension-less quantity defined as

$$y = \int d\tau_e \cdot \frac{k(T_e - T_\gamma)}{m_e c^2}, \tag{2.4}$$

where T_e, T_γ and $\tau_e = \int n_e \sigma_e ds$ are the electron temperature of the plasma, the CMB photon temperature, and the optical depth for the inverse-Compton scattering; σ_e denotes the cross section of inverse-Compton scattering.

The high-precision measurements with the Absolute Microwave Spectrometer onboard the Cosmic Background Explorer (COBE) showed that the CMB spectum agrees with a blackbody spectrum of 2.74 K with an amazing accuracy (up to 0.01%; Mather et al. 1990, 1994). The derived limit on the Comptonization effiect is as stringent as $y < 2.5 \times 10^{-5}$, and the implied high-temperature plasma density can account for at most 0.01% of the CXB brightness. Thus, the hot plasma model for the CXB has apparently ruled out.

We must however keep in mind that the story becomes quite different when the plasma is distributed inhomogeneously, in the form of blobs or filaments. When the volume filling factor of the assumed hot plasma is as small as $< 10^{-3}$, there is a solution for the plasma density that is consistent with both the COBE limit and the CXB brightness (Mineshige and Tajima, private communication).

2.1.3 CXB spectrum below 2 keV

The diffuse X-ray background below 2 keV has been studied with ROSAT, as well as with previous rocket experiments by many groups including Leiden-Nagoya, ISAS (Institute of Space and Astronautical Science; Inoue et al. 1979), and University of Wisconsin. These results are summarized by Tanaka and Bleeker (1977), McCammon et al. (1983), and McCammon and Sanders (1990). Among these experiments, the Japanese K-10-13 rocket experiment (Inoue et al. 1979) is of particular meaning for us, because it provided the startpoint for the gas scintillation proportional counter technique in Japan, which later developed into Tenma GSPC (Koyama et al. 1984) and finally into the ASCA GIS.

In contrast to the simple CXB spectrum above 2 keV (§2.1.1), the CXB properties are much more complex below 2 keV, since there are strong contributions from various Galactic emission components (of mostly thermal nature) as well as effects by the Galactic photoelectric absorption; naturally, the brightness becomes highly anisotropic (appendix G). In so called Carbon band below 0.28 keV, which is the lowest window of the cosmic X-ray observations, the sky is dominated by thermal emission from "Hot Bubble" surrounding the solar system, i.e. an ionized region of temperature (1–2) $\times 10^6$ K (0.1–0.2 keV) presumably created by an ancient supernova explosion.

In the energy range between 0.28 keV and $\sim$ 1 keV, Galactic emission components of somewhat larger scales becomes dominant. These include the $kT \sim 0.2$ keV emission associated with a high-latitude Galactic structure called Loop I or North Polar Spur (figure G.4), and the $kT \sim 0.6$ keV soft component (Kaneda et al. 1996, private communication) of so-called Galactic ridge emission (Koyama et al. 1986) which is seen along the Galactic plane.

In adition to these Galactic components and the truly *cosmic* hard ($\Gamma = 1.4$) emission,

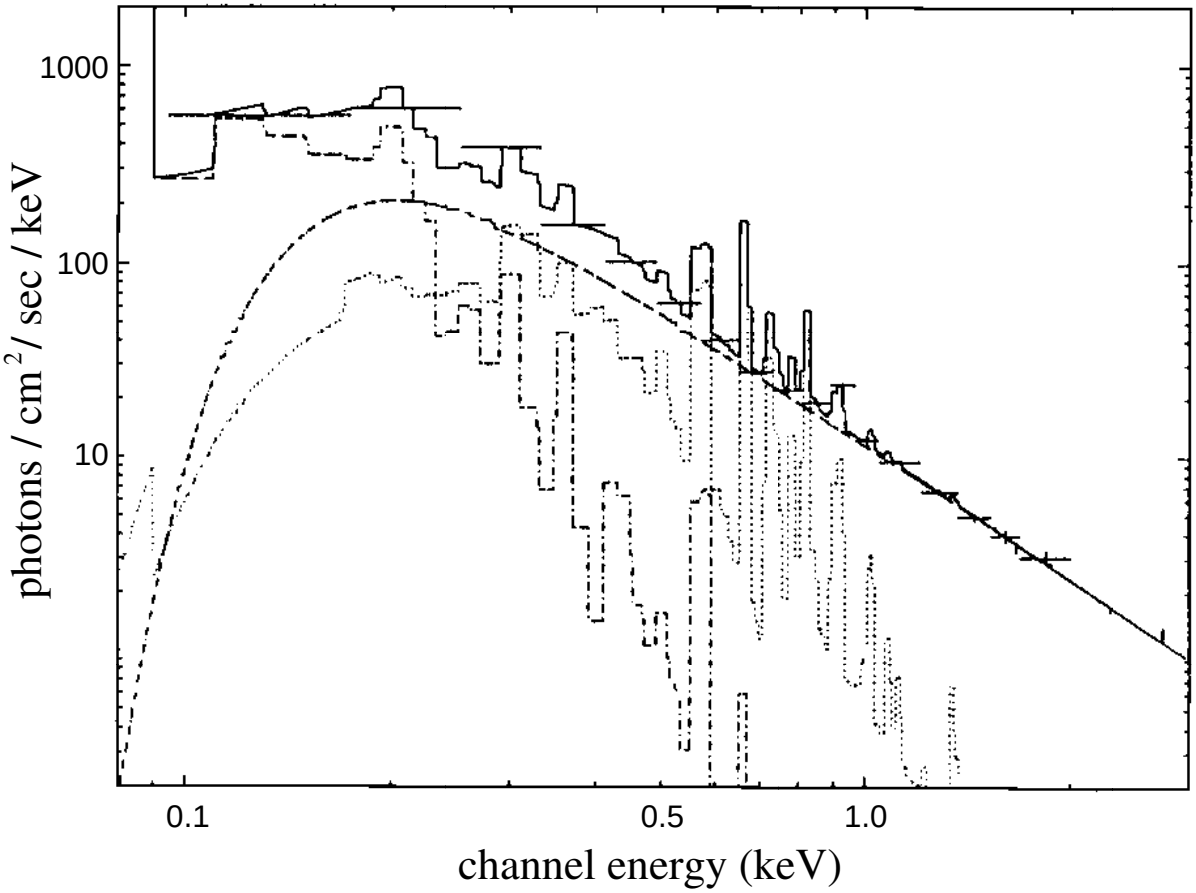

Figure 2.2: The 0.1–2 keV CXB spectrum observed with ROSAT PSPC, adopted from Hasinger (1992); three-component fit to the total background in the HZ43P field: a 10^6 K thermal plasma, a 2–3 $\times$ 10^6 K thermal plasma, and a power-law of $\Gamma \sim 2.2$ for the higher energies.

there is yet another CXB component revealed by ROSAT (figure 2.2; Shanks et al. 1991; Hasinger et al. 1993); as mentioned in §1.1, it is seen as an excess above the hard component in a relatively narrow energy range around 1 keV, where the Galactic components and the hard component cross over. It has a steeper ($\Gamma \sim 2.1$) slope, yet it may be quite isotropic. We have at least four different and mutaually non-exclusive explanations for this enigmatic intermediate component in the CXB, and at present, we can either prove or disprove none of these possibilities:

1. It may be an intrinsic feature of the hard CXB component, produced by the same population of cosmological objects. The soft excess of AGNs is one such possibility.

2. It may be a cosmological phenomenon, but produced by objects of different population (e.g. clusters of galaxies, normal galaxies, etc.) than those responsible for the hard CXB component.

3. It may be a Galactic component (e.g. a thermal halo associated with the Milky Way) with a very large scale height.

4. It may be thermal emission from a hypothesized plasma halo gravitationally bound by the potential of Local Group (a poor galaxy group including our own Galaxy, M31, M33, and so on). This has been conjectured by Makishima (1995, a private communication) and evaluated by Suto et al. (1996).

2.2 Brightness distribution of the CXB

2.2.1 Small-scale fluctuations

The CXB brightness above 2 keV is highly isotropic. However, the CXB is at least partially made up of discrete sources, and each "blank sky" field in fact includes a number of X-ray sources which are individually too faint to be *detected* or *resolved*. Since the number of these faint discrete sources in the f.o.v. statistically fluctuates, a certain level of field-to-field fluctuation is always seen in the CXB intensity when many "blank sky" regions are observed with an X-ray instrument with a field of view Ω_e. Assuming that the source distribution is isotropic, we expect that the relative CXB fluctuation scales as ${\Omega_e}^{-0.5}\ {S_c}^{0.25}$, where S_c is the detection threshold of that particular instrument. Therefore, the narrower the field of view is, the larger the relative fluctuation becomes.

Using a $3^\circ \times 3^\circ$ beam width of the HEAO-1 A2 experiment, Shafer (1983) derived a 3% upper limit on the beam-to-beam relative CXB fluctuation. Later, Hayashida (1990) employed the $1^\circ \times 2^\circ$ beam of the Ginga LAC, and showed that the rms fluctuation in the CXB intensity is of order 5% in the 2–20 keV after excluding sources brighter than $\sim 1 \times 10^{-11}$ erg cm^{-2} s^{-1}.

Then, what can we learn from these fluctuation levels? If we assume that the CXB fluctuation is totally caused by the statistical fluctuation in the number of unresolved sources in the f.o.v., we can put constraints on the $\log N$-$\log S$ relation (see §2.3 for detail) of discrete sources towards flux levels lower than the detection threshold. Actually, Hamilton & Helfand (1987) analyzed the Einstein data from this point of view, and Shafer & Fabian (1983) analyzed HEAO-1 A2 data. Hayashida (1990) applied this technique to his Ginga data, and estimated the $\log N$-$\log S$ relation down to a flux level of $\sim 1 \times 10^{-13}$ erg cm^{-2} s^{-1} in the 2–10 keV energy band. His estimate has been directly confirmed to be correct by the subsequent ASCA observations (Ueda 1996; Ogasaka 1996), implying that the CXB fluctuation observed with Ginga was indeed caused by the statistics of faint source numbers.

If we can somehow have an *a priori* estimate of the $\log N$-$\log S$ relation below the detection threshold (e.g. by estrapolating the $\log N$-$\log S$ relation from the larger flux ranges, or using deeper observations with the same instrument, or utilizing information in

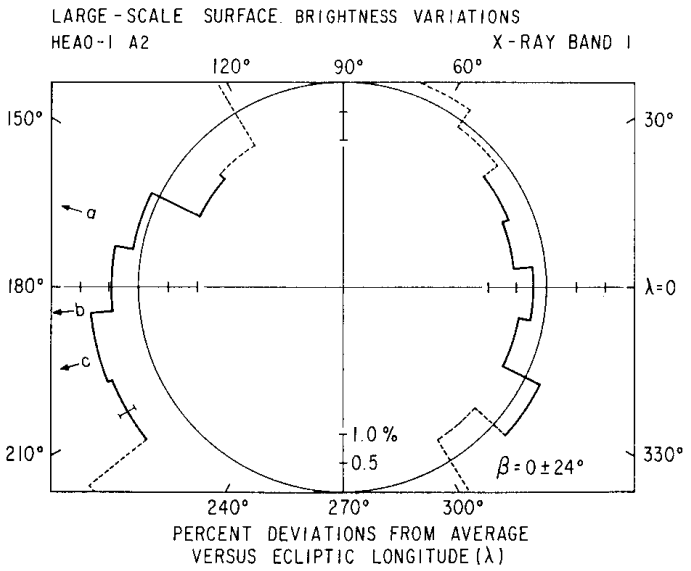

Figure 2.3: The dipole anisotropy of the CXB observed with HEAO-1 A2 all-sky survey, adopted from Boldt (1987); percentage deviations from isotropy (represented by the circle) for the average surface brightness near the ecliptic plane ($\beta = -24^\circ \rightarrow +24^\circ$) as a function of ecliptic longitude (λ). The 1σ error bar shown corresponds to photon counting statistics. Special directions indicated are for the CMB anisotropy results of (a) Smoot et al. (1977), (b) Cheng et al. (1979), and (c) the longitude where the supergalactic plane crosses the ecliptic equator. Surface brightness deviations for those ecliptic longitudes close to the galactic equator (i.e. near $\lambda = 89^\circ$ and $\lambda = 269^\circ$) are indicated with dashed lines.

other wavelengths), we can compare the observed field-to-field CXB fluctuation with what is predicted by the $\log N$-$\log S$ relation. If the observed fluctuation is much larger, we can infer that there is some sort of large-scale spatial structure in the CXB source (e.g. large-scale clustering of the quasars). On the contrary, if the fluctuation is significantly smaller than is expected, it is suggested that the CXB is contributed by something other than discrete celestial objects (e.g. hot plasmas with extremely low filling factor; see §2.1.2).

2.2.2 Global isotropy and dipole anisotropy

Except for the statistical fluctuation mentioned in the previous subsection, the CXB brightness is highly isotropic on the large scale. According to the HEAO-1 A2 result (figure G.2), the large-scale CXB anisotropy is less than 3%. Hayashida (1990) failed to detect any lareg-scale correlation in the Ginga fluctuation analysis.

However, a dipole anisotropy in the CXB brightness has been detected with the HEAO-1 A2 all-sky-survey (figure 2.3; Shafer 1983; Shafer & Fabian 1983). The dipole amplitude of $\sim 0.5\%$, together with its direction, are roughly consistent with the dipole anisotropy in CMB (Smoot et al. 1977). Both these dipole effects are thought to arises from solar

system's proper motion with respect to the Hubble flow.

Possible correlation of the CXB with any Galactic feature (e.g. Galactic quadrupole component, Galactic latitude dependence, and so on) is another subject of interest. For example, Koyama (1989), using the Tenma GSPC, suggested the presence of a $kT \sim 10$ keV diffuse thermal Galactic emission with an extremely low surface brightness, extending up to high galactic latitudes. Such components would show up in the CXB data. However Hayashida (1990) did not find any Galactic latitude dependence in the Ginga CXB intensity. At present, there is no evidence of the *real* CXB above ~ 2 keV correlating with any Galactic feature. This demonstrates the extra-Galactic nature of the CXB.

2.3 Contribution of known classes of discrete sources

2.3.1 Log$N$ - Log$S$ relations above 2 keV

So called $\log N$-$\log S$ relation describes the source number density as a function of source flux in a fixed energy range (in the observer frame). This gives one of the most straightforward way of testing the hypothesis that the CXB is a superposition of numerous discrete sources. Accordingly, the $\log N$-$\log S$ relation has been measured repeatedly with many X-ray experiments, both imaging and non-imaging.

The $\log N$-$\log S$ relation above 2 keV have so far been derived with non-imaging experiments, including UHURU (Schwartz 1979), Ariel V (Warwick & Pye 1978), HEAO-1 A1 (Wood et al. 1984), HEAO-1 A2 (Piccinotti et al. 1982; Shafer 1983), and Ginga LAC (Hayashida 1990; Kondo 1991). These results are summarized in figure 2.4, and they consistently indicates an apparently Euclidian $\log N$-$\log S$ relaion

$$n(S) = (2.2^{+0.3}_{-0.2}) \times 10^{-15}\ S^{-2.5}\ \mathrm{str}^{-1}, \tag{2.5}$$

(Piccinotti et al. 1983) where $n(S)$ is the differential source number density with the 2–10 keV flux S which is given in unit of erg cm^{-2} s^{-1}.

2.3.2 Log$N$ - Log$S$ relations below 2 keV

The $\log N$-$\log S$ relation below 2 keV was first derived with the Einstein observatory through Deep Survey (Giacconi et al. 1979; Primini et al. 1991), and Extended Medium Sensitivity Survey (EMSS; e.g. Gioia et al. 1990; Stocke et al. 1991). These results are shown in figure 2.5. The integral $\log N$-$\log S$ relation of the serendipitously discovered object in the EMSS survey can be expressed as

$$N(>S) = 2.68 \times 10^{-19}\ S^{-1.48\pm0.05}\ \mathrm{str}^{-1}, \tag{2.6}$$

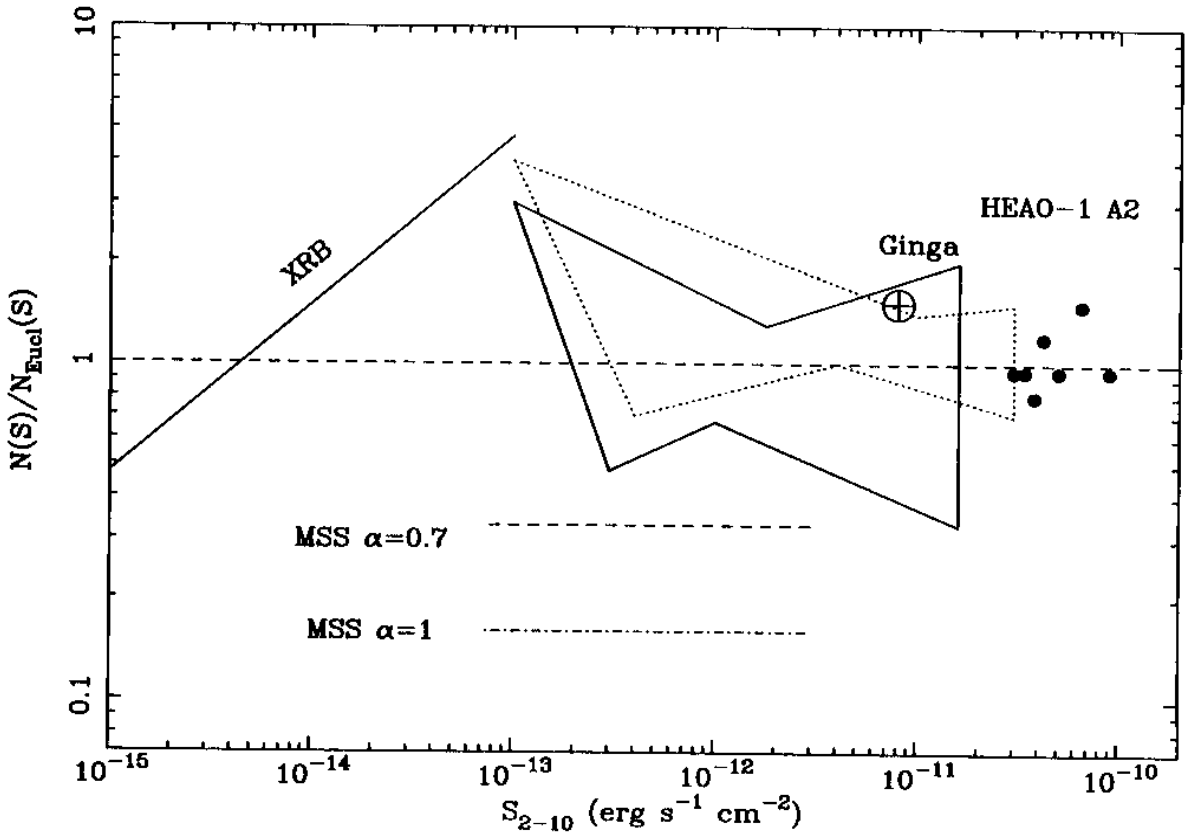

Figure 2.4: The integral $\log N$-$\log S$ relation in the 2–10 keV energy band normalized to that expected in a Euclidean universe, adopted from the review by Fabian & Barcons (1992). The filled circles are from the direct counts of Piccinotti et al. (1982). The dotted contour is the 1σ region from the HEAO-1 A2 fluctuation analysis (Shafer & Fabian 1983), the solid contour from the Ginga fluctuation analysis (Hayashida 1990). The lines marked MSS show the results from the Extended Medium Sensitivity Survey (Gioia et al. 1990) after converted into the 2–10 keV range assuming several spectral indices. The cross represents direct counts from Ginga scans (Kondo 1990). The solid line labeled XRB indicates the level at which 100% of the CXB brightness can be explained.

where S is the 0.3–3.5 keV flux in unit of erg cm^{-2} s^{-1}. At the flux limit of $\simeq 5 \times 10^{-14}$ erg cm^{-2} s^{-1} in the 0.3–3.5 keV band achieved with the Einstein Deep Survey, it was suggested that 16–25% of the CXB was resolved into discrete extragalactic objects (Primini et al. 1991).

Using a deep ROSAT exposure, Hasinger et al. (1993) derived a $\log N$-$\log S$ relation, as shown in figure 2.5, down to a flux limit of $\simeq 3 \times 10^{-15}$ erg cm^{-2} s^{-1} in 0.5–2 keV. At this level, nearly 50% of the 1–2 keV CXB has been resolved into discrete objects. Fluctuation analysis of the ROSAT data (Hasinger et al. 1993) implies nearly 75% of the CXB to be originate in the discrete sources. Also the $\log N$-$\log S$ relation is suggested to deviate from the Euclidian below $S \sim 10^{-14}$ erg s^{-1} cm^{-2}.

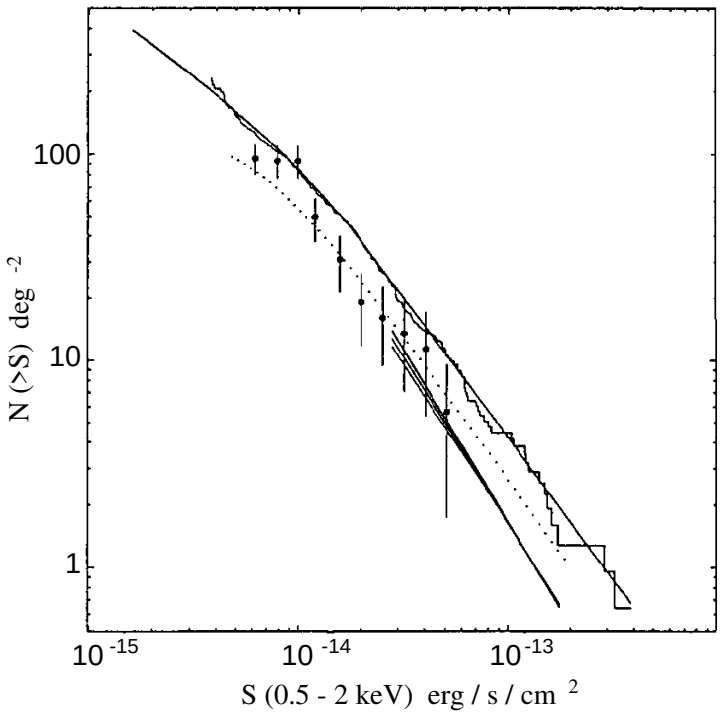

Figure 2.5: The integral $\log N$-$\log S$ relation in the 0.5–2 keV energy band, adopted from Hasinger (1992); ROSAT $\log N$-$\log S$ relation (histogram and solid line) compared to the EMSS (two crossing solid lines) and the data of Shanks et al. (filled circles). Note that the contribution of brighter fluxes has not been added to the latter data.

It has been a matter of considerabale controversy whether the $\log N$-$\log S$ relations derived above and below 2 keV are consistent or not. Since the energy ranges are different, we must assume the source spectrum (specifically the power-law spectral slope) when converting one to the other. When this conversion is done assuming $\Gamma = 1.7$ (figure 2.4), we see a hint of factor 2–3 discrepancy in the sense that the soft-band $\log N$-$\log S$ relation comes in short of the hard-band one, although almost consistent if $\Gamma = 1.4$. This is considered to be an evidence for a possible abundance of hard-spectrum (possibly highly abosrbed) objects. The issue is currently being investigated with ASCA by Ueda (1996) and Ogasaka (1996).

2.3.3 The spectral paradox

Here we review the issue of "spectral paradox" mentioned in §1.2. In the 2–20 keV energy band, type 1 Seyfert galaxies, which form a typical class of AGNs in the universe where redshift is $z \lesssim 0.1$, show an approximately power-law spectrum of $\Gamma = 1.7$ (e.g. Turner and Pounds 1989). Radio-loud and radio-quiet quasars, which represent more distant AGNs, have $\Gamma \sim 2.0$ and ~ 1.6, respectively (Williams et al. 1992). Furthermore, the AGN spectra below 2 keV are generally known to become steeper than those found at higher energies, and $\Gamma \sim 2.3$–2.5 are reported for quasars obtained by the ROSAT all sky survey (Schartel et al. 1994). All these AGN spectra are steeper than the CXB spectrum.

Other celestial objects, such as individual galaxies and clusters of galaxies, generally have still softer spectra because their emission is predominantly of thermal nature. Therefore, it is impossible to synthesize the CXB spectrum from these objects with steeper

spectral slopes, and some population of sources with very hard spectra are required.

As mentioned in §1.2, one possible candidate for such hard-spectrum sources is heavily obscured AGNs, such as a type 2 Seyfert galaxy which is thought to be a type 1 Seyfert galaxy seen along the cold gas disk feeding the central balck hole (Antonucci & Miller 1985). In such objects, X-rays from the central power house exhibit a strong photoelectric absorption presumably by the gas disk, as revealed with Ginga observations (Koyama et al. 1989; Awaki et al. 1990; 1991). Since the absorption makes the spectra of these objects extremely hard in the 2–20 keV energy reange, they can be utilized efficiently to synthesize the CXB spectrum (Fabian et al. 1990). Therefoe, quest for the highly absorved qusars is an important issue to be explored with ASCA, although it is outside the scope of the present thesis.

One issue relevant to the present thesis is that the obscured AGNs usually exhibit very intense fluorescence Fe-K emission lines, sometimes with equivalent widths up to 2 keV (e.g. Fuakazawa et al. 1994). Therefore, if the obscured AGNs are a significant CXB constitutent, we expect to see a trace of Fe-K lines in the CXB spectrum, Although the Fe-K lines must be quite smeared out due to superposition of sources with different redshifts.

Another issue is that a heavily obscured AGN often shows a spectrum which is steeply cut-off below $\sim$ 4–5 keV by absorption (figure 2.6). If such objects are at a redshift of z = 1–3, the cut-off feature will be shifted into an observer energy range of 1–2.5 keV. Therefore, the precise spectral measurement of the CXB in this energy range is extremely important to constrain various models which try to synthesize the CXB spectrum invoking obscured AGNs. Note that the CXB spectrum in this range has remained poorly understood, since previous non-imaging experiments did not have sufficient sensitivity, or sufficient energy resolution to clearly separate the Galactic component. Similarly, soft X-ray telescopes (Einstein, ROSAT) did not have sufficient sensitivity or spectral resolution to firmly fix the $\Gamma = 1.4$ hard component.

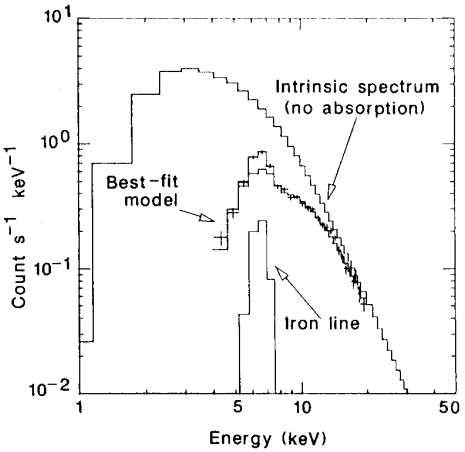

Figure 2.6: Type 2 Seyfert galaxy Mkn3 spectrum (crosses) observed with Ginga LAC, adopted from Awaki et al. (1990). The histograms show the best-fit model (absorbed power-law; $\Gamma = 1.3 \pm 0.3$, $N_{\rm H} = 6^{+3}_{-2} \times 10^{23}$ cm^{-2}, $L_{\rm X}^{2-10\,{\rm keV}} = 4 \times 10^{43}$ erg s^{-2} at a distance of 79 Mpc with $z = 0.0132$) and the intrinsic spectrum of Mkn3 without absorption.

Chapter 3

Instrumentation

3.1 The ASCA satellite

3.1.1 Launch of the ASCA satellite

The scientific satellite ASCA (Advance Satellite for Cosmology and Astrophysics), previously called ASTRO-D, is a project of the Institute of Space and Astronautical Science (ISAS), developed under a Japan-US collaboration (Tanaka et al. 1994). Following Hakucho (1979), Tenma (1983) and Ginga (1987), ASCA is the fourth Japanese satellite devoted to the cosmic X-ray investigations. ASCA has been launched successfully into orbit on 20 February 1993 at 11 a.m. JST, using the three-stage solid-propellant M-3SII-7 rocket, from Kagoshima Space Center (KSC) of ISAS at Uchinoura, Kagoshima. ASCA has achieved a near-circular orbit with a perigee of 520 km, an apogee of 625 km, and an inclination of 31°. ASCA makes about 15 revolutions per day around the Earth, five out of which pass over Japan.

Figure 3.1 shows the in-orbit configuration of ASCA. It weighs 420 kg, and has an octagonal-shaped body of a diameter 1.2 m where six solar panels are attached. The spacecraft has a nested double-cylinder structure, with the outer cylinder serving as the spacecraft body while the inner cylinder serving as an extendible optical bench (EOB). During the launch, the EOB is retracted inside the outer cylinder, and the solar panels are folded around it, so that the entire spacecraft is contained inside the nose fairing of the launch vehicle. Following the launch, the solar panels were successfully deployed on February 25, to ensure the electric power generation up to 490 W. Then the EOB was successfully extended on March 3. Further details of ASCA are given in Tanaka et al. (1994).

At the top of the EOB, four sets of identical imaging X-ray Telescopes (XRTs) are placed. They are all aligned along the satellite Z-axis with a common focal length of 3.5 m. Compared with X-ray telescopes of previous X-ray satellites, the ASCA XRT

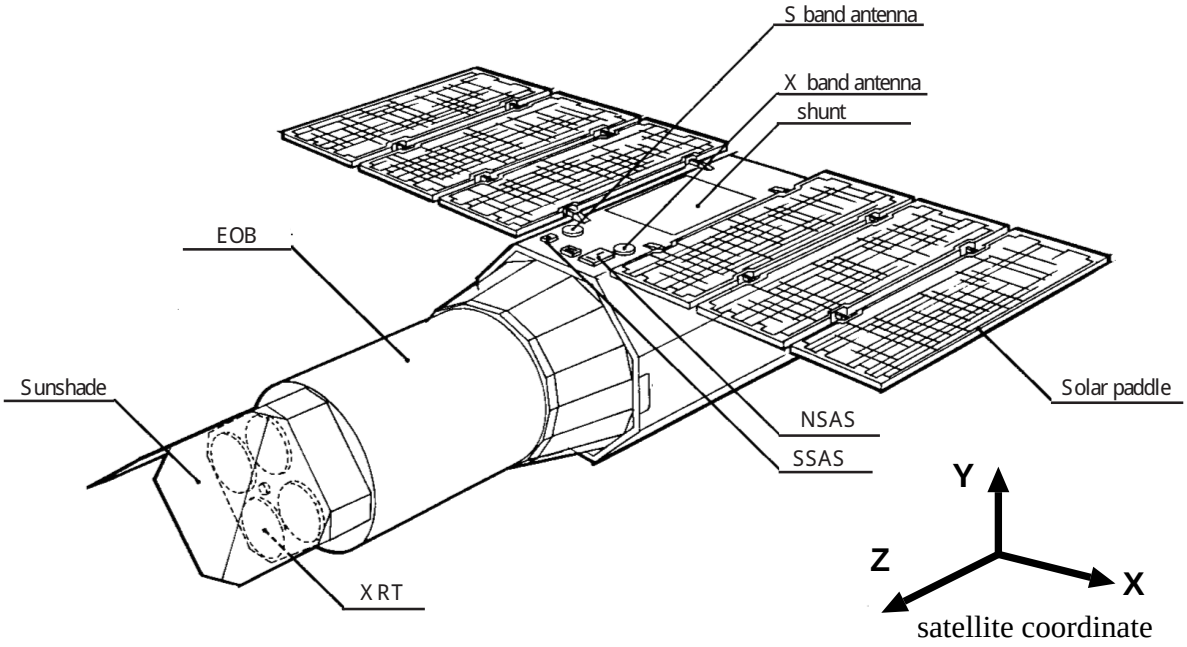

Figure 3.1: In orbit configration of the ASCA satellite

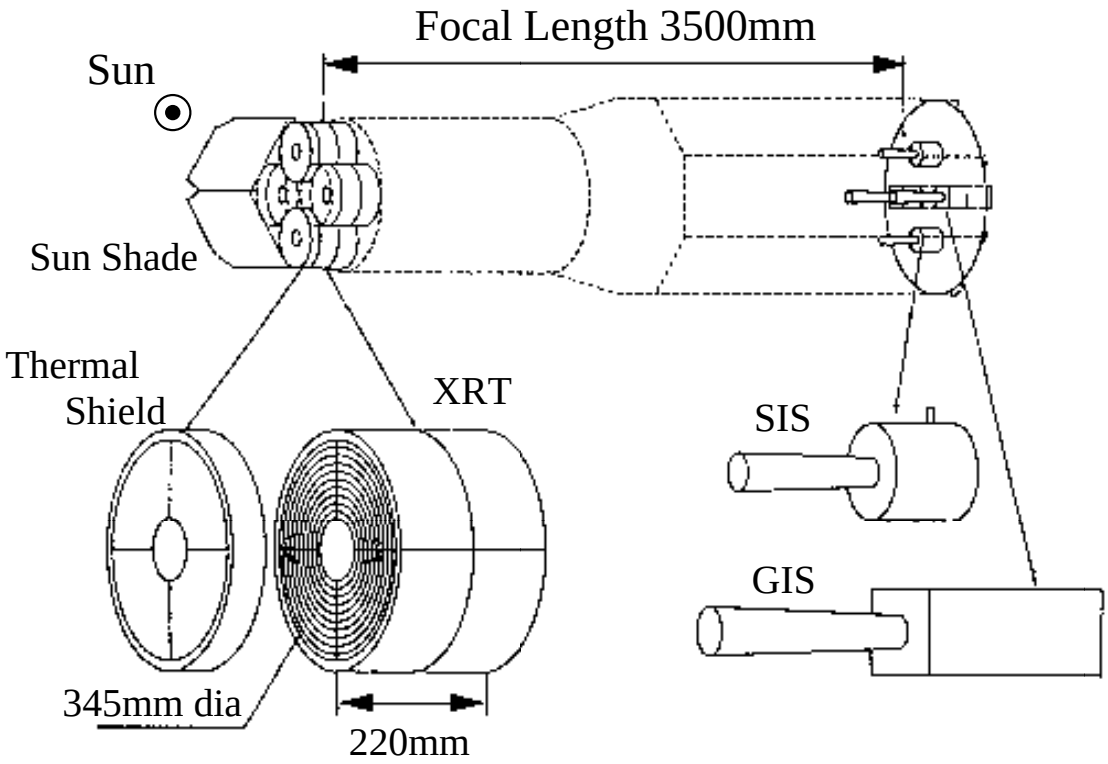

Figure 3.2: Onboard instruments of the ASCA satellite

has a much larger throughput and a drastically wider energy band up to 10 keV (see §3.2). As illustrated in figure 3.2, the focal planes of the XRTs are equipped with four position-sensitive X-ray detectors; two SIS (Solid-state Imaging Spectrometer) detectors called SIS0 and SIS1, and two GIS (Gas Imaging Spectrometer) detectors called GIS2

and GIS3. Each detector is coupled to a fixed XRT, and the four telescope-detector systems acquire data simultaneously for the same target. Both the GIS and the SIS have unprecedent spectral resolutions as well as adequate position resolutions. We describe the XRT, the SIS, and the GIS in §3.2, §3.3 and §3.4, respectively.

3.1.2 Attitude control and attitude determination system

During normal observations, the space craft Z-axis (ref. figure 3.1), along which the XRTs are aligned, is pointed at the target. This can be achieved by an onboard closed loop formed by attitude actuators, attitude sensors, and a CPU-based attitude control processor. The actuators consist of four bias momentum reaction wheels (RW) and three-axis magnetic torquers (MTQ). The attitude sensors include dual star trackers (STT), sun sensors (SSAS and NSAS), three-axis geomagnetic sensors (GAS), and five redundant gyros (IRU). The absolute pointing accuracy is typically 1 arcmin, and the attitude stability is of a similar order. Once the satellite data are transmitted to ground, off-line analysis of the signals from the attitude sensors affords an accurate *post factum* attitude solution up to an accuracy of ~ 1 arcmin.

Changes of the Z-axis pointing direction, called maneuvers, can be done in a semi-automated way, with a typical speed of 5 seconds per degree. ASCA can attain any attitude on condition that the Y-axis direction (ref. figure 3.1) remains within 30° from the Sun to ensure a sufficient power generation by the solar cells. To save the time loss during attitude changes, the maneuvers are performed with a typical frequency of once or twice a day. Therefore each target is observed typically for half a day to one day. However net exposure to the target remains only 50–70% of this gross pointing duration, because useable data cannot be accumulated during passages through regions of high particle background (especially the South Atlantic Anomaly, or SAA), or during the periods when the target is behind the Earth.

3.1.3 Satellite operation and data transfer

We can contact ASCA from KSC five times a day, each lasting for 10–12 minutes. All the necessary commanding must be done during these five contacts. The CPU-based onboard commanding unit keeps control of the satellite all the time, by handling a large number of commands with a given interval, according to the command program which is loaded to the spacecraft from the KSC. The program loading is done typically once a day.

The observed data ($\sim$ 75% scientific and $\sim$ 25% house keeping) are stored in the onboard data recorder (BDR) using magnetic bubble memory of 128 Mbits capacity. The

data acquisition rate is commandable at either 32 (high bit-rate), 4 (medium bit-rate), or 1 kbit/s (low bit-rate). Therefore the BDR becomes full in 1 h 8 m 16 s, 9 h 6 m 8 s, and 36 h 24 m 32 s, in high, medium, and low bit-rate, respectively. In order to continue observations, the stored data must therefore be transmitted to ground via down-link telemetry with a sufficient frequency. It takes 8 m 32 s, and this can be done during passes over the KSC, as well as the US NASA's Deep Space Network (DSN) stations at Canberra, Goldstone, Madrid, Wallaps, and Santiago. The BDR is "played back" typically 10 times a day, thus yielding a daily total of about 1 Gbits of data. Data received at KSC and the DSN stations are transfered to the Sagamihara Space Operation Center (SSOC) of ISAS and stored in a data base. The data is supplied to observers after the attitude determination of the satellite and converting the format into FITS files.

3.1.4 Early operations and observation program

Various common instruments onboard ASCA were turned on, one after another, during the first 2–3 weeks after the launch. In particular the attitude control system has been fully activated, and the spacecraft has achieved the three-axis-stabilized attitude. Spending almost the entire March of 1993, we gradually ran up the four focal plane instruments.

From late April 1993 ASCA entered PV (Performance Verification) phase, which has twofold objectives. One is to exercise various sort of observations to verify and further calibrate the performance of ASCA. The other is to explore scientific capability of ASCA by observing important and attractive objects. The PV-phase data are shared by the entire ASCA team for 1.5 years before they become open to public.

From October 1993, the first round of guest observation phase (GO-1) started; the observation is carried out based on scientific proposals, which are submitted from public to either Japan or US, to get evaluated and accepted by respective committees. After GO-2 (since June 1994) and GO-3 (since November 1994), the fourth GO-phase (GO-4) is going on from December 1995 for one year. In the GO phase, 60% of the total observing time is allotted to the "Japan only" plus "Japan-ESA (European Space Agency)" observations, 25% to the "joint Japan-US" observations, 10% to the "US only" observations, and the remaining 5% is reserved for maintenance and contingency.

For practical reasons, all the targets to be observed (during both PV- and GO-phases) are categorized into seven subfield. These are; stars (including cataclysmic variables), X-ray binaries, supernova remnants (SNRs), galaxies (including our Galaxy), clusters of galaxies, active galactic nuclei (AGNs), and cosmic X-ray background (CXB). Experience through the PV phase has demonstrated that ASCA is capable of innovating our knowledge in all these subfield.

3.2 X-ray telescope (XRT)

The X-Ray Telescope (XRT) onboard ASCA was developed jointly by NASA/GSFC, Nagoya University, and ISAS. It has for the first time enabled cosmic X-ray imaging studies above X-ray energies of a few keV up to about 10 keV (Selemitsos et al. 1995; Tsusaka et al. 1995).

3.2.1 Principle of X-ray telescopes

Soft X-rays are totally reflected off a smooth surface, when their incident angle measured from the surface is shallower than a certain critical value. This phenomenon is known as grazing-incidence reflection. The critical angle, typically of order 1 degree or so, is inversely proportional to the X-ray energy and increases with increasing free electron density of the reflecting material.

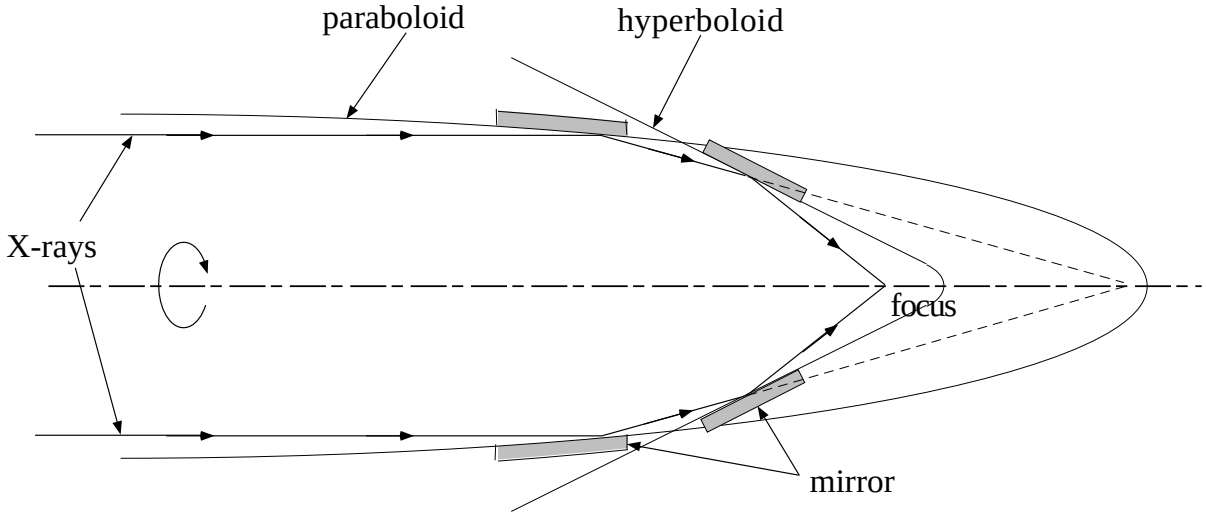

Figure 3.3: Walter type I optics

X-ray telescope mirrors use this mechanism usually in so called Wolter type I configuration (Fig.3.3), which employs paraboloid and hyperboloid surfaces as the primary and the secondary mirrors so as to remove the first-order abberation. The two mirrors have a common focus and reflect X-rays in series (double reflection). This Walter type I optics have been used for many X-ray astronomy satellites, including the X-ray telescope onboard the USA's Einstein Observatory (HEAO-B; 1978–1981), the Low-Energy Telescope onboard the European EXOSAT mission (1983–1986), the main and sub telescopes onboard the joint German/UK/US ROSAT mission (1991–), and the US-made Soft X-ray Telescope onboard the Japanese solar observatory Yohkoh (1991–).

These previous X-ray telescopes have all made the reflecting shells from highly polished glass or glass ceramic, on which heavy metal (Ni, Au, etc.) is evaporated to increase the reflectivity. The effective area is usually increased by having multiple nested set of mirrors

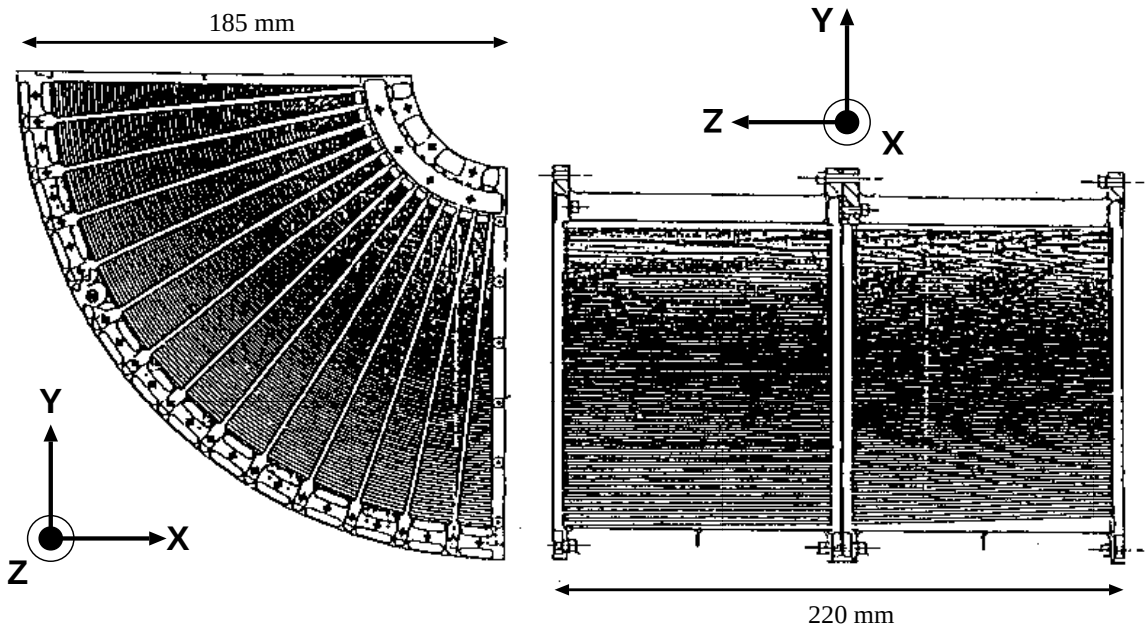

Figure 3.4: One quadrant of the ASCA XRT. The XRT is built up in four quadrants; 120 foils are ajusted by alignment bars running radially.

with a common focus. For example, the Einstein telescope and the ROSAT telescope both use four nesting.

3.2.2 Design and structure of the XRT

Since the critical angle for the total X-ray reflection decreases with increasing X-ray energy, it becomes progressively more difficult to reflect X-rays at higher energies. In order to ensure a high reflectivity for harder X-rays, we must operate the mirror shells under a very small incident angle, hence very small projected area. In order to achieve a large effective area up to higher energies, we must then increase the number of mirror nesting. This can be realized by a design called multiple thin-foil optics, a special version of the Wolter I optics. This design makes each shell extremely thin by using metal foils instead of polished glass, and drastically increase the number of nesting. However it is very difficult to shape a thin foil into a paraboloid or a hyperboloid. Thus, a conical surface is instead used as its approximation, which reduces the imaging quality. A prototype multiple thin-foil mirrors were used successfully in the BBXRT (Broad-Band X-Ray Telescope) experiment flown onboard Space Shuttle mission ASTRO-1 in December 1990. Then the technique has been applied to the ASCA XRT.

As shown in figure 3.4, the reflector shells of the ASCA XRT are all made of thin (127 μm) aluminium foils, bent in a conical form to approximate paraboloid or hyperboloid. The bent foils are $\sim$ 10 μm lacquer-coated to improve the surface smoothness,

and then $\sim$ 50 nm gold-evaporated to increase the reflectivity. 120 of these foils are closely packed together in an onion-ring configuration with a typical spacing of 1 mm, to cover a large fraction of the mirror aperture. The innermost and the outermost shells have diameters of 120 mm and 345 mm, respectively. In practice, the foils are produced and packed in four quadrants, and aligned by 13 alignment bars into 14 sectors. The first and the last sector is masked because shape error is severe. Four quadrants make up the "paraboloid" section of 100 mm long, and another set of four quadrants make up the "hyperboloid" section. One XRT unit thus fabricated weighs about 9.8 kg. Design parameters and performance of the XRT are shown in table 3.1.

Table 3.1: Design parameters and performance of the ASCA XRT.

Mirror substrate	Aluminum foil (127 μm)
Mirror surface	Acrylic lacquer (10 μm) + Au (50 nm)
Mirror length	100 mm
Number of foils per quadrant	120 foils
Inner / outer diameter	120 mm / 345 mm
Focal length	3500 mm
Incident angle	0.24° – 0.7°
Total weight of four XRTs	$\sim$ 40 kg
Geometrical area	558 cm^2 / telescope
Field of view	$\sim 24'$ (FWHM at 1 keV) / $\sim 16'$ (FWHM at 7 keV)
Energy range	$\lesssim$ 10 keV
Effective area of four XRTs	$\sim$ 1300 cm^2 (1 keV) / $\sim$ 600 cm^2 (7 keV)
Half power diameter	$\sim$ 3 arcmin

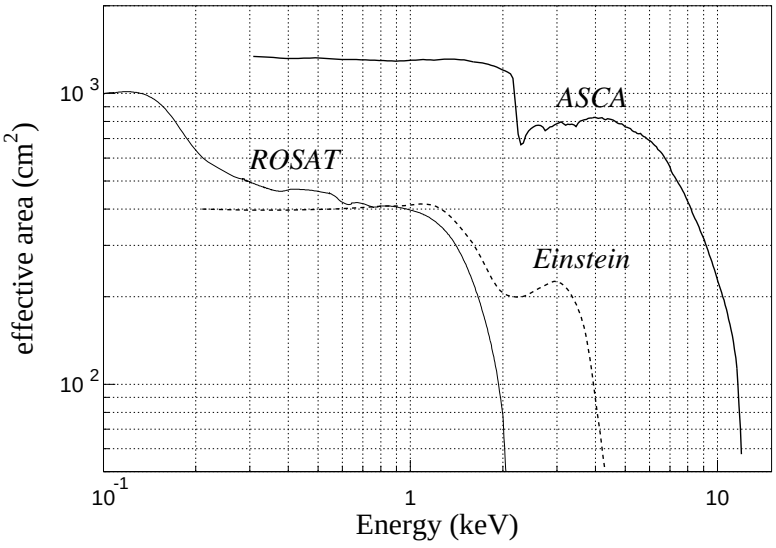

Figure 3.5: Effective area of the ASCA XRT (4 XRTs summed up, on-axis) compared with that of polished mirrors used in previous missions.

The XRT has successfully achieved a very large effective area and a wide energy range, as shown in figure 3.5. When the four units are summed up, the effective area reaches ~ 1100 cm^2 below ~ 2 keV, almost by a factor of 6 and 2 larger than those of Einstein and ROSAT respectively. A sudden drop in the reflectivity at 2.2 keV is caused by the M-edge of the gold used as reflective coating. The XRT maintains a very large reflecting area towards higher energies, e.g. ~ 600 cm^2 at 7 keV, with the upper energy bound as high as ~ 10 keV. X-ray imagery above 3–4 keV has never been achieved by polished mirrors used in previous missions. More detailed performance of the XRT will be discussed in chapter 4.

3.2.3 Alignments of four XRTs to each focal plane detector

The effective area of the XRT for X-ray reflection depends on the direction of incident X-ray, and this effect is called vignetting (see §4.2.2 for further detail). The optical axis of an XRT is defined as a line passing through the mechanical XRT center, along which the effective area is maximized. Due to possible tilt of the XRT mounting onto the satellite, the optical axes of the four XRTs point to slightly different directions. Also, centers of the four focal plane detectors (two SIS and two GIS) correspond to slight different positions on the sky due to positional displacements between an XRT and the corresponding detector. These effects give different vignetting functions to different detectors. Relationships between these positions are measured by instrument teams for the XRT, the SIS, and the GIS. These sets of information are very important for building the instrumental response, and the results are compiled as a telescope definition file (teldef file) of each detector which is registered in the calibration data base (ref. §4.2). In figure 3.6, we summarize measured positions of the detector centers in reference to that of SIS0, together with the optical axis positions projected on the focal plane. The figure also shows "nominal positions" for various observation modes, where the target source of an observation is planned to be placed. In the 1CCD mode, for example, the spacecraft attitude is controlled so that the target centers on the 1CCD nominal position.

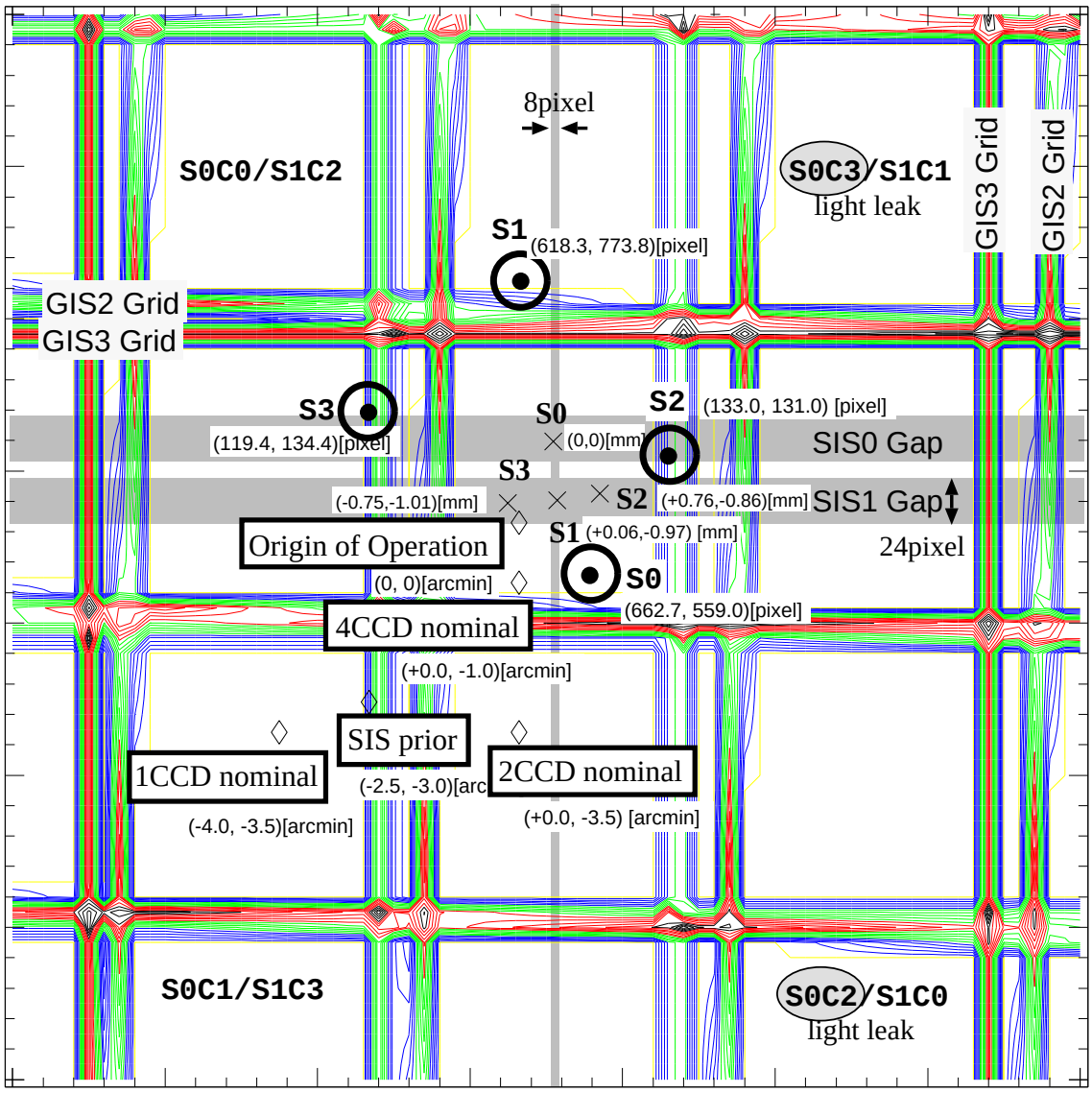

Figure 3.6: Alignment of the four focal plane detectors. Optical axes are shown by "⊙" and their positions are expressed in unit of pixel of the corresponding detectors. Detector centers are shown by "×" and their positions in reference to the center of SIS0 are given in unit of mm. Nominal positions for various observation modes (1CCD nominal, 2CCD nominal, 4CCD nominal, and SIS prior) are shown by "♢" and their positions in reference to the "Origin of Operation" are given in unit of arcmin. The gaps between the CCD chips of SIS0 and SIS1, and the support grids on the entrance windows of GIS2 and GIS3, are also superposed.

3.3 Solid-state Imaging Spectrometer (SIS)

The Solid State Spectrometer (SIS) experiment is the first X-ray detector in orbit that utilizes CCDs (charge coupled devices) in the photon counting mode. It was jointly developed by Massachusetts institute of Technology (MIT), Pennsylvania State University, ISAS, and Osaka University (Burke et al. 1991).

3.3.1 Design and structure of the SIS

The SIS experiment consists of two detectors (SIS camera; SIS0 and SIS1), an analog electronics unit (SIS-AE), and a digital processing unit (SIS-DE) which is combined with the satellite data processor (DP). Figure 3.7 shows a cross section view of the SIS camera.

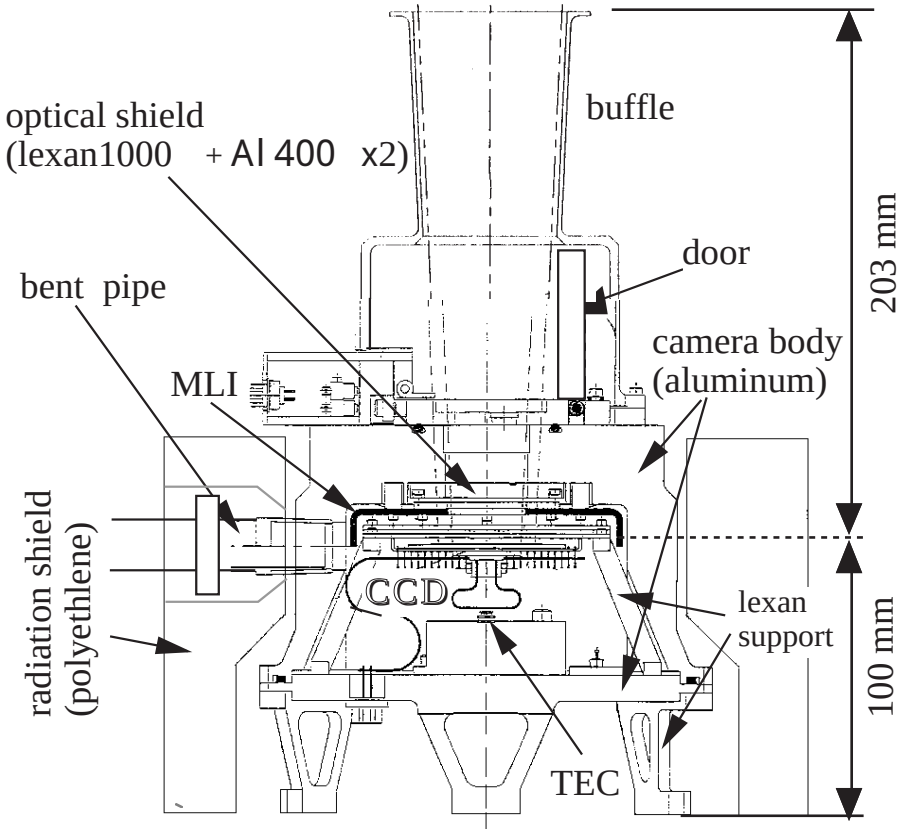

Figure 3.7: Cross section view of the SIS camera

Each SIS detector is made up of four CCD chips of 11 mm square each developed in the MIT Lincoln laboratory, to achieve a 22 mm × 22 mm square area for X-ray detection. The four CCD chips are aligned in square with narrow gaps shown in figure 3.6, to cover about $20' \times 20'$ square region on the sky. Each chip has 4096 by 4096 pixels of 27 μm square each, and a depletion layer of about 40 μm thick which ensures an improved efficiency for harder X-rays than conventional CCDs. Design parameters and performance of the SIS are summarized in table 3.2.

Table 3.2: Design parameters and performance of the SIS

Irradiation Method	Front irradiation
Charge Transfer Method	Frame Transfer
Clock	3-phase drive
Number of pixels in Image Region	420 pixels × 422 lines per chip
Pixel Size	27 μm
Area	11×11 mm square per chip
Field of View	11×11 arcmin square per chip
Thickness of Depletion Layer	$\sim$ 40 μm
Optical Blocking Filter	100 nm Lexan film coated with 40 nm aluminium
Drive temperature	~ -62 °C
Energy Band	0.4–12 keV
Quantum Efficiency	$\sim$ 80% at 5.9 keV
Energy Resolution	2% at 5.9 keV (FWHM)

The CCD chip used for the SIS is a frame transfer type CCD and has the same structure as an optical CCD of the same type. Its detection part is made of an Si semiconductor of p-type and n-type connected each other through p-n junction. An insulator layer made of SiO_2 are attached on the front surface of the n-type Si, and electrodes are built on it. By supplying specific patterns of voltages on the electrodes charges in a pixel are transfered from a pixel to a next pixel. An electrode is also attached on the back. A depletion layer is developed in the device by supplying a bias voltage between the electrodes on the front and on the back.

The aperture is covered by an optical blocking filter (100 nm Lexan film coated with 40 nm aluminium) in front of the CCD chips, in order to prevent visible lights. The whole CCDs are supported by Lexan supports and shielded from charged particles by poly-ethylene of 4 cm thick and aluminum of 1.9 cm thick at the side, aluminum plate of 3.5 cm thick at the bottom, and aluminum of 2.1 cm thickness at the top except for the aperture. A baffle is attached to shield stray light and high energy X-rays as a background.

Electric signals from the SIS camera are fed into SIS-AE and their pulse height are converted into digital signals with analog-to-digital converters. SIS-AE also generates driving clocks for the CCD chips, and monitors and controls temperature of the CCD chips. SIS-DE picks up X-ray events in the digital signals from SIS-AE with two digital signal processor (DSP) and sends them to the satellite data processor (DP), which commonly processes data from the SIS and the GIS and edits them into a telemetry format.

Figure 3.8a illustrates the quantum efficiency of the SIS as a function of incoming X-ray energy. Thus the SIS sensitivity covers approximately 0.4–10 keV. The CCD chips and preamplifiers are cooled down to -60 °C with a thermo-electric cooler (TEC) from the backside of the chips in order to reduce thermal noise down to $N \sim 5$ electrons level. Thus the SIS achieves an energy resolution of about 150 eV FWHM over the whole energy range (figure 3.8b); this is the best energy resolution ever achieved by non-dispersive X-ray spectrometers so far put into orbit.

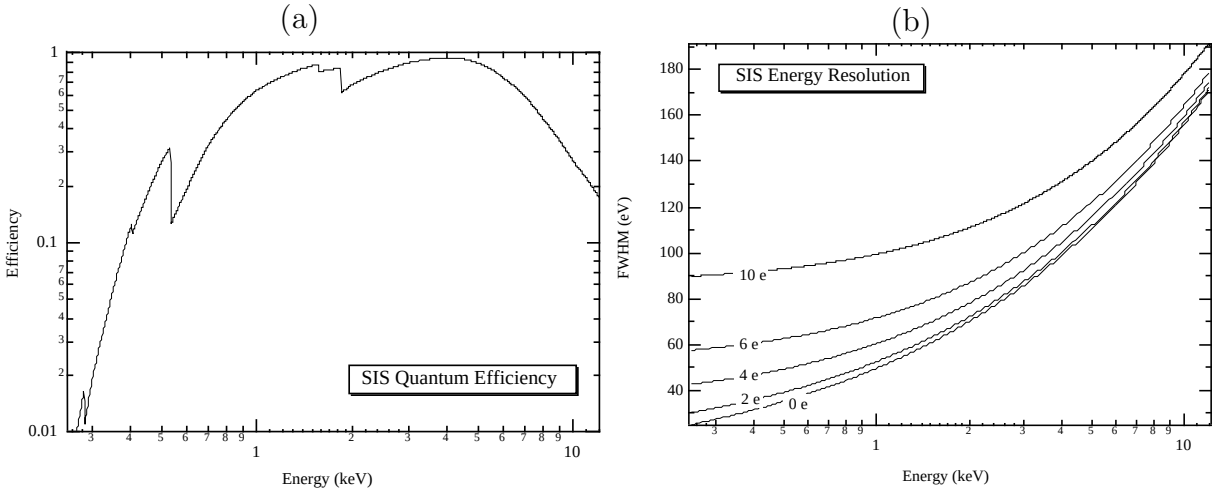

Figure 3.8: (a) Detection efficiency of the SIS as a function of incoming X-ray energy. K-edges of O (0.53keV), Al (1.56keV), and Si (1.84keV) are clearly seen in the figure. This efficiency does not includes optical blocking filter. (b) Energy resolutions of the SIS as a function of incoming X-ray energy for the single event. Energy resolutions with different read-out noise N are plotted ($N \sim 5$ for the SIS). The read-out noise levels are given as the equivalent number of electrons.

3.3.2 Data processing of the SIS

In order to perform proper photon-counting spectroscopy, the CCD frame must be scanned and read out fast enough so that event pile up (i.e. one pixel receiving more than one X-rays) is virtually negligible. Since the read out cycle is usually limited by the telemetry capacity, the SIS performs an extensive onboard CPU processing to compress the information. Instead of sending data from all the pixels to ground, the SIS basically picks up only those pixels in which the charge exceeds a certain threshold, and sends out their positions and pulse-heights. Moreover, to handle targets with different X-ray intensities and angular sizes under different telemetry rates, the SIS uses four different clocking modes; 1CCD, 2CCD and 4CCD modes. In the nCCD mode ($n = 1, 2, 4$), data from n chips for each detector are read out. In the 1CCD mode, e.g., the useable field of view becomes limited to a quarter of the detector, but the event pile up becomes least severe so that we can use slower telemetry rates and observe brighter sources than in

other clocking modes.

The electrons produced in the depletion layer by an X-ray photon may be split into several adjacent pixels. The pattern of charge splitting over 3×3 pixels is called "event grade". When the charge is spread over more than 3×3 pixels, the event is rejected by the onboard CPU as a background event. In order to cope with the splitting of normal X-ray events, the SIS incorporates several data selection modes. For example, in so called "faint mode", pulse-height of a certain pixel with event detection is always accompanied with pulse-heights of the eight surrounding pixels. We can then examine the event grade on ground, and restore the total pulse-height if necessary. In so called "bright mode", the onboard CPU recognizes the charge splitting pattern, and sends only the total pulse-height for events with specified grades. The faint mode requires a larger telemetry capacity, but provides more information than the bright mode. Actually we can convert the faint mode data into the bright mode data on ground, but the reverse is impossible.

After the launch, several additional complications have been recognized with the SIS. One is so called "hot pixels", i.e. particular pixels (though not necessarily fixed ones) which report false event detections too frequently. We must carefully remove these hot pixels in data analysis. When the hot pixels become too many, the SIS data suffer from significant telemetry deadtime. The hot pixels are increasing, and it has become almost impossible to utilize 4CCD mode with the faint mode. Another problem is the light leakage, particularly in chip 2 and chip 3 of SIS0 (S0C2 and S0C3, respectively), presumably caused by a damage in the optical blocking filter. This makes the observation with S0C2 and S0C3 almost impossible when the day Earth is within $\sim 25^\circ$ from the target. It also affects the dark current of the whole CCDs in the daytime, and causes a subtle change in the energy to pulse-height relation. Furthermore the SIS background varies in a complicated way, depending on the SIS operation condition (clocking mode, data mode, split threshold, etc.), as well as the particle environment. There also exists a serious long-term degrading of the SIS performance due to the accumulated radiation damage (Yamashita 1995; Dotani 1995 in ASCA News No.3). These effects make the SIS observations of extended sources quite difficult. Because of these reasons, and also because of the smaller f.o.v. of the SIS, we mainly use the data from the GIS rather than the SIS in this thesis.

3.4 Gas Imaging Spectrometer (GIS)

The Gas Imaging Spectrometer (GIS) has been developed mainly by the University of Tokyo, ISAS, Tokyo Metropolitan University, Meisei Electric Co.Ltd., and Japan Radio Corporation Co.Ltd., with collaborators at Institute of Physical and Chemical Researches (RIKEN), Kyoto University (Department of Physics), NASA/Goddard Space Flight Center (GSFC), and so on (Ohashi et al. 1996; Makishima et al. 1996). The GIS design is mainly based on the GSPC experiment (Koyama et al. 1984) onboard Tenma (Tanaka et al. 1984) which was operating for 1983–1984.

3.4.1 Design and structure of the GIS

The GIS is a general-purpose X-ray imaging spectroscopy system. It consists of the two detector assemblies (GIS-S), namely GIS2 and GIS3 serving as X-ray detectors, and the main electronics called GIS-E. GIS2 and GIS3 are almost identical except that there is a Radiation Belt Monitor (RBM), a small PIN-diode particle monitor, attached to the bottom of GIS2. GIS2 and GIS3 are coupled to two of the four XRTs, and measure pulse-heights and positions of X-rays reflected by the XRTs, photon-by-photon basis. Design parameters and performance of the GIS are summarized in table 3.2.

Table 3.3: Design parameters and performance of the GIS

Energy Band	0.7–15 keV
Energy Resolution	8% at 5.9 keV (FWHM)
Effective Area	50 mm diameter
Entrance Window	10 μm beryllium
Absorption Material	Xe (96%) + He (4%), 10 mm depth, 1.2 atm at 0 °C
Positional Resolution	0.5 mm (FWHM)
Time Resolution	$\sim$ 61 μsec (Minimum in PH Mode)
	1.95 msec (Minimum in MPC Mode)

Sensor assemblies

We show the structure of GIS2 in figure 3.9. GIS2 and GIS3 are weighing 4.30 kg and 4.16 kg respectively. The small difference of the weight is because of RBM. Each sensor consists of a detector assembly and a high-voltage supply unit. Each detector assembly in turn consists of a gas cell, an imaging photo-multiplier tube (IPMT) and front-end electronics, all of which are placed in a housing made of coated magnesium-alloy with a

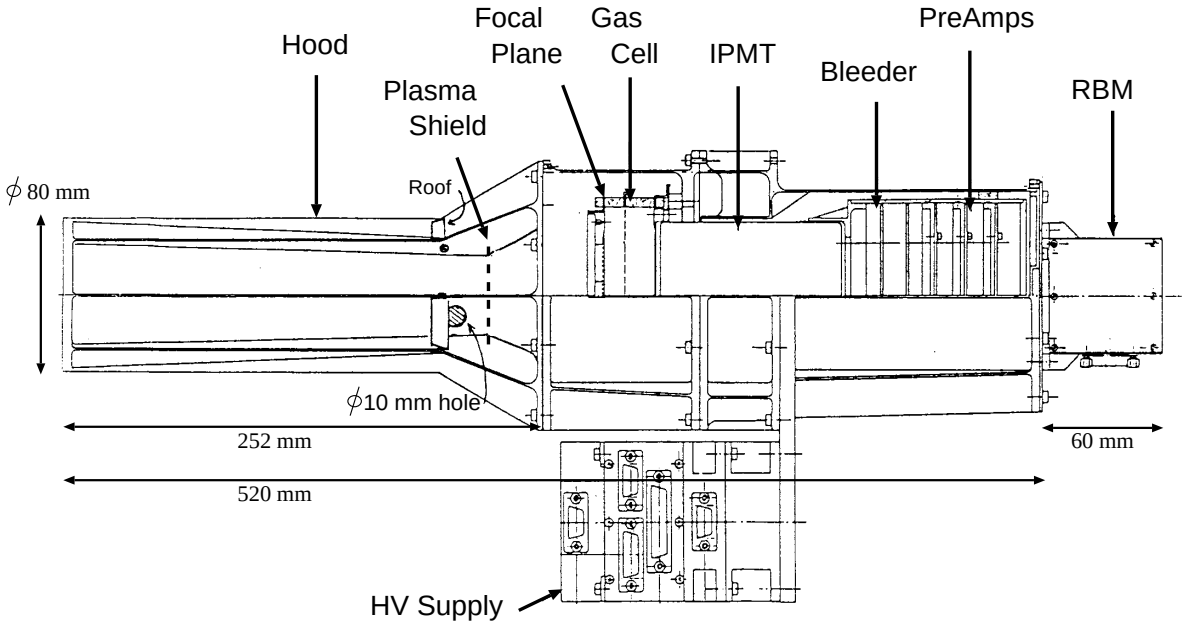

Figure 3.9: Cross section view of the GIS sensor

maximum diameter 150 mm and a length of 520 mm (without RBM). We have covered the housing with tin of 0.2–0.5 mm thick and molybdenum foil of 0.1 mm thick as a shield for hard X-ray background. The top section is a hood, which limits the field of view of the GIS into the XRT direction. In order to prevent ionospheric plasmas from entering into the gas cell section, an aluminized mylar film of 540 nm thick with 37 nm of aluminum (plasma shield) is placed inside. The middle section accommodates the gas cell and the phototube, and the bottom section holds the front-end electronics.

Gas cell as a detection part

We have developped the gas cell together with Japan Radio Corporation Co.Ltd. It is made of ceramic tube (25 mm high and 92 mm inner diameter) with a berylium entrance window and a quartz exit window, filled with a mixture of 96% xenon and 4% helium of 1.2 atm at 0 °C. Inclusion of helium is mainly to help detection of small leak with helium leak detectors. The gas is continuously purified with a small built-in getter (SAES ST172). The gas volume is divided by a mesh electrode made of molybdenum into two parts, the drift region in the top 10 mm and the scintillation region in the bottom 15 mm.

Figure 3.10 shows a schematic view of the GIS sensor system. X-rays reflected by the XRT enter through the window, whose electric potential is held at −6000 V, and are absorbed in the drift region. Through photo-ionization, primary electrons are generated on average at the rate of one electron per 21.5 eV. The electron cloud thus created slowly drifts to the intermediate mesh (−5300 keV), and then the cloud is accelerated due to the strong field toward the ground mesh which is placed in front of the quartz window. In this process, the electrons excite Xe and produce a large number of UV photons of

$\sim$ 170 nm wavelength. The excitation energy for one UV photon is $\sim$ 10 eV. Through the quartz window, these UV photons are collected by the IPMT which measures light distribution and the overall intensity of UV flux, which is proportional to the X-ray energy with accuracy of several %.

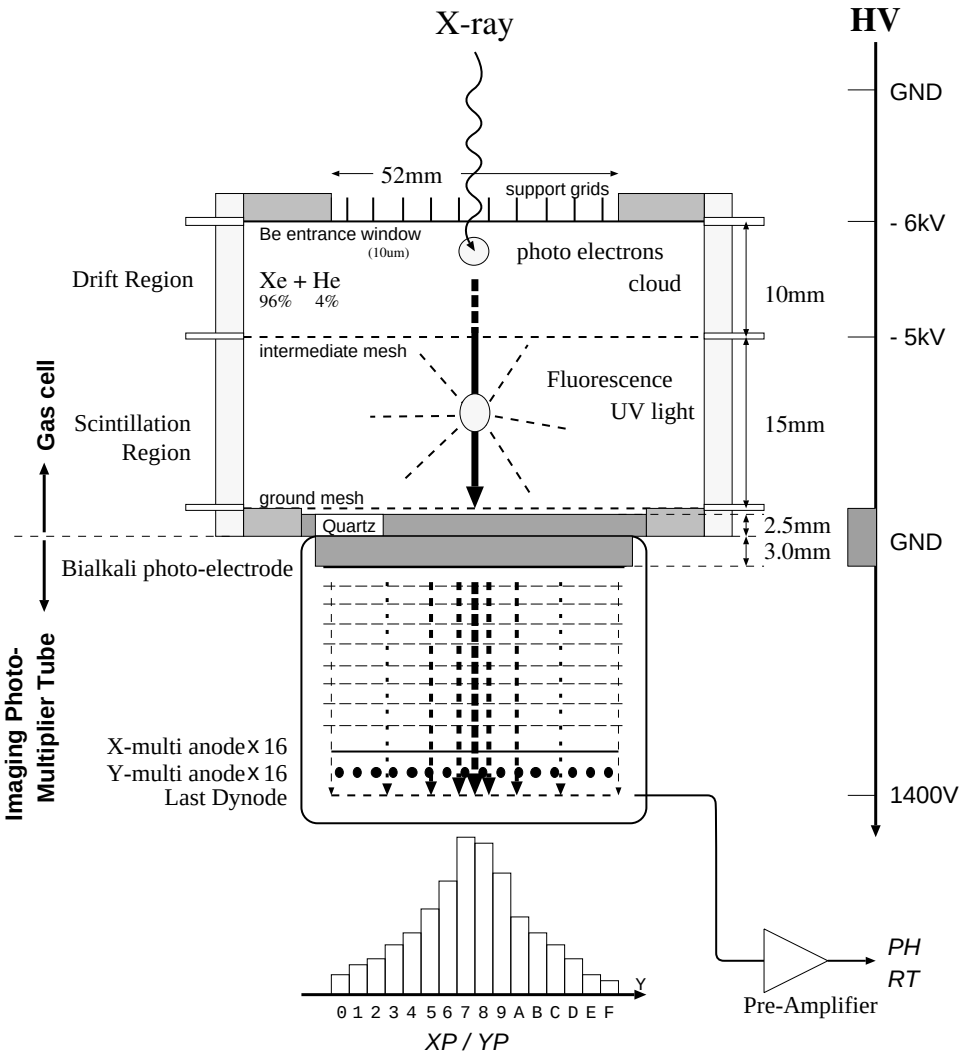

Figure 3.10: Schematic view of the GIS sensor system

We have drastically improved the soft X-ray sensitivity of the GIS as compared with previous gas counters, by using the X-ray entrance window made of vacuum tight 10 μm thick berylium foil. This has newly been developed by Yamaha Corporation, which is employed for the first time in space. The window has a 10% transmission at 0.7 keV, and the opening area is 52 mm in diameter. The foil material has a diameter of 66 mm and bonded to a cupro-nickel flange with high temperature epoxy. The window support is made of a thin molybdenum grid plated with copper, and a stainless steel mesh coated with tin is placed between the grid and the berylium foil to provide a fine support. The molybdenum grid has a height of 3.5 mm and a thickness of 0.1 mm and runs at 5 mm

pitch. The grid itself can stand against several atmospheric pressure. The shadow of the grid onto the X-ray image is not a major problem since the wall thickness is thinner than the point spread function of the XRT. The fine-supporting mesh has 1.2 mm pitch and 84% transmission with a wire thickness of about 80 μm.

The exit window, with 2.5 mm thickness and a diameter of 72 mm quartz plate, is bonded to the Kovar flange using pressed indium and a small amount of high temperature epoxy resin as an additional sealant. Quartz has short-wavelength cutoff of $\sim$ 150 nm and a relatively high transmission for the UV lights ($\lambda \sim 170$ nm). Kovar has been chosen because its thermal expansion coefficient matches that of quartz. The sealing has turned out to be successful over a temperature range from -25 °C to 110 °C against a pressure of 1.5 atm.

Imaging photo-multiplier tube (IPMT)

We employ Hamamatsu Photonics type R4268 IPMT, which is equipped with a quartz window and 10-stage dynodes. The anode has a cross-wire configuration with 16 wires running in each X and Y direction at an interval of 3.75 mm. We obtain the position information from the anode signals, and derive the pulse-height (PH) and the rise-time (RT) information from the last dynode. A pencil-beam light input to the IPMT shows a distribution of the output charge of about 7 ± 1 mm FWHM and the intrinsic position resolution of the phototube to be about 0.1 mm FWHM. To avoid hitting the gas cell by the pohotocathode during the launch, a kapton ring is inserted along the edge of the quartz surface to create a gap of $\sim$ 0.1 mm.

Radiation belt monitor (RBM) and high voltage supplys (HV-H and HV-L)

In order to monitor the radiation environment, a radiation belt monitor (RBM) is equipped to GIS2. Its purpose is to generate an alarm signal (RBM-flag) for the high radiation flux based on the count rate. This RBM flag automatically turns down the high voltages of the GIS. The RBM sensor is made of a small PIN diode of 1 cm $\times$ 1 cm size with a thickness of the Si 100 μm. The entranse window is 15 μm thick Al. The field of view has a solid angle of 1.8 str, and its direction is opposite to the GIS entranse direction.

We use two types of high voltage units for the GIS. One produces about +1000 V for the IPMT, and the other provides negative potential down to -8000 V to the gas cell. The former is called HV-L and the latter is HV-H. In the orbit, we keep the entrance window of the gas cell at -6000 V and the mesh at -5300 V. An automatic control of the high voltage for both HV-H and HV-L is carried out in orbit by the RBM-flag.

3.4.2 Onboard data processing of the GIS

We outline the signal processing in the GIS system in figure 3.11. The front-end processing is carried out within the GIS sensor part (GIS-S), and it is followed by a detailed handling in the main electronics section (GIS-E). The front-end electronics attached to the IPMT accommodates 33 charge-sensitive preamplifiers, one for the last dynode, and the other for the 32 anode wires (16 X-anode + 16 Y-anode). The time constant of the each preamplifier is 110 μsec.

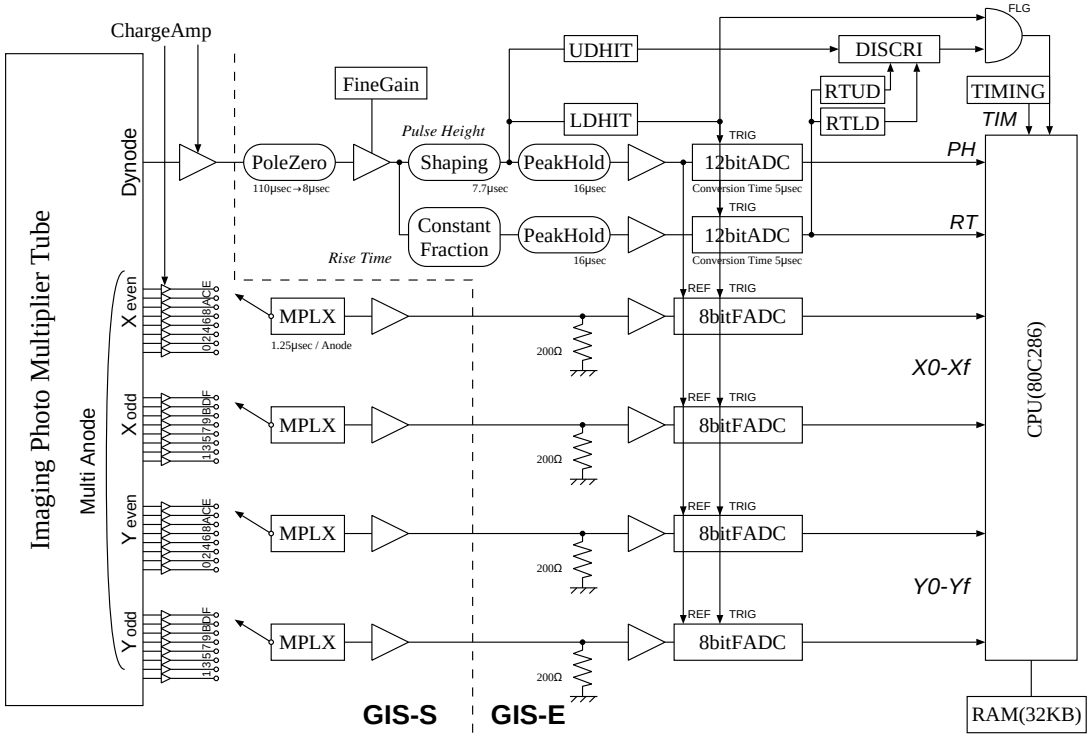

Figure 3.11: Data flow chart of the GIS electronics

The signal from the last dynode goes through fine-gain adjustment, upper (UD) and lower discriminators (LD), and then to pulse-height and rise-time ADCs. The pulse-height ADC converts the pulse-height of the signal into 12 bit value of PH. The rise-time ADC converts the rise-time of the signal into 8 bit value of RT. For the rise-time measurement, we employs the same logic as established for the Tenma GSPC (Koyama et al. 1984). The upper and the lower RT discriminators (RTLD and RTUD, respectively) operate on the digitized RT after the rise-time ADC. The arrival time of the signal is measured by clock, and is converted into 10 bit value of TIM. The 32 anode signals are treated by 4 flash ADCs incorporating analog multiplexer, and their pulse-heights are converted into 8 bit values of $X0$–Xf and $Y0$–Yf in reference to the dynoe pulse-height. If the event satisfies the condition that LD $\leq PH \leq$ UD and RTLD $\leq RT \leq$ RTUD, all these data (PH, RT, TIM, $X0$–Xf, $Y0$–Yf) are sent to the onboard CPU (80C286) and subjected to further data processing.

The main tasks of the onboard CPU are: (1) calculating the event position, (2) rejecting background with spread discriminator (SPD), (3) formating event data and sending it to the satellite data processor (DP).

The two-dimensional position of an X-ray event ($RAWX$, $RAWY$) is calculated by onboard CPU using offset- and gain-compensated values of $X0$–Xf and $Y0$–Yf. The standard calculation algorithm employs a linearized fitting to one-dimensional Lorenzian distribution (FLF). The time for the position calculation is $\sim$ 8.5 ms/event. The alternative algorithm calculates the center of gravity for square of the anode pulse-heights. This requires the calculation time of only $\sim$ 2 ms/event but results in a image distortion toward the edge. The CPU calculates the width of the distribution together with the event position, which is called spread (SP). The CPU performs a background rejection with ($RAWX$, $RAWY$) and SP.

In PH mode, digital signals collected or calculated by the onboard CPU are formated into 32 bit data per event. The 32 bit data usually consits of sensor ID (1 bit), PH (10 bit), $RAWX$ (8 bit), $RAWY$ (8 bit), and RT (5 bit). We can change this bit assignment by a command, in such case as timing observations. These 32 bit data are sent to the telemetry in every 3.9 ms interval in high bit-rate.

3.4.3 Background rejection of the GIS

One of the major design goals of the GIS is to achieve a very low level of non X-ray background (NXB). For this purpose, the GIS employs both hard-wired and software-based rejection. The hard-wired part performs usual PH and RT discrimination similar to that used for Tenma. We can control the RT window (RTLD–RTUD) by commands. When X-rays are properly absorbed in the drift region, all the signal should exhibit a RT of about 3 μsec which corresponds to the drift time of electrons in the scintillation region (see §3.4.1). On the other hand, particle events creating a long electron track in the drift region exhibit longer RT. Compton scattered electrons by γ-rays in the ceramic wall also produce signals with rather long RT because the electric field near the wall is weak. If Compton scattering of γ-rays or ionization by a particle are reacted only in the scintillation region, a signal with shorter RT is observed. Using the RT discrimination employing hard-wire electronics, we can efficiently remove NXB.

However, the RT distribution broadens significantly for lower values of PH, because the signal to noise ratio gets worse. Therefore we set the RT window rather large in orbit. We can further reduce NXB by applying a PH dependent RT mask on ground. Although pre-launch and in-orbit calibration revealed the position dependence of RT (degraded by $\sim$ 4% near the rim of the detector), the measured RT can be converted to

a position independent value (rise-time invariant; RTI) to allow the strict background rejection using this post-observation RT mask. Figure 3.12 and figure 3.13 demonstrates the background rejection with the strict RT mask on ground.

Besides the RT discrimination (RTD), we utilize another background rejection logic called SP discrimination (SPD). As described in §3.4.2, SP means the width of the light

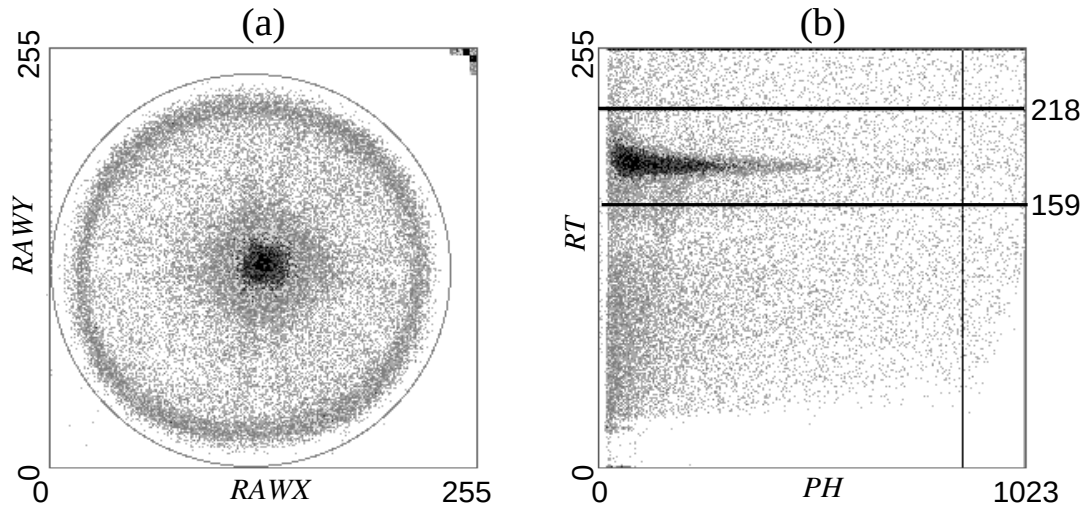

Figure 3.12: (a) An example of $RAWX$-$RAWY$ image of a celestial X-ray point source, obtained with GIS2 in a very early observation (in fact, this is the first light target for the GIS). No background rejection was applied, except the pulse-height UD. An event concentration near the detector rim is partly due to the background enhancement, and partly due to the position non-linearity. (b) The X-ray events contained in the image of panel (a), displayed on the plane of PH vs. RT. Two horizontal lines represent the standard onboard RTD window (RTLD–RTUD).

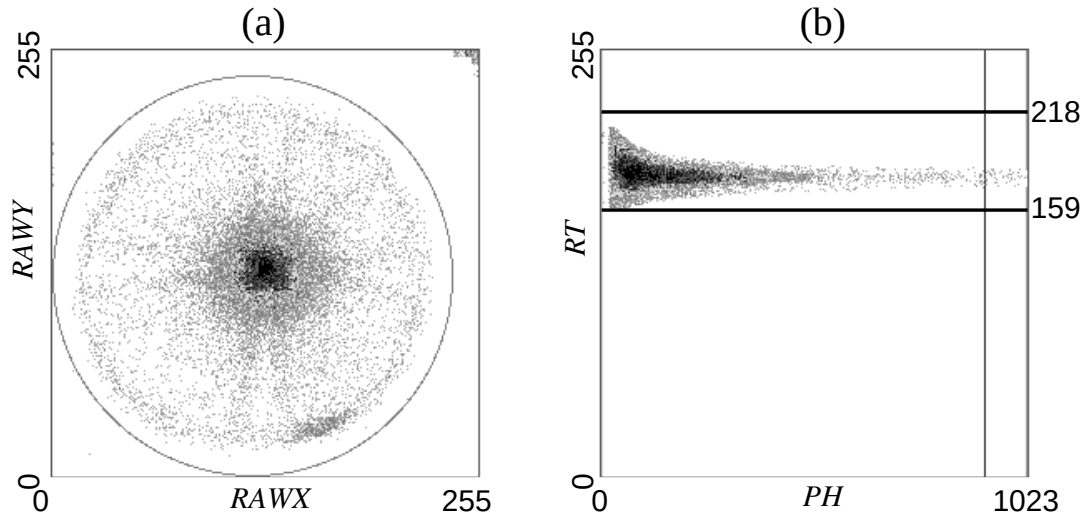

Figure 3.13: (a) Almost the same as figure 3.12a except strict RT mask applied. A bright spot near the center is the target source, while another spot to the lower right is the ^{55}Fe calibration isotope. (b) The X-ray events contained in the image of panel (a), displayed on the plane of PH vs. RTI.

distribution, and the onboard CPU performs SPD. SPD is sensitive to the direction of a charge track perpendicular to the electric field. If an ionizing particle runs in parallel to the window plane, RTD does not work efficiently. We can reject these events by SPD, which have much larger SP than those for the X-ray events. As shown in figure 3.14, SP is usually plotted against the squared radius from the detector center. Figure 3.14 also indicates the thresholds of SPD employed in orbit. We enabled SPD on 28 May 1993, and we have kept SPD in the same setting since then, except for a few observations conducted during 11 to 13 June 1993 in order to verify the function of SPD.

In the data analysis performed on ground, we can further reduce NXB by the strict RT mask mentioned above, and by discarding events near the detector edge, which also eliminates the ^{55}Fe calibration isotope events. The combined use of these discriminations gives the GIS detector a similar performance to that of the multi-cell proportional counters, such as LAC onboard Ginga, with respect to the background performance. Table 3.4 summarize the background rejection mechanisms of the GIS and background rate at each stage. In §4.4, we describe in-orbit performance of the GIS background rejection scheme.

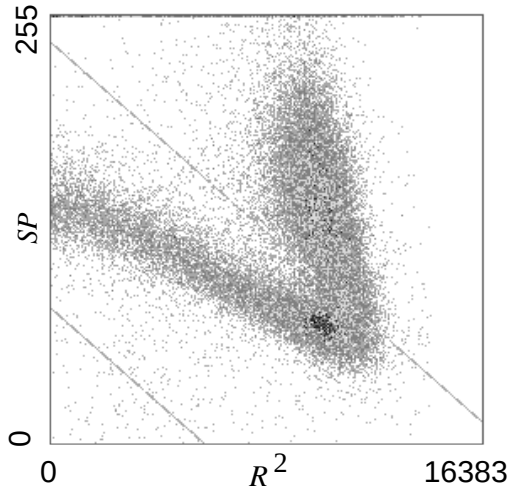

Figure 3.14: A scatter plot of events of a blank sky displayed on the plane of squared radial distance from the center in $RAWX$-$RAWY$ image vs. SP. A nearly horizontal branch is formed by signal X-rays of the CXB, while a nearly vertical branch, which means a large scatter in the spread of UV light, originates from background near the detector wall. Two slant lines indicate the standard SPD window.

Table 3.4: NXB count rate of the GIS in the 0.17–11 keV range under various rejection conditions

Condition	Radius (mm)	Rate (c s^{-1} sensor^{-1})	Remark
Raw NXB	whole detector	23–78*	$LDHIT$†
+ Hard-wired rejection (RTD)	whole detector	1.7–4.7*	$L1$†
+ onboard CPU rejection (SPD)	whole detector	0.7–1.2*	$CPUOUT$†
+ Radius cut	≤ 17	0.059–0.11	
+ strict RT mask	≤ 17	0.044–0.086	Final value‡

* Including ~ 0.3 c s^{-1} from the calibration isotope.

† Monitor items in telemetry. See §3.4.4.

‡ Final NXB level (RNXB), corresponding to $(5\text{–}9) \times 10^{-4}$ c s^{-1} cm^{-2} keV^{-1}.

3.4.4 Monitor counts and house keeping (HK) data of the GIS

To estimate the NXB rate and the dead time, processed event rates at various stages in GIS-E are read out as the GIS monitor counts. Table 3.5 shows a list of the GIS monitor counts. All monitor counts are counted by 8 bit non-reset counter, and read out to be edited into the telemetry format. RBM events are also counted with 16 bit non-reset counter and sent to the telemetry. These event numbers except $CPUIN$ and $CPUOUT$ are processed by hard-wire electronics to avoid the dead time from CPU calculation. Distributions projected on X or Y axes are also provided for quick look or to inform spatial distribution of the X-ray image even if some regions of the GIS f.o.v. are masked by commands. Figure 3.11 also displays sampling points of the monitor counts.

We can correct the GIS data for the dead time using these monitor counts, as

$$dead\ time\ fraction = \frac{TLMOUT}{CPUOUT} \cdot \frac{CPUIN}{L1} \cdot (1 - LDHIT \cdot \tau_{PH}). \tag{3.1}$$

Here $TLMOUT$ is the number of events which appeared to the telemetry. A constant factor τ_{PH} means the hard-wired dead time per event and was confirmed to be $\tau_{PH} \sim 25\ \mu$s in PH mode. The factors $\frac{TLMOUT}{CPUOUT}$, $\frac{CPUIN}{L1}$, and $(1 - LDHIT \cdot \tau_{PH})$ represent the dead time due to the telemetry saturation, that due to the onboard CPU, and that due to the hard-wire electronics, respectively.

As for the house keeping (HK) monitor items, voltage of both HV-H and HV-L, output current of HV-H, and temperatures of the IPMT heads and the RBM sensor are converted into 8 bit values and sent to the telemetry.

Table 3.5: Summary of the GIS monitor counts

Name	Remark
$LDHIT$	counts of ($\mathsf{LD} \leq PH$)
$L0$	counts of ($\mathsf{LD} \leq PH \leq \mathsf{UD}$ *and* $RT < \mathsf{RTLD}$)
$L1$	counts of ($\mathsf{LD} \leq PH \leq \mathsf{UD}$ *and* $\mathsf{RTLD} \leq RT \leq \mathsf{RTUD}$)
$L2$	counts of ($\mathsf{LD} \leq PH \leq \mathsf{UD}$ *and* $\mathsf{RTUD} < RT$)
$H0$	counts of ($\mathsf{UD} < PH$ *and* $RT < \mathsf{RTLD}$)
$H1$	counts of ($\mathsf{UD} < PH$ *and* $\mathsf{RTLD} \leq RT \leq \mathsf{RTUD}$)
$H2$	counts of ($\mathsf{UD} < PH$ *and* $\mathsf{RTUD} < RT$)
$CPUIN$	counts taken in by the onboard CPU
$CPUOUT$	counts output by the onboard CPU

3.4.5 Basic event conversion for the GIS

The raw GIS outputs for an event are PH, RT, and calculated position ($RAWX$, $RAWY$), as mentioned in §3.4.2. However, these value are subject to various non-ideal instrumental properties of the GIS. Therefore, we convert them into linearlized quantities: PI, RTI, and ($DETX$, $DETY$), respectively. We useually use PI and ($DETX$, $DETY$) for scientific analyses. RTI is utilized to apply the strict RT mask described in §3.4.3. The procedure of converting ($RAWX$, $RAWY$) into ($DETX$, $DETY$) is called "position linearlization", and that of PH into PI is called "gain correction". We explain these procedure in the following.

Position linearization

Raw X-ray images obtained with the GIS are somewhat distorted toward the detector rim, by the non-linearity in the position response. Figure 3.15 shows an image of the sunlit earth, where solar X-rays scattered off the atmosphere provides an X-ray source of uniform brightness. Slightly deformed lattice of shadows are cast by the rectilinear window support grids.

Pre-launch calibrations, including scanning measurements with collimated X-ray beams, provided look-up tables for conversion from raw position outputs ($RAWX$, $RAWY$) to the *linearized* detector coordinates ($DETX$, $DETY$). Rotation (0° for GIS2 and −90° for GIS3) and Y-flip of the coordinates are also applied in the course of this

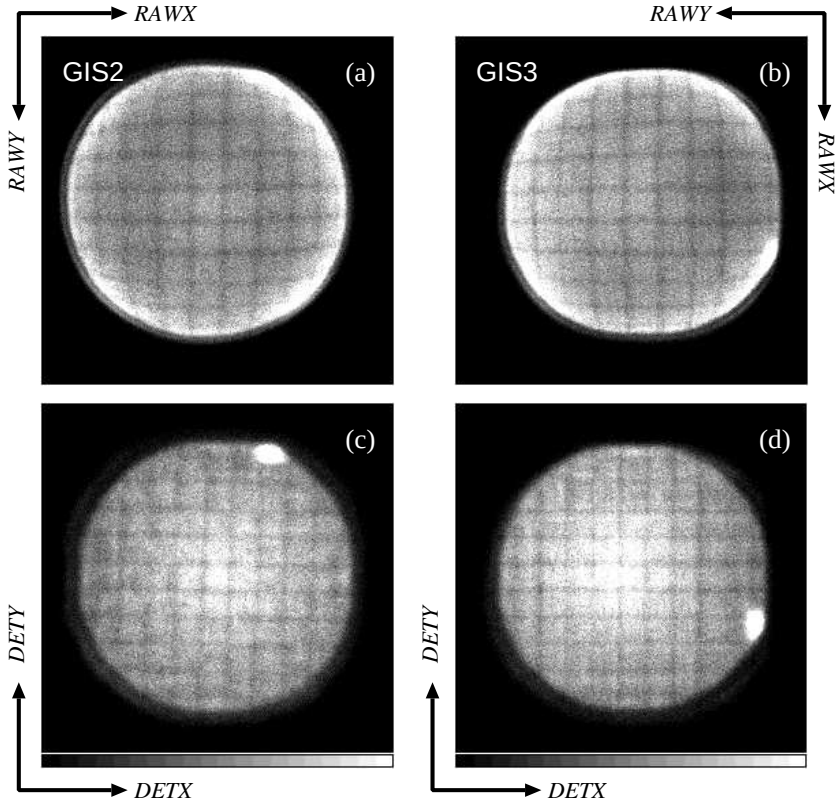

Figure 3.15: X-ray images of the sunlit earth in the 1–3 keV energy band from GIS2 (panel a) and GIS3 (panel b), presented in the $RAWX$-$RAWY$ coordinates. Images are rotated and Y-fliped so that the coordinates match the direction of the $DETX$-$DETY$ coordinates. Panels (c) and (d) are the same images from GIS2 and GIS3 respectively, after converted to the $DETX$-$DETY$ coordinates.

conversion (see figure 3.15). Figure 3.16 illustrates how the conversion tables look. The tables have been confirmed in orbit in reference to the window support girds. In the linearized $DETX$-$DETY$ image of figure 3.15, the grid lattice appears quite rectilinear.

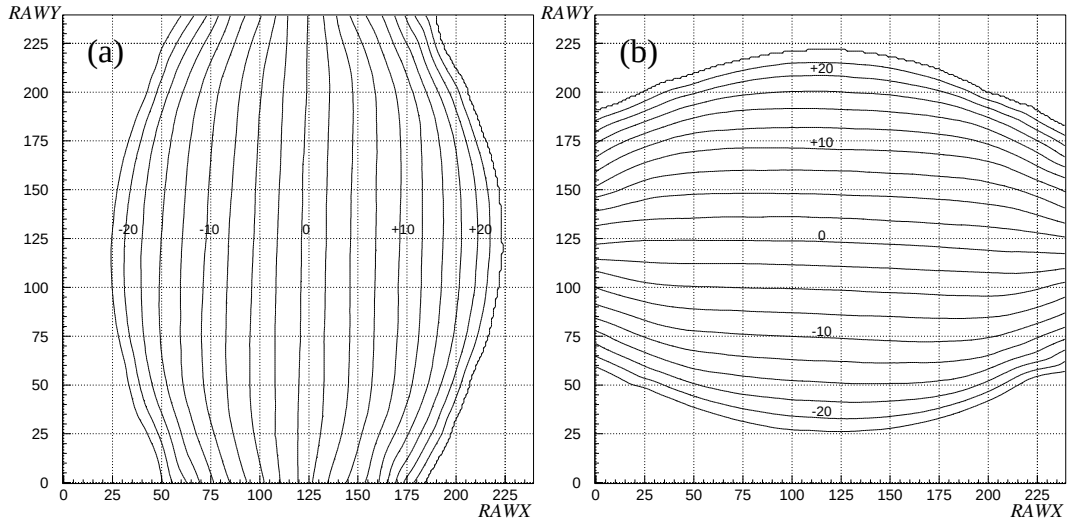

Figure 3.16: The position linearlization maps in $RAWX$-$RAWY$ coordinates for GIS2. (a) ($RAWX$, $RAWY$) to $DETX$, and (b) ($RAWX$, $RAWY$) to $DETY$. Contour levels are -22.5–25 mm in 2.5 mm step. The map versions are `xflf_s2.table` and `yflf_s2.table`.

Gain correction

When accumulating X-ray photons into an X-ray spectrum, we usually convert PH (pulse-height) of each detected event into PI (pulse-invariant) so that X-rays of the same energy give the same PI value (except the finite energy resolution) independently of the position, the temperature of phototube or the observation period. The conversion factor from PH to PI is called gain. The gain depends on four factors: (1) detected position of the incoming X-rays, (2) the temperature of the GIS, (3) the long-term gain drift, and (4) the signal count rate of the GIS.

The GIS gain is position dependent by $\sim \pm 10\%$ peak-to-peak due to non-uniformity in the IPMT gain. Calibration of this effect involves a look-up table called "gain map", which summarizes relative gains of each detector as a function of the position of event occurrence. Preliminary gain maps were generated based on the pre-launch calibration. In order to compensate for possible gain changes at the launch, and to increase the reliability, we have updated the gain maps several times in orbit. This procedure utilized the instrumental Cu-K line seen in the NXB spectrum (§4.19) after a long data integration. We also utilized intense Fe-K lines from celestial sources (largely extended objects, or those observed at different positions), e.g. clusters of galaxies and supernova remnants (SNRs). In the latest

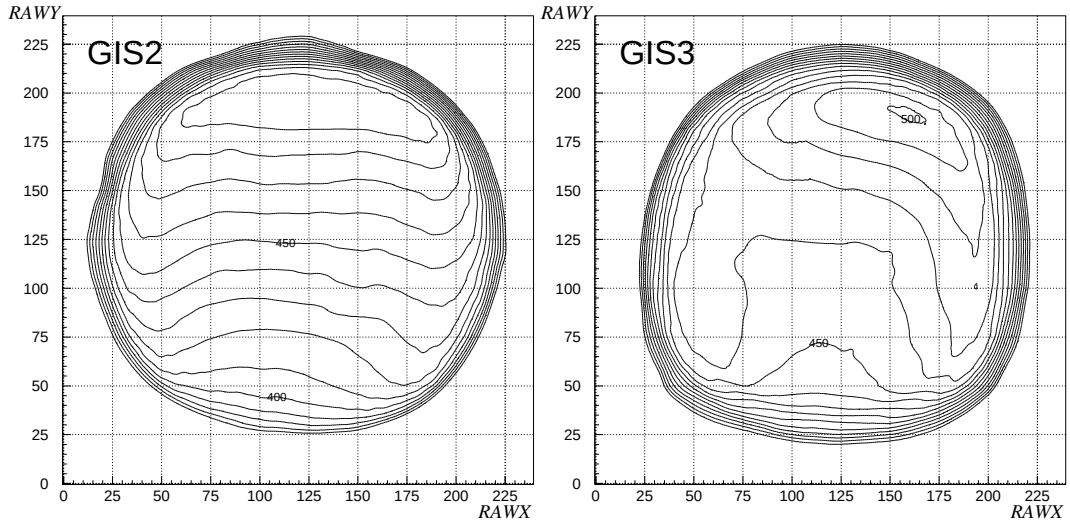

Figure 3.17: The gain maps in ($RAWX$,$RAWY$) coordinates for GIS2 (left panel) and GIS3 (right panel). Contour levels are every 10 step from 350. The gain map versions are `phfl_s2_v3.table` and `phfl_s3_v3.table` for GIS2 and GIS3, respectively.

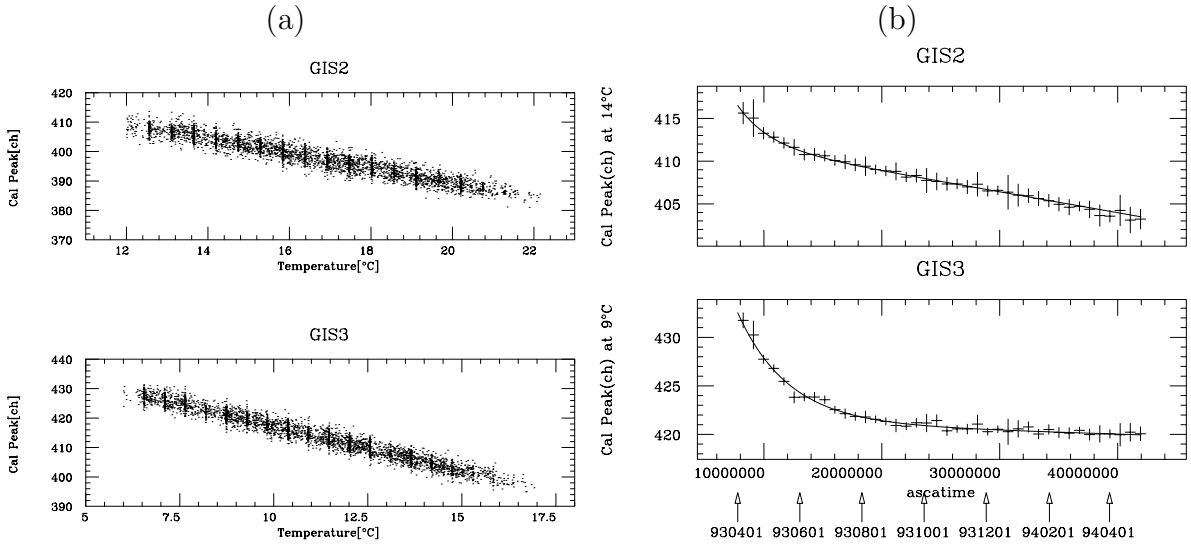

Figure 3.18: (a) Peak PH channels of the ^{55}Fe calibration isotope, plotted against the detector temperature measured in orbit on the side wall of IPMT. (b) Long-term gain history since the launch till April 1994, expressed in terms of the temperature-corrected ^{55}Fe PH. Upper and lower panels are for GIS2 and GIS3, respectively.

version of gain maps as of May 1995 (figure 3.17), the reliability has been improved to within ±1% and ±2% for the regions of radius < 15 mm and 15–20 mm, respectively, for both detectors.

The GIS gain depends significantly on the temperature, because of the temperature dependence in the IPMT and gas cell. The GIS gain is monitored continuously in orbit in reference to the built-in ^{55}Fe isotope, and so is the IPMT temperature. We show in

figure 3.18a, the gain vs. temperature relation thus calibrated in orbit, which reconfirms the behavior observed on ground. We have frequently updated this relation to take into account the long-term gain change (see next paragraph), and use it to correct the GIS gain for the temperature dependence. This relation of the temperature and the GIS gain, including the long-term gain change, is called "gain history", and summarized in the FITS file format table of `gis_temp2gain.fits`. The temperatures of the two GIS detectors vary by ~ 10 °C in orbit, mainly in response to satellite attitude changes. It is therefore recommended not to use the GIS data for 2–3 hours after a large attitude maneuvering, until the GIS detectors attain a new thermal steady state. The GIS2 temperature is higher by ~ 5 °C than that of GIS3, since GIS2 is mounted on the sunlit side of the satellite.

Figure 3.18b shows the long-term GIS gain history in reference to the ^{55}Fe isotope, after correction for the temperature variation. Thus, the gain of both detectors decreased by 2–3% for the first several months in orbit, but the trend has gradually flattened. This slow gain decrease is possibly due to a slow degradation in the UV transmission of quartz windows of the gas cell and the IPMT, through, for example, gradual developments of cosmic-ray induced crystalline defects. This gradual gain decrease is unlikely to be caused by out-gassing in the detector, since the RT characteristics have remained constant. The temperature coefficient and long-term trend are both reliable to an accuracy of $\pm 0.4\%$.

The GIS gain is pushed up slightly when the signal count rate exceeds ~ 100 c s^{-1} (sources brighter than ~ 100 mCrab), although it is negligible for extra-Galactic objects which are $\lesssim 50$ c s^{-1}. This effect is due to a pulse pile-up in pole-zero cancellation circuits of GIS-E. We re-calibrated this effect in orbit, using the Crab nebula data obtained at various offset angles (hence with different counting rates). The results, shown in figure 3.19, confirms the ground calibration.

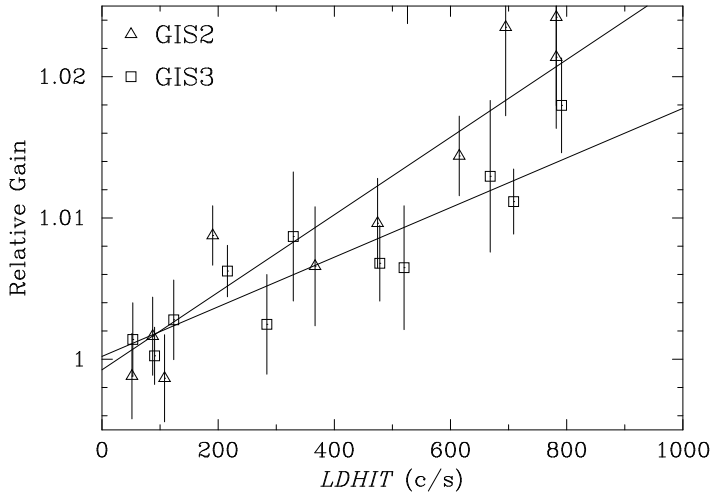

Figure 3.19: Relative GIS gains plotted as a function of the incident source count rate ($LDHIT$). A slight gain increase is seen in high counting rates. Two lines superposed on the data points show the the best line of

$$\begin{cases} y = 0.9993 + 0.27438 \times 10^{-4} LDHIT \\ y = 1.0002 + 0.17559 \times 10^{-4} LDHIT \end{cases}$$

for GIS2 and GIS3, respectively.

Thus, the formula to convert PH to PI is:

$$PI = \frac{norm \times PH}{gainmap(RAWX, RAWY)\ gainhistory(t, T)\ f(LDHIT)} \tag{3.2}$$

where t, T, and $f(LDHIT)$ are the arrival time of the event, the temperature of the GIS, and the $LDHIT$-gain relation of figure 3.19, respectively. The factor $norm$ determines the *absolute* GIS gain scale. Although this was well established once in pre-launch calibration, an independent in-orbit determination is of vital importance because the IPMT gain can change by up to several percent due to the launch vibration. However the built-in calibration isotope cannot provide a required accuracy, since it is attached at the detector edge where the gain map becomes most uncertain. Accordingly, we have accumulated the instrumental Cu-K fluorescence line within the central region of 12 mm radius, for a long time utilizing night- and day-earth observations, with the temperature and gain-map corrections. We have used the resulting Cu-K line as a fiducial to determine the absolute energy scale.

We then cross calibrated the results of gain correction using the Au-M absorption edge structure produced by the gold plated surface of the XRT, seen in the spectra of bright sources such as the Crab nebula. For an additional confirmation, we also used collisionally-excited intense Fe-K emission lines from several celestial sources, particularly SNRs and clusters of galaxies. Although energies of these celestial Fe-K lines are intrinsically somewhat uncertain due to mixture of different ionization states, they have provided an accurate cross calibration with the SIS energy scale. We believe that the absolute GIS gain scales thus established is accurate to $\sim 1.2\%$ within ~ 15 mm from the center.

Chapter 4

In Orbit Calibration of the GIS

4.1 Overview

In the present thesis, we will perform a detailed investigation of the spectrum and brightness of the CXB. For this sort of quantitative ASCA data analysis, accurate knowledge on the instrumental response and the detector background is of essential importance. However, ASCA's response and background depend very much on the position and shape of the target sources, so that a number of carefull calibrations have to be carried out in orbit. Some of these calibration results are compiled as a part of the calibration data base, in the form of FITS files, which are made publicly available. Response and background builder are also needed, which access those calibration results and generates specified responses or backgroud spectra/images at any positions/energy-bands on the detector. After the launch of ASCA, we have been conducting extensive efforts of in-orbit calibration using the GIS detector, and the results have been fed back efficiently to the response and background builder.

Since the CXB is extended all over the detector plane, importance of these calibration effort is much greater than is required in nominal point source analysis. In particular, stray light of the XRT causes a severe difficulty when we try to generate a response for the CXB spectrum. In this chapter, we will explain how the response is built in §4.2, effects of stray light for the CXB analysis in §4.3, and the non X-ray background (NXB) of the GIS in §4.4.

4.2 Response of the XRT+GIS system

4.2.1 Formulation of the ASCA response and an ARF builder

Here we formulate the response of the XRT+GIS system, with some definitions of the coordinates. Let $F(\theta, \phi, E)$ be a source X-ray distribution, where E is the X-ray energy and (θ, ϕ) is the two-dimensional position on the sky. Angles of θ and ϕ are defined from

Table 4.1: Summary of the coordinates

Notation	Figure label	Unit	Comments
E	Energy	keV	Energy of the incident X-ray
PI	channel energy	ch	500 ch = 5.8942 keV, starts from 0 ch
θ	offset angle	arcmin	offset angle from the optical axis
ϕ	azimuth angle	degree	measured clock-wise from X-axis on detector plane
$DETX$	detector coordinates	mm	1 mm = 4 ch = 0.9822′, centered the detector center. (0, 0) mm corresponds to (128.5, 128.5) ch
$DETY$		ch	
$XRTX$	XRT coordinates	mm	1 mm = 4 ch = 0.9822′, centered the optical axis. Y-axis filpped to the detector coordinate
$XRTY$		ch	

the optical axis of the XRT (nearly parallel to the Z-axis of the satellite) as an offset-angle and an azimuth-angle, respectively. E, θ, and ϕ are usually expressed in unit of "keV", "arcmin", and "degree", respectively. Note that ϕ increases in the clock-wise direction from the X-axis on the detector plane, because it is defined in the satellite coordinates (look-down) while the detector coordinates is look-up. Also, let $D(DETX, DETY, PI)$ denote the observed data, i.e. distribution of detected X-ray photons with pulse-invariant PI (gain corrected pulse-height), and detected position ($DETX$,$DETY$). PI is expressed in unit of "ch", which begins from 0 and is scaled so that 500 ch correspond to 5.8942 keV (energy of the Kα line from ^{55}Fe calibration source). $DETX$ and $DETY$ is measured in "mm" or "ch" which is defined so that $1\,\mathrm{mm} = 4\,\mathrm{ch}$ and the center of the detector $(0\,\mathrm{mm}, 0\,\mathrm{mm})$ corresponds to $(128.5\,\mathrm{ch}, 128.5\,\mathrm{ch})$ for the GIS. As the focal length of the XRT is 3500 mm, 1 mm on the detector coordinates correspond to $60 \times \tan^{-1}(1/3500) \times 180/\pi = 0.9822$ arcmin on the sky. There also is a coordinate called ($XRTX$,$XRTY$), the scale of which is similar to ($DETX$,$DETY$) but centered on the optical axis of the XRT and the Y-axis flipped. Table 4.1 is a summary of these coordinates.

$F(\theta, \phi, E)$ and $D(DETX, DETY, PI)$ are related as

$$
\begin{aligned}
& D(DETX, DETY, PI) \qquad (4.1)\\
&\quad = \int dE\ R_{GIS}(E, PI)\\
&\quad \times \int dx\, dy\ P_{GIS}(E, x, y; DETX, DETY)\ A_{GIS}(E, x, y)\\
&\quad \times \int d\theta\, d\phi\ P_{XRT}(\theta, \phi, E; x, y)\ A_{XRT}(\theta, \phi, E)\\
&\quad \times A_{T.S.}(E)\\
&\quad \times F(\theta, \phi, E)
\end{aligned}
$$

Table 4.2: Summary of factors constituting the response function

Notation	Description
$A_{T.S.}(E)$	transmission of the thermal shield
$A_{XRT}(\theta, \phi, E)$	effective area of the XRT
$P_{XRT}(\theta, \phi, E; x, y)$	point spread function (PSF) of the XRT
$A_{GIS}(E, x, y)$	quantum efficiency of the GIS
$P_{GIS}(E, x, y; DETX, DETY)$	point spread function (PSF) of the GIS
$R_{GIS}(E, PI)$	energy redistribution matrix for the GIS

where (x,y) is the position on the entrance window of the GIS. This complicated integral transform, as a whole, is what is called the instrumental response. The meaning of each factor constituting the response is summarized in table 4.2. More detailed explanations for them are given in the following section. In particular, we usually integrate the data $D(DETX, DETY, PI)$ over a specified area Ω on the detector to obtain a spectrum $H(PI; \Omega)$, as

$$H(PI; \Omega) = \int_{\Omega} dDETX\, dDETY\ D(DETX, DETY, PI) \tag{4.2}$$

The method of spectral fitting is a procedure of finding a set of parameters for $F(\theta, \phi, E)$ which give the most similar model spectrum $H(PI; \Omega)$ to the observed PI spectrum.

If the target is a point source or have a uniform spectrum in the effective integration region on the sky, $F(\theta, \phi, E)$ can be factorized as $F(\theta, \phi, E) = B(\theta, \phi)\, S(E)$, where $B(\theta, \phi)$ is a surface brightness profile and $S(E)$ is a spectrum. Then, equation (4.1) will have a simpler form of

$$H(PI) = \int dE\ R_{GIS}(E, PI)\ A_{XRT+GIS}(E)\ S(E) \tag{4.3}$$

where:

$$A_{XRT+GIS}(E) = \int_{\Omega} dDETX\, dDETY \tag{4.4}$$

$$\times\ \ A_{T.S.}(E) \int dx\, dy\ P_{GIS}(E, x, y; DETX, DETY)\ A_{GIS}(E, x, y) \tag{4.5}$$

$$\times\ \ \int d\theta\, d\phi\ P_{XRT}(\theta, \phi, E; x, y)\ A_{XRT}(\theta, \phi, E)\ B(\theta, \phi) \tag{4.6}$$

$R_{GIS}(E, PI)$ is called an RMF (energy Redistribution Matrix File) and $A_{XRT+GIS}(E)$ is called an ARF (Auxiliary (or Ancillary) Response File). Note that the RMF is determined only by the elementary process of the detector, and that only one RMF for one detector is sufficient for all the analysis. We should rebuild only ARFs when changing the target position or the integration area. This is a great merit of saving time and disk

Table 4.3: Summary of the calibration files of XRT and GIS for jbldarf

Function	Calibration file
$A_{T.S.}(E)$	analytic
$A_{XRT}(\theta, \phi, E)$	`xrt_ea_110494.fits`
$P_{XRT}(\theta, \phi, E; x, y)$	`xrt_psf_v1.1.fits` (not in the caldb)
$A_{GIS}(E, x, y)$	`s2bev1.fits` / `s3bev1.fits` (Be window thickness)
	`s2gridv3.fits` / `s3gridv3.fits` (GIS grid transmission)
	analytic (others)
$P_{GIS}(E, x, y; DETX, DETY)$	analytic
XRT-GIS alignment	`gis2_ano_on_flf_180295.fits` /
	`gis3_ano_on_flf_180295.fits`

spaces to build/hold a response. To be accurate, the RMF of the GIS slightly depend on a position of incoming X-rays, but in most case it is negligible.

There is a spectral fitting package called XSPEC, which is commonly used for X-ray astronomy in the world. XSPEC needs four files to conduct a spectral fitting: (1) a spectrum file to be fitted, (2) a background spectrum file to be subtracted, (3) an RMF, and (4) an ARF. RMFs for GIS2 and GIS3, which XSPEC can read, are released and occasionally updated by the GIS team in FITS file format. The latest RMFs of GIS2 and GIS3 as of December 1995 are `gis2v4_0.rmf` and `gis3v4_0.rmf`, respectively, and registered in the calibration data base (here after caldb). An ARF, also an XSPEC-readable FITS file, is created by a program so called an ARF builder.

There are several kinds of ARF builders for ASCA. jbldarf (present version 2.10) is the most commonly used ARF builder in Japan, which has been developped by M. Hirayama and Y. Ishisaki. A user inputs the target position, integration area on the detector plane, and some other information such as detector ID or output file names, to jbldarf. Then, jbldarf conducts the integral calculation of equation (4.4) and create an ARF. To calculate the functions shown in table 4.2, jbldarf interpolates pre-calculated tables or utilize an analytic form of the function. Most of the pre-calculated tables are also registered in the caldb. Table 4.3 summarizes how these calculations are carried out.

In the following sections, we will explain ARF (§4.2.2, §4.2.3) and RMF (§4.2.4) for the XRT+GIS system. If the point spread function of the detector ($P_{GIS}(E, x, y; DETX, DETY)$) is approximated as a δ-function like in the SIS, ARF is furthermore splitted into the XRT part (equation (4.6)) and the detector part (equation (4.5)). Although this is not the case with the GIS, we describe the XRT part (§4.2.2) and the GIS part (§4.2.3) of the ARF separately, for convenience.

4.2.2 XRT part of ARF

Since the XRT does not change the energy of incident X-rays, its contributions can be confied to the ARF. An XRT response is usually expressed by two functions, an effective area $A_{XRT}(\theta, \phi, E)$ and a point spread function (PSF) $P_{XRT}(\theta, \phi, E; x, y)$. The XRT PSF is normalized so that the volume in $r \leq 6$ mm are equal to 1.0, and the effective area takes in charge of the normalization. The present XRT response is identical to all the four detectors, and have mirror symmetries with respect to the lines of $\phi = 0°$, $\pm 45°$, and $90°$.

Figure 4.1 shows energy- and θ/ϕ-dependence of the effective area. The big jump at 2.2 keV is the M-edge of Au, evaporated on the foil of the XRT. The effective area declines as θ gets larger, which is known as vignetting effect. When θ increases, e.g., along the direction of $\phi = 0°$, the projected geometrical area for mirror foils in the direction of $\phi = 0°$ (near-side) decreases, while for the foils in the direction of $\phi = 180°$ (far-side), reflectivity decreases because the grazing angle gets larger. These two effects cause the vignetting. Because of the reflectivity effect, vignetting is severer in higher energy bands. There is also ϕ-dependence by $\sim 20\%$, in such a way that the effective area becomes maximum at $\phi = 45°$, and becomes minimum at $\phi = 0°$.

Although the XRT has a large effective area up to ~ 10 keV, it sacrifices the imaging quality. Due to waving (shape error) of the thin aluminium foils, as well as to the conical approximations of paraboloid (primary mirror) and hyperboloid (secondary mirror) surfaces, the PSF of the XRT has largely extended wings. Upper panels of figure 4.2 show exapmles of the XRT PSFs, taken by GIS2. Although the XRT PSF in fact has a more sharply peaked core, it is broadened to some extent in the image by the finite position resolution of the GIS. Thus the XRT PSF has four butterfly-like wings, which reflects the quadrant structure of the XRT, with significant flux extending almost over the whole GIS f.o.v. Horn like structures seen on the edges of the four wings are caused by the larger distortion of the conical shape at the outermost sector of each quadrant. As θ gets larger, the PSF shape is also distorted, as characterized by a squeezing into the radial direction and an increase in the fraction of wings. Moreover, these effects are all energy-dependent. Lower panels of figure 4.2 clearly show that the PSF has wider outskirts in the higher energy bands. This is mainly due to the scattering of incident X-rays by the micro-roughness of the foil surface, which generally increases with increasing X-ray energy.

All these properties of the XRT PSF complicate the analysis of extended X-ray sources. For example, they cause artificial temperature increase in the data of cluster of galaxies toward outer rings (Ikebe 1995). Energy dependence of the XRT PSF has been calibrated

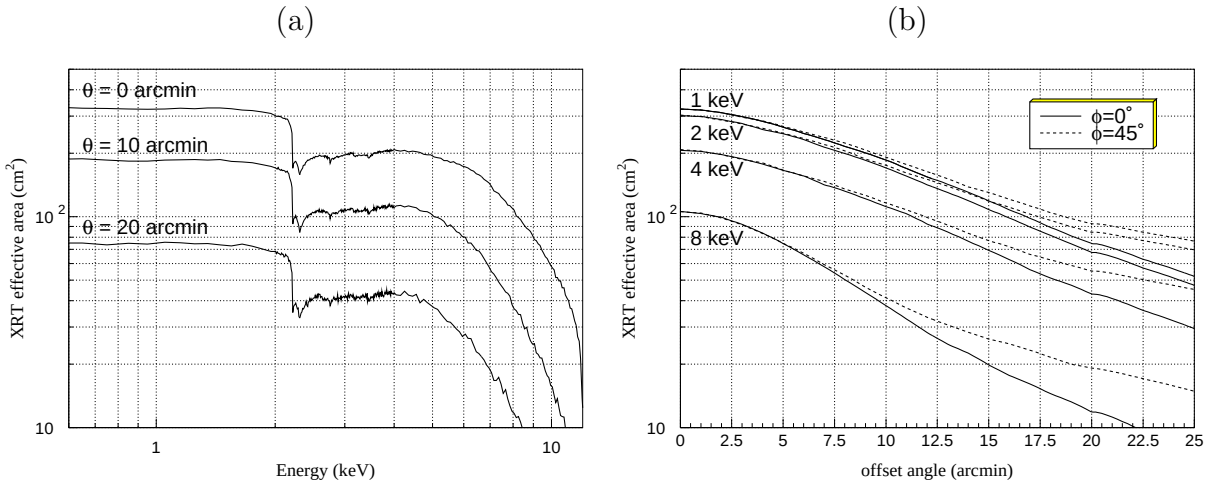

Figure 4.1: Properties of the XRT effective area. (a) Energy dependence at $\theta = 0$, 10, and 20 arcmin, for $\phi = 0°$. (b) θ-dependence (vignetting) at E =1, 2, 4, and 8 keV, for $\phi = 0°$ (solid lines) and 45° (dashes). The effective area shown here are based on the calibration data base file : `xrt_ea_110494.fits`.

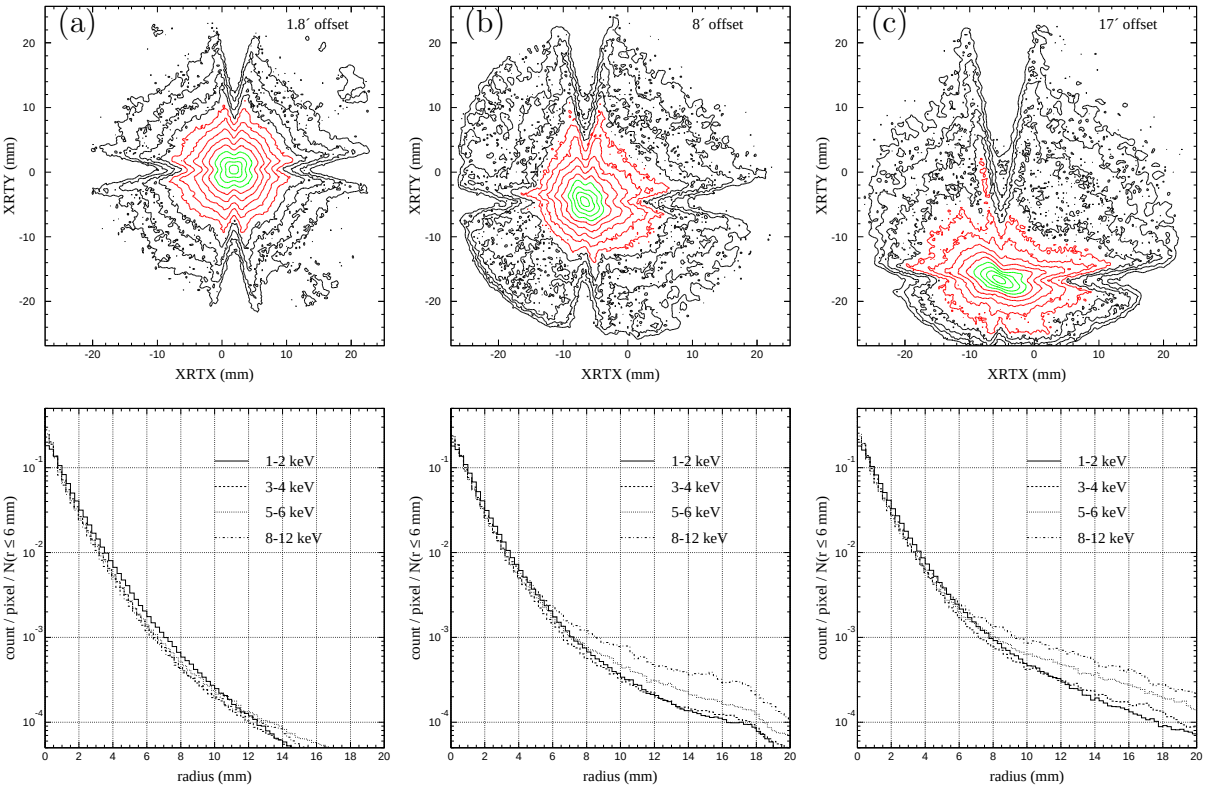

Figure 4.2: Examples of the XRT PSF taken by GIS2. (a) 1.8′ offset, (b) 8′ offset, and (c) 17′ offset Cyg X-1 images (upper panels) in the 0.5 – 12 keV band and the radial profiles (lower panels) in the 1–2 keV (solid lines), 3–4 keV (dashed), 5–6 keV (dotted), and 8–12 keV (dot-dashed) energy bands. For upper panel images, contour levels are every factor of 2, and origins of the coordinates are the optical axis of GIS2. All radial profiles in lower panels are scaled so that the volume in $r \leq 6$ mm are equal to 1.0.

with hard point-like X-ray sources, such as GRO-J1008 or Cyg X-1. It is comfirmed that the ray-tracing images agree with data within 20% level in radial profile (Furuzawa 1995, ASCA calibration meeting).

4.2.3 GIS part of ARF

Here we explain non-XRT factors for building the XRT+GIS ARF, described in equation (4.5). The quantum efficiency of the GIS ($A_{GIS}(E,x,y)$) depends on the window transmission and the absorption probability in the drift region (1 cm depth) of the gas cell, filled with 96% Xe and 4% He gas up to 1.2 atm at 0 °C. The entrance window of the GIS is made of thin belyllium foil with a mean thickness of 10.83 ± 0.02 / 10.5 ± 0.02 μm (GIS2 / GIS3, respectively). The Be window is supported by grids of 3.5 mm height, 0.1 mm thick and 5.0 mm pitch, and a mesh of 1.2 mm pitch and 84% transmission with a wire thickness of about 80 μm. The plasma shield, which locates 55 mm above the Be window, is made of aluminized myler of 37 nm (Al) + 540 nm ($C_{10}H_8O_4$) thick, supported by a mesh of 90% transmission. Thermal shield is placed just before the XRT and is almost identical to the plasma shield except that the mesh transmission is 94.2%.

Thus, the total quantum efficiency for the non-XRT factor is expressed as :

$$A_{T.S.}(E)\ A_{GIS}(E,x,y) = \qquad (4.7)$$
$$0.942\ T_{myl}(E) \cdot 0.90\ T_{myl}(E) \cdot 0.84\ T_{grid}(x,y) \cdot T_{Be}(E, t_{Be}(x,y)) \cdot (1 - T_{gas}(E))$$

where $T_{myl}(E)$, $T_{grid}(x,y)$, $T_{Be}(E,t(x,y))$, and $T_{gas}(E)$ are the transmissions of the aluminized myler, the support grid, the Be window, and the Xe + He gas, respectively. The function $t_{Be}(x,y)$ represents the thickness of the Be window at (x,y). Figure 4.3 shows the functions of $T_{myl}(E)$, $T_{Be}(E, 10.5\mu\mathrm{m})$, and the total quantum efficieny of equation (4.7) without the grid transmission. The Be window thickness map $t_{Be}(x,y)$ is measured on the ground and re-calibrated in orbit. Figure 4.4a shows the Be map for GIS2. The Be map for GIS3 is filled with a constant value of 10.5 μm. The grid transmission map of $T_{grid}(x,y)$ is measured in orbit utilizing the image of sunlit earth and summation of extended sources. Figure 4.4b shows the grid map for GIS2 smoothed by the position resolution of the GIS at 2.0 keV.

The point spread function of the GIS ($P_{GIS}(E,x,y;DETX,DETY)$) is expressed by a superposition of 1–6 Gaussians depending on the number of Xe-L escape lines, and the volume is normalized to 1.0. The reason why not a single Gaussian is used is that escape events of Xe-L exhibit a wider position scatter. The position resolution of the GIS is about 0.6 mm FWHM at 6 keV, and have an energy dependence of $\propto 1/E^{\sim 0.5}$ (thin line in figure 4.5). It also has a position dependence. It stays almost constant out to $r \sim 15$ mm, becomes worse at $r > 15$ mm, and is by 20–30% worse at $r = 20$ mm.

We basically utilize the position resolution measured on ground before launch. The overall position resolution of the XRT+GIS system is not a simple convolution of the GIS PSF with the XRT PSF, since there is an additional effect caused by the XRT+GIS combination: X-rays enters the GIS gas cell as a converging beam of $\sim 2^\circ$ from the XRT, while the gas cell has a finite depth of 1 cm for the X-ray absorption. These effects produce a parallax which adds to the overall position resolution. The parallax is expected to be significant for harder X-rays which has larger penetrating depths in the detector. The thick line in figure 4.5 shows the position resolution of the GIS with the effect of parallax.

It is not easy to verify the position resolution of the GIS alone in orbit, because it is usually combined with the XRT PSF. Unresolved attitude jittering of the satellite (typically $\sim 1'$) also contributes to the broadening of the PSF core. However, it is confirmed that the half power diameter of the combined PSF of the XRT+GIS is almost consistent with the observed one.

4.2.4 GIS part of RMF

The RMF of the GIS ($R_{GIS}(E, PI)$) is intrinsic to the gas process of the GIS, and independent of the position of the incoming X-rays. Even the difference between GIS2 and GIS3 is negligible, completely identical tables (except sensor ID) are provided for GIS2 and GIS3. The GIS RMF is normalized as $\int R_{GIS}(E, PI)\, dPI = 1$, and the slice at $E = E_0$ gives a PI distribution for monochromatic X-rays of E_0 keV. Figure 4.6 shows a contour map of the GIS RMF and its slices at 1, 2, 4, and 8 keV. The GIS spectrum for monochromatic X-rays exhibits a Gaussan-like peak with a low energy tail which is due to the loss of some fraction of the electron cloud because of absorption by the Be window. This effect is modeled by a diffusion of electron clouds (Inoue et al. 1978), and the PI spectrum can be approximated by the formula:

$$F(PI) = \int_0^1 \frac{\kappa}{\sqrt{2\pi\sigma^2}} \exp\left(-\frac{(PI/\eta - PI_0)^2}{2\sigma^2}\right) \eta^{-1}(1-\eta)^{\kappa-1} d\eta \tag{4.8}$$

where PI_0, σ, and κ represent peak channel, energy resolution, and tail fraction, respectively. The energy resolution of the GIS is about 8.0% FWHM at 6 keV, and have an energy-dependence of $\propto 1/E^{\sim 0.5}$ (figure 4.7). Escape lines appear above Xe-L edges (4.78 keV), where the small jump of PI-E relation is also seen.

When calculating $R_{GIS}(E, PI)$, we slightly modify equation (4.8) (enhance the tail at lower PI channels), and interpolate the parameters derived from the monochromatic or semi-monochromatic spectra obtained in the ground calibration. Fine tuning of the parameters, particularly in the low energy band, has been carried out in several times, in order to explain a spectrum of the Crab nebula as a standard candle (ref §4.2.5), or

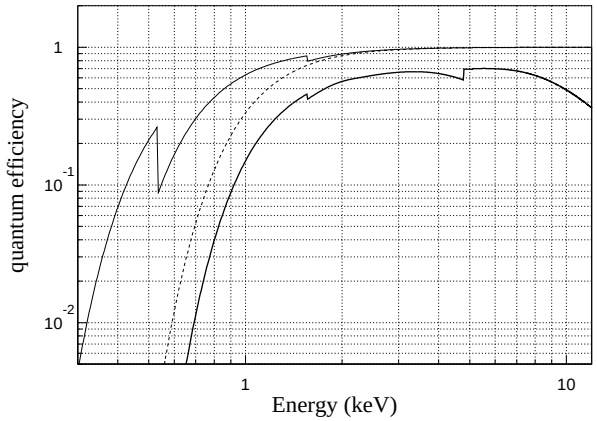

Figure 4.3: Energy dependence of the thermal shield transmission (thin solid line), 10.5 μm thick Be window transmission (dashed line), and total GIS quantum efficiency including thermal shield, plasma shield, Be window, and meshes (thick solid line). This plot is based on the version 4.0 GIS response.

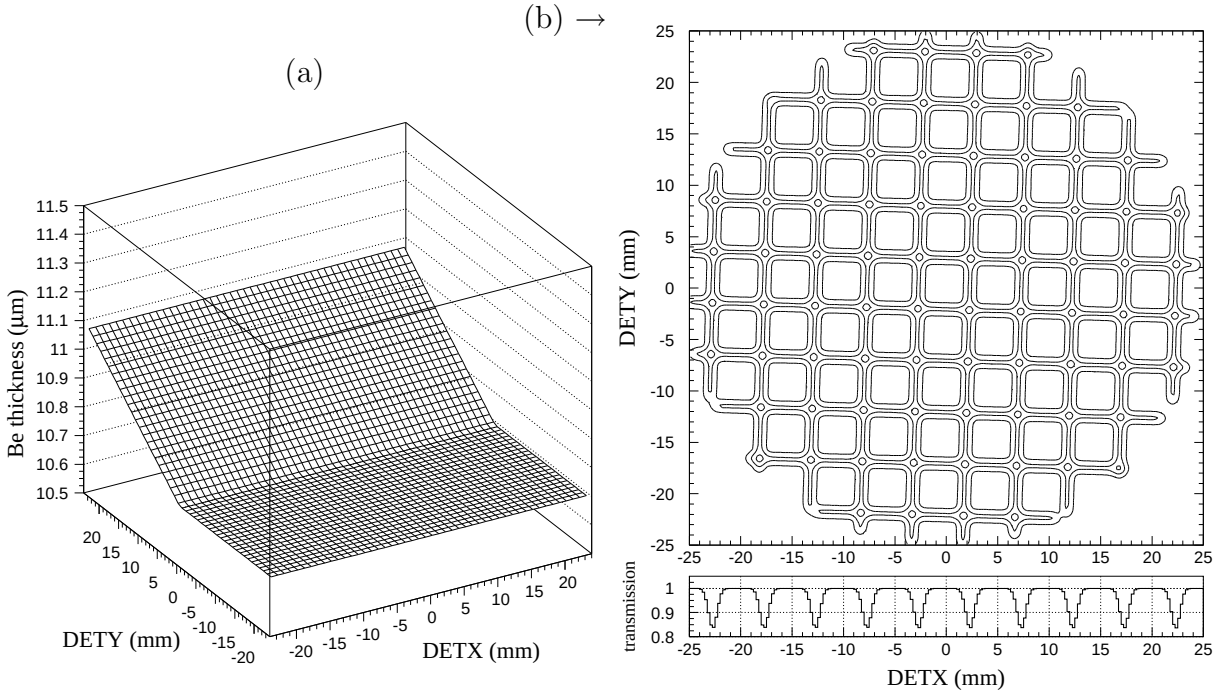

Figure 4.4: (a) Berylium thickness map for GIS2 on the detector coordinates based on the calibration data base file `s2bev1.fits`. (b) Upper panel shows a contour map of the GIS2 support grid transmission on the detector coordinates, based on the calibration data base file `s2gridv3.fits`, smoothed by the position resolution of GIS at 2.0 keV. Contour levels are 0.75, 0.85, and 0.95. Lower panel shows a cross section at $DETY = 0.0$.

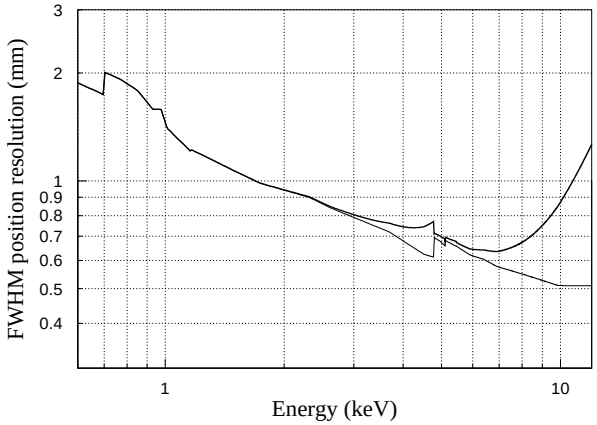

Figure 4.5: Energy dependence of the position resolution (FWHM) of the GIS with (thick line) and without (thin line) the effect of parallax. This plot is based on the version 4.0 GIS response.

strongly absorbed spectra such as EXO 2030+375 (for the low energy tail). For example, we have so far carried out modifications of the low energy tail function, energy dependence of κ and energy resolution, etc.

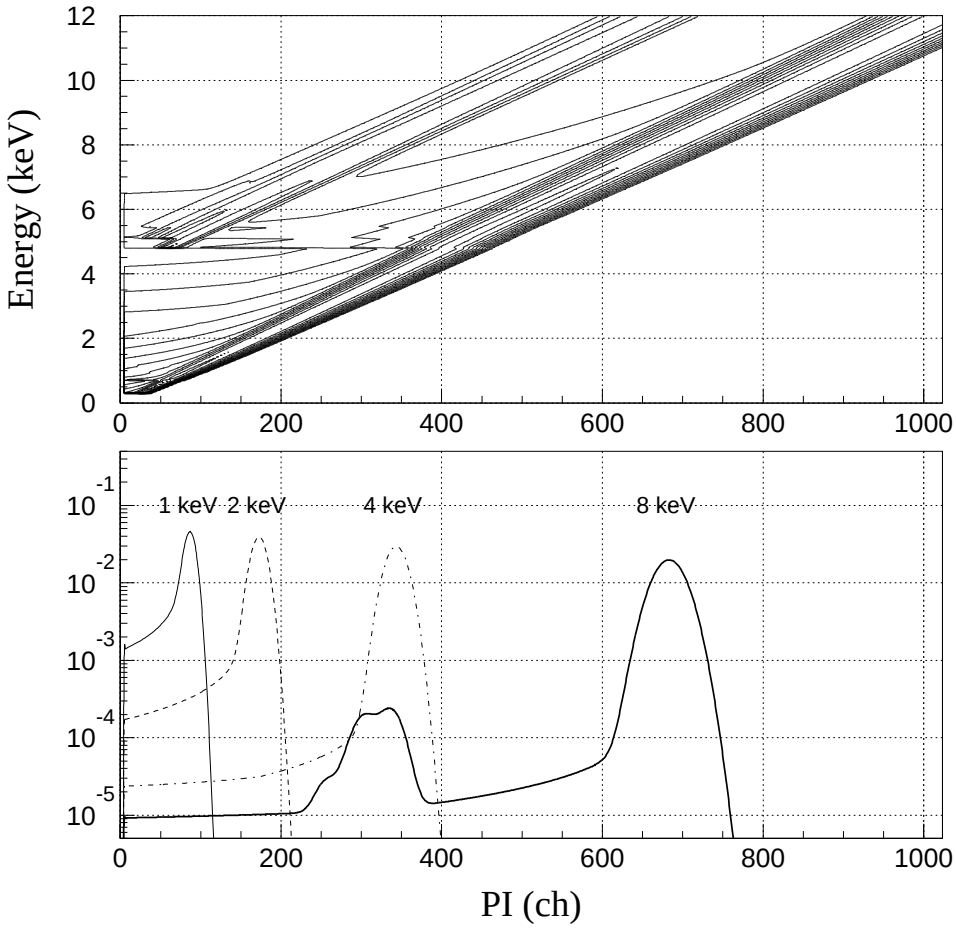

Figure 4.6: Upper panel shows a contour map of the GIS RMF `gis2v4_0.rmf`. Contour levels are every factor of 2. Lower panel shows the slices at 1 (thin solid line), 2 (dash), 4 (dot-dash), and 8 (thick solid line) keV.

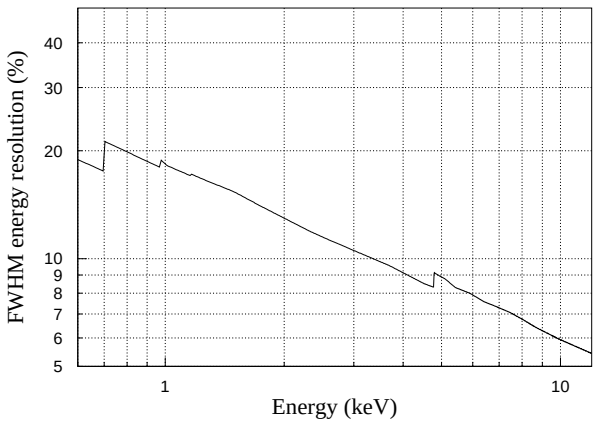

Figure 4.7: Energy dependence of the energy resolution (FWHM) of the GIS. This plot is based on the version 4.0 GIS response.

4.2.5 Verification of the XRT+GIS response for a point source

The Crab nebula has been used for an important calibration source as a standard X-ray object. The Crab is very bright (but too bright for the SIS) and have a stable X-ray emission, with an extent of 2′ or less, which is effectively a point source for the spectral calibration. Its X-ray spectrum has been measured with a number of experiments, and is known to be well expressed with a power-law function modified by low energy absorption due to the Galactic interstellar medium. The generally accepted values for the photon index, power-law normalization at 1 keV, and column density are 2.08–2.11, 9–11 c s^{-1} cm^{-2} keV^{-1}, and (2.7–3.3)$\times 10^{21}$ cm^{-2}, respectively. Especially the values measured by Ginga are that $\Gamma = 2.083 \pm 0.014$ and Norm $= 11.2 \pm 0.4$ c s^{-1} cm^{-2} keV^{-1} (Ueda 1993, internal report).

ASCA observed the Crab nebula many times at various positions on the detector. Figure 4.8 shows these pointing positions. In particular, a very deep observation for 97 ks (becase of deadtime, effective exposure is much less) was carried out on 28 September 1994 at the 1CCD nominal position. We performed fine tunings of the GIS RMF with the deep pointing data (§4.2.4). Energy-independent normalization of ARF was also scaled so that the X-ray flux in the 2–10 keV energy band is consistent with the generally accepted value.

Figure 4.9 shows the GIS2+3 spectrum of the Crab nebula at the 1CCD nominal position, fitted with an absorbed power-law model convolved with the standard RMF

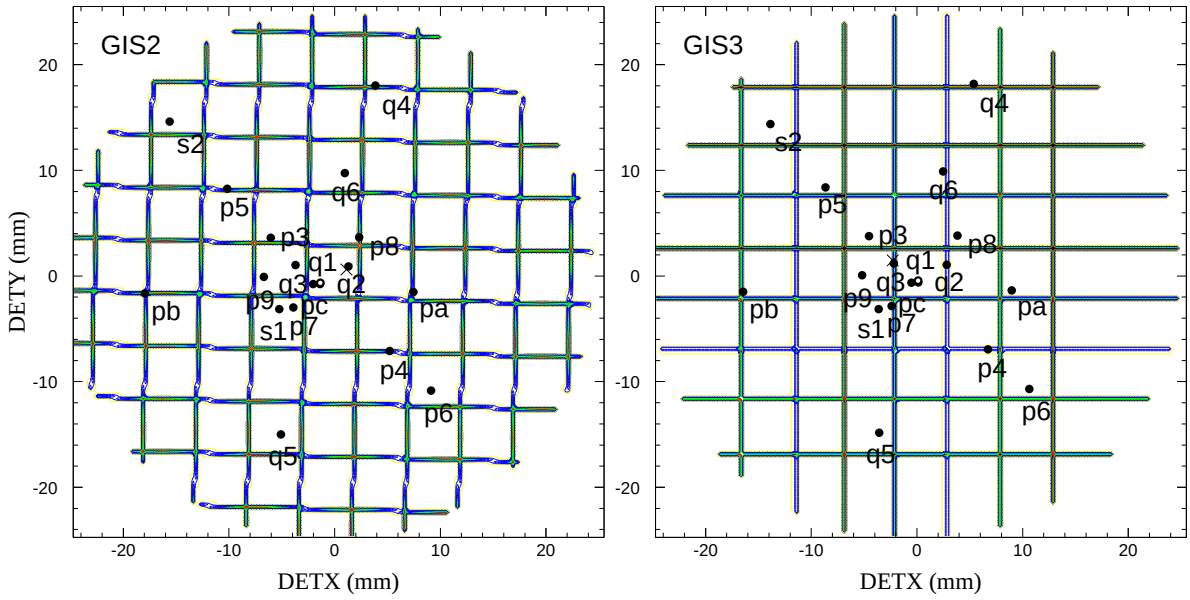

Figure 4.8: Pointing positions of the Crab nebula (•) overlayed on the grid maps of GIS2 and GIS3. Open circle labeled “q1” shows the 1CCD nominal position, and ’×’ shows the optical axis.

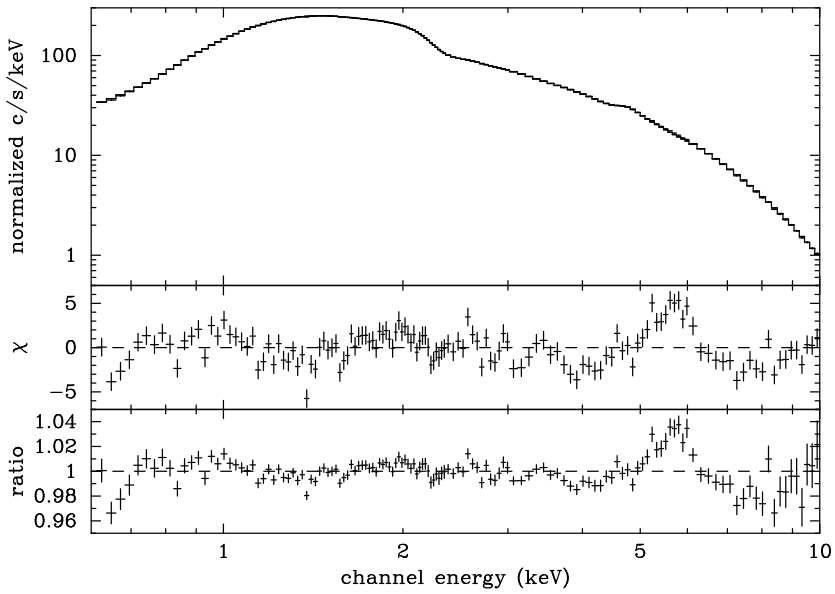

Figure 4.9: The Crab nebula spectrum fitted in the entire 0.6–10 keV energy band with an absorbed power-law model. The observation was conducted at the 1CCD nominal position on 28 Sep 1994. The spectrum is dead-time corrected and the CXB + NXB spectrum is subtracted. Deadtime corrected effective exposure is 14,466 s. The best fit parameters are shown in table 4.4. Upper panel shows the GIS2+3 spectrum (crosses) and the best fit model (solid line). Middle panel shows residuals plotted in unit of σ. Lower panel shows ratios of the data to the model.

Table 4.4: An absorbed power-law fits to the 0.6–10 keV spectrum of the Crab nebula

Sensor	GIS2	GIS3
χ^2/d.o.f	621 / 304	501 / 304
photon index	2.16	2.17
$N_{\rm H}$ (10^{22} cm^{-2})	0.32	0.34
norm (c s^{-1} cm^{-2} keV^{-1} at 1 keV)	10.3	10.8
2–10 keV flux (10^{-8} erg s^{-1} cm^{-2})	2.04	2.11

(figure 4.5) and ARF (figure 4.18). Table 4.4 shows the fitting results. Although the fit is not acceptable because of the extremely high statistics of the spectrum, ratio of the data to the best-fit model is within 5% in the full energy band of 0.6–10 keV. The most prominent structure is a hump around 5–6 keV, and further tuning of the optical constants for the XRT is still in progress to eliminate the structure. The best fit Crab parameters thus obtained are roughly consistent with the generally accepted values. The photon index shows somewhat steeper value of $\Gamma = 2.16$.

Utilizing the Crab observations, we also examined whether the position dependence

of the XRT+GIS system has been adequately compensated by ARF. Figure 4.10 shows the Crab spectral parameters plotted versus offset angle θ. Since the Crab has a stable spectrum, the scatter seen there should originate in systematic errors that could not be compensated perfectly by the ARF builder. In the range of $\theta < 20'$, the derived Crab index scatters only by about ± 0.03, the absorbing column density by $\pm 0.3 \times 10^{21}$ cm^{-2}, and the inferred Crab flux by $\pm 8\%$. We can say that the spectral parameters are correct within the above uncertainties over the whole area of $\theta < 20'$. The reason why the flux scatters so much is thought to be an effect caused by the support grids on the GIS window. Furthermore, the flux appears to increase systematically and the spectrum appears to flatten, as offset angle gets larger. We discuss its possible influence upon the CXB analysis in §6.4.

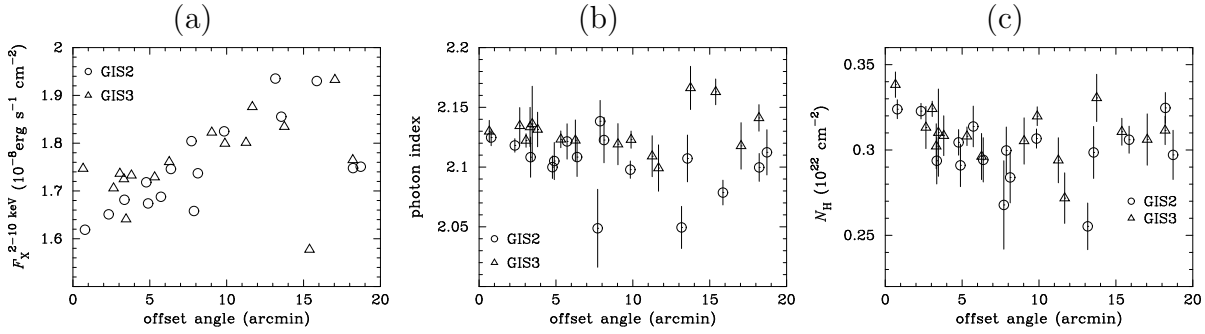

Figure 4.10: Offset angle dependences of the best fit parameters for the Crab nebula spectra, observed at different positions on the detector plane. (a) Absolute flux in the 2–10 keV energy band, (b) photon index, (c) column density. Open circles show GIS2, and triangles GIS3. Note that the results shown here are based on a slightly older version of the XRT response, which gives some inconsistensy with the value shown in table 4.4.

4.3 Stray light effect to the CXB analysis

4.3.1 What is stray light?

The XRT of ASCA allows some fraction of the X-rays, even outside of the f.o.v. from an offset angle $\theta > 30'$, to reach the focal plane detector. This phenomenon is somewhat different from the large outskirts of the XRT PSF, discussed in §4.2.2. The large outskirts of the XRT PSF are mainly due to the waving of the thin XRT foils, and those photons also undergo the normal sequence of two successive reflections on the primary and the secondary mirrors of the Wolter type I optics. Whereas most of the photons which come from outside of the f.o.v. have gone through abnormal paths, which are not on the assumption of the Wolter type I optics. These X-rays are called stray lights. The XRT configuration provides X-rays with four kinds of light paths, as shown in figure 4.11. The normal path is (a), and others are stray. For short, we call these paths (a) normal reflection, (b) primary only reflection, (c) secondary only reflection, and (d) multiple reflection. Multiple reflection is somewhat specific to the ASCA XRT (Tsusaka et al. 1995). Because both sides of the mirror foils of the XRT are coated with acrylic lacquer before Au is evaporated on the front sides, soft X-rays can reflect on the backside, too. The critical angle of the acrylic surface at 1.5 keV is $\sim 1^\circ$.

Figure 4.12 shows an example of stray lights taken by GIS3. The Crab nebula is placed at the position of the filled circle, $60'$ offset from the optical axis in the direction of $\phi = 45^\circ$ / 135° / 225°. A shell-like image is seen spreading over the whole detector plane. The stripes represents the XRT sector structure divided by the alignment bars.

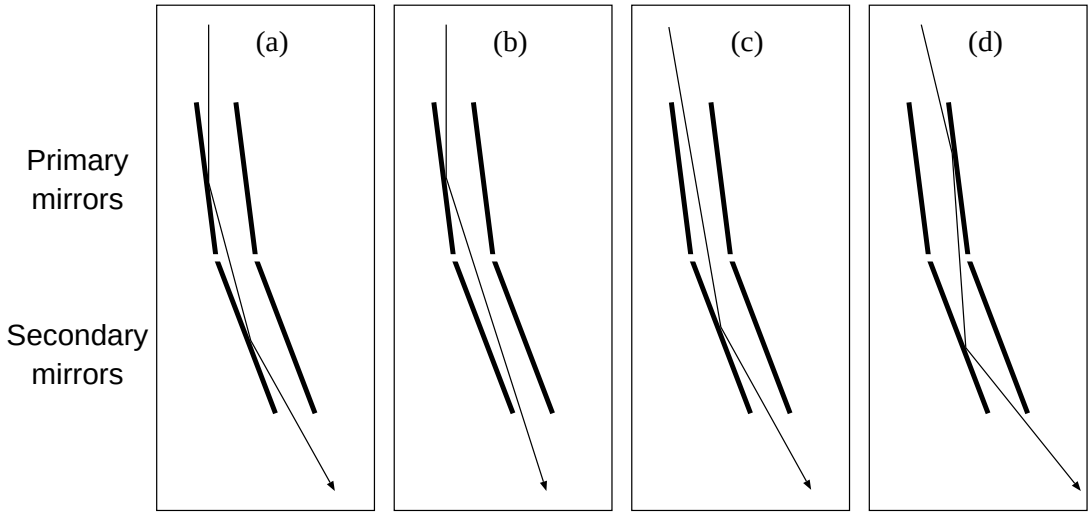

Figure 4.11: Four examples of XRT light paths: (a) normal path, (b) reflection only by primary mirrors, (c) reflection only by secondary mirrors, (d) multiple reflections by front and back surfaces of mirrors.

4.3.2 Evaluation of stray light effects by ray-tracing

Since the CXB is uniformly extending on the whole sky, we must fully take the stray light effect into account for the CXB analysis. Stray lights occupy a significant fraction of the CXB photons detected at outer rings on the detector, especially in lower energy bands (see text below). However, a stray light image has a complex shape as seen in figure 4.12, and it is not easy to express it in an analytic formula. It is also unrealistic to observe the Crab nebula in various offset and azimuth angles. There are observational time constraints and interpolation of observed patterns is also a problem. One solution is to utilize the ray-tracing (Tsusaka et al. 1995). Fortunately, stray light pattarns are well determined by the foil structure of the XRT. Therefore the ray-tracing program with reliable XRT parameters is expected to reproduce the stray light effects pretty well. Figure 4.13 shows a ray-tracing image for $\theta = 60'$ and $\phi = 225°$, which well reproduces the lower right image of figure 4.12.

Then, using a ray-tracing program, we simulate the effects of stray lights for the CXB analysis. First of all, how far the CXB photons can come from? This is very important because the CXB is distributed all over the sky and it is time consuming to integrate over large sky area. Figure 4.14a shows how much fraction of photons is expected to come from the sky $\theta > \Theta$ into the integration area of $r < 20$ mm. This figure shows that we must take into account the photons up to $\theta_{max} = 100'$ at $E = 1.0$ keV in order to determin the CXB flux at 1.0% level. We have therefore adopted $\theta_{max} = 150'$ for the CXB analysis. Since the multiple reflection component disappears rapidly in the higher energy bands, the range of θ which we must consider gets smaller as energy increase. Figure 4.14b shows predicted spectral contributions of photons which come from rings of $\theta = 0$–$20'$, 20–$40'$, 40–$60'$, 60–$80'$, and 80–$150'$. Contributions from 20–$40'$, 40–$60'$, and 60–$80'$ rings are thus expected to be comparable, but the spectrum turns softer.

Figure 4.15 shows the predicted stray light contributions in the radial profile for a uniformly extending source. At the position of $r = 20$ mm from the optical axis, stray lights are thus expected to contribute about 60/50/40/20% at 1.0/2.0/4.0/8.0 keV, respectively. The multiple reflection component contribute a significant fraction at 1.0 keV, but it is almost negligible at 4.0 keV. It is because the backside reflectivity of the foils rapidly drops in hard bands. On the contrary, the secondary only reflection component is expected to contribute almost the same fraction to the normal reflection component. The primary only reflection component can be neglected.

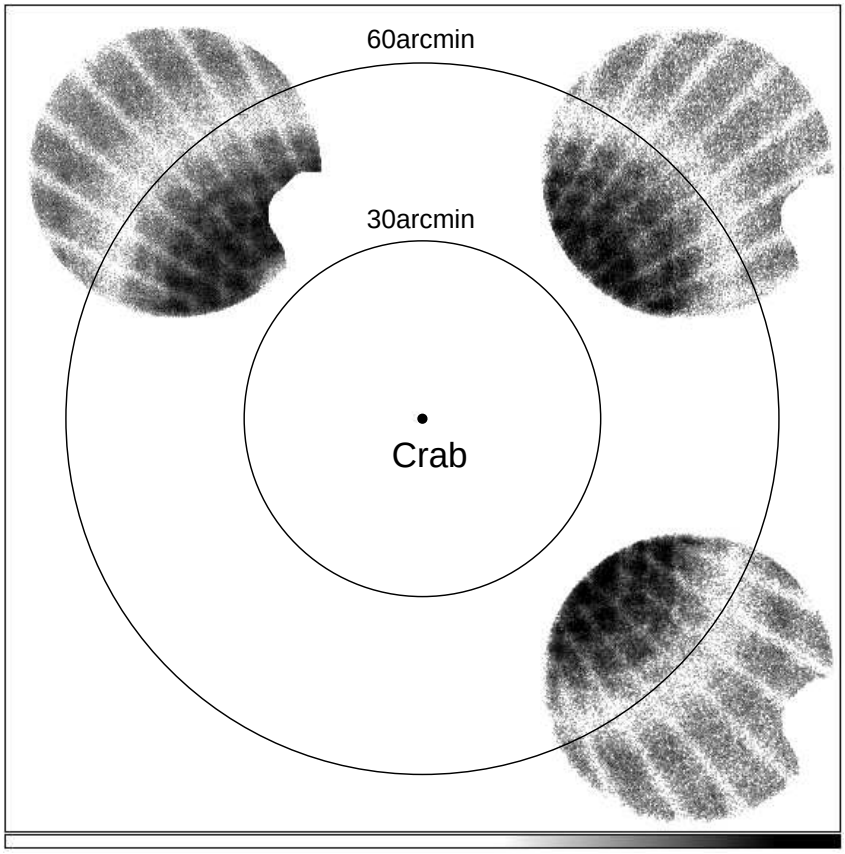

Figure 4.12: Three of the Crab stray light images taken by GIS3 in the 0.7–10 keV band, shifted and superposed on the detector plane so as to reproduce correct angular relations with respect to the Crab nebula. The location of the Crab is indicated with a filled circle, and the optical axis for each observation is offset by $60'$ from the Crab.

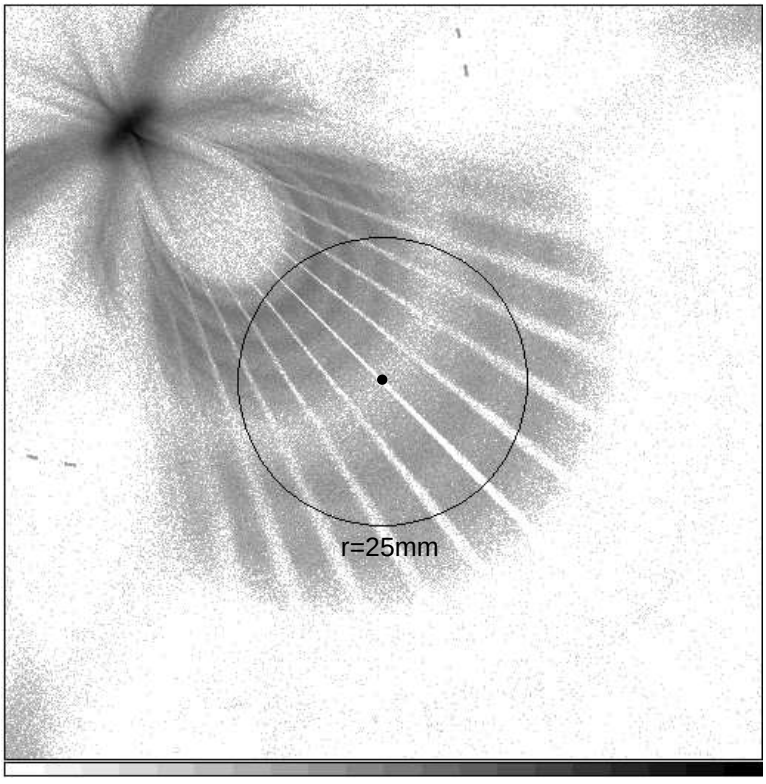

Figure 4.13: Ray-tracing image of the stray light pattern at 1 keV for the offset angle $\theta = 60'$ and the azimuthal angle $\phi = 225°$. A filled circle shows a position of the optical axis. A superposed circle of $r = 25$ mm on the image corresponds to the GIS f.o.v.

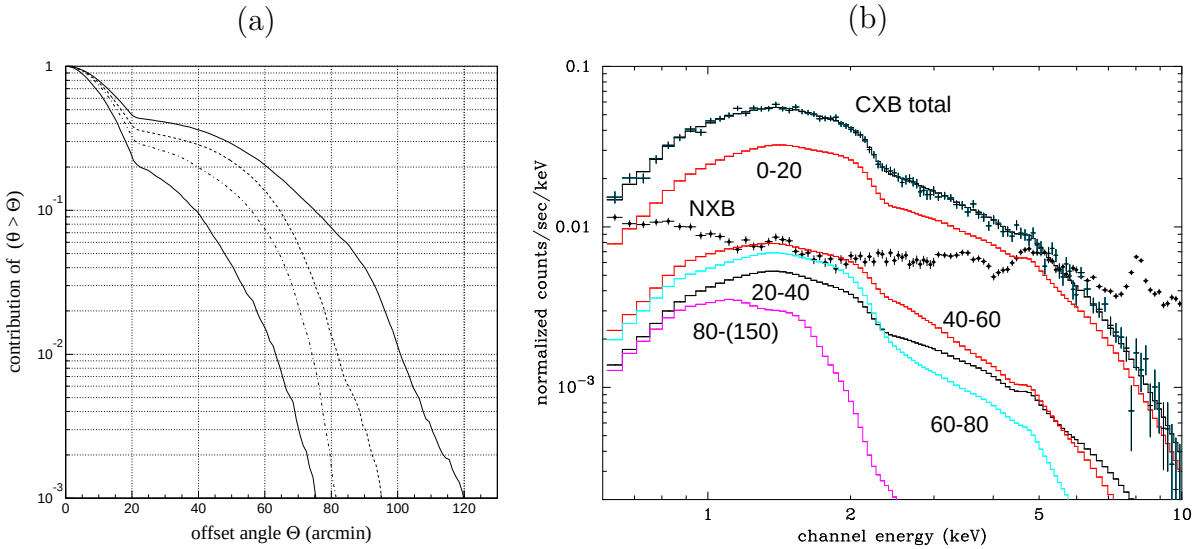

Figure 4.14: (a) Calculated ratios of the CXB photons which come from the offset angle $\theta > \Theta$, to the total CXB photons integrated within the radius of 20 mm from the optical axis, at 1 (thick solid line), 2 (dashed), 4 (dot-dashed), and 8 (thin solid line) keV. (b) The averaged CXB spectrum (crosses) and the NXB spectrum (filled circles), plotted with calculated contributions from θ = 0–20′, 20–40′, 40–60′, 60–80′, and 80–150′.

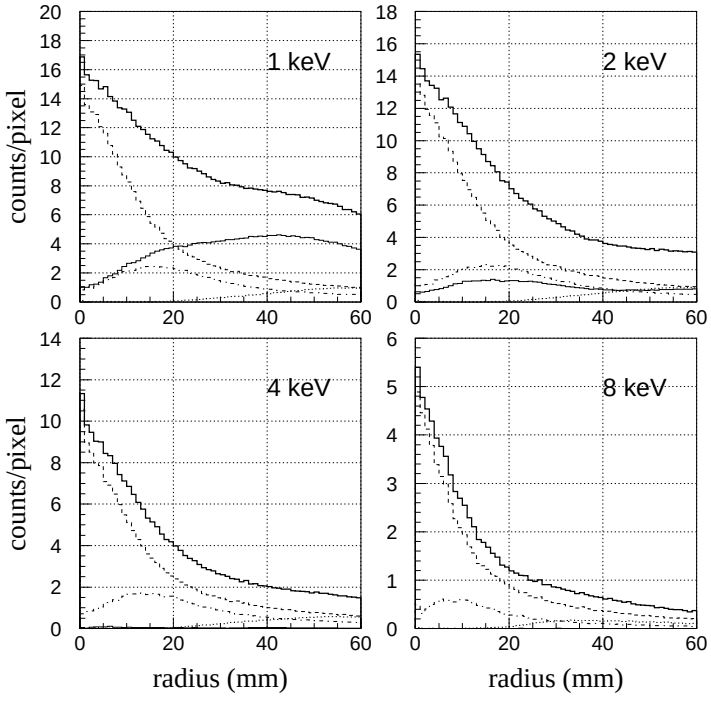

Figure 4.15: Azimuthally averaged radial profiles of the CXB image (thick solid lines) calculated by ray-tracing at the energies of 1, 2, 4, and 8 keV. Contributions of the normal reflection (dashed), the primary only reflection (dotted), the secondary only reflection (dot-dashed), and the multiple reflection (thin solid lines) are also plotted.

4.3.3 Comparison of ray-tracing with Crab stray obserbations

We carried out large offset observations of the Crab nebula at several offset angles, for the purpose of calibrating the stray light effects in comparison with the ray-tracing predictions. Table 4.5 shows the list of these Crab observations. Azimuth angles are basically arranged in the $\phi = 225^\circ$ direction, where the stray light strength is the maximum (it is minimum at $\phi = 0^\circ$, 90°, 180°, and 270°). For $\theta = 60'$, the direction of $\phi = 45^\circ$ and 135° are also observed to check the symmetry of the image. Although there are also large offset observations of Sco X-1, the data cannot be utilized for the present purpose because Sco X-1 is variable.

Left panels of figure 4.16 show the observed spectra taken by GIS2 (upper panel) and GIS3 (lower panel). Right panels show the simulated spectra using the ray-tracing. We can say that the simulation roughly reproduces the spectral shape and normalization in the range of as much as five orders of magnitude. Figure 4.17 compares the counting rate from the actual observations with those based on the simulation. There seems to exist a systematic difference between GIS2 and GIS3, although the reason is still unclear. However we are thus confident that the systematic error of the simulation is about -30%–$+10\%$ within $\theta \sim 80'$, where effective CXB photons come from. As can be seen in figure 4.12, the stray light pattern also has a good 90° symmetry within a deviation up to a few arcmin. From these investigations, we conclude that the current ray-tracing program has a sufficient accuracy and reliability in quantifying the stray light effects upon the CXB analysis.

Table 4.5: Log of the Crab stray observations

Date		Exposure	GIS2		GIS3	
yy/mm/dd	START – END	(sec)	θ	ϕ	θ	ϕ
93/04/06	07:38 – 00:55	13,261	$57.6'$	47.3°	$61.5'$	44.5°
95/09/29	17:57 – 21:31	5,346	$64.0'$	222.4°	$60.0'$	225.0°
95/09/29	03:36 – 06:44	5,462	$63.1'$	138.3°	$60.1'$	134.8°
95/09/30	02:11 – 06:30	2,206	$21.4'$	219.9°	$17.0'$	228.0°
95/09/28	22:51 – 03:34	8,110	$33.8'$	220.0°	$29.8'$	224.9°
95/09/28	18:21 – 22:50	6,354	$48.8'$	221.1°	$44.8'$	224.5°
95/09/28	06:46 – 12:52	8,777	$83.7'$	223.0°	$79.7'$	224.9°
95/09/29	21:32 – 02:10	9,476	$103.8'$	223.3°	$99.9'$	224.9°

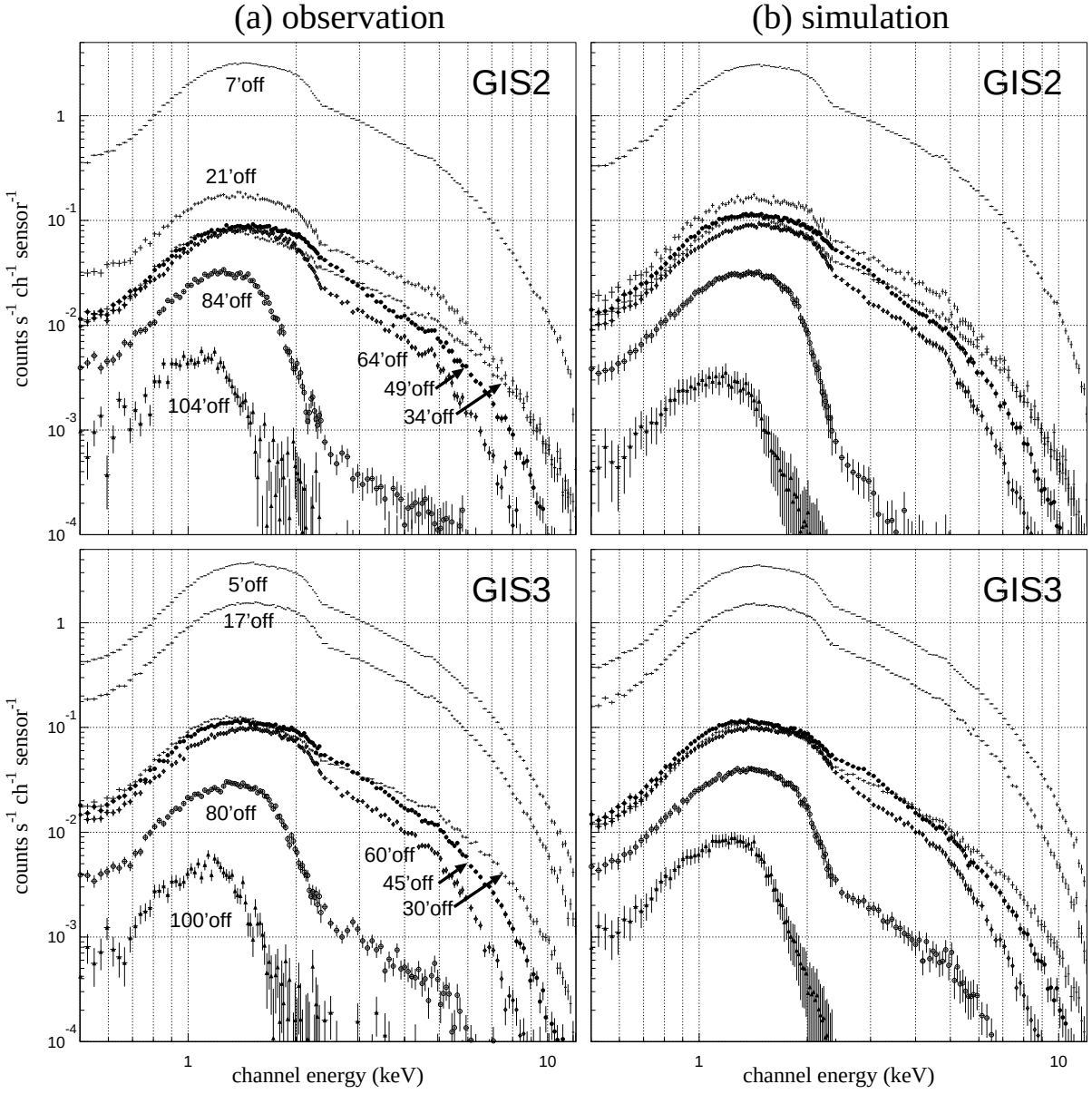

Figure 4.16: (a) Spectra of the Crab stray observations taken by GIS2 (upper panel) and GIS3 (lower panel) integrated in the radius of 20 mm from the optical axis of each sensor. The Crab has been placed at various offset angles as specified in the figure. The CXB+RNXB spectra are subtracted after dead time correction. (b) Simulated spectra of the Crab stray observations. The Crab nebula is assumed to have an absorbed power-law spectrum of $\Gamma = 2.10$, $N_{\rm H} = 3.0 \times 10^{21}$ cm^{-2}, and the power-law normalization of 9.7 c s^{-1} cm^{-2} keV^{-1} at 1.0 keV.

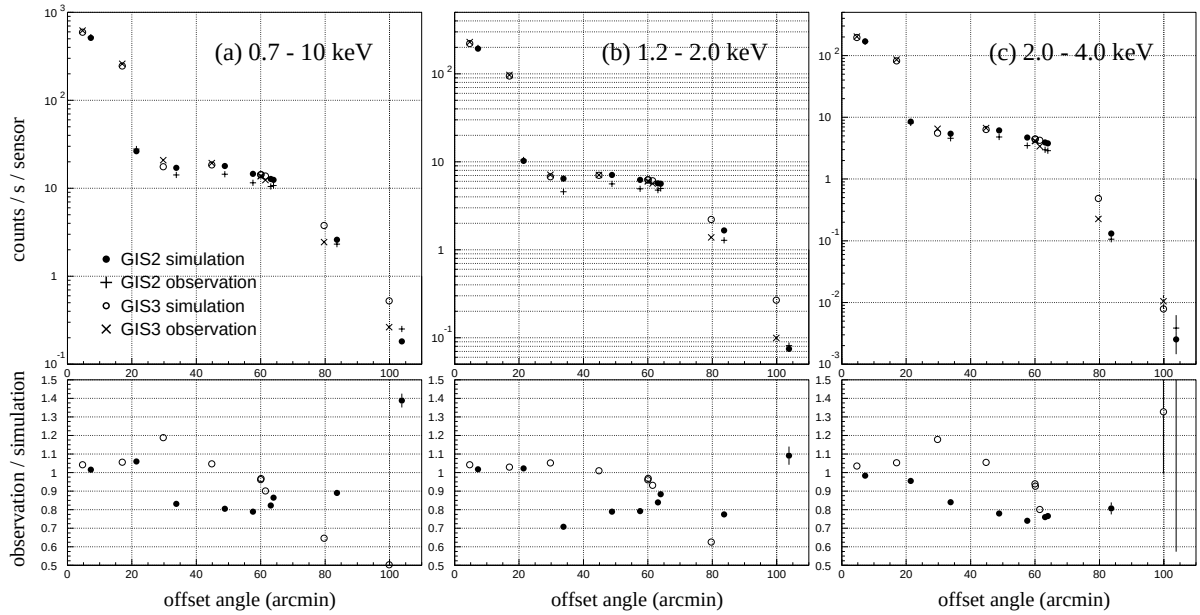

Figure 4.17: Upper panels show counting rates of the Crab stray observations and the ray-tracing simulations in (a) 0.7–10 keV, (b) 1.2–2.0 keV, and (c) 2.0–4.0 keV energy band, plotted versus offset angle of the Crab nebula. Lower panels show the ratios of observation to simulation.

4.3.4 The ARF builder for the CXB spectrum

The CXB is thought to have not only a uniform spectrum but also an almost constant brightness on the whole sky, so that we can approximate the CXB photon flux distribution F_{CXB} as

$$F_{CXB}(\theta, \phi, E) = \cos\theta \; S_{CXB}(E). \tag{4.9}$$

The factor $\cos\theta$ means a reduction of the XRT aperture by the inclination. This makes the ARF calculation of equation (4.6) much easier. However, there are some problems to use jbldarf (ref. §4.2.1) to make an ARF for the CXB. The first problem is that we must take the stray light effects (§4.3) into account in order to make the correct CXB ARF. However the pre-calculated XRT tables for the effective area and the PSF are both defined only in the range of $\theta < 20'$, i.e. within the nominal f.o.v., which is totally insufficient to consider the stray lights. The second problem is that, even if there were tables covering $\theta > 20'$, it would take unrealistically huge time or CPU power to integrate over the whole sky where effective CXB photons come from.

To solve these issues, we make use of an ASCA simulator called SimASCA, developped mainly by M. Hirayama, Y. Ogasaka, T. Kotani, and Y. Ishisaki. Instead of conducting the numerical integration of equation (4.4), we generate a number of Monte-Carlo photons of energy E, according to the surface brightness distribution $B(\theta, \phi)$, we run XRT+GIS simulator, and we count how many photons come into the integration area on the detector

plane. Here, we denote the number of the Monte-Carlo photons which has been generated N_{gen}, the number of photons detected N_{detect}, and the geometrical aperture of the XRT D_{XRT}. Then, $D_{XRT} \times \frac{N_{detect}}{N_{gen}}$ gives the expected value of $A_{XRT+GIS}(E)$ in equation (4.4). The Monte-Carlo error Δ of this value is expected to be $\frac{\Delta}{A_{XRT+GIS}(E)} = \sqrt{\frac{N_{gen}-N_{detect}}{N_{gen} \cdot N_{detect}}}$. We continue generating the Monte-Carlo photons of energy E, until this error ratio becomes typically less than 2%. M. Hirayama, H. Honda and R. Shibata have developped a code doing this procedure, and they named it SimARF. The SimARF has been modified and tuned for the CXB analysis.

The XRT simulator is the key module for the CXB ARF. We selected the ray-tracing program as the XRT simulator, which can take into account the stray light effects in a natural way. This ray-tracing program is released by the XRT team and also used to make the pre-calculated XRT tables for the effective area and the PSF shown in table 4.3, although the version of the program is somewhat different. As seen in the previous section, the ray-tracing program has sufficient accuracy and reliability in quantifying the stray light effects on the CXB analysis.

Figure 4.18 shows examples of the point source ARFs and the CXB ARFs created by the SimARF which is adopted in the analysis of the present thesis. The main difference is that the CXB ARF has much less effective area in higher energy bands than the ARF at 1CCD nominal position, because of both vignetting and the soft spectra of stray lights. About 40% difference is seen in the range of 0.6–10 keV, which corresponds to ~ 0.2 in terms of the phton index.

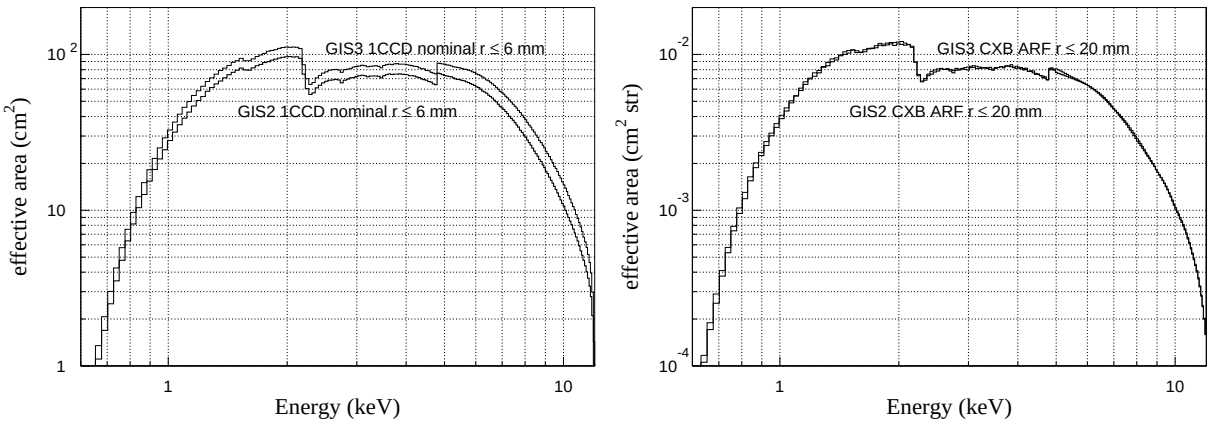

Figure 4.18: Plot of the ARFs for GIS2 (thick line) and GIS3 (thin line). Left panel shows the point source ARFs at 1CCD nominal position with integration radius 6 mm. Right panel shows the CXB ARFs with integration radius 20 mm from the optical axis.

4.4 Residual non X-ray background (RNXB) of the GIS

4.4.1 Importance of RNXB in the CXB analyses

To begin with, we define RNXB (residual non X-ray background) to mean false events of non X-ray origin (mainly charged particles and γ-rays), which survived standard background rejection process described in §3.4.3, and appear in the GIS main data. All data shown in this section are already cleaned with *RT* discrimination (RTD), *SP* discrimination, and strict *RT* mask.

In the usual analysis of a point source data, we subtract CXB+RNXB as a background, whereas only RNXB should be subtracted in the analysis of the CXB itself. Therefore, more carefull RNXB estimation is required for the CXB analyses. Particularly, we need to make full use of the detector area to get a CXB spectrum of good statistics. As a result, fraction of the RNXB counts also increases. When we choose an integration radius of 20 mm, the RNXB counts are abount 32% of the pure CXB counts in the 0.6–10 keV energy band. Furthermore, as seen in figure 4.14b, the RNXB counts exceeds the CXB counts above ~ 5 keV.

As described in §3.4.3, the GIS is equipped with various mechanism to reject background events efficiently, and the GIS thus has realized very low background level of 0.044–0.086 c s^{-1} $sensor^{-1}$ (table 3.4). Properties of RNXB is also well investigated so far (Kubo 1993; Kubo et al. 1994 in ASCA News No.2). We briefly introduce the results in §4.4.2, explain how to restrain/monitor the time variation of RNXB in §4.4.3, and test the RNXB reproducibility in §4.4.4.

4.4.2 Rough properties of RNXB

We cannot distinguish RNXB from the real X-ray events. Therefore, we utilize the night-earth data surviving the full background rejection, i.e. events obtained when the XRT was pointing to the night-side of the Earth, to study the RNXB properties. Although there is a possibility of oxygen line or harder X-rays from auroras, we assume that the night-side of the Earth emits no X-rays; hence we believe that the night-earth data consist solely of RNXB. We have collected the night-earth data since the GIS started the operation. Results shown in this section are based on the night-earth observations from June 1993 to June 1995. It turned out that there are some contamination of solar X-rays when the day-side of the Earth are partially visible from the satellite even if it is outside the GIS f.o.v. Therefore, we adopted the selection condition that

$$\text{target elevation from the rim of the Earth} \leq -5^\circ$$

.AND.

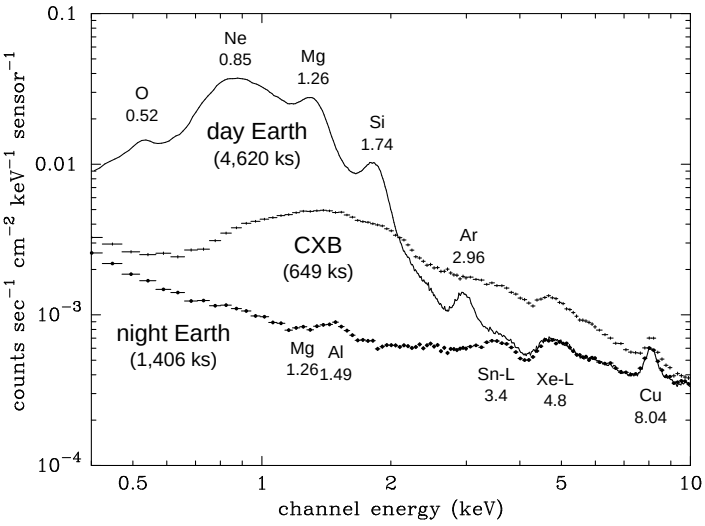

Figure 4.19: Integrated spectra of the day-earth (smooth line), the CXB (crosses), and the night-earth (filled circles) observations taken by the GIS2+3 on the whole detector area as shown in figure 4.20. Each of exposure time is given in the parentheses. The CXB and the day-earth spectra contains RNXB. Possible origin of the line feature with the energy in keV are also given in the figure. The flare-cut (table 4.6) is NOT applied.

sun height from the rim of the Earth $\leq -5^{\circ}$.

Integration time of the resultant data amounts to 1,400 ks.

Figure 4.19 shows the average night-earth spectrum, presented together with the day-earth and the CXB spectra. The unit of cm^2 in the count rate unit refers to the detector area, not to the XRT area. Thus the in-orbit RNXB level is about 1×10^{-3} c s^{-1} cm^{-2} keV^{-1} below 1 keV, and (4–7)$\times 10^{-4}$ c s^{-1} cm^{-2} keV^{-1} above 1.5 keV. This is 2–3 times larger than that measured on ground. The night-earth spectrum exhibits several instrumental features, including Cu-K line (from copper-plated molybdenum support grid; 8.04 keV), a hump around 5 keV due to Xe-L edges (from the detection gas; 4.78 keV, etc), Sn-L line (from the tin-plated stainless support mesh; 3.44 keV), a possible blend of Mg-K (from the GIS case made of Mg-alloy; 1.26 keV) and Al-K (not yet determined; 1.49 keV) lines. All these lines and edges arise from materials used in the GIS. The day-earth spectrum consist of RNXB and solar X-rays scattered off the atomosphere. Error bars are omitted because of the extensively high statistics. Mg-K and Si-K lines are of solar origin (ionized species), while the Ar-K line (neutral) is due to atmospheric fluorescence. A close agreement of the night-earth and the day-earth spectra above 5 keV visualizes the RNXB stability.

Figure 4.20 shows images for GIS2 and GIS3 during the night-earth observations. There are several regions where the residual night-earth counts are high, such as lower rim of GIS2 and upper rim of GIS3. It is probably due to to the incompleteness of SPD. There is also a little spill of the calibration source around the masked-out regions, although its level is negligible. Except such local inhomogeneities, the residual night-earth counts increase at the outer region of the detector in general. This trend is more significant below 1 keV, as shown in figure 4.21. However, inside about 10 mm from the detector center,

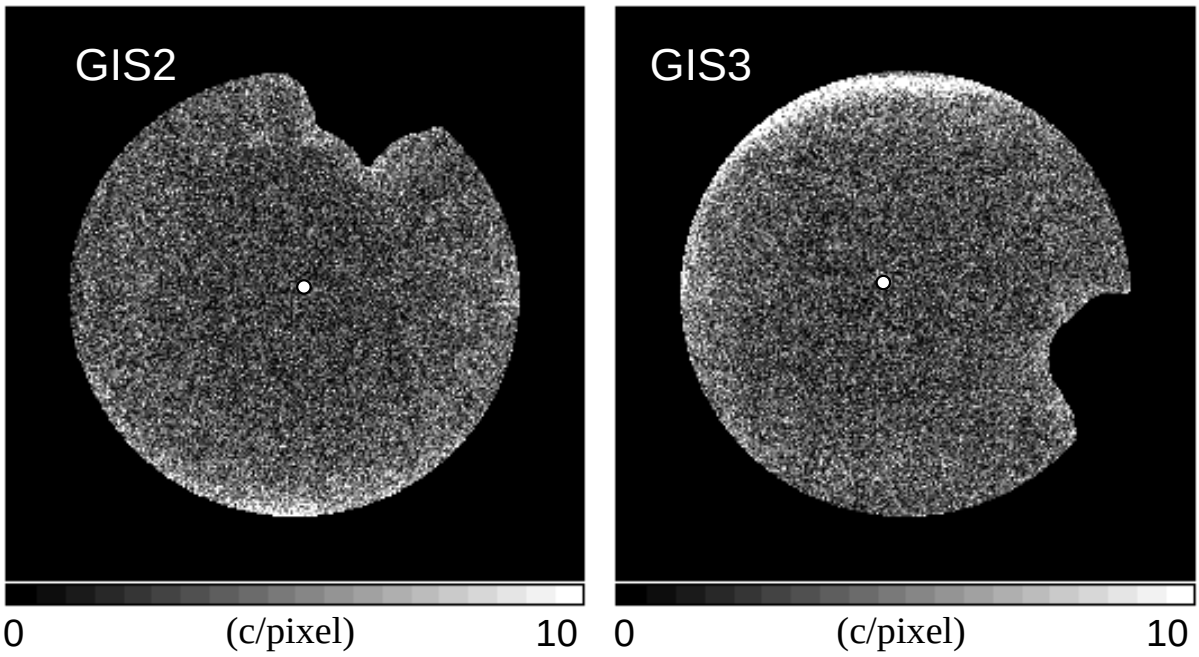

Figure 4.20: Integrated images taken by GIS2 (left panel) and GIS3 (right panel) for the entire night-earth observations with exposure time of 1,202 ks in the 0.6–10 keV energy band. The white spot in the figure shows the optical axis of each detector. Both images are masked by the standard image masking, i.e. selection of $r \leq 25$ mm from the detector center and elimination of the calibration isotope. The flare-cut (table 4.6) is applied.

the residual night-earth data show fairly constant spectra and intensity as a function of the detector position. Therefore, we may presume that there are approximately two RNXB components; (1) a "hard component", which has a flat spectral shape and an almost constant intensity over the whole detector area, and (2) a "soft component", which rises below 1 keV and significantly increases towards the detector rim. In contrast, the CXB intensity is the strongest at the optical axis of the XRT because of the vignetting effect. The CXB intensity at $\theta = 20'$ is roughly half the on-axis CXB intensity. Therefore influence of RNXB gets much severer towards the detector rim, because of both vignetting and the RNXB profile, as shown in figure 4.22. Irregularities of ~ 5 mm step seen in the CXB counts are shadows of the window support grids.

Time variation of RNXB is predominantly correlated with geomagnetic cutoff rigidity (COR) for cosmic rays along the satellite orbit. COR defines the minimum momentum of charged particles that can penetrate against electro-magnetic force due to terrestrial magnetism. When cosmic rays (charged particles) run across the Xe gas, gas creates long electron track along the path. Most of these events can be rejected by RTD. Electrons ejected from the ceramic wall of the gas cell struck by cosmic rays are also a candidate of background events. It is probably the origin of the *soft* component of RNXB, and these events can be rejected by RTD or SPD for the most part. Cosmic rays also generate high

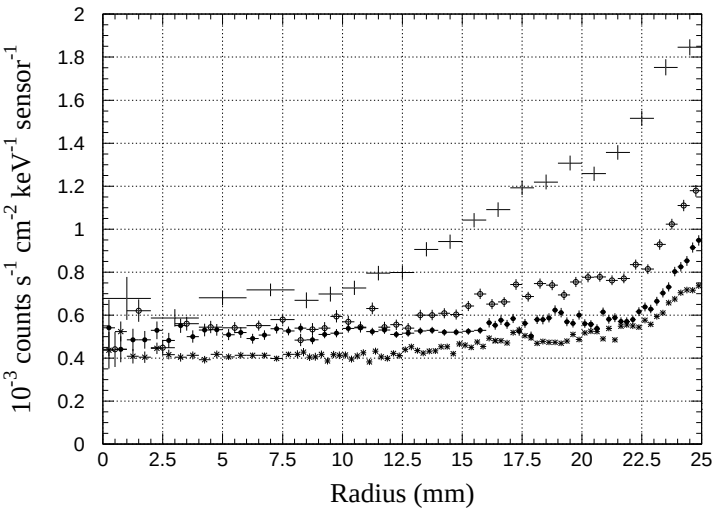

Figure 4.21: Energy sorted radial profiles of the GIS counts during the night-earth observations. GIS2 and GIS3 data are summed up. The mark of '+' shows 0.6–1.0 keV, '○' 1.0–2.0 keV, '•' 2.0–4.0 keV, and '×' 4.0–8.0 keV. The flare-cut (table 4.6) is applied.

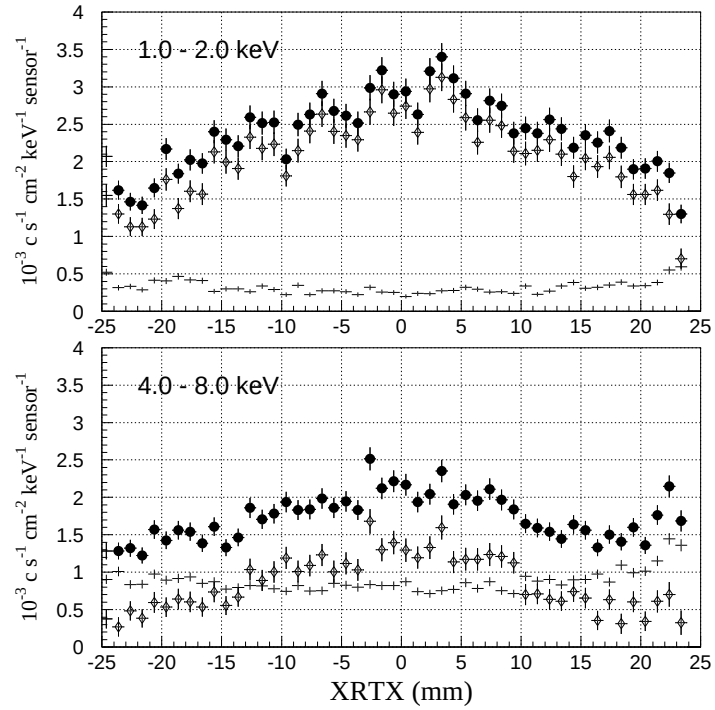

Figure 4.22: Band profiles during the CXB and night-earth observations in -5 mm $\leq$ XRTY $\leq +5$ mm for GIS2. Upper panel shows a profile in the 1–2 keV energy band, and lower panel 4–8 keV. The origin of the coordinates for $XRTX$-$XRTY$ is the optical axis. Filled circles, crosses, and diamonds represent the raw CXB including RNXB, the residual night-earth, and the CXB after subtracting the residual night-earth, respectively. The flare-cut (table 4.6) is applied for both the CXB and the residual night-earth data.

energy γ-rays reacting with the satellite body or the atmosphere. Compton-scattered electrons by γ-rays especially in the drift region of the gas cell is rather hard to eliminate. Figure 4.23 shows a correlation between COR and $LDHIT$ during the night-earth observations. $LDHIT$ increases as COR gets lower. Especially, the correlation gets steeper below $COR \sim 6$ GeV/c. There is also a branch in the $LDHIT$-COR correlation for $COR \leq 10$ GeV/c, as well as a large scatter around $COR \sim 11$–12 GeV/c. These two phenomena will be discussed in §4.4.3.

A long-term RNXB increase by $\sim 10\%$ in two years has been seen, as shown in figure 4.24. Although the spectral shape has not changed significantly, it is probably caused by a gradual build-up of long-term decay radioisotopes.

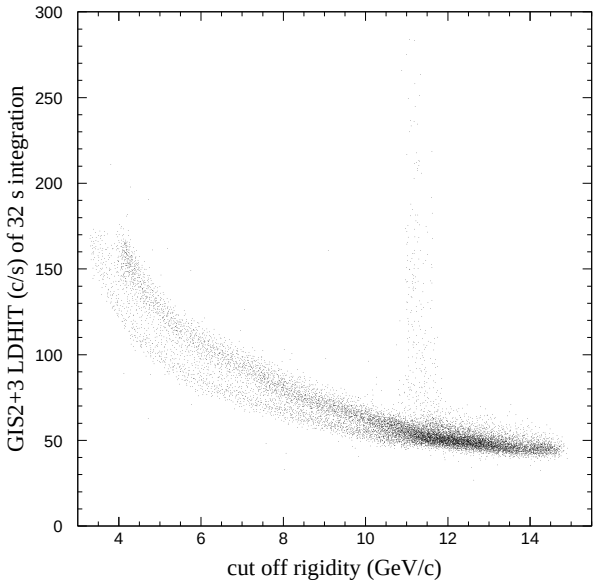

Figure 4.23: Correlation between COR and $LDHIT$ during the night-earth observations. $LDHIT$ is integrated for every 32 s. The flare-cut (table 4.6) is NOT applied

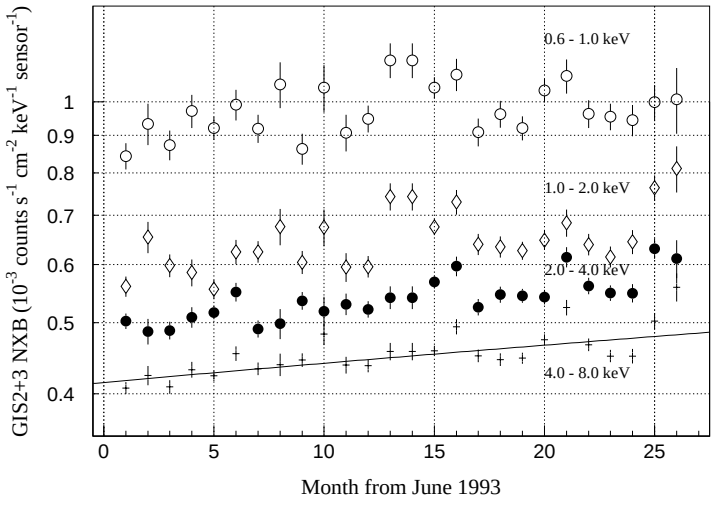

Figure 4.24: Long term (June 1993 – June 1995) variations of the GIS2+GIS3 counting rate during the night-earth observations in the 0.6–1.0 (open circle), 1.0–2.0 (diamond), 2.0–4.0 (filled circle), and 4.0–8.0 (crosses) keV energy bands, integrated within the radius of 20 mm from the optical axis. A solid line on the data of 4.0–8.0 keV band shows the best fit line of $y = 0.00257x + 0.414$. The flare-cut (table 4.6) is applied.

4.4.3 Flare events and the GIS monitor counts

Although COR is a good indicator of RNXB, there exists a secondary branch below $COR \sim 10$ GeV/c on the COR vs. $LDHIT$ correlation, as shown in figure 4.23. This is probably due to a slight inaccuracy of the COR-map. If we plot the satellite positions on the Earth, those periods which fall on the secondary branch appear only at the north east region of the map above the north Atlantic Ocean (dots in figure 4.25). Since the COR-map which we use does not refer to the satellite height, this discrepancy may change in future when the satellite altitude decreases. Moreover, COR is merely one of many factors that affect RNXB.

Therefore, we have decided to utilize the GIS monitor counts to estimate RNXB. Among nine GIS monitor counts described in §3.4.4, we selected $H0$ and $H2$ as the RNXB indicator, because they are almost free from signal X-rays in the f.o.v., even during the

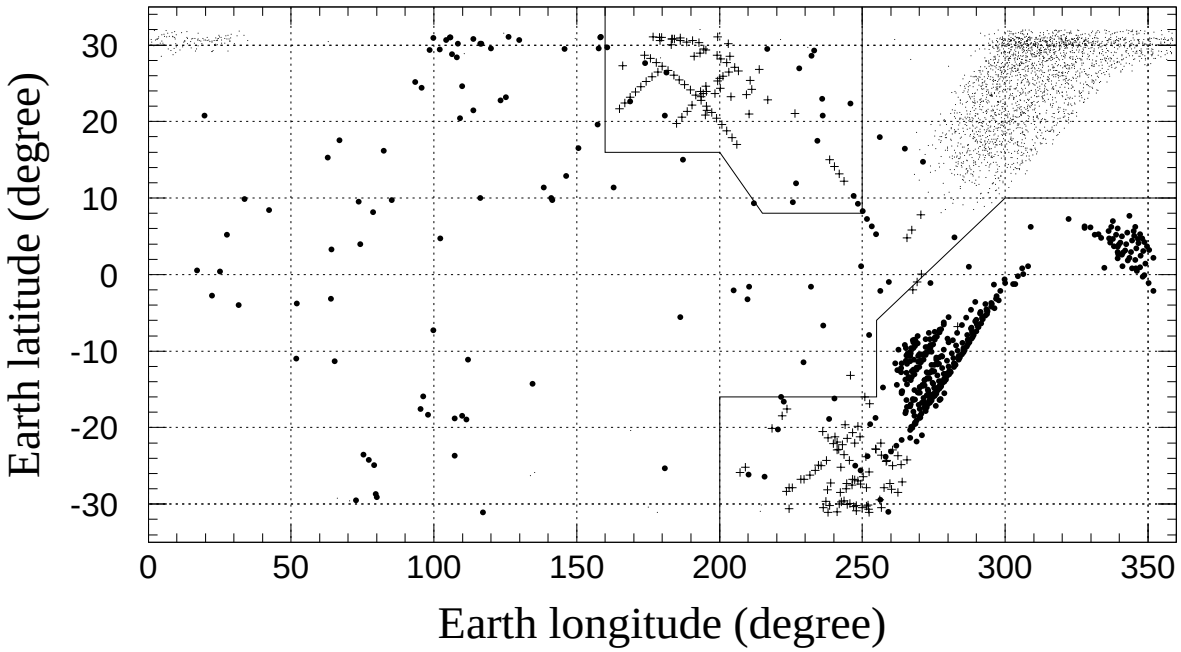

Figure 4.25: Distribution map for three types of phenomena on the Earth surface. The mark "·" represents a position when $H02$ is less than the lower solid line in figure 4.26, where the COR-map is thought to be inaccurate. The mark "•" represents a position when $H02$ is greater than the upper solid line in figure 4.26 (the hard-flares). The mark "+" represents a position when $H02 < 1000$ c/32 s = 31.25 c/s and $RNTE > 15$ c/32 s = 0.46875 c/s in figure 4.27a (the soft-flares). Two regions surrounded by solid lines define the dangerous areas where we should be cautious of the hard- and the soft-flares.

on-source observations. $H0$ and $H2$ have adequate statistics of 10–30 c s^{-1} sensor^{-1} when they are summed up. Since GIS2 and GIS3 show similar variations, we also sum the counts of GIS2 and GIS3 in order to reduce statistical errors. Hereafter, we call this summed up counts $H02$. Figure 4.26 shows a correlation between COR and $H02$, which has almost the same distribution as COR vs. $LDHIT$ (figure 4.23). As shown in figure 4.27, $H02$ and COR also correlate well to the residual night-earth counts within $r = 17$ mm (here after $RNTE$). However, there are two more issues on these correlations.

The first problem is a large scatter around $COR \sim$ 11–12 GeV/c in the COR vs. $H02$ plot, which is also seen in COR vs. $RNTE$ (figure 4.27b). We call the phenomanon which causes the scatter "hard-flares". If we plot the satellite positions on the Earth, the hard-flare periods are concentrated in the region peripheral to the south Atlantic anomaly (SAA) (filled circles in figure 4.25). SAA is a *hole* in the geomagnetic field which allows particles trapped in the magnetosphere to come down than usual. It is located up in the sky around Brazil, where protons of $E < 100$ MeV are confined by terrestrial magnetic fields. The particle background in SAA is extremely high, so that the high voltage of the GIS is turned off in SAA. The hard-flares are probably caused

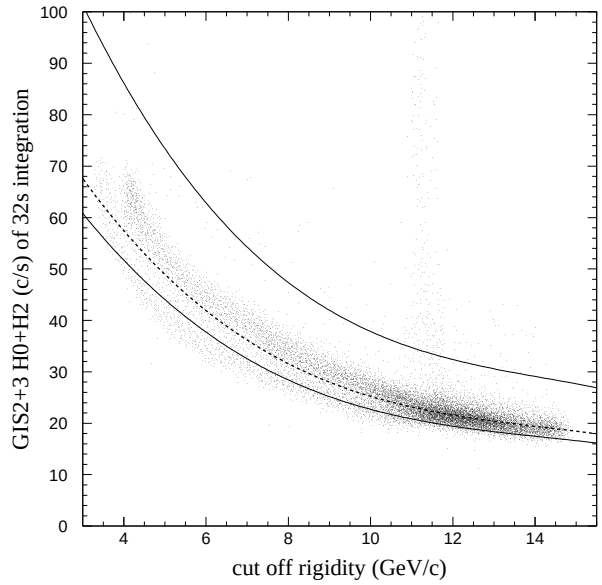

Figure 4.26: Correlation between COR and $H02$ counts during the night-earth observations. $H02$ is integrated for every 32 s. A dashed line means a function $f(x) = (109.3 - 17.05x + 1.127x^2 - 0.02627x^3)/32$ derived from fitting. Two solid lines below and above show $f(x)$ scaled by 0.9 and 1.5 times, respectively. The flare-cut (table 4.6) is NOT applied.

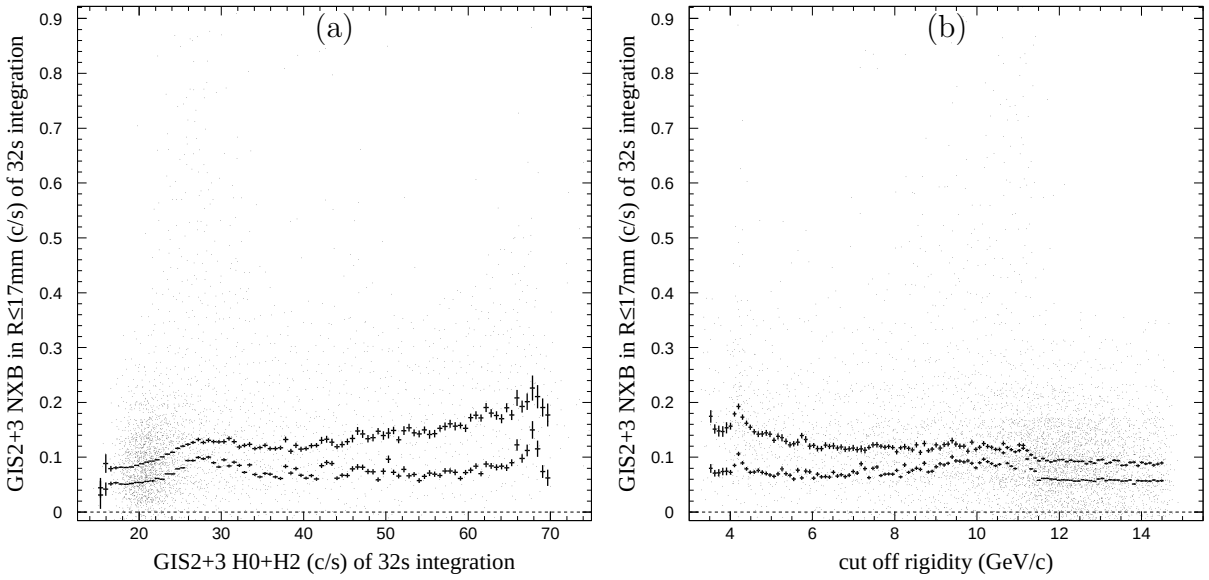

Figure 4.27: (a) A correlation between $H02$ and $RNTE$, and (b) a correlation between COR and $RNTE$. $H02$ and $RNTE$ are integrated for every 32 s. $RNTE$ is integrated in $r \leq 17$ mm in the 0.3–11 keV energy band. Crosses superposed on the figure show averages (upper) and standard deviations (lower) in each $H02$ or COR bins. The flare-cut (table 4.6) is NOT applied.

by particles trapped in SAA. These events can be eliminated by rejecting time intervals when $H02 > 1.5 \times f(COR)$ in figure 4.26.

After eliminating the hard-flares, does $RNTE$ well correlate with $H02$? In fact, there is the second issue, i.e. the component which scatters upwards around $H02 \sim$ 20–40 in figure 4.27a. We call the phenomenon which cause the scatter "soft-flares". During the soft-flares, the RNXB counts increase without an increase of $H02$. They are more dangerous than the hard-flares, because they cause mis-estimation of the RNXB counts, and furthermore, the spectrum during the soft-flares show acutually harder profile than

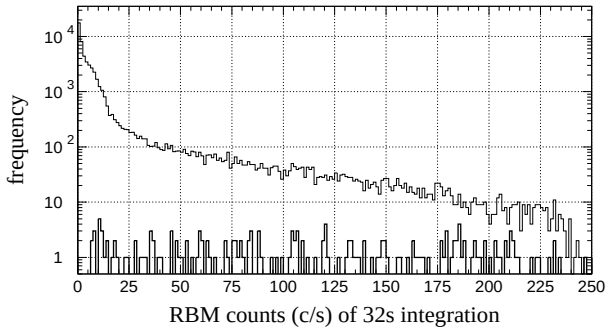

Figure 4.28: $RBMCNT$ distribution for the entire night-earth observations (thin solid line) and during the soft-flares.

the average spectrum for the entire night-earth observations. If we plot the satellite positions on the Earth, the soft-flare periods concentrated in two regions: the south west to SAA and above Hawaii (crosses in figure 4.25). Although the soft-flares can be eliminated by masking these regions, masking area is a little too large to ignore a decrease of integration time. We have founded that $RBMCNT$, i.e. a counting rate of the radiation belt monitor (RBM; ref. §3.4.1), can reject the soft-flares efficiently. As shown in figure 4.28, $RBMCNT$ distribution during the soft-flares (thick line) is almost flat, in contrast to the distribution for the entire night-earth observations (thin line) which is concentrating towards $RBMCNT < 25$ c/s. Therefore we reject the time intervals when $RBMCNT > 300$ c/16 s = 18.75 c/s everywhere, and especially $RBMCNT > 100$ c/16 s = 6.25 c/s in the dangerous areas (solid line in figure 4.25). The frequency of the soft-flares have a slight correlation with the angle θ_{mag} of the terrestrial magnetic field to the XRT direction. The soft-flares seem to happen more frequently when $\theta_{mag} \sim 60$–$120°$. It is possible that the physical origin of the soft-flares is electrons which come into the GIS from the direction of the XRT.

From these investigations, we have arrived at the conditions to reject the hard- and soft-flares as summarized in table 4.6. To avoid high RNXB periods, we usually restrict $H02$ in the range of 15–45 c/s, too. We call the procedure to apply these conditions "flare-cut". Correlations between $H02$ vs. $RNTE$ and between COR vs. $RNTE$ after the full flare-cut are shown in figure 4.29. Compared with figure 4.27, the humps around $H02 \sim 20$–40 and $COR \sim 10$–12 have almost disappeared. The standard deviation of $RNTE$ in each bin are approximately equal to the square root of the average $RNTE$ of that bin, which means the Poisson statistics. Note that we must multiply 32 s to convert counting rate (c/s) to the original counts. This means that the RNXB counts can be successfully estimated by $H02$.

4.4.4 RNXB reproducibility by H02-sorting method

To generate an RNXB spectrum or image to be subtracted from the raw CXB data which includes RNXB, we integrate the night-earth data which are screened on the same

Table 4.6: Summary of the flare-cut conditions

Condition	Reason
15 c/s $\leq$ H02 $\leq$ 45 c/s	to avoid high NXB
H02 $\leq 1.5 \times f(\mathrm{COR})^{\dagger}$ c/s	for hard flares
RBM $\leq$ 300 c/16 s = 18.75 c/s everywhere	for soft flares
RBM $\leq$ 100 c/16 s = 6.25 c/s in the dangerous areas (figure 4.25)	for soft flares

† $f(x) = 0.5(109.3 - 17.05x + 1.127x^2 - 0.02627x^3)$ c/ 16 s.

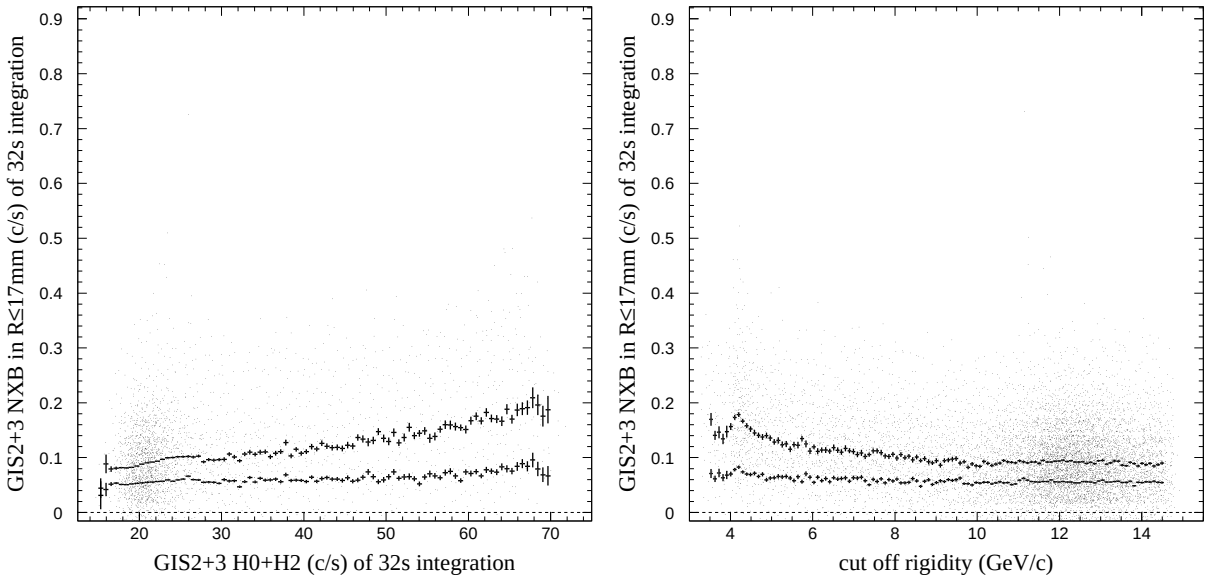

Figure 4.29: Almost the same as figure 4.27 except that the flare-cut (table 4.6) is applied.

conditions as the raw CXB events, at the same detector region (for a spectrum) or in the same energy band (for an image). However, the RNXB counts can vary by $\sim$ 40% in the range of $COR > 6$ GeV/c (figure 4.29). If the exposure time is long, this variation is averaged to a reasonable level of $\sim$ 10% depending on the length of the observation, but it will be better to take into account the RNXB variation by some methods. As seen in §4.4.3, $H02$ can be a good indicator of RNXB. Thus we choose $H02$ to predict the RNXB variation. In the next paragraph, we explain how to generate the expected RNXB spectrum for a specified on-source observation.

We sort the residual night-earth data by $H02$ in every 5 c/s step, i.e. 15–20 c/s, 20–25 c/s, 25–30 c/s, etc. $H02$ is counted in the 16 s time interval including the arrival time when the corresponding event is detected. Figure 4.30 shows the residual night-earth spectra and radial profiles corresponding to five $H02$ intervals. As $H02$ increases, the spectrum gets softer and the slope of the radial profile gets steeper towards the detector rim. It is probably due to the increase of the *soft* component of RNXB described in §4.4.2. We usually restrict $H02$ to the range of 15–45 c/s, where the influence of the *soft*

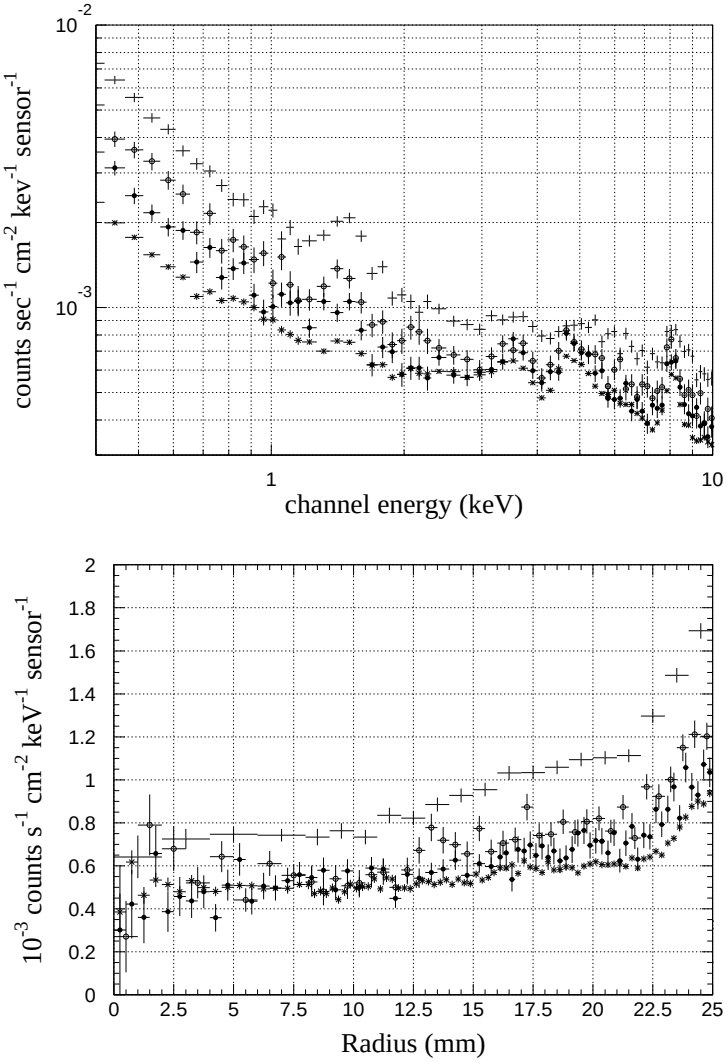

Figure 4.30: $H02$ sorted spectra (upper panel) and radial profiles (lower panel) of the GIS counts during the night-earth observations in the 0.6–7.0 keV energy band. The mark '+' represents the data when $H02$ is in the range 50–80 c/s, '○' 40–45 c/s, '●' 30–35 c/s, and '×' 20–25 c/s. $H02$ are integrated for every 16 s. The flare-cut (table 4.6) is applied.

component is not severe. Figure 4.31 shows exposure time out of the entire night-earth observations when $H02$ is in the range of each X-axis bin. We denote each exposure time T_i^{NTE}, and each spectrum $H_i^{NTE}(PI)$, both of which are counted or created on the same condition and in the same detector region as the on-source observations. When T_i^{OBS} is the exposure time in the i-th $H02$ bin during the on-source observation, the RNXB spectrum contained in the on-source data is estimated as:

$$H(PI) = \sum_i H_i^{NTE}(PI)\ \frac{T_i^{OBS}}{T_i^{NTE}}. \tag{4.10}$$

We call this method "H02-sorting method".

To check the reproducibility of RNXB by the H02-sorting method, we splitted the entire night-earth data into 122 × 10 ks intervals. Then we compared the counting rate of each interval with that estimated by H02-sorting method using the entire night-earth data. The results are shown in figure 4.32. Crosses in the upper panel show the actual counting rate of each interval, and the histogram show the prediction. It seems that 10 ks-integrated $RNTE$ varies more than the prediction. There is a general trend of increasing counting rate with time, which means that the long-term RNXB increase which is seen

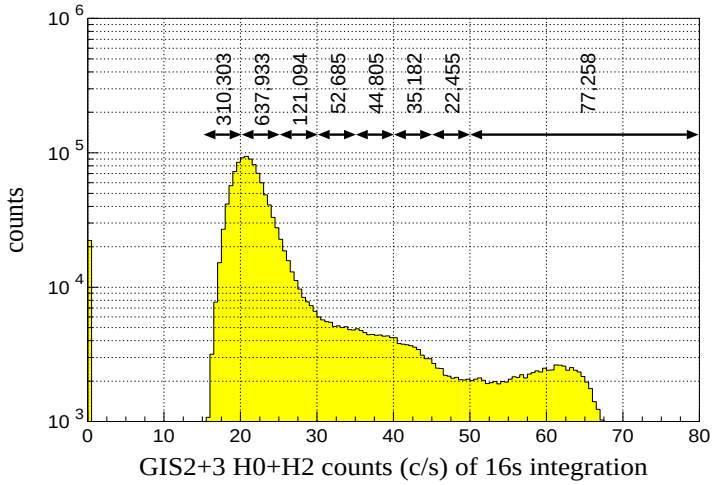

Figure 4.31: $H02$ distribution for the entire night-earth observations. Net exposure time (sec) in each $H02$ 5 c/s bin is given in the figure. The flare-cut (table 4.6) is applied.

in figure 4.24 cannot be reproduced by the H02-sorting mothod. As seen in the lower panel of figure 4.32, the mean value of observed / predicted ratio is 0.9983 and very close to 1.0, which is rather natural because their mother groups are the same. The standard deviation of the distribution is 0.07429, which mean 7.4% rms variation of the RNXB counts. This value includes a Poission error of 3.4%; therefore, systematic error of the H02-sorting method for 10 ks observation is thought to be 6.7%. If we use the average $RNTE$ instead of the H02-sorting method prediction, the systematic error increases to 7.8%. Thus the H02-sorting method reduces the systematic errors by about 1% level. Since the χ^2/d.o.f of the line fitted to the ratio shown in middle panel is $412.4/121 = 3.4$, the systematic error will be reduced to $\sqrt{3.4 - 1.0} \times 3.4\% = 5.2\%$, if the prediction of H02-sorting method are corrected for the long-term trend.

This long-term RNXB increase of $\sim 15\%$ in two years can be a serious problem in the CXB analyses. No compensation of this long-term trend results in the ~ 0.1 difference of the CXB photon index between two observations at intervals of two years (ref. §6.4.1). We, therefore, decided to adjust the normalization of the RNXB image or spectrum estimated by the H02-sorting method with the formula:

$$scaling\ factor = 0.9983 + 2.1255 \times 10^{-9} \cdot (ascatime - 45878400) \tag{4.11}$$

where $ascatime$ represents the time in second from 00:00:00 (UT) on 1 January 1993, and is calculated from the mean observation time.

The systematic errors described above are summarized in table 4.7. We conclude that we can achieve a $\sim 3.5\%$ rms reproducibility in RNXB, by a combined use of the standard background rejection, the flare-cut procedure, the H02-sorting method, and the long-term RNXB trend correction. In the following, we quote 3.5% (rms) as a typical systematic uncertainty associated with the RNXB estimation.

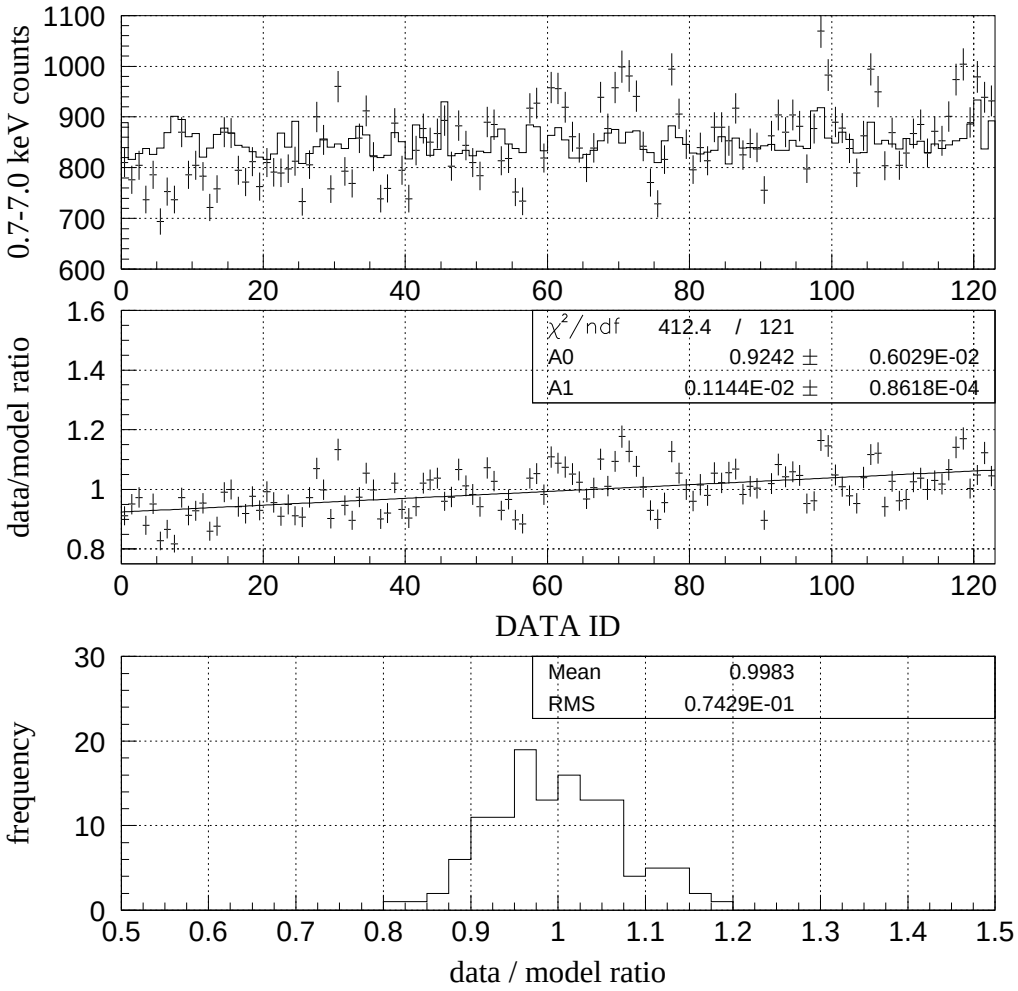

Figure 4.32: Figures to check the RNXB reproducibility by H02-sorting method. Upper panel shows the actual *RNTE* (crosses) and the H02-sorting method prediction (solid line), in the 0.7–7.0 keV energy band, for every 10 ks exposure. Middle panel shows ratios of the *RNTE* to the prediction. The solid line shows the best fit line, and fitting results are indicated in the figure inset. Lower panel shows a distribution of the ratios. The mean value and the standard deviation for the distribution are indicated in the inset.

Table 4.7: Systematic errors of the RNXB counts in the 0.7–7.0 keV energy band

data screening condition	RNXB generating method	0.7–7 keV† counting rate (c s^{-1} cm^{-2} keV^{-1})	drop‡ of data	Exposure time 10 ks	Exposure time 40 ks
$COR \geq 6$ GeV/c	average *RNTE*	4.01×10^{-4}	92%	16%	14%
flare-cut	average *RNTE*	3.59×10^{-4}	74%	7.8%	5.6%
flare-cut	H02-sorting method	3.59×10^{-4}	74%	6.7%	5.3%
flare-cut	+ long-term correction	3.59×10^{-4}	74%	5.3%	3.4%

† Average *RNTE* in the 0.7–7 keV energy band within the radius of 20 mm from the optical axis

‡ Reduction rate of exposure time to the entire night-earth observations

Chapter 5

Observations

5.1 Selection of observed fields

We have chosen ten fields observed with ASCA, as shown in table 5.1, for the CXB analyses in this thesis. Among them, Draco, NEP, and QSF3 are the PV-phase (Performance Verification phase) observations in the CXB category (ref. §3.1.4). There are two more observations in the CXB category, i.e. "Lynx Field" and "Lockman Hole". However, these observations were carried out when the GIS SP-discrimination was disabled (ref. §3.4.3), so that the RNXB counting rate is significantly higher. Therefore, we decided

Table 5.1: Summary of the observed fields to be employed in this thesis.

Name	Position*		Pts.*	Exp.†	Area‡	$N_{\rm H}^\sharp$	PI$^\diamond$
Large Sky Survey (LSS)	198.6	31.5	76	515,392	7.22	1.1	Tsuru
SA57	197.2	29.4	6	461,343	0.68	1.0	Kii
Draco Field	257.0	71.0	3	57,002	0.71	4.1	PV
NEP	269.8	66.6	8	118,434	0.58	4.2	PV
QSF3	55.4	−44.1	4	60,157	0.43	1.7	PV
z-system (ZSYS)	40.0	−23.0	5	109,893	1.68	2.3	Yamasaki
Braccesi Field (BF)	195.3	35.6	4	114,738	1.47	1.2	Ishisaki
Jupiter	184.9	−0.6	1	20,389	0.40	2.1	PV
Arp 220	233.6	23.5	1	23,039	0.40	4.2	PV
3C368	271.2	10.9	1	19,934	0.40	9.8	PV

* Approximate field center (RA,DEC) in J2000.

* Number of pointings.

† Total exposure time (s) after data screening.

‡ Covered area (deg^2) on the sky.

$^\sharp$ Galactic line of sight column density (10^{20} cm^{-2}) from Einstein On-line Service (*EINLINE*).

$^\diamond$ Principal Investigator. PV means observations in the PV-phase.

not to include them in our analyses. Large Sky Survey (LSS) and Deep Survey in SA57 are the team projects of ASCA, proposed by T. Tsuru (Kyoto Univ) and T. Kii (ISAS), respectively, with many co-PIs in various institutes in Japan. Survey areas of LSS and SA57 are partially overlapped. "z-system" (ZSYS) and "Braccesi Field" (BF) are the observations in GO-phase (Guest Observation phase) in the CXB category, proposed by N. Yamasaki (Tokyo Metro Univ) and Y. Ishisaki (Tokyo Univ), respectively. Jupiter, Arp 220, and 3C368 are the target observations in the PV-phase, but the targets turned out to be so faint that the data can be utilized for the present purpose. Positions of these fields are plotted in figure 5.1 in the Galactic coordinates.

Most of these observations (except Jupiter, Arp 220, and 3C368) have multiple pointings with different Euler angles, and are covering larger sky area than that available with a single ASCA pointing. We show the observation log and contour-map images of these fields in appendix A and B, respectively. The way these images have been synthesized is explained in §5.3. In §5.2, we briefly describe each field.

5.2 Description of Individual Fields

5.2.1 LSS

In the LSS project, we have systematicaly surveyed a continuous $\sim 1^\circ \times 5^\circ$ region at high Galactic-lattitides with ASCA, located around $(l, b) = (75.4^\circ, 83.4^\circ)$. The observa-

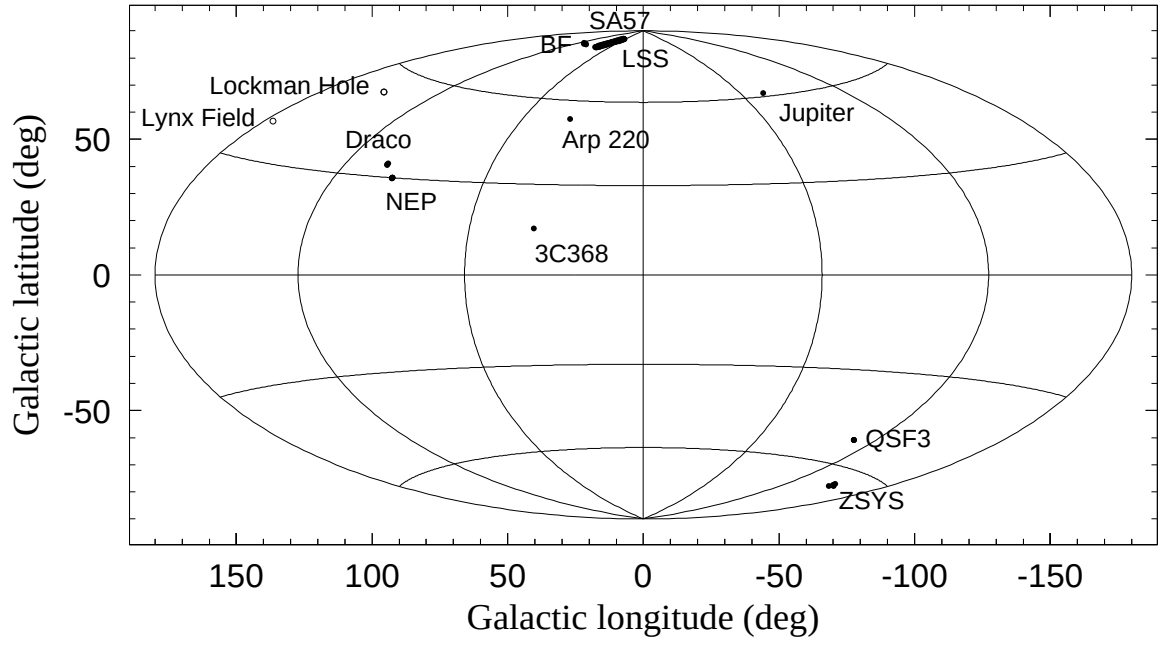

Figure 5.1: Galactic positions of the observed fields in table 5.1. "Lynx Field" and "Lockman Hole" are also included.

tion is splitted into many different epochs, and the total area observed so far in GO-1, GO-2 and GO-3 phases amounts to > 5 deg^2. Optical follow-up observations is undergoing to indentify the X-ray detected sources, using the mosaic CCDs in Kiso observatory and other instruments. The LSS survey field is partially overlapped with SA57 (left edge of figure B.1). The already covered area, more than 5 deg^2, is larger than any other surveys conducted with ASCA so far. This is the great advantage to study the average properties of the CXB. Furthermore, Ueda (1996) has searched point sources in the LSS field, and a list of point sources down to a 2–10 keV flux limit of several times 10^{-14} erg s^{-1} cm^{-2}, detected with the ASCA GIS and SIS, is available.

In LSS, 76 pointings have been made so far, which consist of 16 pointings in GO-1, 20 pointings in GO-2, and 40 pointings in GO-3. The sky mapping has been arranged so that the SIS f.o.v. ($22' \times 22'$) is aligned in mosaic. Each point has been observed twice with SIS with two different attitude, by shifting f.o.v. by its half size. Although mean exposure for each pointing is about 10 ks, which is shorter than typical exposure ($\sim$ 40 ks) for one target obtained with ASCA, at least 20 ks of exposure per sensor is guaranteed for each sky position by this multiple pointings. Because the GIS f.o.v. is about two times larger than that of the SIS, the total exposure achieved with the GIS multi pointings becomes much longer on the average.

In figure 5.2, we show the 76 pointing positions in LSS. For convinience, we split these pointings into four groups as shown in the figure, and call them a-LSS, b-LSS, c-LSS, and d-LSS, respectively. As shown in figure B.1, tens of sources are seen over the entire LSS fields. Among them, the brightest one, at $(\alpha_{2000}, \delta_{2000}) = (13^{\rm h}20^{\rm m}15^{\rm s}, +33°08'36'')$, is identified with the galaxy NGC 5098, which appears extended in the ROSAT image (Y.Tanaka, private communication).

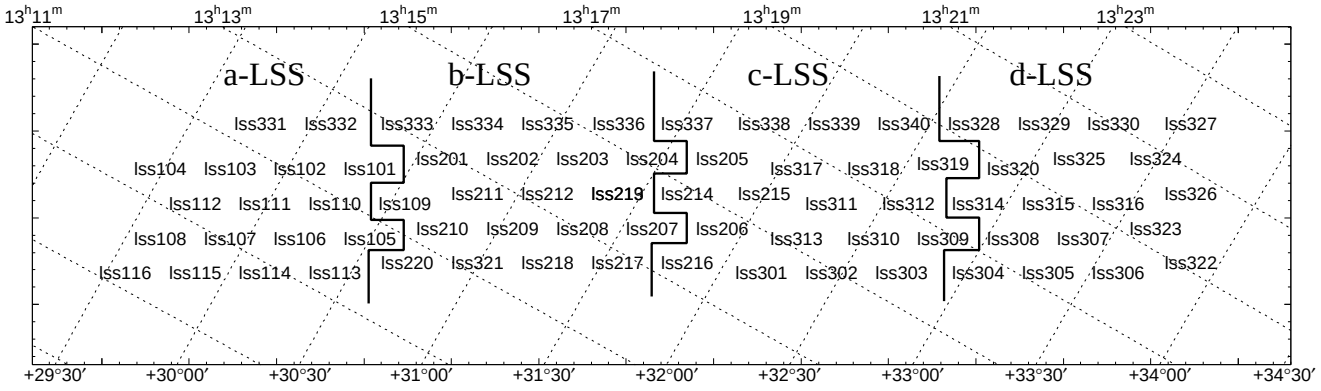

Figure 5.2: LSS pointing positions

5.2.2 SA57

Selected Areas are optically selected survey fields, and among them, Selected Area 57 (SA57) is one of the most deeply surveyed fields (Koo 1986; Koo and Kron 1988; Majewski et al. 1994). The limiting magnitude is $B \sim 24$, which is one of the deepest in the whole sky. In radio waveband, Windhorst el al. (1984) surveyed this field with Westorbork Synthesis Radio Telescope down to a flux limit of 0.6 mJy at 1.4 GHz.

SA57 is located near the north Galactic pole, thus has a low Galactic column and is suitable for X-ray surveys. However, there were no X-ray studies on this field prior to ASCA. ASCA has observed SA57 in GO-1 and GO-3. In GO-1, the scheduled 400 ks observation time was splitted into five pointings, intending to cancel the non-uniform sensitivity due to the XRT vignetting and the SIS gaps. In GO-3, all of the scheduled 400 ks observation time was devoted to a single pointing to extend the flux limit. SA57 has thus become the deepest field observed with ASCA. Ogasaka (1996) has searched faint sources in SA57 using the ASCA SIS.

There is a distant cluster of galaxies IIZw 1305.4+2941 in the central region of SA57 (the brightest source in figure B.2). The flux measured by Einstin is 3×10^{-13} erg s^{-1} cm^{-2} and not so bright for ASCA.

5.2.3 Draco Field

There is an unusual interstellar cloud in Draco (Draco cloud; Goerigk et al. 1983). The Draco cloud is located at $(l, b) \simeq (90°, +39°)$. It has a distinctive narrow 21 cm line centered at a local standard rest velocity of ~ -21 km s^{-1} with a width of ~ 2 km s^{-1}, which enables us to separate the forground and background emission. The distance of this cloud is uncertain by at least a factor of two, but a lower limit of 300 pc is presented. Burrows and Mendenhall (1991) observed Draco cloud with ROSAT PSPC, and found a shadowing of soft X-rays below 0.3 keV.

ASCA observed the Draco Field in PV-phase with three pointings. We can see several IPC sources in the GIS f.o.v. (figure B.3). The brightest ASCA source may in fact be a composite of three IPC sources.

5.2.4 NEP

Being free from the Sun angle constraint, the North Ecliptic Pole (NEP) can be observed with ASCA all through the year. Therefore, NEP has been observed 10 times in PV-phase, intending to calibrate the SIS background. Two from the 10 observations were carried out in March 1993, when GIS SP-discrimination was disabled. Therefore, we did not include these two observations in our analyses. There are two outstanding sources

in the GIS f.o.v. One is IPC source and the other is the Seyfert 2 galaxy NGC 6552 at a redshift of $z = 0.026$ (Fukazawa et al. 1994). NGC 6552 has a heavily absorbed ($N_{\rm H} \sim 6 \times 10^{23}$ cm^{-2}) hard continuum with prominent iron K line of neutral species of an equivalent width ~ 0.9 keV. Its 2–10 keV flux is $\sim 6 \times 10^{-13}$ erg s^{-1} cm^{-2}.

There are also deep ROSAT observations in the NEP region (Hasinger et al. 1991; Shanks et al. 1991), and a structure in the background with a $\sim 20'$ scale (NEP blotch) were reported.

5.2.5 QSF3

The QSF3 field is located in the Southern Sky at $(l, b) = (250.86°, -51.99°)$, and the Galactic absorption is low ($N_{\rm H} = 1.66 \times 10^{20}$ cm^{-2}; Heiles and Cleary 1979) because of a high Galactic latitude. QSF3 was observed to search for UV excess quasars, and later, ROSAT observations (Shanks et al 1991) resolved $\sim 30\%$ of the CXB into point sources at the flux limit of 10^{-14} erg s^{-1} cm^{-2}.

ASCA has observed the QSF3 field four times in PV-phase centered on almost the same position. There are two point sources clearly detected in the GIS f.o.v. The brighter one is a star with rather soft spectrum, and the other is a QSO at $z = 0.38$ (Chen et al. 1995).

5.2.6 z-system

There is a distant QSO ($z = 2.23$), PKS 0237−233, at the center of this field. PKS 0237−233 is known to have as many as 30 absorption lines of C_{IV} at $z = 1.3$–2.2 (Hewitt and Burbidge 1989), and the existence of "Absorption Supercluster" in size of ~ 20 Mpc are suggested (Heisler 1989). Thus, detailed survey in the optical bands are carried out in this field, and it turned out that 32 QSOs of $z = 0.17$–2.63 are concentrating in the $2° \times 2°$ regions around PKS 0237−233. The Einsein IPC also observed this field with tree pointings of 12 ks in total, and detected four QSOs.

ASCA observed this field with two pointings in GO-2 and another three pointings in GO-3. Several QSOs are detected and PKS 0237−233 is the brightest (Yamasaki et al. in ASCA Third Anniversary Symposium of "X-Ray Imaging and Spectroscopy of Cosmic Hot Plasmas", March 1996).

5.2.7 Braccesi Field

Braccesi Field is a region around $(l, b) = (108°, 81°)$, and the line-of-sight Galactic absorption is low ($N_{\rm H} \sim 1.2 \times 10^{20}$ cm^{-2}). This sky region has been surveyed for QSOs in the optical (Cristiani et al. 1984), radio (Fanti et al. 1977), and X-ray (Einstein IPC

and HRI; Marshall et al. 1984) wavebands, and a complete catalogue of $B < 19.9$ QSOs of $z = 0.2$–2.2 is available. There is also a concentration of 35 QSOs in 1.7 deg^2 area. Einstein made deep observations in this field (3 pointings with a total exposure of 114 ks with the IPC, and 7 pointings total 129 ks with the HRI), and found 34 IPC sources, which is about twice as much as expected from $\log N$–$\log S$ relation derived from the Einstein Extended Deep Survey.

ASCA observed this field with two pointings in GO-3 and another two pointings in GO-4. There are several point sources clearly detected in the GIS f.o.v. If we exclude sources seen at the detector rim, the brightest is the IPC 2961 at $(13^{\rm h}04^{\rm m}, 35^\circ35')$, which is thought to be a QSO at $z = 0.327$. Its 2–10 keV flux is about 8×10^{-13} erg s^{-1} cm^{-2}.

5.2.8 Jupiter, Arp 220, and 3C368

These are the target observations in the PV-phase. However, the main targets turned out to be very faint, and we adopted them for the CXB analyses. Searching such observations are carried out as a part of the ASCA Medium Sensitivity Survey (MSS). ASCA MSS is a team project proposed by T. Takahashi (ISAS), which utilize the large GIS f.o.v. after removing the main targets. We have selected about 30 observations with exposure time > 30 ks at high latitude ($|b| > 10^\circ$) in PV-phase. We particularly use these three fields in this thesis, because of the faintness of the target sources.

The target positions are $(\alpha_{2000}, \delta_{2000}) = (12^{\rm h}19^{\rm m}53^{\rm s}, -00^\circ37'12'')$, $(15^{\rm h}34^{\rm m}57^{\rm s}, +23^\circ30'11'')$, and $(18^{\rm h}05^{\rm m}06^{\rm s}, +11^\circ01'30'')$, respectively. Arp 220 was faint but detected with ASCA ($kT = 0.4$ keV, $F_{\rm X} = 4 \times 10^{-13}$ erg s^{-1} cm^{-2}; Kii et al. in "IRAS galaxies observed with ASCA"). Detections of Jupiter and 3C368 are marginal. The observation of Jupiter was conducted in June 1993, about 1 year before the collision with the SL9 commet.

5.3 Data processing

5.3.1 Basic event selection

In order to ensure the RNXB reproducibility, we have employed almost the same event selection criteria for the CXB observations as that of the night-earth observations (§4.4). In practice, we have set the following conditions:

$$\begin{cases} \text{target elevation from the rim of the Earth} \geq 5^\circ \\ \text{target elevation from the rim of the sunlit Earth} \geq 25^\circ \\ \text{flare-cut conditions (table 4.6)} \\ \text{attitude jittering} \leq 1' \text{ for the pointing center, and} \leq 1^\circ \text{ for the roll angle.} \end{cases}$$

Exposure times shown in table 5.1 are subjected to these screenings. Other data processings such as position linearlization, gain correction, and strict *RT*-mask are carried out in a standard way on the ASCA_ANL. ASCA_ANL is the framework of the analysis software mainly utilized for the event by event processing of the ASCA data. It has been developed by the ASCA_ANL working group, which consists of M. Hirayama, H. Kubo, and Y. Ishisaki, as main members.

In creating images, we masked calibration sources and the detector rim with the standard masking images for GIS2 and GIS3 (figure 4.20). We usually utilized the events whose PI channels are within the 0.7–7.0 keV energy band, to avoid high RNXB rate in energy bands below and above the thresholds. Conversion of the detector coordinates into the sky coordinates (see next subsection) is conducted using the mean satellite attitude of each pointing. As described in §3.1.2, the accuracy of the attitude determination is $\sim 1'$, and the attitude is subjected to jittering to a similar level.

When discussing the CXB spectra, we use the events within 20 mm from the optical axis of each detector. The covered sky areas shown in table 5.1 refers to this detector region. In spectral fitting, we usually restrict the PI channels to be fitted in the 0.6–10 keV energy band.

5.3.2 Handling of multiple pointings

As mentioned in §5.1, most of the sample fields are observed with multiple pointings, which makes the analyses quite complicated.

In creating the CXB spectra, we simply accumulated the events inside 20 mm from the optical axis, as described in the previous subsection. Therefore, the spectra are in fact biased to the regions where exposure is deep owing to the overlap of the multiple pointings. However, even a single pointing observation is biased to the central region considering the vignetting effect, and we did not make a correction for exposure to compensate the bias while creating the CXB spectra.

In the image analyses, it is desirable to construct a mosaic image by superposing multiple pointing images into a single large one, in order to reduce statistical errors. This procedure is usually carried out by converting the detector coordinates $(DETX, DETY)$ into the sky coordinates $(SKYX, SKYY)$, utilizing the knowledge of the satellite Euler angles. On the sky coordinate image, the coordinates are rectangular and each pixel corresponds to a particular sky position, which is calculated from the Euler angles and a fixed reference-sky-position (= SKYREF). As far as the SKYREF are the same, we can sum up the sky coordinate images of multiple observations which were carried out with different Euler angles. We define the operator $det2sky\Big[B\Big]$ which convert the detector coordinate

image $B(DETX, DETY)$ into the sky coordinate image $M(SKYX, SKYY)$. Using this operator, we can create the mosaic image $M^{OBS}(SKYX, SKYY)$ by calculating

$$M^{OBS}(SKYX, SKYY) = \sum_{GIS2,3} \sum_{j} det2sky\Big[B^{OBS}_{j,n}(DETX, DETY)\Big], \tag{5.1}$$

where j represents the pointing number in the observed field, and $B^{OBS}_{j,n}$ is the detector coordinate image taken by GISn ($n = 2$ or 3) in the j-th pointing. Each pixel of M^{OBS} contains the number of detected events, accumulated over the entire pointings.

Exposure of each pixel is calculated by:

$$M^{EXP}(SKYX, SKYY) = \sum_{GIS2,3} \sum_{j} T_j \; det2sky\Big[B^{MASK}_{n}(DETX, DETY)\Big], \tag{5.2}$$

where T_j is the exposure time of the j-th pointing, and $B^{MASK}_{n}(DETX, DETY)$ is the standard image masking for GISn (figure 4.20). By dividing M^{OBS} by M^{EXP}, we can obtain a sky coordinate image in which each pixel value corresponds to event counting rate. In figure 5.3a and 5.3b, we show M^{EXP} and M^{OBS} for the observations in the Braccesi Field.

5.3.3 Image smoothing

Since M^{OBS} is straightforward but not intuitive, we usually smooth the image with the position-dependent XRT+GIS point spread function $P^{PS}(\theta, \phi\,; DETX, DETY)$, and then correct each pixel for the exposure time. This $P^{PS}(\theta, \phi\,; DETX, DETY)$ represents the brightness profile on $DETX$-$DETY$ plane when a point source is located at offset angle θ and azimuth angle ϕ from the XRT optical axis. It is normalized so that the peak value is constant for any set of (θ, ϕ). Introducing the normalization factor $A^{PS}(\theta, \phi)$, $P^{PS}(\theta, \phi\,; DETX, DETY)$ is expressed by the response functions of the XRT and GIS in a formula:

$$\begin{aligned} A^{PS}(\theta,\phi)\; P^{PS}(\theta,\phi\,;DETX,DETY) &= \int dPI\; D(DETX, DETY, PI) \\ &= \int dPI \int dE\; R_{GIS}(E, PI) \int dx\, dy \\ &\times\; P_{GIS}(E, x, y\,; DETX, DETY)\; A_{GIS}(E, x, y) \\ &\times\; P_{XRT}(\theta, \phi, E\,; x, y)\; A_{XRT}(\theta, \phi, E) \\ &\times\; A_{T.S.}(E)\; S(E), \end{aligned} \tag{5.3}$$

where $S(E)$ stands for the energy spectrum of the point source, and other symbols are the same as in §4.2.1. The factor $A^{PS}(\theta, \phi)$ effectively takes charge of vignetting. We have calculated $P^{PS}(\theta, \phi\,; DETX, DETY)$ by interpolating the Cyg X-1 images, which were observed with various offset angles and azimuth angles within $\theta \leq 17'$. As seen in equation (5.3), both $A^{PS}(\theta, \phi)$ and $P^{PS}(\theta, \phi\,; DETX, DETY)$ depend on the source

spectrum $S(E)$. However, it mainly affects only the normalization of $A^{PS}(\theta,\phi)$, and changes of the function profiles are almost negligible in the range of $\Gamma \sim 1.4$–2.2 in terms of photon index. Therefore, we assumed $\Gamma = 1.7$ in calculating $A^{PS}(\theta,\phi)$ and $P^{PS}(\theta,\phi\,;DETX,DETY)$.

Here, we define the operator $ccf\Big[B\Big]$ which conduct the image smoothing as:

$$\begin{aligned} M(SKYX,SKYY) &= ccf\Big[B(DETX,DETY)\Big] \\ &\equiv det2sky\Big[\int dDETX\,dDETY\ P^{PS}(\theta,\phi\,;DETX,DETY)\ B(DETX,DETY)\Big], \end{aligned} \tag{5.4}$$

i.e. cross correlation of $B(DETX,DETY)$ with $P^{PS}(\theta,\phi\,;DETX,DETY)$. At the same time, this operator converts the image into the sky coordinates. Using this operator, we can create the smoothed and exposure-corrected mosaic image $M^{CCF}(SKYX,SKYY)$ by calculating

$$M^{CCF}(SKYX,SKYY) = \frac{\sum\limits_{GIS2,3}\sum\limits_{j} ccf\Big[B^{OBS}_{j,n}(DETX,DETY)\Big]}{\sum\limits_{GIS2,3}\sum\limits_{j} T_j\ ccf\Big[B^{MASK}_{n}(DETX,DETY)\Big]}. \tag{5.5}$$

In figure 5.3c, we show a contour-map image of M^{CCF} for the Braccesi Field. We also show M^{EXP} and M^{CCF} for all the sample fields in appendix B. Note that M^{CCF} has been corrected for exposure overlaps among different pointings, so that it is uniform in terms of counts/s. However it is not corrected for the XRT vignetting; as a result, it is not uniform in terms of counts/s/cm^2, and we can see a slight step-wise structure in figure 5.3c at the rims of the overlapping fields. More complicated image processing will be discussed in §7.2.

We have conducted these image processings on DISPLAY45. DISPLAY45 is a command-driven interactive histogram browsing program based on CERN libraries; particularly HBOOK4 as the histogram management and HPLOT5 as the histogram plotting. DISPLAY45 has been developped by A. Shirahashi, A. Takahashi, and R. Itoh. A user can add his/her own external commands written in C or FORTRAN languages without re-compiling the main program, utilizing the method of dynamic linking. A number of useful commands and analysis tools for the ASCA data have been collected and compiled by Y. Ishisaki, and he released them as dis45userlib. The operators such as $det2sky\Big[B\Big]$ and $ccf\Big[B\Big]$ are realized as the external commands on DISPLAY45.

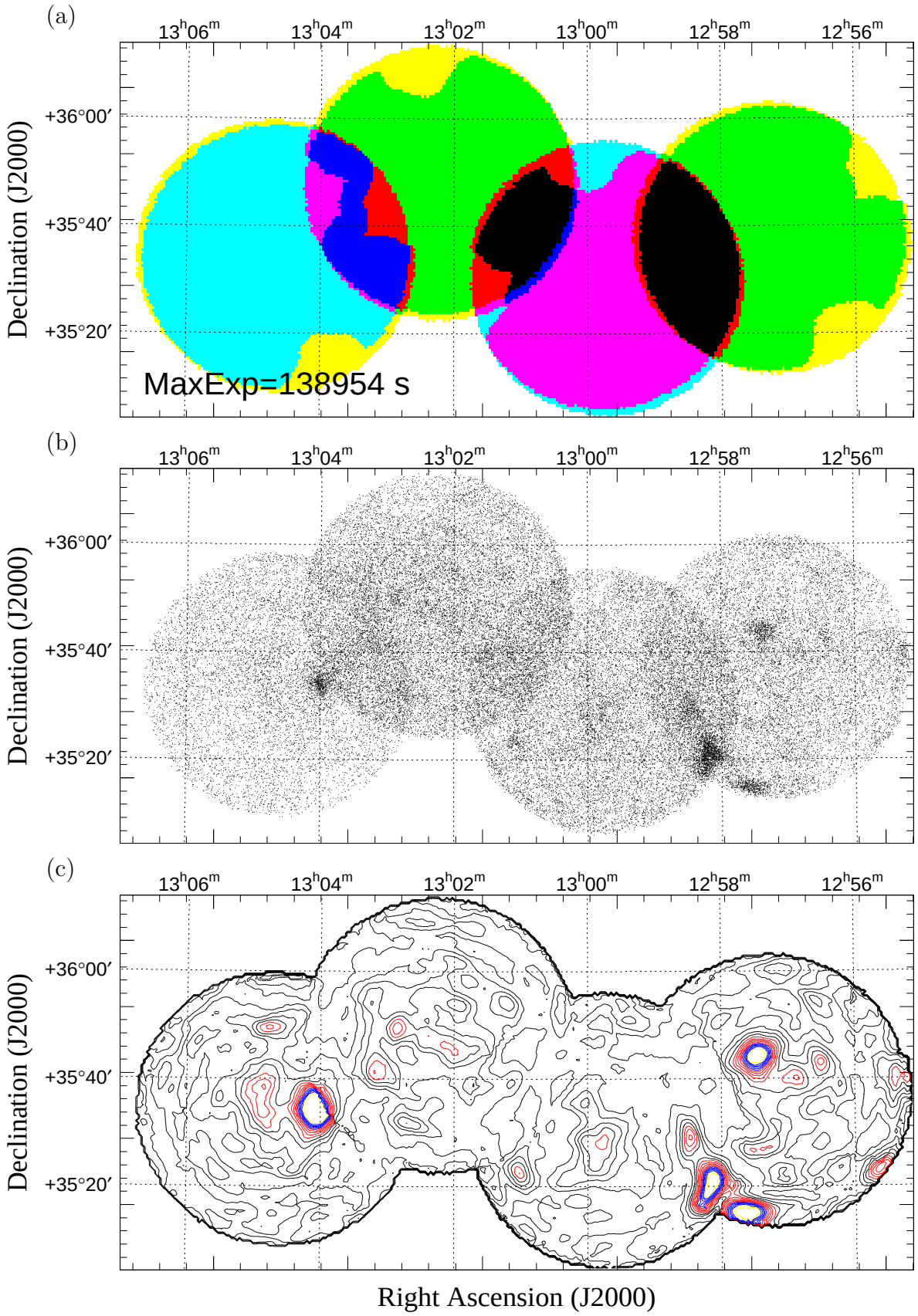

Figure 5.3: Images of (a) M^{EXP}, (b) M^{OBS}, and (c) M^{CCF} for the four pointing observations in the Braccesi Field. Coordinates superposed on the images are J2000. (a) Gray scale image of M^{EXP}. White and black pixels correspond to 0 s and 138,954 s exposure, respectively. (b) Dot-map image of M^{OBS} in the 0.7–7.0 keV energy band. (c) Contour-map image of M^{CCF} in the 0.7–7.0 keV energy band. Contour levels are (5, 10, ..., 95, 100) $\times 10^{-6}$ c s^{-1} pixel^{-1}.

Chapter 6

Average CXB spectrum in the LSS field

6.1 CXB data sampling and data analysis method

In order to study the average properties of the CXB, it is preferable to sum up data from as many different sky regions as possible, so as not to be affected by particular point sources which happen to be in the f.o.v. Even though total exposure time were long, observations which are biased in a particular small region would have a risk of contaminations with point sources and local structures. Therefore, we have chosen to utilize all the LSS observations to construct an average CXB spectrum. The LSS observations cover large sky area of 7.2 deg^2 by 76 pointings with exposure time of 5–10 ks for each (ref. §5.2.1), which matches the above conditions. Moreover, the LSS field is well surveyed by Ueda (1996), and a list of point sources detected with ASCA GIS and SIS is available. Therefore we can easily and reliablly take into account the effects of point sources. However, since the LSS fields are restricted to sky directions around $(l, b) = (75.4°, 83.4°)$, we might not be able to regard the LSS spectrum as the average CXB over the whole sky, if the CXB has a global structure, which will be discussed in the next chapter.

We adopt the data selection criteria described in §5.3, and the total exposure time of the LSS observations amounts to 515.4 ks. We evaluate the RNXB spectra by the H02-sorting method, with the normalization adjusted to correct the long-term RNXB trend, as described in §4.4.4. We include only the statistical errors for the RNXB spectra; we believe the systematic error of the RNXB spectrum for the entire LSS observations to be less than $\pm 2.5\%$ for the following two reasons. Firstly, the total exposure time of the LSS observations is very long. Secondly, the LSS observations are splitted into four periods from December 1993 to July 1995, with about half a year interval so that the long-term RNXB change is also averaged. The effects of the RNXB systematic error will be discussed in in §6.4.1. In the following spectral fitting, we used `gis2v4_0.rmf` and `gis3v4_0.rmf` as RMF, and we created ARF with SimARF described in §4.3.4.

6.2 Ring-sorted CXB spectra

Figure 6.1a shows the ring-sorted CXB spectra, i.e. spectra of the entire LSS data which are accumulated in annular regions in 5 mm step centered on the XRT optical axis on the GIS detector plane. Although the XRT effective area drops as the offset angle gets larger because of vignetting, integration area on the detector plane also gets larger; thus the fluxes of 10–15 mm, 15–20 mm, and 20–25 mm rings are roughly comparable. We can see the trend of spectral softening toward outer rings, which is caused by the following two effects. Firstly, the vignetting effect is stronger for harder X-rays, which makes the spectrum to appear softer toward the detector rim. Secondary, the stray CXB photons, which has a much softer spectrum than the normal CXB photons, become also dominant toward the detector rim. As described in §4.3, stray lights thus supress the offset angle dependence of the effective area, while enhance its energy dependence.

In order to show that these ring-sorted CXB spectra are originally flat on the sky, we compare them with the ring-sorted day-earth spectra which are shown in figure 6.1b. These day-earth spectra were obtained by integrating all the data when the XRT pointed to the sunlit Earth, for two years from June 1993 to June 1995, so that we can regard them to have a very uniform surface brightness. After subtracting RNXB spectra from these day-earth spectra in just the same way as the CXB spectra, flux above 4 keV becomes almost zero. Therefore we compare the day-earth and CXB spectra in the 0.6–4.0 keV energy band. This also means that the evaluation of RNXB spectra has been properly carried out.

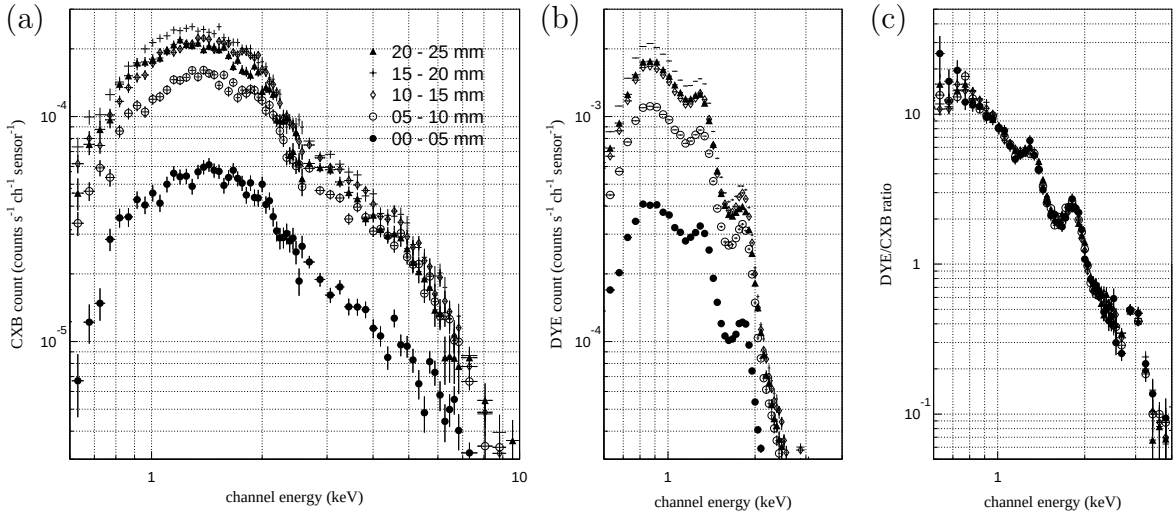

Figure 6.1: Ring-sorted spectra of (a) CXB and (b) day-earth, integrated in the radius of 0–5 mm (•), 5–10 mm (○), 10–15mm (◇), 15–20 mm (+), and 20–25 mm (△), centered on the optical axis on each detector plane. Panel (c) shows ratios of (b) to (a). GIS2 and GIS3 spectra are summed up.

Figure 6.1c shows ratios of the day-earth spectra to the CXB spectra in the same ring. All ratios have the same profiles and the same normalizations within error bars typically of 10% order, independently of the ring radii. Thus we confirm that the CXB data which we used here are uniform on the sky, in both spectral shape and surface brightness, at least below 4 keV. This justifies the assumption we made when we created the CXB ARF in §4.3.4. Furthermore, the day-earth spectra are brighter than the CXB spectra by about one order of magnitude at 1 keV, so that the day-earth spectra is much less affected by RNXB. The results shown in figure 6.1c also demonstrate the accuracy of the RNXB evaluation.

To quantify the CXB spectrum, it is of critical importance to verify that the CXB ARF (ref. §4.3.4) has been generated correctly. For this purpose, it is the most straightforward to examin whether all the ring-sorted CXB spectra can be reproduced by a single, common spectral model without introducing ring-to-ring adjustment of the model shape. For

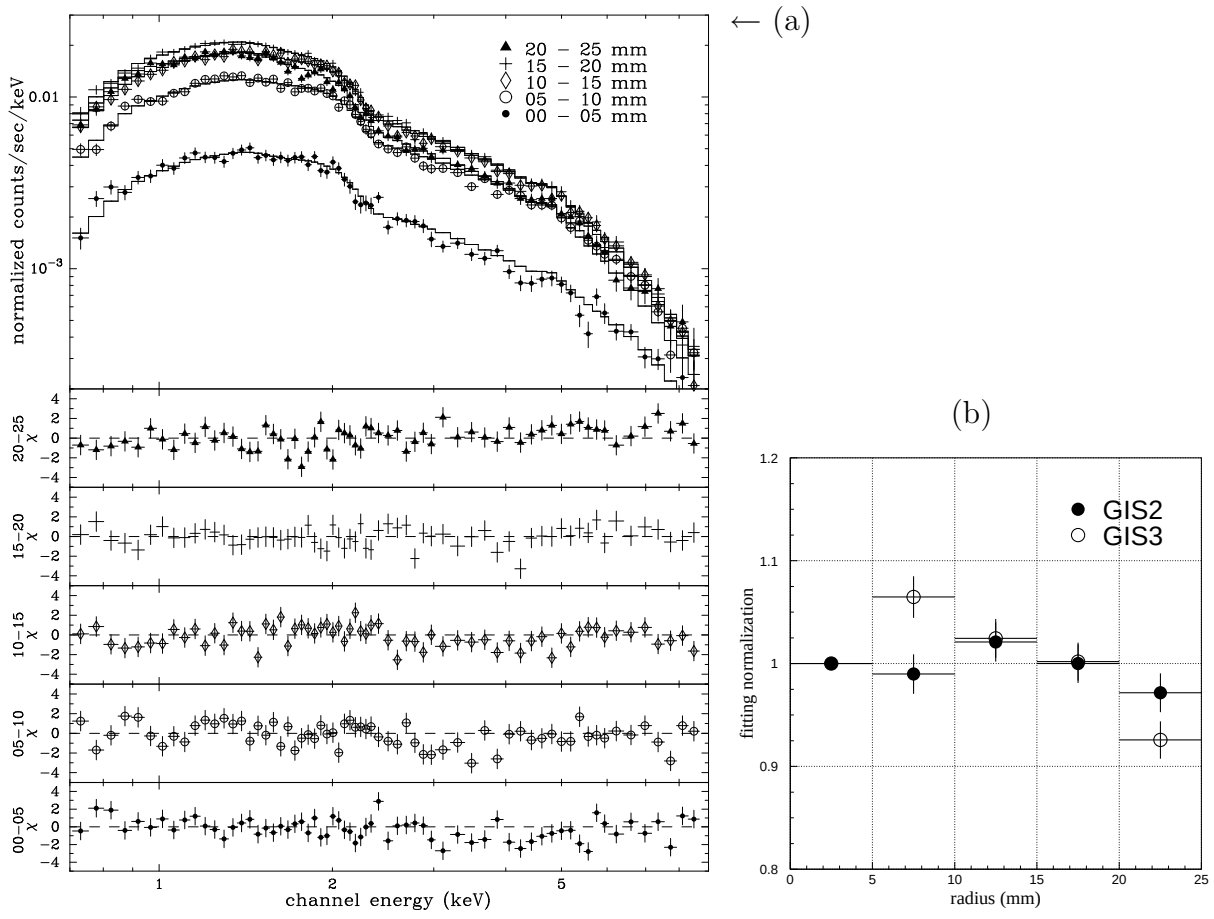

Figure 6.2: (a) The ring-sorted CXB spectra of figure 6.1a, fitted with a power-law plus *RS* model of one solar abundances. Top panel shows each spectrum (markers) and the best fit model (solid lines). Lower five panels show residuals from each spectrum. All the fit parameters except normalization are common to all the spectra. (b) The model normalization for each spectrum plotted versus radius of the rings. Normalization of the inmost ring is defined to be 1.0.

the fitting model, we employ the power-law + Raymond-Smith (here after *RS*) model, which is often chosen to fit a CXB spectrum; in the next section, we will check whether this model is appropreate for our CXB spectrum. The number of free parameters are eight in total: power-law photon index Γ, power-law normalization, *RS* temperature kT, *RS* normalization, and relative normalizations for the five ring-sorted spectra with normalization for the innermost region fixed to 1.0. That is, the model spectrum has an identical shape for all the rings, but allowed to have different normalizations for different rings. Element abundances for the *RS* model are fixed to one solar. To examine the consistency between the two detectors, for the moment we analyze the GIS2 and GIS3 data separately.

The results of this joint fitting have been acceptable at 95% confidence level, as presented in figure 6.2a, with χ^2/d.o.f = 363/325 = 1.14. We plotted the derived normalizations for the five rings in figure 6.2b. Thus, the normalizations are consistent with 1.0 within $\pm$5% level. If all the relative normalizations are fixed to 1.0, χ^2/d.o.f becomes 448/325 = 1.40 and the model is rejected at 99% confidence level. However, if we remove the spectrum of the 20–25 mm outermost ring, the model again becomes acceptable at 95% confidence level, with χ^2/d.o.f = 292/260 = 1.14. This is probably because the GIS performance, such as gain, energy resolution, and detection efficiency, gets worse beyond the 20 mm radius. If we compare GIS2 and GIS3, the best fit parameters are consistent except that the normalization of GIS3 is $\sim$ 3.5% larger than than that of GIS2.

Thus, we conclude that differences of the detector ID (GIS2 / GIS3) or the integration region (except $>$ 20 mm) do not affect fitting parameters significantly. This confirms that the CXB ARF has been created with a sufficient accuracy and reliability. Therefore, in the following analyses, we sum up GIS2 and GIS3 spectra within 20 mm from the optical axis. We come back to these ring-sorted CXB specra in §6.4.4 to evaluate the systematic errors.

6.3 Spectral fits to the average CXB in the LSS field

6.3.1 Results in the 2–10 keV range

As seen in the previous section, we can obtain roughly similar results regardless of the detector ID almost all over the whole GIS f.o.v. We therefore conduct a spectral fitting using the CXB spectrum of the all LSS observations integrated within the radius of 20 mm, in order to get higher statistics. The total exposure time is 515.4 ks, and the number of signal photons we obtained with the two GIS detectors is 187,726 counts in the 0.6–10 keV energy band. We estimate that about 32% of these events are due to RNXB.

The data also contain 23 point sources of $F_{\rm X}^{2-10{\rm keV}} > 2 \times 10^{-13}$ erg s^{-1} cm^{-2}, with their total flux $\sim 5.2 \times 10^{-12}$ erg s^{-1} cm^{-2}, in the 7.2 deg^2 area of the LSS sky (Ueda 1996). Therefore, this spectrum is not an unresolved CXB spectrum for ASCA. However, we quantify this spectrum including point sources for the moment.

First of all, we fit the spectrum in the 2–10 keV energy band. As the fitting model, we choose power-law and thermal bremsstrahlung models, both modified with absorption due to the Galactic column density of $N_{\rm H} = 1.1 \times 10^{20}$ cm^{-2} which is appropriate for the LSS sky. They are generally accepted models to explain the CXB spectrum in the 2–10 keV energy band. Fitting results are shown in figure 6.3 and table 6.1. The fit with the power-law model is acceptable, and the derived photon index is $\Gamma = 1.496 \pm 0.026$. This is a little steepr than the generally accepted value of 1.4, but probably consistent within various systematic uncertainties. Thermal bremsstrahlung model is rejected at 99% confidence level, and shows rather high temperature of $kT = 19.8 \pm 2.3$ keV, which is practically meaningless value considering the energy range of ASCA (up to $\sim$ 10 keV). Since we

Table 6.1: Model fits to the 2–10 keV spectrum of the CXB

Model	absorbed power-law*	absorbed thermal bremsstrahlung*
χ^2/d.o.f	89 / 74	114 / 74
Parameter	$\Gamma = 1.496 \pm 0.026$	$kT = 19.8 \pm 2.3$ keV
Flux (2–10 keV)	6.12×10^{-8} (erg s^{-1} cm^{-2} str^{-1})	5.99×10^{-8} (erg s^{-1} cm^{-2} str^{-1})

* Absorption is fixed to the Galactic line-of-sight value ($N_{\rm H} = 1.1 \times 10^{20}$ cm^{-2}).

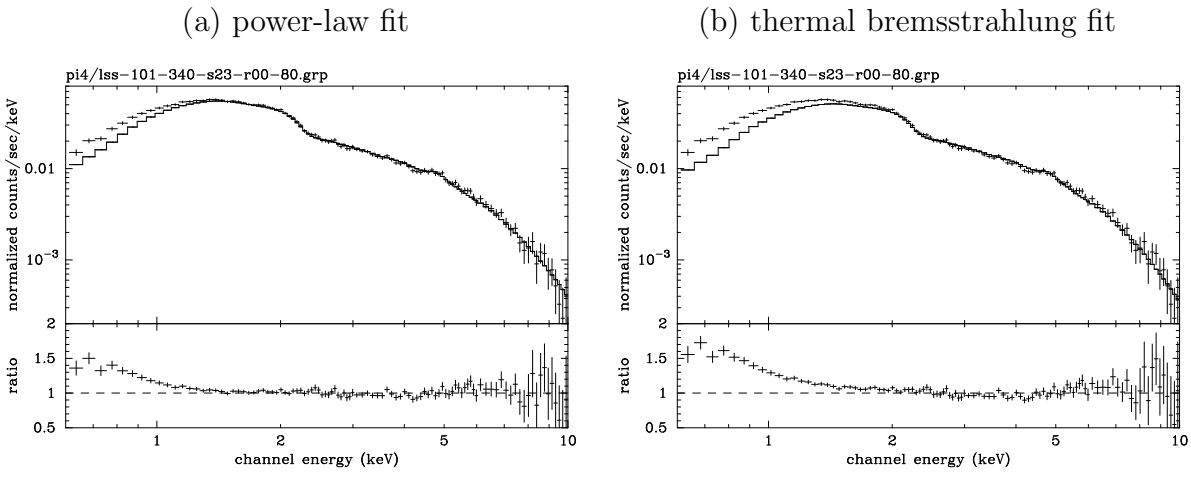

Figure 6.3: The average CXB spectrum fitted with (a) power-law and (b) thermal bremsstrahlung model, both with galactic absorption, in the 2–10 keV band. Upper panel of each figure shows GIS2+3 spectrum (crosses) and the best fit models (solid lines). Although the fitting ignored the energy range below 2 keV, the best-fit model is extended to < 2 keV to illustrate the soft-excess.

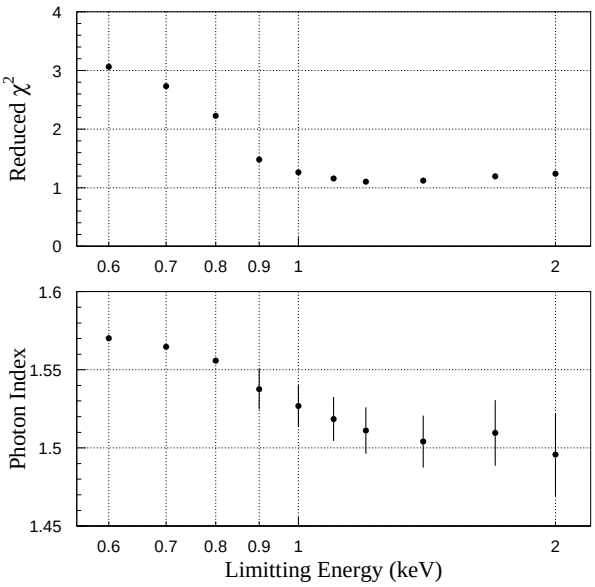

Figure 6.4: Changes of χ^2/d.o.f (upper panel) and the CXB photon index (lower panel) when the lower limit of the fitting energy range is shifted down from 2.0 keV to 0.6 keV, with upper limit fixed to 10 keV. Error bars of photon indices at 0.6–0.8 keV are not plotted because χ^2 is too big to evaluate the errors.

can get an acceptable fit with the absorbed power-law model, we hereafter evaluate the 2–10 keV energy band spectrum with the power-law model, and call this component "hard power-law component" ($PL^{\rm hard}$). Comparison of the observed $PL^{\rm hard}$ with the previous measurements will be performed in chapter 8.

If we extrapolate the fitted model below 2 keV, we can see a significant excess of data above the model (soft-excess). This soft-excess becomes significant at ~ 1.2 keV, and the ratio of data to model increases to about 1.5 at 0.7 keV (lower panel of figure 6.3). Thus, the GIS data have comfirmed the existence of the soft-excess in the CXB spectrum, which has already been known with previous observations of the CXB (ref. §2). In order to show the soft-excess more clearly, we plot the change of reduced χ^2 and photon index of $PL^{\rm hard}$ in figure 6.4, as a function of lower-bound energy used for the spectral fitting. Because of the soft-excess, a single power-law model becomes unacceptable if we move the lower limit below 0.9 keV, and the photon index gets larger accordingly.

6.3.2 Results in the 0.6–10 keV range

Then, we quantify the soft-excess by fitting the spectrum in the whole energy of 0.6–10 keV, introducing a soft model component to represent the soft-excess. We choose a steep power-law or a low temperature Raymond-Smith (RS) model of one solar abundances as the soft component. Fitting results are shown in figure 6.5 and table 6.2. Both these models have given acceptable fits in the 0.6–10 keV energy band. If we choose a steep power-law as the soft component, its photon index shows very steep value of $\Gamma = 6.42 \pm 0.76$. Similarly, if we choose a low temperature RS model, its temperature shows a very low value of $kT = 0.31^{+0.15}_{-0.08}$ considering the GIS energy range (down to ~ 0.6 keV). Flux of the soft component in the 0.5–2 keV energy band is also shown in

table 6.2. The two soft-excess models cannot be distinguished from each other in view of the fit χ^2. However, the calculated soft component flux depends significantly on the choice between these two.

Because the power-law model is easier to evaluate errors than the *RS* moldel, we first use the steep power-law as the soft component in evaluating the fitting errors. Hereafter we call this component "soft power-law component" ($PL^{\rm soft}$). Figure 6.6 shows error contours between various pairs of the $PL^{\rm hard}$ and $PL^{\rm soft}$ parameters. There are correlations between the photon index Γ and the flux $F_{\rm X}$ for both $PL^{\rm hard}$ and $PL^{\rm soft}$, but the directions of the correlations are different from each other. With respect to the $PL^{\rm hard}$, $F_{\rm X}^{\rm hard}$ increases as $\Gamma^{\rm hard}$ gets flatter, while $F_{\rm X}^{\rm soft}$ increases as $\Gamma^{\rm soft}$ gets steeper. We note that these confidence contours does not include the effect of systematic errors, which we disscuss in detail in

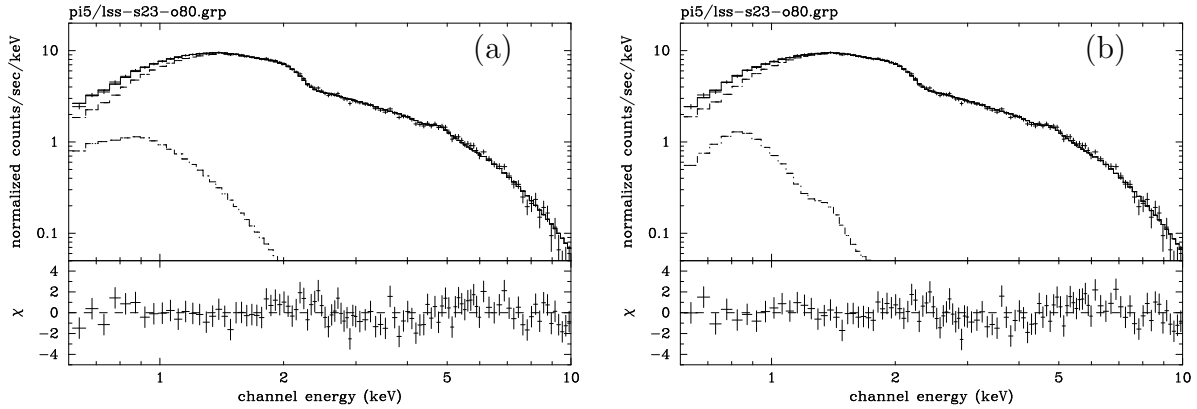

Figure 6.5: The average CXB spectrum in the LSS field, fitted in the entire 0.6–10 keV energy band with an absorbed power-law models plus a soft component. The soft component is represented by (a) a steep power-law or (b) a low temperature *RS* model of 1 solar abundances. Upper panel of each figure shows GIS2+3 spectrum (crosses), the best fit models (solid lines), the absorbed power-law component (dashed lines) and the soft component (dot-dashed lines). Lower panels show residuals plotted in the unit of σ.

Table 6.2: Model fits to the 0.6–10 keV spectrum of the average CXB

Model	power-law + abs. power-law*	Raymond-Smith + abs. power-law*
χ^2/d.o.f	105.7 / 100	103.7 / 100
Parameter	$\Gamma^{\rm hard} = 1.486 \pm 0.021$	$\Gamma^{\rm hard} = 1.502 \pm 0.017$
	$\Gamma^{\rm soft} = 6.41 \pm 0.76$	$kT = 0.31^{+0.15}_{-0.08}$ keV
$F_{\rm X}^{\rm hard}$ (2–10 keV)‡	6.14×10^{-8} (erg s^{-1} cm^{-2} str^{-1})	6.11×10^{-8} (erg s^{-1} cm^{-2} str^{-1})
$F_{\rm X}^{\rm soft}$ (0.5–2 keV)†	1.40×10^{-8} (erg s^{-1} cm^{-2} str^{-1})	0.48×10^{-8} (erg s^{-1} cm^{-2} str^{-1})

* Absorption is fixed to the Galactic line-of-sight value ($N_{\rm H} = 1.1 \times 10^{20}$ cm^{-2}).

‡ Flux of the hard power-law component in the 2–10 keV band.

† Flux of the soft component in the 0.5–2 keV band.

the next section.

Similarly, figure 6.7 shows error contours for $PL^{\rm hard}$ + RS model. If we take RS normalization as $F_{\rm X}^{\rm soft}$ and take $(kT)^{-1}$ as $\Gamma^{\rm soft}$, these correlations resemble those of figure 6.6. It appears that the fit with the low temperature RS wants lower element abundances, as seen in figure 6.5b. If we free the abundances of the RS model with their ratio fixed to the solar value, we get abundances $A = 0.09$ solar, and $kT = 0.28$ keV at χ^2/d.o.f = 102.1/104. However, these parameters are very poorly determined as shown in the confidence contour of kT vs. abundances (figure 6.8).

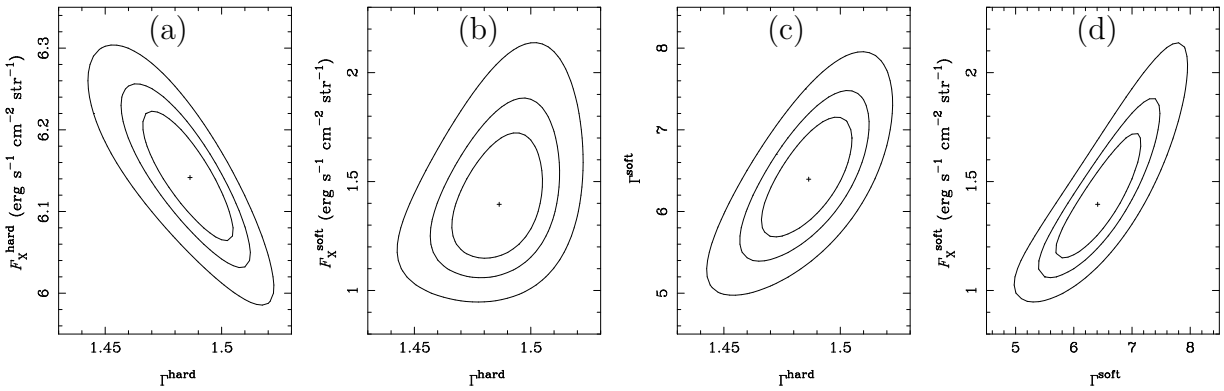

Figure 6.6: Confidence contours of the fitting parameters to the average CXB spectrum in the LSS field with the absorbed power-law ($PL^{\rm hard}$) + steep power-law ($PL^{\rm soft}$) model shown in figure 6.5a. Contours (from inner to outer) represent 68, 90 and 99% confidence levels. Crosses show the best fit position. (a) Photon index of $PL^{\rm hard}$ ($\Gamma^{\rm hard}$) vs. 2–10 keV band flux of $PL^{\rm hard}$ ($F_{\rm X}^{\rm hard}$). (b) $\Gamma^{\rm hard}$ vs. 0.5–2 keV band flux of $PL^{\rm soft}$ ($F_{\rm X}^{\rm soft}$). (c) $\Gamma^{\rm hard}$ vs. Photon index of $PL^{\rm soft}$ ($\Gamma^{\rm soft}$). (d) $\Gamma^{\rm soft}$ vs. $F_{\rm X}^{\rm soft}$.

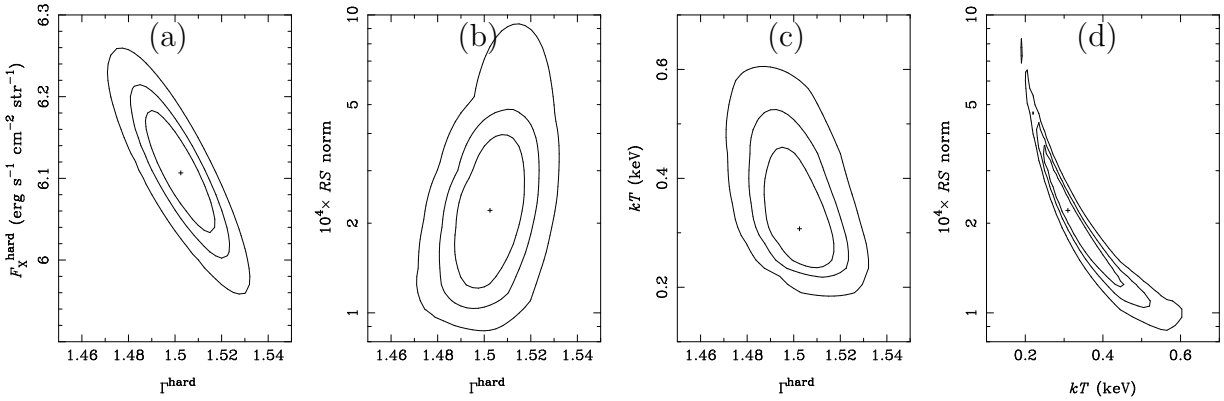

Figure 6.7: Same as figure 6.7, but for the absorbed power-law ($PL^{\rm hard}$) + Raymond-Smith (RS) model shown in figure 6.5b. (a) $\Gamma^{\rm hard}$ vs. $F_{\rm X}^{\rm hard}$. (b) $\Gamma^{\rm hard}$ vs. RS normalization. (c) $\Gamma^{\rm hard}$ vs. RS temperature. (d) RS temperature vs. RS normalization.

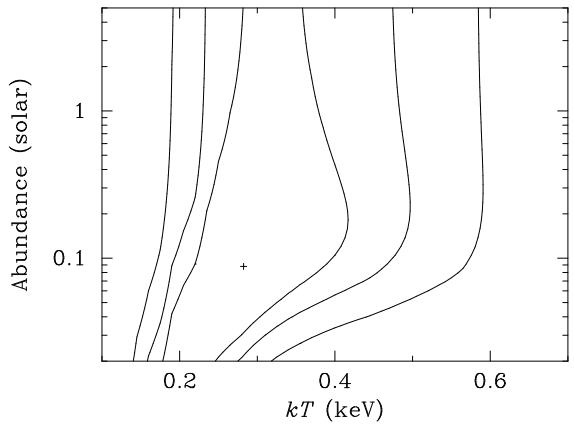

Figure 6.8: Confidence contour of *RS* temperature vs. *RS* abundance, when fitting the average CXB spectrum in the LSS field with $PL^{\rm hard}$ + *RS* model. Contours (from inner to outer) represent 68, 90 and 99% confidence levels. Cross shows the best fit position.

6.4 Systematic error of the CXB spectrum

In this section, we examine the effects of the systematic errors on the fitting parameters, mainly about $\Gamma^{\rm hard}$ and $F_{\rm X}^{\rm soft}$. Considered systematic errors are RNXB subtraction (§6.4.1), GIS low energy response (§6.4.2), stray light evaluation (§6.4.3), and the XRT effective area uncertainty (§6.4.4). Although we check these systematic error with the LSS spectrum, error regions can be applicable to other CXB spectra, too.

6.4.1 RNXB uncertainty

The RNXB (residual non X-ray background) spectrum to be subtracted from the raw CXB spectrum was created from the night-earth data utilizing the $H02$ distribution (for the H02-sorting method), considering the mean observation epoch (for the long-term RNXB trend correction), as described in §4.4.4. The prediction is subject to about 3.5% systematic error (table 4.7). However, we adopt the ±2.5% systematic error in this section, because of the reasons mentioned in §6.1.

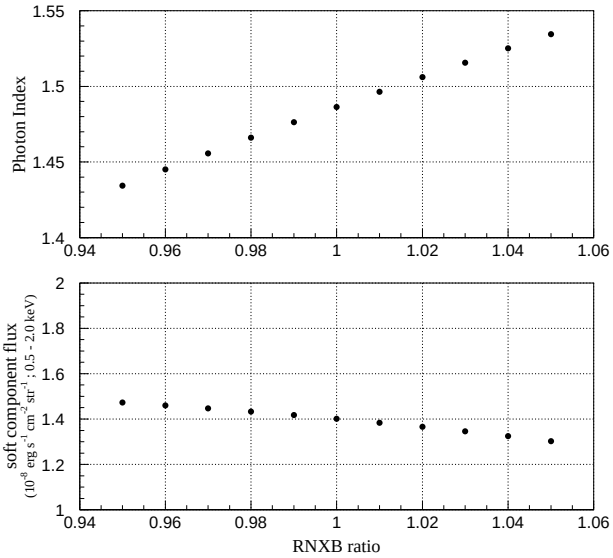

Figure 6.9: Changes of the CXB hard power-law component photon index ($\Gamma^{\rm hard}$; upper panel) and the soft power-law component flux ($F_{\rm X}^{\rm soft}$; lower panel) when the RNXB level is scaled to 0.95–1.05 from the nominal value.

In order to evaluate how the RNXB uncertainty affects the fitting results, we scaled the RNXB spectrum by -5% to $+5\%$ from the prediction, and examined the corresponding change of the best fit parameters. Figure 6.9 shows the results of this study. Since the RNXB spectrum has a flatter profile than the CXB spectrum, $PL^{\rm hard}$ gets steeper as we substract RNXB more. As for the $PL^{\rm soft}$, $F_{\rm X}^{\rm soft}$ gets smaller as we substract RNXB more, because the RNXB spectrum is extending straight below 1 keV where the CXB counts drop. Therefore, $\Gamma^{\rm hard}$ and $F_{\rm X}^{\rm soft}$ can vary 1.46–1.51 and (1.36–1.44) $\times 10^{-8}$ erg s^{-1} cm^{-2} str^{-1}, respectively, in respect to the $\pm 2.5\%$ systemaic error of the RNXB subtraction.

6.4.2 GIS low energy response uncertainty

In order to quantify the soft component of the CXB, we must know the accurate response of the GIS in the lower energy bands. In this subsection, we evaluate the systematic error caused by the uncertainty of the GIS low energy response. It is the Be entrance window that dominates the low energy response of the GIS (figure 4.3). The thickness of the Be foil was measured in the pre-launch calibration with an accuracy of ~ 0.1 μm (Ueda 1992), and the results showed variations over 10.7–11.1 μm and 10.45–10.55 μm for GIS2 and GIS3, respectively, depending on the foil positions. Variations in the absorption column density by about $\pm 2 \times 10^{20}$ cm^{-2} was also seen in the Crab spectra obtained at different positions (figure 4.10c). This variation by $N_{\rm H} \sim 2 \times 10^{20}$ cm^{-2} corresponds to 0.5 μm in berylium thickness.

We examined the change of the best fit CXB parameters, by artificially changing the Be window thickness. Figure 6.10 shows the best fit value of $\Gamma^{\rm hard}$ and $F_{\rm X}^{\rm soft}$ plotted versus adittional Be window thickness. Although $\Gamma^{\rm hard}$ is little affected by the Be

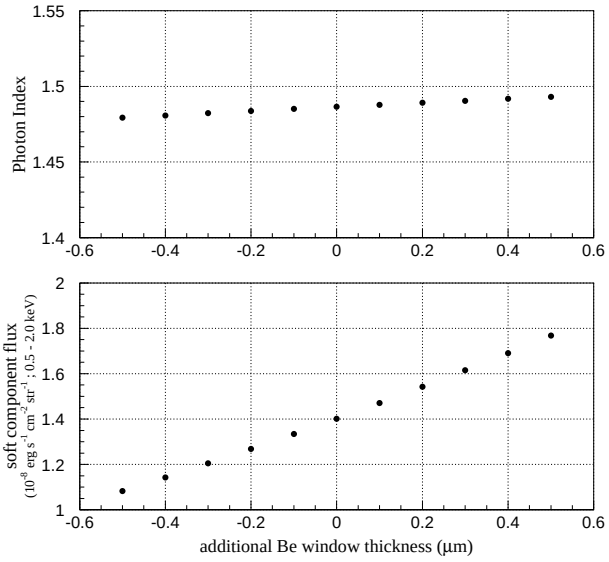

Figure 6.10: Changes of the CXB hard power-law component photon index ($\Gamma^{\rm hard}$; upper panel) and the soft power-law component flux ($F_{\rm X}^{\rm soft}$; lower panel) when GIS beryllium window have adittional thickness of -0.5 – $+0.5$ μm from the nominal value.

thickness, $F_{\rm X}^{\rm soft}$ are significantly affected. $F_{\rm X}^{\rm soft}$ gets larger as Be window gets thicker, because the detection efficiency of the GIS drops in low energy bands. If we assume the uncertainty of the Be window thickness by about ± 0.3 μm, $F_{\rm X}^{\rm soft}$ can vary by (1.20–1.61) $\times 10^{-8}$ erg s^{-1} cm^{-2} str^{-1}.

6.4.3 XRT stray light uncertainty

As described in §4.3, we cannot neglect the stray light effects in creating the CXB ARF. In this subsection, we evaluate the systematic errors caused by the uncertainty in the stray light fraction to the normal reflection component. The stray light effects have been calibrated by the large offset observations of the Crab nebula (ref. §4.3.3). As far as $\theta \lesssim 80'$, in which most of the CXB photons come from, the ray-tracing program can reproduce the stray lights from the Crab nebula pretty well, within the range of -30–$+10$%. We also note that the stray lights mainly consist of the secondary only reflection and the multiple reflection components (figure 4.15).

We examined the change of the best fit CXB parameters, by changing the fraction of the secondary only reflection or the multiple reflection component, in the range of -30–$+10$% from the nominal value obtained with the ray-tracing program. Figure 6.11 shows the results of this study. Since multiple reflection component significantly increases in

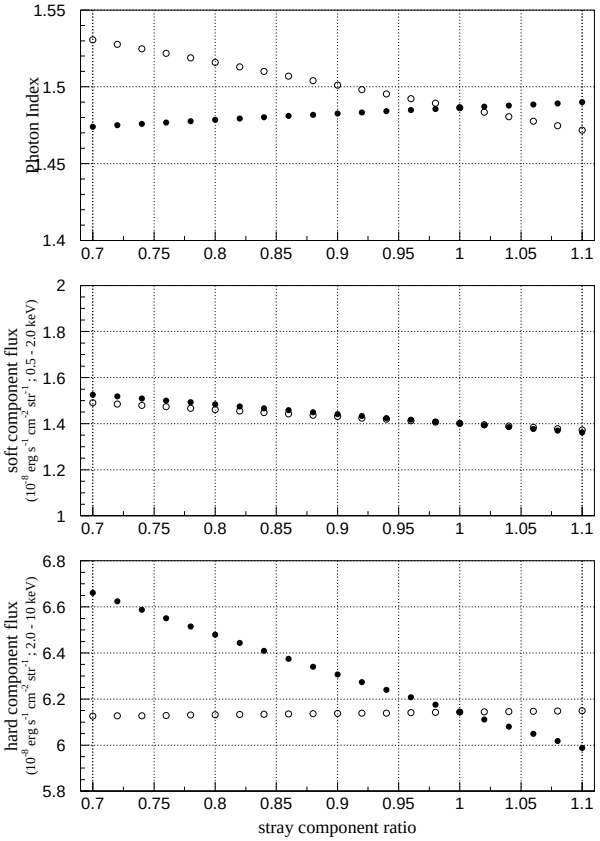

Figure 6.11: Changes of the CXB hard power-law component photon index ($\Gamma^{\rm hard}$; upper panel), the soft power-law component flux ($F_{\rm X}^{\rm soft}$; middle panel), and the hard power-law component flux ($F_{\rm X}^{\rm hard}$; lower panel), when stray light (filled circles for secondary only reflection, open circles for multiple reflection) level is scaled to 0.7–1.1 from the nominal value derived in §4.3.

the lower energy bands, $PL^{\rm hard}$ gets flatter due to the increase of the soft band effective area, when we increase the multiple reflection component. $F_{\rm X}^{\rm soft}$ does not show particular changes, because the reflectivity of the XRT foils are almost constant below $\sim$ 2 keV. Since the secondary only reflection component has similar energy dependence with that of the normal reflection, changing the fraction of the secondary only component does not significantly affect $\Gamma^{\rm hard}$ or $F_{\rm X}^{\rm soft}$. However, it affects $F_{\rm X}^{\rm hard}$ by $\sim$ 10% level. From these considerations, we estimate the systematic error of $\Gamma^{\rm hard}$ due to the stray light uncertainty to be 1.47–1.53.

6.4.4 XRT effective area uncertainty

If we fit the ring-sorted spectra shown in §6.2 one by one, $PL^{\rm hard}$ of outer rings appear to be flatter than those of inner rings, as shown in figure 6.12b by filled circles. Also the $F_{\rm X}^{\rm hard}$ values of the inner rings appear to be smaller by $\sim$ 5% compared with those of outer rings. These trends are also seen in the Crab pointings which has been carried out at various detector positions (figure 4.10). It is possibly because the ray-tracing program cannot perfectly reproduce the position- and energy-dependence of the XRT effective area. In order to compensate these incompleteness of the XRT effective area, we try introducing an artificial correction factor for the XRT effective area represented by an analytic formula:

$$f(\theta, E) = 1 - p \cdot \exp\left(-\frac{\theta^2}{2a^2}\right) + q \cdot \exp\left(-\frac{(\theta-\theta_b)^2}{2b^2}\right) \tag{6.1}$$

$$\begin{cases} a = 5, \quad b = 2.5, \quad \theta_b = 14 \\ p = 0.2\ (1 - \exp(-E/3.0)) \\ q = 0.05 - 0.002E \end{cases}$$

where θ (arcmin) and E (keV) means the offset angle from the optical axis and the energy of the incident X-ray, respectively, as previously defined in §4.2.1. Figure 6.13 shows this function, superposed on to the ratio of the observed flux to the ray-tracing prediction at each point of the Crab observations.

We re-created the CXB ARF using the XRT effective area which is modified by equation (6.1), and again fit the ring-sorted spectra with the modified CXB ARF. Open circles in figure 6.12 show the results. Since this modification have little effect beyond $r \sim 20$ mm, fitting results are almost unchanged in the 20–25 mm outermost ring. If we neglect the outer most ring, photon indices become nearly constant by this modification. However, $F_{\rm X}^{\rm hard}$ of the inner rings gets large in turn. This is probably related to the fact that the ray-tracing program seems to over-estimate stray lights by $\sim$ 10%. If we fit the total spectrum integrated inside 20 mm from the optical axis with the modified CXB ARF,

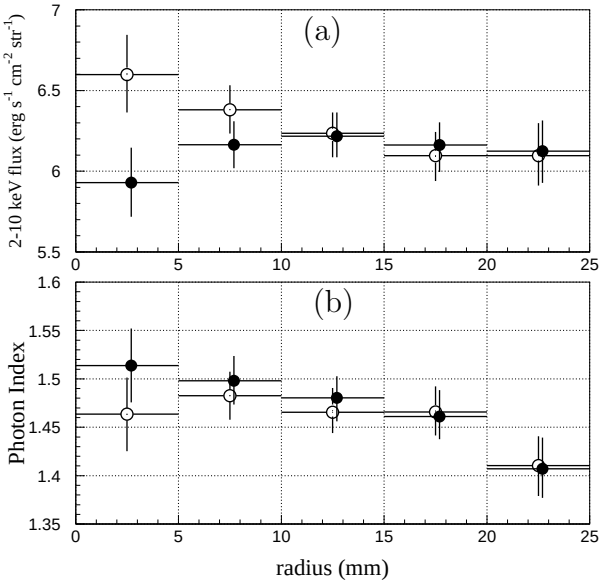

Figure 6.12: (a) Flux and (b) photon index of the ring-sorted CXB spectra plotted versus the radius of each ring. Filled circles show the fiting results with the nominal XRT response, and open circles show the results with the modified XRT response.

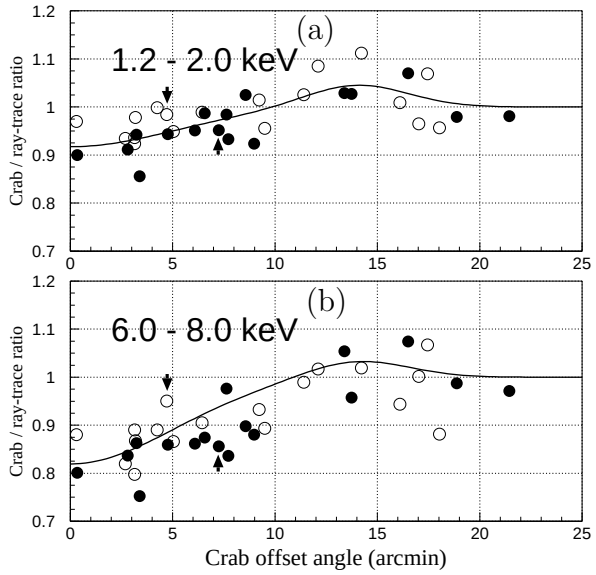

Figure 6.13: Ratio of the observed Crab counts to that predicted by the ray-tracing calculation in (a) 1.2–2.0 keV and (b) 6.0–8.0 keV plotted against the offset angle from the XRT optical axis. Integration radius is 6 mm centered on the Crab nebula. Filled circles represent GIS2 and open circles GIS3. The point with an arrow show the observation at the 1CCD nominal position. Smooth solid lines show the function of equation (6.1). We assume that the Crab nebula has a constant spectrum of an absorbed power-law, i.e. $\Gamma = 2.1$, $norm = 9.7$ c s^{-1} cm^{-2} keV^{-1}, and $N_{\rm H} = 3.0 \times 10^{21}$ cm^{-2}.

we get $\Gamma^{\rm hard} = 1.468$ and $F_{\rm X}^{\rm soft} = 1.46 \times 10^{-8}$ erg s^{-1} cm^{-2} str^{-1}. Since these values agree with those derived with the nominal CXB ARF (table 6.2), we do not find the necessity of introducing the modification. Therefore, we do not apply the XRT effective area correction by equation (6.1) in the following analyses.

The accuracy of the XRT effective area directly affects the ARF normalization, hence absolute flux of the CXB. The normalization of the CXB ARF which we have used in fitting the CXB spectra is determined from the deep Crab observation at 1CCD nominal position (ref. §4.2.5). However, the Crab flux measured with the GIS itself varies by $\sim$ 10%, depending on the pointing position of the Crab nebula (figure 6.13). This is probably due to the shadowing of the support grids on the GIS entrance window. Since there exists $\sim$ 10% error on the reference flux, the absolute flux of the CXB also have at

least $\sim 10\%$ uncertainty. This uncertainty is comparable or rather large than that caused by the stray light uncertainty (ref. §6.4.3).

6.4.5 Summary of the systematic errors

In table 6.3, we summarize the systematic errors considered in the preceding subsections. $\Gamma^{\rm hard}$ is most affected by the RNXB uncertainty, and $F_{\rm X}^{\rm soft}$ is most affected by the Be window thickness uncertainty. As a result, our best estimates for the CXB parameters for the LSS field can be summarized as:

$$\begin{aligned} \Gamma^{\rm hard} &= 1.486 \quad \pm 0.021 \quad \pm 0.040 \\ F_{\rm X}^{\rm hard} &= 6.14 \quad \pm 0.08 \quad \pm 0.92 \quad (10^{-8} \ \text{erg s}^{-1}\ \text{cm}^{-2}\ \text{str}^{-1}) \\ F_{\rm X}^{\rm soft} &= 1.40 \quad \pm 0.27 \quad \pm 0.22 \quad (10^{-8} \ \text{erg s}^{-1}\ \text{cm}^{-2}\ \text{str}^{-1}), \end{aligned} \tag{6.2}$$

where the former error represents the 90% confidence level statistic erorr and the latter represents the systematical errors. The systematic error for the absolute CXB flux is $\sim 15\%$ (10% by the stray light uncertainty and another 10% by the absolute effective area uncertainty). However, relative errors in fluxes measurements, from different field to field, should be much smaller. We estimate the relative flux errors to be less than 3%, taking into account the $\sim 3.5\%$ RNXB uncertainty.

Furthermore, it must be noted that the XRT+GIS has been adjusted in such a way that the Crab nebula spectrum observed at the 1CCD nominal position becomes as shown in table 4.4. Whereas, generally accepted value of the photon index for the Crab nebula is $\Gamma \sim 2.1$. We emphasize that our response gives a little steep photon index by $\Gamma \sim 0.06$. Therefore, $\Gamma^{\rm hard}$ can be ~ 1.4, if we modify our response to fit the Crab spectrum with $\Gamma = 2.10$.

Table 6.3: Summary of the systematic errors for the CXB spectrum in the LSS field

Origin	uncertainty	Error region of Photon Index	Error region of soft component flux (10^{-8} erg s^{-1} cm^{-2} str^{-1})	ref.
RNXB to be subtracted	$\pm$ 2.5%	1.461 – 1.511	1.36 – 1.44	§ 6.4.1
Be window thickness	$\pm$ 0.3 μm	1.482 – 1.490	1.20 – 1.61	§ 6.4.2
stray light strength	-30% – $+10\%$	1.472 – 1.531	1.37 – 1.49	§ 6.4.3
XRT effective area	$\lesssim$ 20%	1.468 – 1.486	1.40 – 1.46	§ 6.4.4
Total*	—	1.486 ± 0.040	1.40 ± 0.22	—

* Quadratic sum of all errors.

Chapter 7

Field to field properties of the CXB

7.1 CXB spectra of individual fields including point sources

We have studied the average CXB spectrum in the LSS field in chapter 6, and have established the method of quantifying the CXB spectrum using the GIS data. Then, as a next step, we examine the CXB properties in the other fields described in chapter 5. We also split the overall LSS observations into four groups, a-LSS, b-LSS, c-LSS, and d-LSS, as described in §5.2.1, and analyze them individually.

We created the spectrum of each field just in the same way as the average LSS spectrum was created. All events inside 20 mm from the optical axis were utilized, even though point sources are clearly present in most of the f.o.v. Each RNXB spectrum to be subtracted was generated by the H02-sorting method with the normalization adjusted to correct the long-term RNXB trend. We fitted each spectrum thus created with the $PL^{\rm hard} + PL^{\rm soft}$ model, using the same RMF and ARF as were used to fit the LSS spectrum. We fixed $\Gamma^{\rm soft}$ to 6.0, because it was practically unconstrained in several fields, due to low statistics or poor fits to the data (e.g. NEP). Absorption column for $PL^{\rm hard}$ was also fixed, according to the information from *EINLINE*, as given in table 7.1. The fitting results are summarized in table 7.1. We also show all the spectra in appendix D.

The errors shown in table 7.1 are the 90% confidence level statistical errors, and do not include the systematic errors. However, systematic errors due to uncertainty of the XRT+GIS response are common to all the fields, so that the RNXB uncertainty of $\sim$ 3.5% is the dominant systematic error when we compare different fields. If we ignore the NEP about which we cannot get an appropriate fit, the values for $\Gamma^{\rm hard}$ are distributed in the range of 1.39–1.55, and the $F_{\rm X}^{\rm hard}$ values in the range of (5.5–6.7)$\times 10^{-8}$ erg s^{-1} cm^{-2} str^{-1}. Mean values and standard deviations are 1.461 ± 0.047, and $(6.10 \pm 0.30) \times 10^{-8}$ erg s^{-1} cm^{-2} str^{-1}, respectively. Thus the relative 1σ variation of $F_{\rm X}^{\rm hard}$ is 5.0%, which is a little larger than both statistical and systematic errors. Variation of $\Gamma^{\rm hard}$ is marginal, considering the systematic errors. The Arp 220 and 3C368

fields show apparently larger $F_{\rm X}^{\rm soft}$.

Among these fields, particularly the NEP spectrum could not be fitted with the $PL^{\rm hard} + PL^{\rm soft}$ model, as shown in figure 7.1. The NEP spectrum shows clear excess around 6 keV, which is undoubtedly due to the Seyfert 2 galaxy NGC 6552 (Fukazawa et al. 1994) which happen to be in the f.o.v. This exemplifies that the CXB observations which are restricted in a small region have a risk of being influenced by particular point sources. However, ASCA has an imaging capability, so that we can remove point sources brighter than some levels depending on the deepness of the exposure. In the next section, we consider removing point sources in the observed fields in order to study the remaining CXB spectra.

Table 7.1: ($PL^{\rm hard}$+$PL^{\rm soft}$) fits to the 0.6–10 keV spectrum of each field including point sources. All errors are 90% confidence level. $\Gamma^{\rm soft}$ is fixed to 6.0.

ID	Name	Exp.†	Area‡	$N_{\rm H}^\sharp$	χ^2/d.o.f	$\Gamma^{\rm hard}$	$F_{\rm X}^{\rm hard\triangleleft}$	$F_{\rm X}^{\rm soft*}$
1	SA57	461,343	0.68	1.0	69.0/67	1.414 ± 0.017	6.00 ± 0.09	1.31 ± 0.14
2	a-LSS	119,221	2.09	1.1	101.0/67	1.446 ± 0.032	5.85 ± 0.16	0.75 ± 0.26
3	b-LSS	130,206	2.32	1.1	84.0/67	1.444 ± 0.031	6.07 ± 0.15	1.28 ± 0.26
4	c-LSS	138,641	2.27	1.1	52.6/67	1.461 ± 0.030	5.93 ± 0.15	1.32 ± 0.26
5	d-LSS	127,324	2.19	1.1	57.6/67	1.552 ± 0.028	6.73 ± 0.16	1.64 ± 0.30
6	Draco	57,002	0.71	4.1	94.7/67	1.494 ± 0.048	5.47 ± 0.22	1.42 ± 0.38
7	NEP	118,434	0.58	4.2	217.4/67	$1.257 \pm 0.000^\star$	$6.70 \pm 0.00^\star$	$2.41 \pm 0.00^\star$
8	QSF3	60,157	0.43	1.7	60.2/67	1.429 ± 0.044	6.15 ± 0.22	1.42 ± 0.38
9	ZSYS	109,893	1.68	2.3	28.7/67	1.474 ± 0.032	6.41 ± 0.17	0.93 ± 0.29
10	BF	114,738	1.47	1.2	117.5/67	1.524 ± 0.030	6.46 ± 0.16	0.57 ± 0.30
11	Jupiter	20,389	0.40	2.1	64.6/67	1.521 ± 0.076	5.99 ± 0.37	1.01 ± 0.67
12	Arp 220	23,039	0.40	4.2	78.7/67	1.393 ± 0.077	5.64 ± 0.35	4.77 ± 0.66
13	3C368	19,934	0.40	9.8	104.5/67	1.480 ± 0.078	6.10 ± 0.38	4.64 ± 0.70

† Total exposure time (s).

‡ Integration area (deg^2) on the sky.

$^\sharp$ Absorption for $PL^{\rm hard}$ (10^{20} cm^{-2}) from Einstein On-line Service (*EINLINE*). Fixed while fitting.

$^\triangleleft$ Flux of $PL^{\rm hard}$ (10^{-8} erg s^{-1} cm^{-2} str^{-1}) in the 2–10 keV energy band.

* Flux of $PL^{\rm soft}$ (10^{-8} erg s^{-1} cm^{-2} str^{-1}) in the 0.5–2 keV energy band.

* χ^2 is too big to evaluate errors.

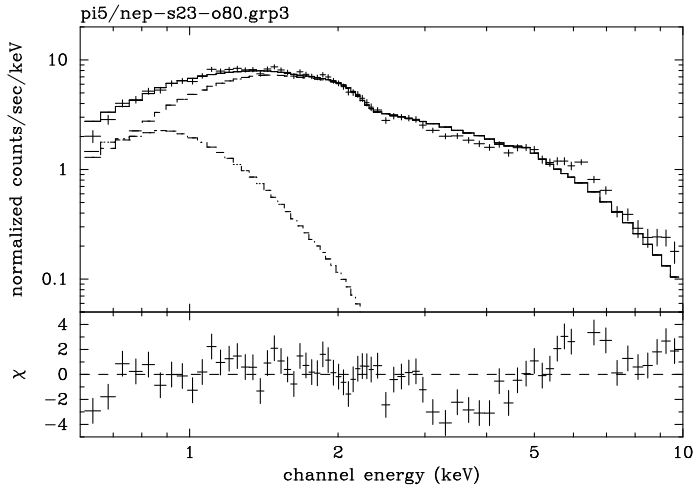

Figure 7.1: The NEP spectrum fitted with the $PL^{\rm hard} + PL^{\rm soft}$ model in the 0.6–10 keV energy band. $PL^{\rm hard}$ is modified with Galactic absorption of $N_{\rm H} = 4.2 \times 10^{20}$ cm^{-2}. Upper panel shows GIS2+3 spectrum (crosses), the best fit models (solid lines), the absorbed $PL^{\rm hard}$ component (dashed lines), and the $PL^{\rm soft}$ component (dot-dashed lines). Lower panel shows residuals plotted in the scale of σ.

7.2 How to eliminate point sources

7.2.1 Outline of the source-finding

We consider eliminating point sources brighter than a certain fixed level, in order to better quantify the CXB properties. To do this, we have to detect point sources and evaluate their fluxes (source-finding). We carried out the source-finding on the GIS image taken in the 0.7–7.0 keV energy band in the following way.

We first rebinned the image by 2×2 pixels into 0.5×0.5 mm resolution, in order to speed up the image analyses. Since the XRT+GIS response is not so sharp ($\sim 3'$ in half power diameter) and has severe offset-angle-dependence (ref. §4.2), subsequent procedure of the source-finding is somewhat complicated. The image $B^{OBS}(DETX, DETY)$ observed with the XRT+GIS system can be decomposed into:

$$B^{OBS}(DETX, DETY) = B^{RNXB}(DETX, DETY) \quad (7.1)$$
$$+ B^{UCXB}(DETX, DETY) \quad (7.2)$$
$$+ \sum_i B_i^{PS}(DETX, DETY), \quad (7.3)$$

where B^{RNXB} is the RNXB image, B^{UCXB} is the image of the CXB that cannot be resolved into point sources (unresolved CXB), and B_i^{PS} are the images due to point sources in the f.o.v. Here, B^{UCXB} also includes the image created by the stray lights. Although the boundary between B^{UCXB} and B_i^{PS} is not necessarily well defined, the ambiguity does not matter as far as we deal with point sources that are bright enough ($\gtrsim 10^{-13}$ erg s^{-1} cm^{-2}).

In order to single out $\sum_i B^{PS}$, we try estimating B^{RNXB} and B^{UCXB}. As for B^{RNXB}, we can estimate it just in the same way as was done in §4.4.4. Therefore, we generated it by the H02-sorting method with correction for the long-term RNXB trend. On the other hand, it is a difficult issue to estimate B^{UCXB}. Among several choices, we have decided to utilize the entire LSS data in combination with the day-earth image B^{DYE} (figure 3.15) in the following way.

As described in §6.1, the LSS data provide the best sample of the CXB, so that we basically utilized the entire LSS data to construct the template CXB image when observed with the XRT+GIS. We first summed up the entire LSS data in the 0.7–7.0 keV energy band on $DETX$-$DETY$ coordinates to generate the image $B^{LSS}(DETX, DETY)$. Even though they have been averaged to some extent by summing up 76 pointings, the result is still subjected to local clumpiness due to point sources. Furthermore, B^{LSS} is at most 5 c pixel^{-1}, and are not satisfactory in statistics, either. Therefore, we smoothed B^{LSS} with a Gaussian of $\sigma = 2$ pixel, and azimuthly averaged B^{LSS} centered on the optical axis to create an azimuthly-averaged radial-profile $R^{LSS}(r)$ as:

$$R^{LSS}(r) = \frac{\int d\phi \; smo\Big[B^{LSS} - B^{RNXB}\Big]}{\int d\phi \; smo\Big[B^{MASK}\Big]}, \tag{7.4}$$

where B^{MASK} is the standard image masking (figure 4.20), and $smo\Big[B\Big]$ represents the operation of the Gaussian smoothing. Applying these procedures, the local clumpiness was smeared out and the statistics were much improved. However, this procedure has also smeared out local instrumental structures such as shadows cast by the window support grids of the GIS (figure 3.15). Although such local instrumental structures imprinted on the CXB image are difficult to model analytically, we can reproduce the patterns utilizing the day-earth image B^{DYE}, which has very high statistics (40–80 c pixel^{-1}) and is created by a reasonably uniform source. We therefore created $B^{\overline{CXB}}$ as:

$$B^{\overline{CXB}}(DETX, DETY) = \frac{R^{LSS}(r)}{R^{DYE}(r)} \times (B^{DYE} - B^{RNXB}), \tag{7.5}$$

where R^{DYE} is the radial-profile of B^{DYE}. This $B^{\overline{CXB}}$ can be regarded as the template image of the CXB, in which contributions of the point sources in the LSS field (up to $F_{\rm X}^{2-10\,{\rm keV}} \sim 2 \times 10^{-12}$ erg s^{-1} cm^{-2}) have been flattened out (but not subtracted).

In creating $B^{\overline{CXB}}$ via equation 7.5, we integrated the day-earth data in the 1.0–3.0 keV energy band to reduce the RNXB fraction. GIS2 and GIS3 were treated separately, and two $B^{\overline{CXB}}$ were created for GIS2 and GIS3, respectively. We have examined the azimuth-angle-dependence of B^{DYE}, and did not find significant structure over $\pm 5\%$. This justifies the procedure of azimuthly-averaging to create $B^{\overline{CXB}}$. We think this approximation of

equation (7.5) gives a sufficient quality for the template CXB image. Then, we assume that B^{UCXB} can be approximated as:

$$B^{UCXB}(DETX, DETY) = \alpha \times B^{\overline{CXB}}(DETX, DETY), \tag{7.6}$$

where α is a positive constant value less than 1.0, which gives the fraction of the CXB unresolved with the XRT+GIS. This factor α is expected to be mainly determined by the imaging performance of the XRT+GIS system, and not to vary significantly field to field. We will evaluate the value of α in the next subsection.

Supposing that B^{RNXB} and B^{UCXB} have been known, we can extract the contribution of point sources as:

$$\sum_i B_i^{PS}(DETX, DETY) = B^{OBS} - B^{RNXB} - B^{UCXB}. \tag{7.7}$$

Although the image produced with equation (7.7) contains full information on point sources, it is difficult to be utilized without smoothing. We therefore smooth it, just taking its cross correlation with the XRT+GIS point spread function, as described in §5.3.2. At the same time, using the knowledge of satellite Euler angles, we convert the image into the sky coordinates, for the purpose of creating a mosaic image. The operator $ccf\Big[B\Big]$ denotes this procedure, as defined by equation (5.4).

Finally, we can realized a nearly flat-field mosaic image for point sources, in which exposure, vignetting, and backgrounds (both RNXB and unresolved CXB) are cancelled, as:

$$M^{FLAT}(SKYX, SKYY) = \frac{\sum_j T_j \; ccf\Big[B_j^{OBS} - B_j^{UCXB} - B_j^{RNXB}\Big]}{\sum_j T_j \; det2sky\Big[A^{PS}\Big]}, \tag{7.8}$$

where j represents the pointing number in the field, and T_j represents the exposure time for the j-th pointing. The term of $A^{PS}(\theta, \phi)$ takes charge of the XRT vignetting, as defined in §5.3.2. On $M^{FLAT}(SKYX, SKYY)$, image peaks are expected to be seen at the positions where point sources are likely to exist. The peak value is expected to be precisely in proportion to its flux, because M^{FLAT} has been corrected for both exposure and vignetting. Therefore, we apply a fixed threshold on $M^{FLAT}(SKYX, SKYY)$, and consider that a point source exists where the pixel values exceed the threshold.

7.2.2 Determination of the CXB base level

Before actually performing the source-finding and subsequent source-elimination, we must fix the value of α in equation (7.6), which determins the base level of the unresolved

CXB. To do this, we again utilized the LSS data. For this purpose, we created a mosaic image of the LSS observations as:

$$M^{RATIO}(SKYX, SKYY) = \frac{M^{RAW}}{M^{\overline{CXB}}} = \frac{\sum_j T_j \; ccf\left[B_j^{OBS} - B_j^{RNXB}\right]}{\sum_j T_j \; ccf\left[B_j^{\overline{CXB}}\right]}. \tag{7.9}$$

The numerator (M^{RAW}) and the denominator ($M^{\overline{CXB}}$) of M^{RATIO} are basically created from the same data set, i.e. entire LSS. However, the former is the raw event map with RNXB subtracted and then smoothed with the PSF, while the latter is our best estimate of the CXB, in which fluxes from resident point sources have been re-distributed almost uniformly over the entire survey area via equation (7.5). Therefore, $M^{RAW}/M^{\overline{CXB}}$ has a ratio less than 1.0 in most pixels where resolved point sources do not exist, although the mean values of M^{RAW} and $M^{\overline{CXB}}$ are equal.

Since the image excesses due to point sources are localized around the positions where individual sources are present, the pixel values of $M^{RATIO}(SKYX, SKYY)$ should have values close to α in off-source regions within statistical errors which vary from pixel to pixel. We show the mosaic images of M^{RAW}, $M^{\overline{CXB}}$ and M^{RATIO} in figure 7.2, 7.3, and 7.4, respectively.

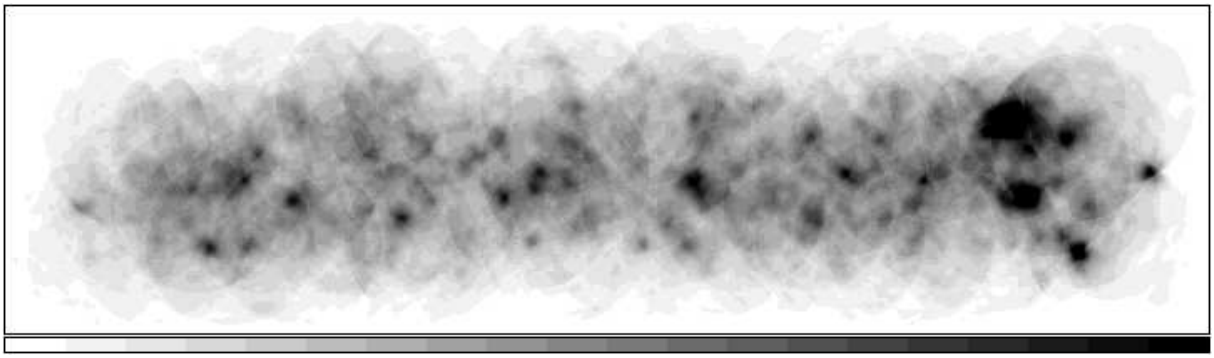

Figure 7.2: Gray scale image of $M^{RAW} = \sum_j T_j \; ccf\left[B_j^{OBS} - B_j^{RNXB}\right]$ for the entire LSS observations. White and black pixel corresponds to 0.0 and 10.0 c pixel^{-1}, respectively.

To determine the most frequent pixel values on the M^{RATIO} map, we created histogram of the pixel values on M^{RATIO} as shown in figure 7.5. In order not to be affected by statistical errors, we discarded the pixels where $M^{\overline{CXB}} < 1.0$ c pixel^{-1}. This histogram consists of mainly three components. Firstly, it is contributed by the Poisson error due to photon counting statistics. This effect is not easy to evaluate, because of the multi-exposure nature and the $ccf\left[B\right]$ operation. Considering that the pixel values of M^{RAW} range over $\sim$ 1–5 c pixel^{-1}, and $ccf\left[B\right]$ operation reduces statistical errors typically by $\sim$ 17%, we estimate the contribution of the Poisson error to the peak width to be 0.16–0.07. Secondly, the CXB fluctuation due to unresolved sources further broaden the peak.

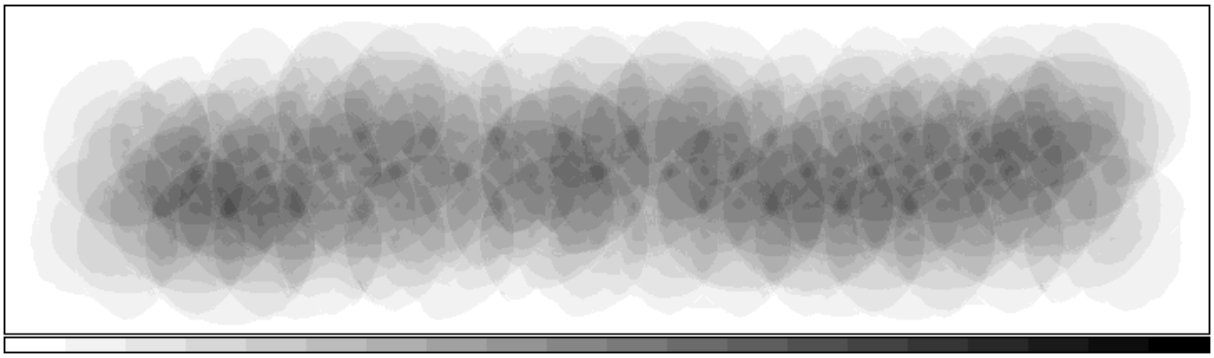

Figure 7.3: Gray scale image of $M^{\overline{CXB}} = \sum_j T_j \; ccf\Big[B_j^{\overline{CXB}}\Big]$ for the entire LSS observations. White and black pixels correspond to 0.0 and 10.0 c pixel^{-1}, respectively.

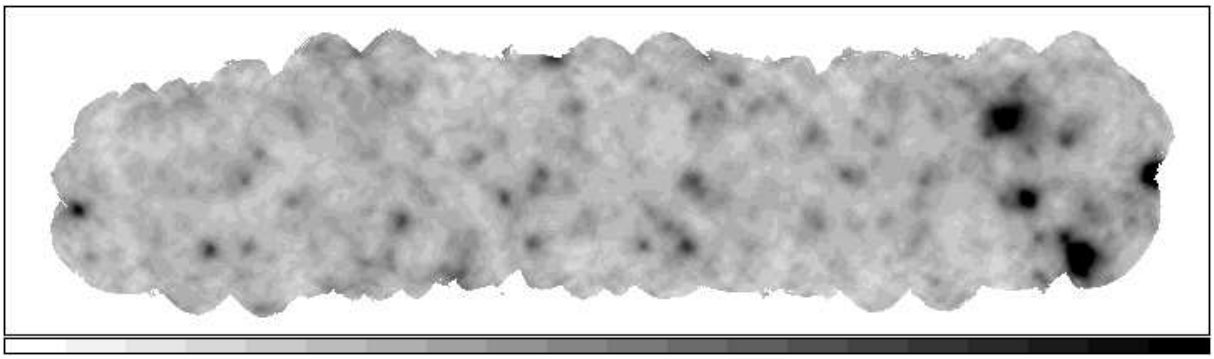

Figure 7.4: Gray scale image of $M^{RATIO}(SKYX, SKYY)$ for the entire LSS observations. White pixel corresponds to 0.0 and black pixel corresponds to 3.0. Values of pixels where $M^{\overline{CXB}} < 1.0$ c pixel^{-1} are set to 0.0.

Lastly, the component trailing a tail to the positive direction is created by the resolved point sources. Our present purpose is to determin the peak position created by the first and the second components, eliminating the third component.

Therefore, we fitted the histogram in the range of 0.55–2.0 with a function:

$$f(x) = N_1 \exp\Big(-\frac{(x-\mu)^2}{2\sigma_1^2}\Big) + N_2 \exp\Big(-\frac{(1-\mu/x)^2}{2\sigma_2^2}\Big). \tag{7.10}$$

This function is chosen for practical reasons that it successfully reproduces the shape of the distribution and that the peak position μ is clearly defined. Although pixels are not independent with each other due to the $ccf\Big[B\Big]$ operation, we tentatively put square root errors in each bin. From the fitting, we get $\mu = 0.882 \pm 0.001$, $\sigma_1 = 0.150 \pm 0.001$, and $\sigma_2 = 0.201 \pm 0.001$. Thus, we decided to fix $\alpha = 0.88$ to estimate B^{UCXB} in equation (7.6). This means that the 0.7–7.0 keV GIS flux from the entire LSS field is contributed by $\sim 12\%$ by point sources which can be resolved with ASCA.

7.2.3 Point-source images

Now that α in equation (7.6) has been determined, we can substitute equation (7.6) into equation (7.8) and obtain $M^{FLAT}(SKYX, SKYY)$. We show M^{FLAT} of the LSS

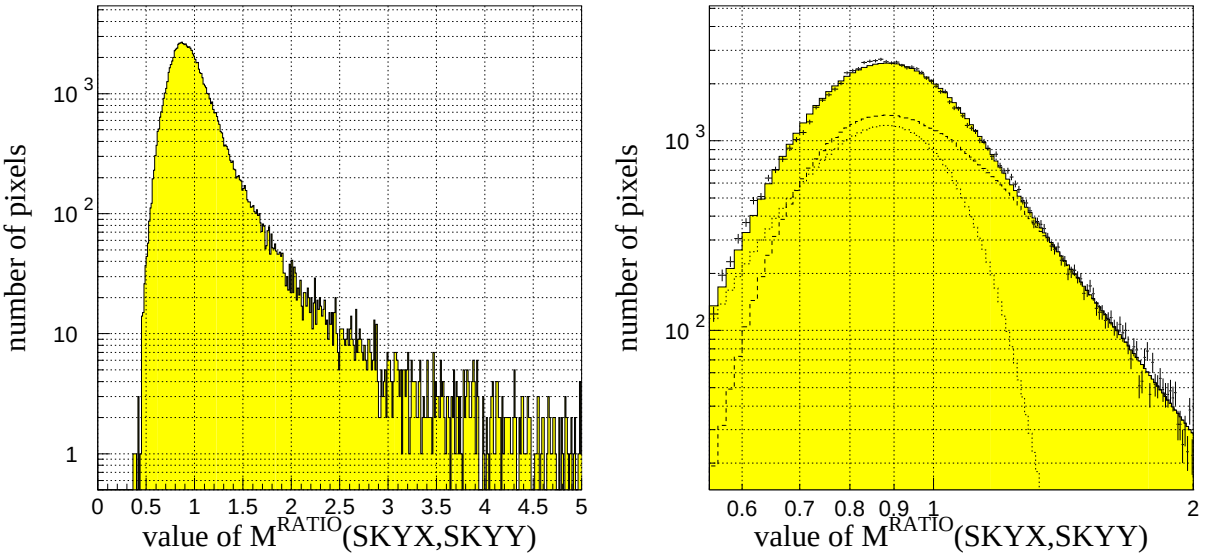

Figure 7.5: Distribution of pixel values in figure 7.4. Left panel shows the distribution in the range of 0–5, and right panel shows in the range of 0.55–2.0. In right panel, the distribution (crosses) is fitted with the function of equation (7.10) and the best fit line (solid line) and each component (two dashed lines) are overlaied.

observations thus obtained with $\alpha = 0.88$ in figure 7.6, and its pixel-value distribution in figure 7.7. Just to remember, M^{FLAT} is our best estimate for the 0.7–7.0 keV point-source image for the LSS sky, after subtracting RNXB and UCXB. It is expressed in rather arbitrary scale, but pixel values are expected to be in proportion with the source flux. The distribution has a sharp peak at 0.0, which demonstrates the correctness of the RNXB and UCXB subtraction. Similar to the case of figure 7.5, the width of distribution in figure 7.7 represents the superposition of the statistical errors which depend on the deepness of the exposure, and the fluctuation of the CXB brightness due to confusion of faint sources. The long tail extending toward the positive direction is created by the point sources in the LSS fields.

We set a rather loose threshold of 0.1 to define point sources to be removed, in order to ensure the completeness of source detection even at the edge of the GIS f.o.v. This threshold roughly correspond to a few $\times 10^{-13}$ erg s^{-1} cm^{-2}, which we will discuss in the next section. Since the number of pixels below -0.1 and 0.0 is 486 and 49,925, respectively, we can estimate the probability of mistaking chance fluctuations for point sources is $\sim 1\%$, assuming that the distribution blow 0.0 is completely determined by the statistics and the CXB base level fluctuations, and that these effects are symmetric below and above 0.0. Moreover, if we fit the distribution with a Gaussian in the range of -0.04–0.0 fixing the peak position to 0.0, the fit gives $\sigma = 0.018$, which is $\sim 1/5$ of the proposed threshold. Therefore, in most regions where exposure is much deeper than

the image edge (typically ~ 20 ks), the probability of chance detection of false sources is expected to be much less.

We remark here again that the point-source map M^{FLAT} has been smoothed with the $ccf\left[B\right]$ operation according to equation (7.8), so that the map has a typical coherence length comparable to the PSF width ($\sim 3'$). Accordingly, a point source detection cannot occur in a single pixel, unless it is very close to the threshold by chance.

Here, we explain how M^{RATIO} and M^{FLAT} are different, and why we have to take this dual step, i.e. M^{RATIO} and M^{FLAT}, to produce the point-source-masks. As can be seen from equation (7.9), M^{RATIO} is optimized in such a way that the image of a uniform-brightness source (specifically, B^{UCXB}) appears flat; dividing by $B^{\overline{CXB}}$ is meant to normalize $B^{OBS} - B^{RNXB}$ to the effective XRT+GIS response (including vignetting and stray lights) for a uniform X-ray source. On the other hand, M^{FLAT}, as given in equation (7.8), is constructed in such a way that the pixel intensity for each point source is directly proportional (except for spectral differences) to the incident source flux. This has been achieved by dividing $B^{OBS} - B^{RNXB} - B^{UCXB}$ by the factor A^{PS}, which gives

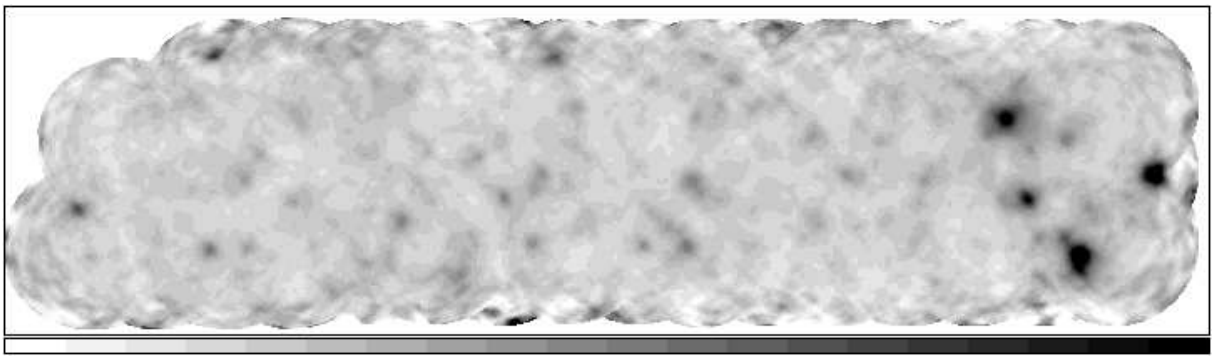

Figure 7.6: Gray scale image of $M^{FLAT}(SKYX, SKYY)$ for the entire LSS observations. White pixel corresponds to -0.1 and black pixel corresponds to 0.4.

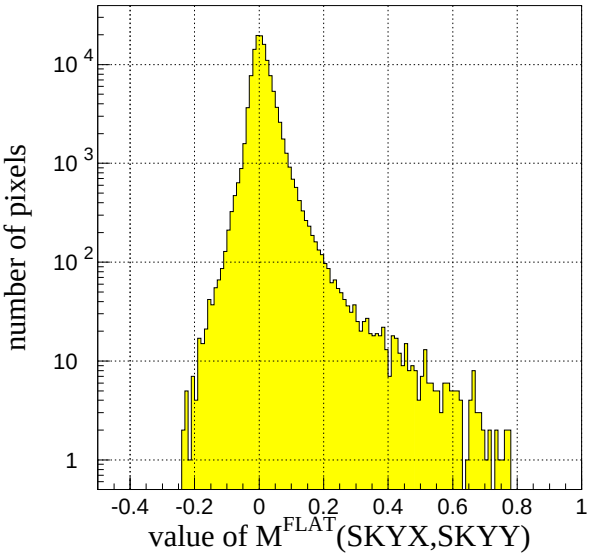

Figure 7.7:
Distribution of pixel values in figure 7.6.

the effective area of the XRT. Since this normalization factor does not make the CXB image appear flat, B^{UCXB} must be evaluated in advance using M^{RATIO}, and subtracted from B^{OBS} when calculating M^{FLAT}.

7.2.4 Source-masking

In order to remove the point sources thus detected, we decided to mask the regions centered on the point sources within an *appropriate* radius depending on the source flux, because a brighter source affects a wider region around it than a fainter source. To do this, we have created the sky coordinate images called source-mask which is utilized to mask out the point sources. In the source-mask, the pixels to be removed is set to 1.0, whereas other pixels are set to 0.0. We then generate the CXB spectra and responses without point sources, in reference to the source-masks.

It is an important issue how to set the *appropriate* radius for each point source. Since our aim is to study the properties of the CXB without point sources brighter than a certain level, we have chosen the mask radius to be r_{mask} where surface brightness B_i^{PS} created by the i-th point source gets less than 3% of the unresolved CXB (B^{UCXB}). Figure 7.8 shows an example of the azimuthally averaged XRT+GIS PSF. Although the XRT+GIS PSF has slight energy- and offset-angle-dependences (figure 4.2), they matter little for the present purpose. The observed radial profile of the PSF can be roughly expressed by a double exponential, as seen in figure 7.8. Therefore, we have calculated the masking radius r_{mask} by a formula:

$$0.03 \times 116.5 \times \frac{\alpha\, N^{\overline{CXB}}}{N^{RAW}} = 528.5\ \exp(-0.96\, r_{mask}) + 4.95\ \exp(-0.16\, r_{mask}), \quad (7.11)$$

where N^{RAW} and $N^{\overline{CXB}}$ are the pixel values of M^{RAW} and $M^{\overline{CXB}}$ in equation (7.9),

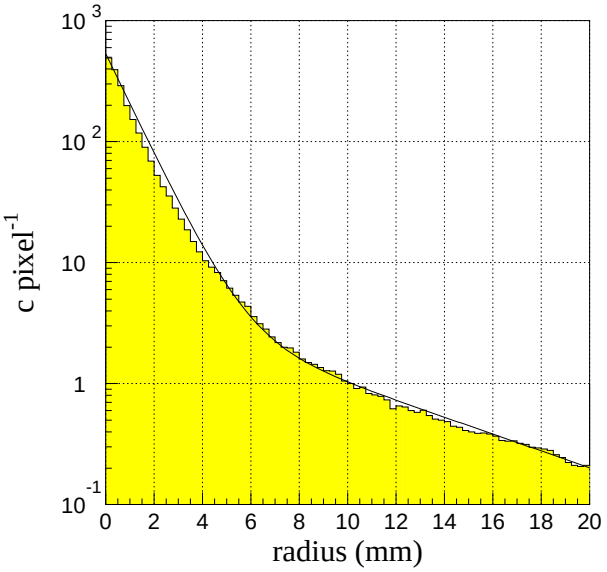

Figure 7.8: Hatched histogram shows a radial profile of 8′ offset Cyg X-1 image taken by GIS2 in the 5–6 keV energy band after the $ccf\Big[B\Big]$ operation. Smooth solid line superposed on the histogram shows the function of $f(x) = 528.5\ \exp(-0.96\ x) + 4.95\ \exp(-0.16\ x)$. The peak pixel counts of the original image (before ccf) was 116.5.

respectively, at $(SKYX, SKYY)$ where the point source was detected. We also set the minimum value of r_{mask} as 3 mm.

We have applied this masking for every pixel of M^{FLAT} that exceeds the threshold level of 0.1. As mentioned in the previous section, a point source detection usually occurs in a cluster of pixels, especially for the bright sources. Therefore, multiple masks are usually applied for a single image peak on M^{FLAT}, which is in most cases caused by a single point source. However, since the function for the PSF radial profile gets flatter as the radius gets larger, r_{mask} is expected to be the largest at the peak position among the single cluster of pixels that exceed the threshold level.

We show the source-mask for the LSS observations in figure 7.9. There are many masked regions near the edge of the image, which probably result partially from insufficient statistics. However, we utilize only the events inside 20 mm from the optical axis, so that most of these pixels are originally discarded from the spectral analyses.

Figure 7.9: The source-mask for the entire LSS observations. White and black pixels correspond to 0.0 and 1.0, respectively.

7.3 Threshold flux of the source-masks

We have set the threshold value at 0.1 on the M^{FLAT} map. However, the actual source flux corresponding to this level has remained uncertain. We therefore discuss the threshold flux level in this section.

We carried out the source-finding with the GIS image only in the 0.7–7.0 keV energy band, and as a result, the spectral information has been lost. Therefore, some assumptions on the spectral parameters are required when we attempt to convert the peak value on M^{FLAT} into the source flux. Fortunately, there is a point source-list available by Ueda (1996) in the LSS field. This LSS source-list contains all the point sources which have been detected with the ASCA GIS above 4σ significance, and detailed studies have been carried out in Ueda (1996). Source fluxes and errors in the list have been determined by image fitting.

The primary reason why we have not utilized the LSS source-list itself is that we also deal with fields other than LSS, so that we have to construct ourselves the method of source-finding and source-elimination in all the fields analyzed here. We, however, conducted our analyses in cooperation with Ueda and our source-finding method is a modified version of his method. The major difference is that he searched point sources by the threshold significance, while we searched sources by the threshold flux and masked them out regardless of their significances. His method is optimized to study detected point sources, whereas our method is optimized to study the remaining CXB. We believe our method to eliminate point sources is one of the best choices for the purpose of studying the remaining CXB, over the different fields with different exposures. There is also a merit of utilizing the by-product images like M^{FLAT} and $M^{\overline{CXB}}$, which also provide us important information on the CXB. However, we have not determined the actual source fluxes nor source positions while creating the source-mask, as described in §7.2.4. We only masked out the pixels where the contribution of the bright point sources is likely to be large. On the other hand, Ueda has determined the source fluxes and source positions by the method of image fitting, after finding a point source candidate. In the image fitting, he left the CXB base level free, so that there was some risk of the base level being affected by the point sources in the f.o.v. He also determined the photon index of the detected point source through spectral fitting in five energy bands, although it has a large error. Therefore, below we compare our source-finding results with the Ueda's source-list.

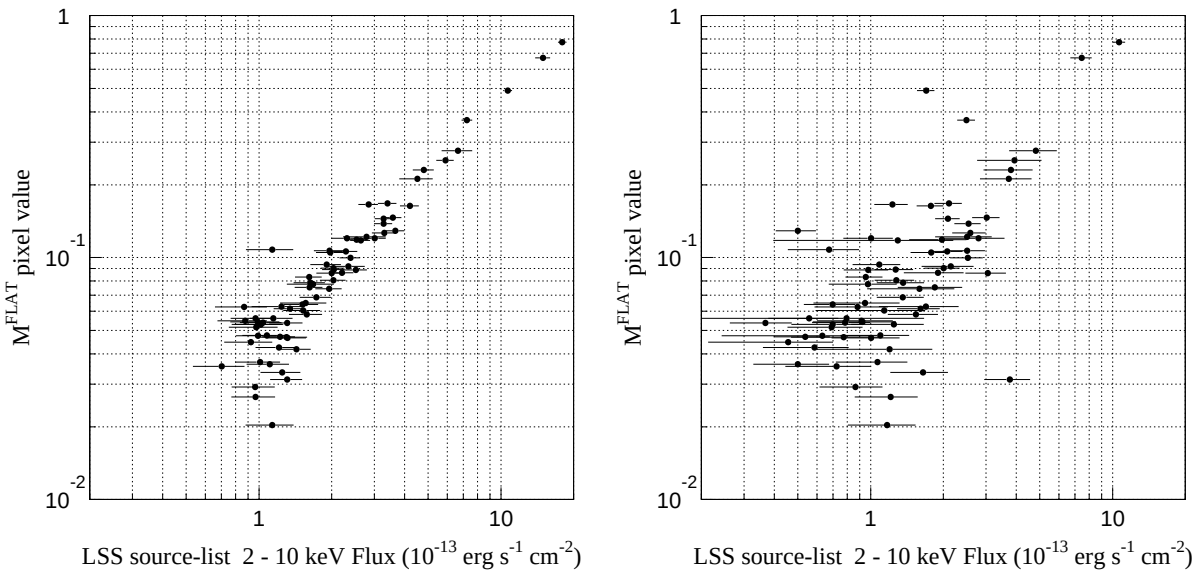

Figure 7.10: Correlation between the source flux in the 2–10 keV energy band listed by Ueda (1996) vs. the pixel value of $M^{FLAT}(SKYX, SKYY)$ from our analysis at each source position. The source-list flux plotted on left panel assumes $\Gamma = 1.7$. On right panel, photon index is derived from the five-energy-band spectrum fitting by Ueda (1996).

In figure 7.10, we plot the pixel value of our $M^{FLAT}(SKYX, SKYY)$ at each source position against the source flux in the 2–10 keV energy band, for all 72 sources in the LSS source-list. The source position and the 2–10 keV flux have both been taken from Ueda (1996). In left panel where all sources are assumed to have a spectrum of $\Gamma = 1.7$, we can see M^{FLAT} to be in good proportion with the source flux. The threshold level of 0.1 thus corresponds to 2–2.5 $\times 10^{-13}$ erg s^{-1} cm^{-2}. If we assume $\Gamma = 1.4$, the source flux should be multiplied by 1.27, so that the threshold flux increases. However, in right panel where photon index of each source is derived from the five energy band spectrum fitting by Ueda (1996), the correlation becomes rather scattered. This means that it is not easy to clearly state the threshold flux. In the following, we quote $\sim 2 \times 10^{-13}$ erg s^{-1} cm^{-2} as a typical threshold. As for the properties of the detected point sources in the LSS field, Ueda (1996) may be referred to.

7.4 CXB properties of individual fields

7.4.1 Strategy to study individual fields

In §7.2, we have developed a method of eliminating point sources using the whole LSS field as an example, and conformed in §7.3 that this method gives a reasonably well-defined flux threshold in comparison with the more direct flux determination by Ueda (1996). We are now ready to apply the same method to all our sample fields, to carry out field-to-field comparisons of the CXB properties.

This can in practice be done in dual ways. On one hand, we can determine the value of α in equation (7.6) for each field in the same way as has been done for the LSS field in §7.2.2. This will give us information as to how the "CXB base level" varies from field to field. On the other hand, we can derive the spectrum of the unresolved CXB, after applying the source-maskings, for each field. This allows us to evaluate the CXB normalization and slope of each field, and to perform comparison among the sample fields. These two methods should lead to the same conclusion, since they are not independent from each other, but we think it is important to confirm the consistensy between them. Therefore, in §7.4.2, we study the CXB base level as indicated by α, while we take the other direction in §7.4.3. We compare, and further examine, these results in §7.4.5.

7.4.2 Field-to-field variation of the CXB base level

We derived α for each sample field, just in the same way as we evaluate α for the whole LSS field. In calculating M^{RATIO} with equation (7.9) for each field, we used the same B^{UCXB} as derived from the LSS data, because it provides the best-quality CXB

Table 7.2: Fitting results of M^{RATIO} pixel values distribution for each sample field

ID	Name	$\alpha^{\dagger}$	$\sigma_1^{\dagger}$	$\sigma_2^{\dagger}$
1	SA57	0.910 ± 0.006	0.121 ± 0.006	0.156 ± 0.008
2	a-LSS	0.875 ± 0.005	0.149 ± 0.004	0.174 ± 0.008
3	b-LSS	0.855 ± 0.004	0.090 ± 0.010	0.173 ± 0.003
4	c-LSS	0.871 ± 0.006	0.164 ± 0.011	0.186 ± 0.005
5	d-LSS	0.917 ± 0.008	0.163 ± 0.014	0.220 ± 0.007
6	Draco	0.837 ± 0.010	0.153 ± 0.007	0.171 ± 0.014
7	NEP	0.889 ± 0.006	0.099 ± 0.011	0.170 ± 0.006
8	QSF3	0.876 ± 0.004	0.029 ± 0.030	0.130 ± 0.003
9	ZSYS	0.890 ± 0.005	0.136 ± 0.006	0.178 ± 0.005
10	BF	0.908 ± 0.005	0.090 ± 0.016	0.184 ± 0.003
11	Jupitar	0.862 ± 0.010	0.097 ± 0.008	0.165 ± 0.004
12	Arp 220	0.865 ± 0.010	0.183 ± 0.055	0.160 ± 0.004
13	3C368	0.990 ± 0.011	0.087 ± 0.006	0.126 ± 0.003

† The best fit value and 90% confidence level fitting error.

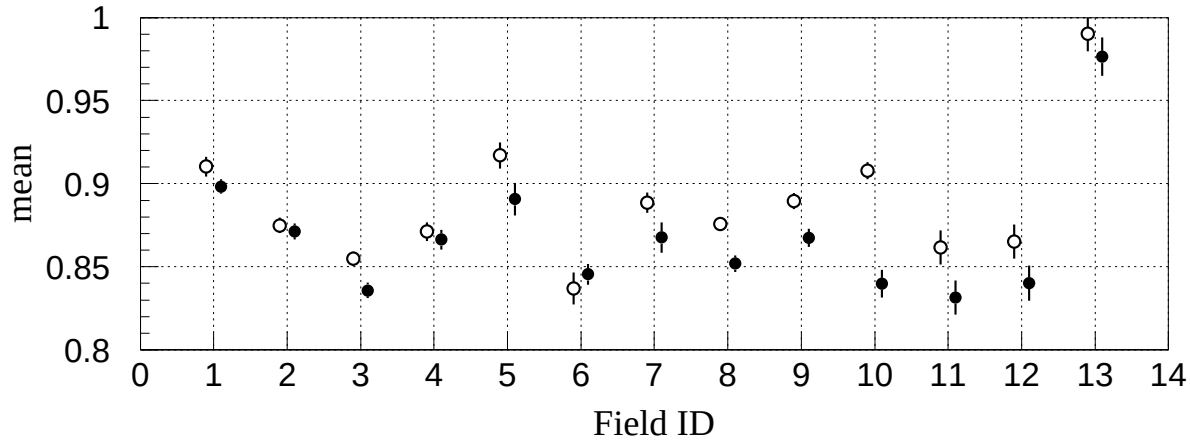

Figure 7.11: CXB base levels (= α) in the 0.7–7.0 keV energy band (open circles), plotted against the field ID. Error bars represent 90% confidence levels. Filed circles represent the results after the point sources have once been excluded at the threshold of 0.1 on M^{FLAT}, and M^{RATIO} was calculated again on the remaining region.

template. We summarize the fitting results in table 7.2. The reason why σ_1 shows a smaller value in QSF3 than other fields is that the distribution was expressed almost only by the second term of equation (7.11), so that the value of σ_1 was effectively unconstrained. As mentioned in §7.2.2, the width of the distribution is determined mainly by the Poisson error and the CXB fluctuation due to the unresolved sources. Since σ_1 and σ_2 in each sample field show similar values with those in LSS, we can say that the statistics of these

sample fields are comparable or better than that in the LSS field.

In figure 7.11, we plot the value of α in each field againt the field ID. For reference, we once again calculated M^{RATIO} of equation (7.9) and re-determined α, using images in which the point sources have been masked out at the threshold of 0.1 on M^{FLAT}. The values of α thus derived from this "second iteration" are shown in figure 7.11 as filled circles. Except the Braccesi Field (ID = 10) where bright sources appear to be abundant, these values of α is not very much different from the original values of α (table 7.2; open circles in figure 7.11) determined by the "first iteration"; the rms difference between two sets of α is only 0.0011. This demonstrates that α is a well defined quantity for each ASCA field analyzed here, and can be confidently identified with the brightness of the unresolved CXB (i.e. CXB "base level"). At the same time, we confirm that our process of the source-finding and source-elimination converges in a single iteration.

In the 3C368 field, α shows apparently a larger value of ~ 1.0. This is probably due to the large soft-excess of the CXB spectrum in this particular field, combined with our method using the single-band brightness. In fact, if we use the 2.0–7.0 keV energy band image instead of the 0.7–7.0 keV image, α in the 3C368 field decreases to 0.90, although statistics gets much worse. Although the Arp 220 field have shown comparable soft-excess with the 3C368 field in §7.1, α in the Arp 220 field is not so large. This suggests that the soft-excess seen in the Arp 220 field is partly due to the Arp 220 itself.

The mean value and standard deviation of α is 0.883 ± 0.025 for the data which have not been processed through the source-maskings (table 7.2). If we remove the data ID = 11–13, α gets 0.881 ± 0.020. Applying the source-maskings and making the second iteration, α becomes 0.864 ± 0.021. This fact implies that the CXB intensity is isotropic by $\sim 2\%$ rms at the 1–2 deg^2 scale, if $\sim 12\%$ of the CXB is resolved by ASCA. Then, could the field-to-field differences of the CXB base level α cause the wrong estimation of the point source fluxes on M^{FLAT}? The 5% difference of the CXB base level α affects the pixel value of M^{FLAT} by ~ 0.002 at the optical axis and by ~ 0.004 at the radius of 20 mm. These are much less compared with the threshold level of 0.1. Therefore, we conclude that the field-to-field variation of the CXB base level does not affect the source-maskings.

As the end of this subsection, we mention whether field-to-field variation of α is significant or not. If we adopt the 1σ error given in table 7.2, χ^2/d.o.f = 144/9 for ID = 1–10, and the variation appears significant. However, as described in §6.4.5, there is the $\sim 3\%$ systematic error for the relative CXB intensity due mainly to the RNXB subtraction. Considering this issue, $\sim 2\%$ variation of α is not significant.

7.4.3 CXB spectra of individual fields excluding point sources

We next examine the second way of comparing the field-to-field CXB properties, i.e. deriving the spectrum of the unresolved CXB after applying the source-maskings. We again made the CXB spectrum of each field, this time masking point sources out by processing the data through the source-masking. We show all the source-masks in appendix C together with the flat-field images M^{FLAT}. The ARFs are also re-created considering the decrease of the integration area on the detector due to the source-maskings. Then we fitted each spectrum individually as we have done in §7.1. The fitting results are summarized in table 7.3. We also show all the spectra in appendix D, together with the best-fit models.

Table 7.3: ($PL^{\rm hard}$+$PL^{\rm soft}$) fits to the 0.6–10 keV spectrum of each field masking point sources at the threshold of 0.1 on M^{FLAT}. All errors are 90% confidence level. $\Gamma^{\rm soft}$ is fixed to 6.0.

ID	Name	Exp.†	Area‡	$N_{\rm H}^{\sharp}$	χ^2/d.o.f	$\Gamma^{\rm hard}$	$F_{\rm X}^{\rm hard\triangleleft}$	$F_{\rm X}^{\rm soft*}$
1	SA57	461,343	0.59	1.0	70.5/67	1.378 ± 0.019	5.83 ± 0.09	1.33 ± 0.15
2	a-LSS	119,221	1.73	1.1	96.2/67	1.459 ± 0.036	5.61 ± 0.17	0.76 ± 0.29
3	b-LSS	130,206	1.78	1.1	71.7/67	1.441 ± 0.035	5.83 ± 0.17	1.19 ± 0.30
4	c-LSS	138,641	1.88	1.1	66.8/67	1.458 ± 0.035	5.57 ± 0.16	1.26 ± 0.28
5	d-LSS	127,324	1.29	1.1	55.1/67	1.485 ± 0.045	5.64 ± 0.21	0.96 ± 0.37
6	Draco	57,002	0.63	4.1	86.4/67	1.473 ± 0.052	5.32 ± 0.23	1.53 ± 0.40
7	NEP	118,434	0.41	4.2	73.1/67	1.393 ± 0.042	5.50 ± 0.19	1.78 ± 0.30
8	QSF3	60,157	0.33	1.7	46.4/67	1.393 ± 0.050	6.31 ± 0.26	1.25 ± 0.42
9	ZSYS	109,893	1.16	2.3	26.8/67	1.500 ± 0.043	5.56 ± 0.20	0.68 ± 0.35
10	BF	114,738	0.82	1.2	102.5/67	1.546 ± 0.041	5.60 ± 0.20	0.13 ± 0.25
11	Jupiter	20,389	0.28	2.1	70.9/67	1.576 ± 0.097	4.98 ± 0.39	1.06 ± 0.77
12	Arp 220	23,039	0.37	4.2	72.0/67	1.377 ± 0.078	5.75 ± 0.36	5.00 ± 0.68
13	3C368	19,934	0.33	9.8	92.2/67	1.480 ± 0.082	6.14 ± 0.40	4.92 ± 0.76

† Total exposure time (s).

‡ Integration area (deg^2) on the sky after applying the source-maskings (threshold 0.1).

♯ Absorption for $PL^{\rm hard}$ (10^{20} cm^{-2}) from Einstein On-line Service (*EINLINE*). Fixed while fitting.

◁ Flux of $PL^{\rm hard}$ (10^{-8} erg s^{-1} cm^{-2} str^{-1}) in the 2–10 keV energy band.

* Flux of $PL^{\rm soft}$ (10^{-8} erg s^{-1} cm^{-2} str^{-1}) in the 0.5–2 keV energy band.

Except the Braccesi Field, the $PL^{\rm hard} + PL^{\rm soft}$ models are accepted at the 99% confidence level. Particularly the fit to the NEP spectrum has been improved. To clearly show the difference of each parameter, we plot $\Gamma^{\rm hard}$, $F_{\rm X}^{\rm hard}$, and $F_{\rm X}^{\rm soft}$ against the field ID in figure 7.12 in comparison with the results obtained in §7.1 without eliminating point sources. We also plot these parameters when very strict source-maskings at the threshold

of 0.06 (appendix E) were applied. In most fields except the d-LSS and NEP field, $\Gamma^{\rm hard}$ did not change significantly by applying the source-maskings. $F_{\rm X}^{\rm hard}$ decreased according to the masked sources, and the variation has become smaller. We will discuss in detail this field-to-field variation of the CXB parameters in the following subsections.

When the source-maskings are applied, the systematic error of the XRT effective area mentioned in §6.4.4 become more influencial, because the ARF response utilized for the spectrum fitting was generated individually for each field. Therefore, we tried fitting each spectrum with the modified XRT response as described in §6.4.4. However, fitting results did not change significantly, and we thus concluded that the systematic error of the XRT effective area was not severe at the threshold of 0.1.

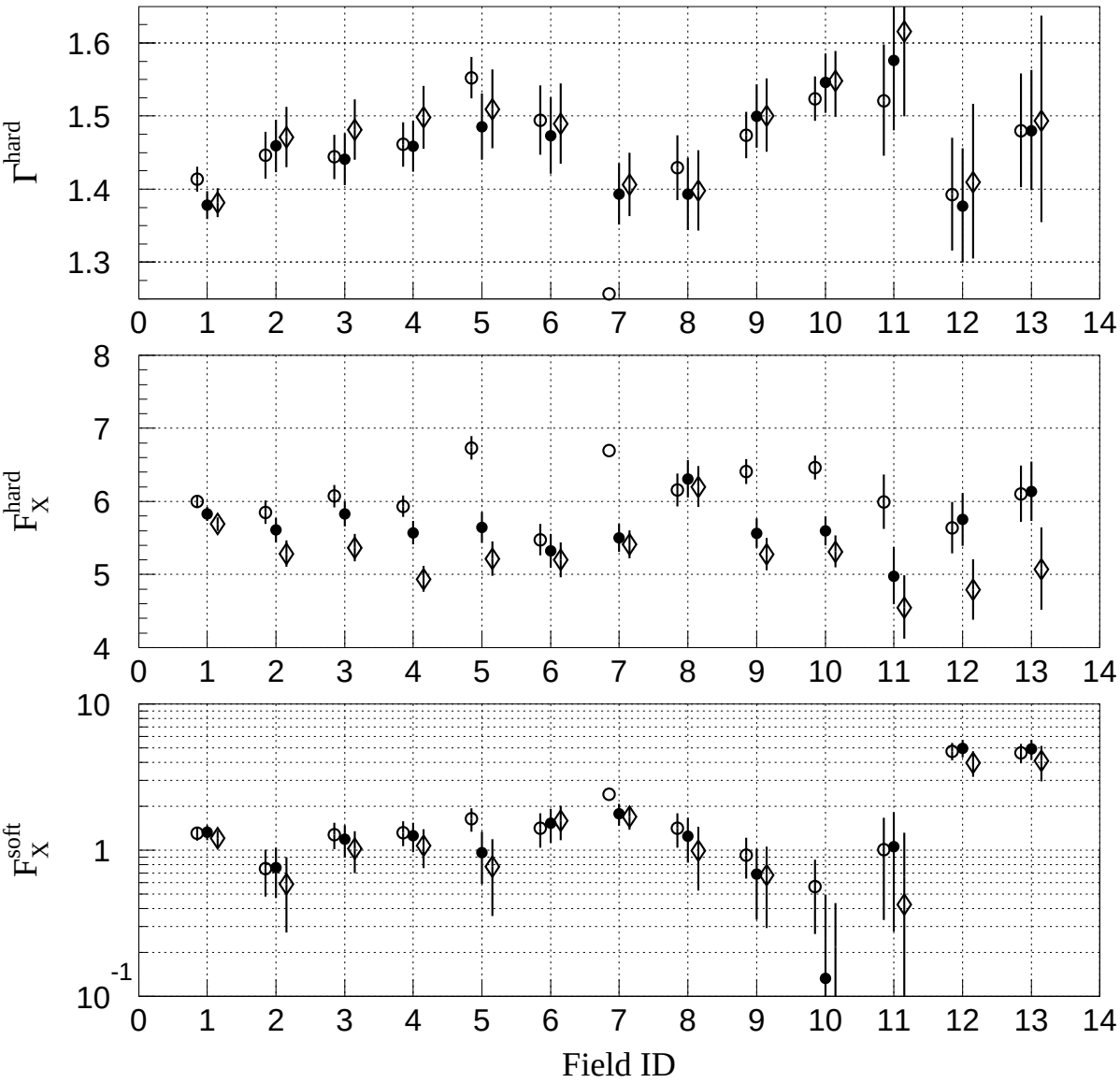

Figure 7.12: $\Gamma^{\rm hard}$, $F_{\rm X}^{\rm hard}$ (2–10 keV), and $F_{\rm X}^{\rm soft}$ (0.5–2 keV) of table 7.1 (no source-masking; open circles), table 7.1 (threshold 0.1; filled circles), and table E.1 (threshold 0.06; diamonds), plotted against the field ID. Error bars represent 90% confidence level.

7.4.4 Field-to-field variation of $\Gamma^{\rm hard}$

Table 7.4: Mean values and standard deviations of $\Gamma^{\rm hard}$, $F_{\rm X}^{\rm hard}$, and $F_{\rm X}^{\rm soft}$.

Source Mask	ID	$\Gamma^{\rm hard}$			$F_{\rm X}^{\rm hard}$			$F_{\rm X}^{\rm soft}$		
		$\mu^\dagger$	$\sigma^\ddagger$	χ^2/d.o.f$^\triangleleft$	$\mu^\dagger$	$\sigma^\ddagger$	χ^2/d.o.f*	$\mu^\dagger$	$\sigma^\ddagger$	χ^2/d.o.f*
None$^\sharp$	1–13	1.461	0.047	185 (21)/11	6.10	0.30	291 (34)/11	1.30	0.66	473 (440)/11
		1.44	—— fixed ——		6.10	0.42	1924 (57)/10	1.42	0.69	777 (658)/10
	1–10	1.461	0.047	175 (16)/8	6.11	0.30	277 (29)/8	1.20	0.29	88 (71)/8
		1.44	—— fixed ——		6.11	0.42	1821 (42)/7	1.32	0.40	246 (176)/7
0.10	1–13	1.435	0.055	188 (34)/12	5.69	0.22	132 (31)/12	1.20	0.78	611 (553)/12
		1.44	—— fixed ——		5.67	0.21	436 (29)/12	1.24	0.67	685 (621)/12
	1–10	1.434	0.053	166 (23)/9	5.70	0.19	98 (16)/9	1.10	0.45	197 (154)/9
		1.44	—— fixed ——		5.67	0.19	367 (17)/9	1.12	0.25	91 (70)/9
0.06	1–13	1.443	0.060	185 (33)/12	5.41	0.31	241 (48)/12	0.98	0.65	399 (339)/12
		1.44	—— fixed ——		5.43	0.20	358 (40)/12	1.12	0.51	355 (314)/12
	1–10	1.442	0.058	168 (24)/9	5.44	0.29	191 (28)/9	0.94	0.50	228 (172)/9
		1.44	—— fixed ——		5.45	0.17	258 (17)/9	1.06	0.31	124 (97)/9

† Weighted mean, i.e., $\mu = \sum_i \frac{y_i}{\sigma_i^2} \,/\, \sum_i \sigma_i^{-2}$. ‡ Standard deviation, i.e., $\sigma^2 = \sum_i \frac{(y_i-\mu)^2}{\sigma_i^2} \,/\, \sum_i \sigma_i^{-2}$.

$^\triangleleft$ The number in parentheses is χ^2 considering the systematic error of 0.03.

* The number in parentheses is χ^2 considering the systematic error of 3%.

* The number in parentheses is χ^2 considering the systematic error of 0.05.

$^\sharp$ NEP is excluded due to the inappropriate fit. BF is further excluded when $\Gamma^{\rm hard}$ is fixed to 1.44.

Firstly, we examine the variation of $\Gamma^{\rm hard}$. As seen in figure 7.12, $\Gamma^{\rm hard}$ of each field does not change significantly by applying the source-mask except NEP. This means that $\Gamma^{\rm hard}$ is not sensitive to the masked-out sources.

In table 7.4, we summarize the mean values, standard deviations, and χ^2/d.o.f of field-to-field $\Gamma^{\rm hard}$ in various conditions, together with those of $F_{\rm X}^{\rm hard}$ and $F_{\rm X}^{\rm soft}$. These χ^2 given in table 7.4 are those when examined against a constant model, i.e., $\chi^2 = \sum_i \frac{(y_i-\mu)^2}{\sigma_i^2}$. According to this table, $\Gamma^{\rm hard} \sim 1.44 \pm 0.06$ (mean value and standard deviation, respectively), when the source-maskings are applied. The nominal χ^2 values are very large, and even taking into account the systematic error of $\Gamma^{\rm hard} \sim 0.03$ due to the RNXB subtraction (ref. §6.4), χ^2/d.o.f = 34/12 for ID = 1–13, and χ^2/d.o.f = 23/9 for ID = 1–10. Therefore, the variation of $\Gamma^{\rm hard}$ is significant at the 99% confidence level. Particularly, high value of $\Gamma^{\rm hard} \sim 1.5$ in BF, ZSYS, and d-LSS, and low values of $\Gamma^{\rm hard} \sim 1.4$ in SA57, QSF3, and NEP are outstanding. However, it is a little too hasty to conclude that we have found the field-to-field variation of $\Gamma^{\rm hard}$. There is a possibility

that other systematic errors, such as that of the XRT effective area, are causing the $\Gamma^{\rm hard}$ variation, although χ^2 decrease only by $\sim$ 1.0 with the modified XRT response (ref. §6.4.4). It is also possible that the source-eliminations are imperfect, even though we have strictly masked out point sources by 3% level (ref. §7.2.4), and $\Gamma^{\rm hard}$ is rather insensitive to the process of source-masking, as mentioned above. One particular concern is that in BF, ZSYS, and d-LSS, where $\Gamma^{\rm hard}$ are high and the decreases in $F_{\rm X}^{\rm hard}$ by applying the source-maskings are large, most of masked-out bright sources are softer than the average CXB (ref. appendix F), whereas in NEP, where $\Gamma^{\rm hard}$ is low and the decrease in $F_{\rm X}^{\rm hard}$ is large, there exists NGC 6552 which has a very hard spectrum. Considering these issues, we conservatively state that the field-to-field variation of $\Gamma^{\rm hard}$ by $\pm$0.06 is marginal.

We next investigate the correlation between $\Gamma^{\rm hard}$ and $F_{\rm X}^{\rm hard}$. In figure 7.13, we plot $F_{\rm X}^{\rm hard}$ against $\Gamma^{\rm hard}$, for three levels of the source-maskings. There appears to exist a positive correlation for (a), while there appear to exist negative correlations for (b) and (c), although all three are at the marginal levels. The possible positive correlation seen in figure 7.13 (a) is due mainly to BF, ZSYS, and d-LSS, where $\Gamma^{\rm hard}$ are high (steep) and there exist very bright, softer sources as mentioned above. Therefore the positive correlation suggested in (a) is a natural consequence of the field selection, and its disappearance in (b) and (c) can be explained as a result of the source-elimination. On the contrary, the negative correlations for (b) and (c) are explained to originate as an artifact of the spectral fitting. In figure 7.14, we show the confidence contours of $\Gamma^{\rm hard}$ vs. $F_{\rm X}^{\rm hard}$ for figure 7.13b (threshold 0.1). The best fit value of each field is scattered in a similar direction as the individual confidence contours are elongated. Therefore, the possible correlations between $\Gamma^{\rm hard}$ and $F_{\rm X}^{\rm hard}$ seen in figure 7.13 (b) and (c) are not significant.

7.4.5 Field-to-field variation of $F_{\rm X}^{\rm hard}$

Secondly, we examine the variation of $F_{\rm X}^{\rm hard}$. As we apply the progressively severer source-maskings. $F_{\rm X}^{\rm hard}$ decrease according to the masked sources. Although $F^{\rm hard}$ is corrected for the decrease in the integration area through the ARFs, the decrease of $F_{\rm X}^{\rm hard}$ should be still roughly proportional to the decrease of the integration area on the sky, because the masked area contains point sources and the area is larger if the source is brighter. In figure 7.15, we plot the remaining fraction of $F_{\rm X}^{\rm hard}$ against that of the integration area. As we expected, there is an apparent correlation between these two, which indicates that point sources have surely been eliminated. Although $F_{\rm X}^{\rm hard}$ in QSF3 is little affected by the source-maskings, this is probably explained by the fact that the masked-out sources in QSF3 (the brightest one is identified as a star with $kT \sim 0.9$ keV

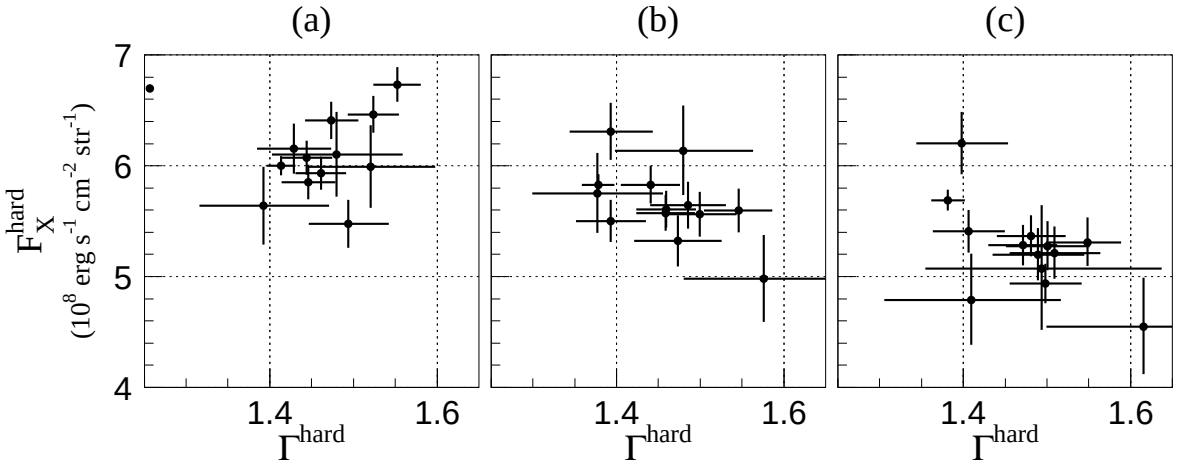

Figure 7.13: Correlations of $\Gamma^{\rm hard}$ vs. $F_{\rm X}^{\rm hard}$ (2–10 keV) in each sample field for (a) no source-masking, (b) after processed through the source-maskings at the threshold of 0.1, and (c) after processed through the source-maskings at the threshold of 0.06. Error bars represent the 90% confidence levels independently derived for $\Gamma^{\rm hard}$ and $F_{\rm X}^{\rm hard}$.

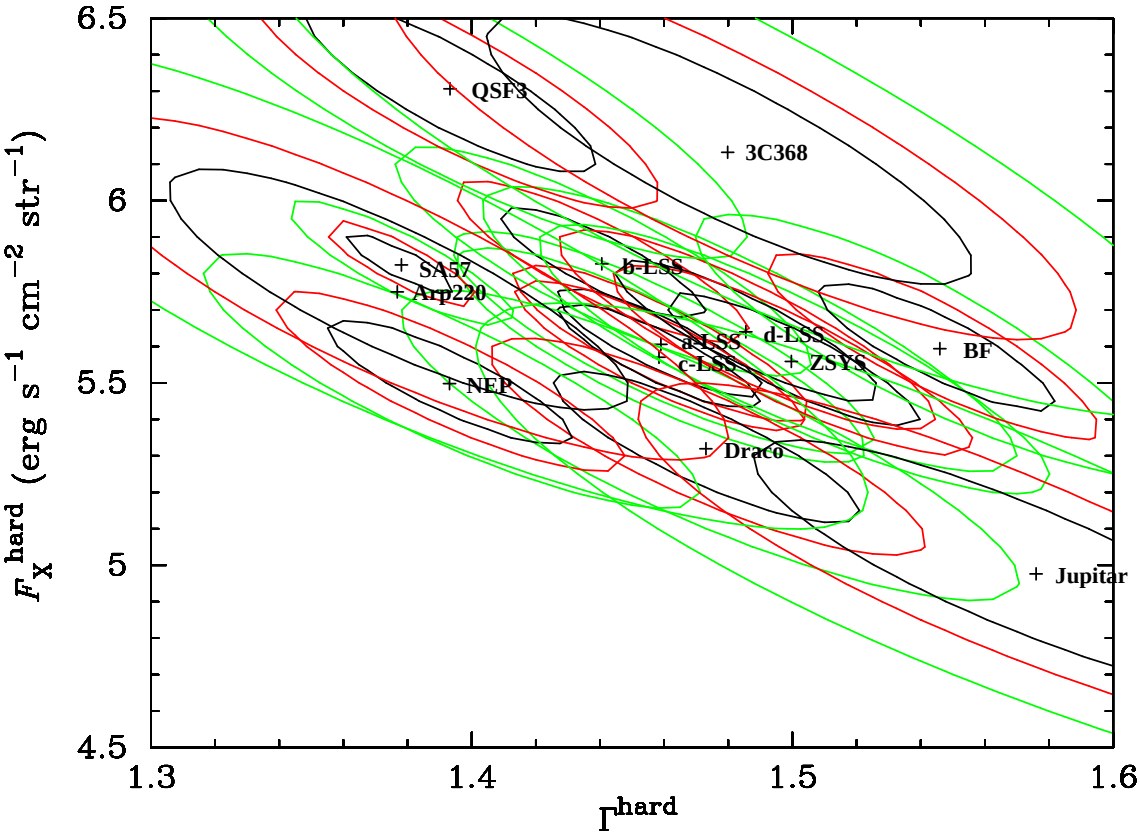

Figure 7.14: Confidence contours of $\Gamma^{\rm hard}$ vs. $F_{\rm X}^{\rm hard}$, in each sample field after processed through the source-masking at the threshold of 0.1. Contours (from inner to outer) represent 68, 90 and 99% confidence levels. Crosses show the best fit position in the labeled fields.

in Chen et al. 1995; ref. §5.2.5) have considerably soft spectra, so that elimination of those sources have reduced only $F_{\rm X}^{\rm soft}$.

By applying the source-maskings at the threshold of 0.1 on M^{FLAT}, the mean value and standard deviation of $F_{\rm X}^{\rm hard}$ have become $(5.69 \pm 0.22) \times 10^{-8}$ erg s^{-1} cm^{-2} str^{-1}, as given in table 7.4. If we remove the data ID = 11–13, $F_{\rm X}^{\rm hard}$ gets $(5.70 \pm 0.19) \times$

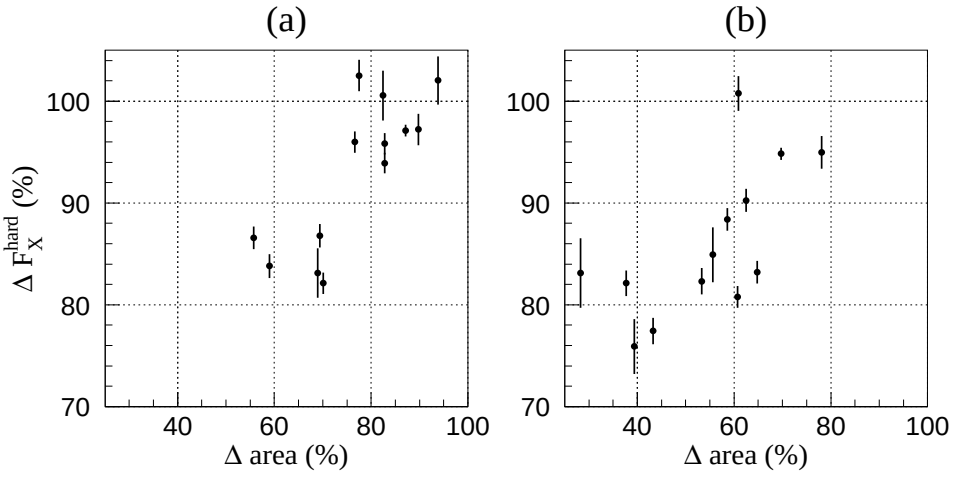

Figure 7.15: The remaining fraction (%) of $F_{\rm X}^{\rm hard}$ plotted against the remaining fraction (%) of the integration area on the sky in each sample field, for (a) after processed through the source-maskings at the threshold of 0.1 and (b) at the threshold of 0.06. Both (a) and (b) are relative ratios to those with no source-masking.

10^{-8} erg s^{-1} cm^{-2} str^{-1}. Thus the field-to-field relative 1σ variation of $F_{\rm X}^{\rm hard}$ is reduced to 3.4%, at the level where $\sim 7\%$ of the CXB is resolved into discrete sources. If we further reduce the threshold down to 0.06, the standard deviation of $F_{\rm X}^{\rm hard}$ again increased to 0.29×10^{-8} erg s^{-1} cm^{-2} str^{-1}. However, this is due partly to the increase of the systematic and statistical errors, which makes it difficult to determine accurate value of $\Gamma^{\rm hard}$. The threshold level of 0.06 is rather too strict especially in low exposure fields, and more than half the integration areas are lost in such fields. As a result, the effect of the systematic error in the XRT effective area, as well as the statistical errors, have become severer. Since the field-to-field variation of $\Gamma^{\rm hard}$ is marginal as described in the previous section, we fixed $\Gamma^{\rm hard}$ to 1.44 in order to reduce the effect of the systematic and statistical errors. We show the fitting results in figure 7.16. By fixing $\Gamma^{\rm hard}$, the field-to-field variation is reduced to 0.17×10^{-8} erg s^{-1} cm^{-2} str^{-1} at the threshold of 0.06, which supports our considerations above.

Taking into account the systematic error of 3% (ref. §6.4.5), we obtain χ^2/d.o.f = 31/12 for ID = 1–13, and χ^2/d.o.f = 16/9 for ID = 1–10. Therefore, the assumption of constant $F_{\rm X}^{\rm hard}$ is acceptable at the 95% confidence level for the latter case. However, there must exist the field-to-field variation of $F_{\rm X}^{\rm hard}$ due to statistical fluctuations of the number of faint unresolved sources in the f.o.v. (§2.2), as far as the CXB is significantly contributed by a superposition of faint point sources. We will discuss this fluctuation level in chapter 8.

On the other hand, we may utilize the observed $\pm3.4\%$ rms relative variation in $F_{\rm X}^{\rm hard}$ to evaluate the maximum allowed fluctuation in the CXB brightness. Let I_0 be the average 0.7–10 keV CXB brightness, and δI be its intrinsic rms fluctuation on the angular scale of

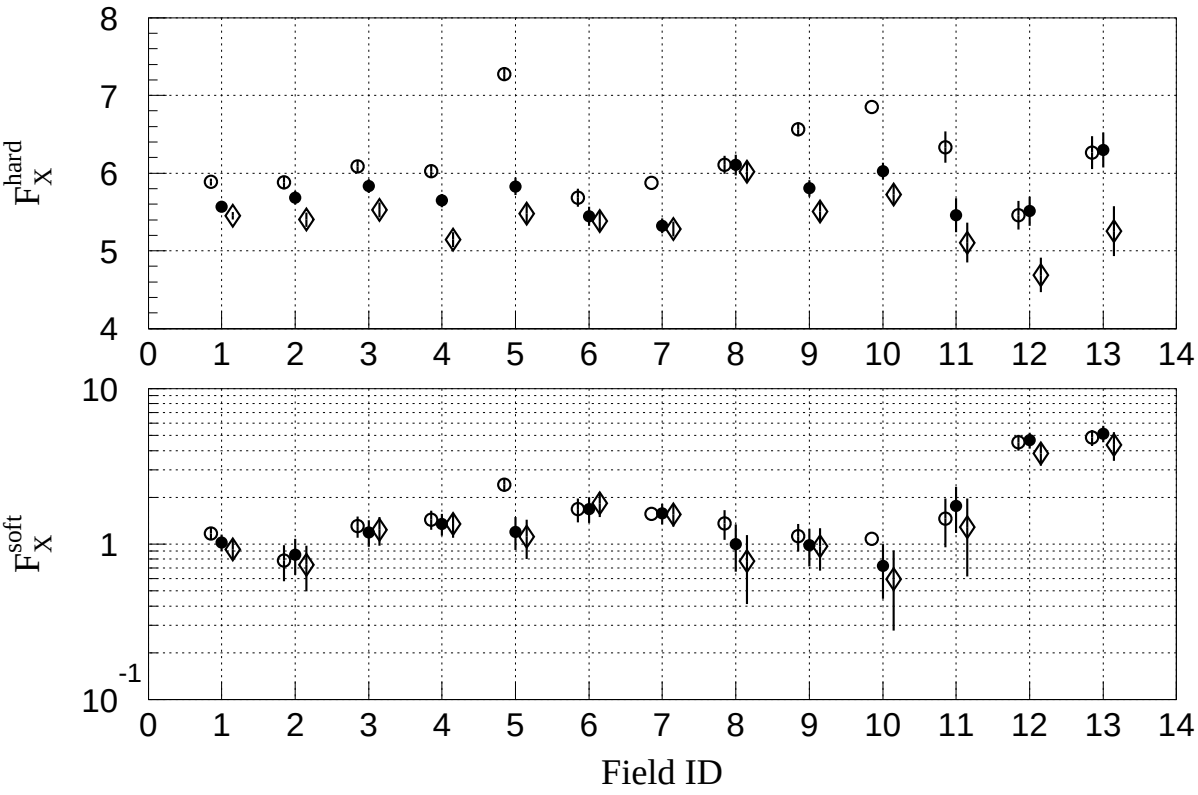

Figure 7.16: Same as middle and lower panels in figure 7.12, but $\Gamma^{\rm hard}$ are fixed to 1.44.

$\sim 1^\circ$. Then, at the 90% confidence level, we can reject the possibility that our 10 sample fields are derived from population with $\delta I/I_0 > 0.092$. In other words, the intrinsic rms fluctuation of the 0.7–10 keV CXB brightness should be less than 9.2% of I_0 on the $\sim 1^\circ$ angular scale, when we remove discrete X-ray sources with 2–10 keV fluxes exceeding $\sim 2 \times 10^{-13}$ erg s^{-1} cm^{-2}.

As described in §7.4.1, it is also important to confirm the consistensy between $F_{\rm X}^{\rm hard}$ and α in equation (7.6) as the CXB base level. We therefore plotted α of each sample field against $F_{\rm X}^{\rm hard}$ derived under several conditions in figure 7.17. There certainly appears to exist a positive correlation between α and $F_{\rm X}^{\rm hard}$, although it is not definite since the variations themselves of these parameters are marginal. Again, QSF3 occupies a little peculiar positions in these correlations; it has a large $F_{\rm X}^{\rm hard}$ of $\sim 6\times10^{-8}$ erg s^{-1} cm^{-2} str^{-1} even after processed through the source-maskings, while its value of $\alpha = 0.88$ is not so high. This is probably because $F^{\rm hard}$ put more weights on the regions where exposure is deep due to vignetting or overlap of the multiple observations, whereas α essentially deals with every pixel on M^{RATIO} equally. We point out that there appear to exist three or four point sources with $\sim 0.5 \times 10^{-13}$ erg s^{-1} cm^{-2} in the central region of QSF3, which have not been masked out by the source-maskings.

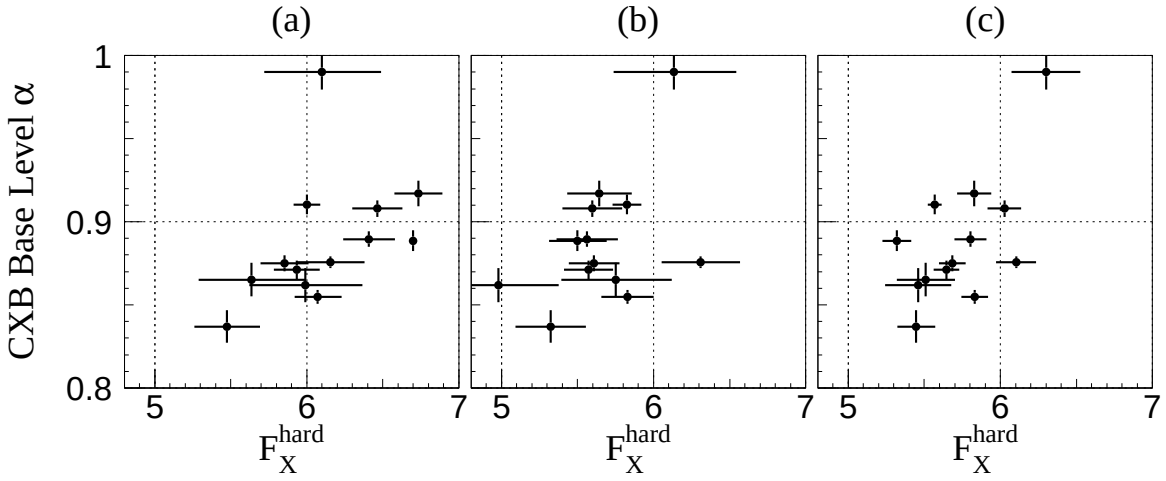

Figure 7.17: The CXB base level α without the source-maskings, plotted against $F_{\rm X}^{\rm hard}$ for (a) no source-masking with $\Gamma^{\rm hard}$ left free, (b) after processed through the source-maskings at the threshold of 0.1 with $\Gamma^{\rm hard}$ left free, and (c) after processed through the source-maskings at the threshold of 0.1 with $\Gamma^{\rm hard}$ fixed to 1.44. Error bars represent the 90% confidence levels independently derived for α and $F_{\rm X}^{\rm hard}$.

7.4.6 Effects of the soft component

Lastly, we examin the variation of $F_{\rm X}^{soft}$ and its possible effect on the hard component. The field-to-field variation of $F_{\rm X}^{\rm soft}$ is quite significant, even though considering the systematic errors. Particularly, the soft-excess in the Arp 220 and 3C368 fields is evident. As described in §7.4.2, the soft-excess in the Arp 220 field can be partly due to the Arp 220 itself, but the soft-excess still remains after processed through the source-masking at the threshold of 0.06, where Arp 220 is masked out. Even excluding ID = 11–13 (Jupiter, Arp 220, and 3C368), χ^2/d.o.f shows huge value and the field-to-field variation of $F_{\rm X}^{\rm soft}$ is still significant, which suggests that the soft component of the CXB is in large part of the Galactic origin. There also appear to exist a positive correlation between $F_{\rm X}^{\rm soft}$ and the absorption column $N_{\rm H}$. There is a possibility that the absorption to the hard component ($PL^{\rm hard}$) has artificially created the soft-excess. As described in §6.4.2, $F_{\rm X}^{\rm soft}$ is affected by a factor of ~ 1.6, if we change $N_{\rm H}$ by 4×10^{20} cm^{-2}. Therefore, we cannot reject the possibility that the mis-estimations of $N_{\rm H}$ have caused the field-to-field variability of $F_{\rm X}^{soft}$ for ID = 1–10, but at least the large soft-excesses in the Arp 220 and 3C368 fields are real.

As we apply the source-maskings, significant decreases of $F_{\rm X}^{\rm soft}$ were seen in d-LSS, QSF3, and BF. This is because there are bright soft sources in these fields, e.g. NGC 5098 in d-LSS and a star in QSF3, as already mentioned in preceding subsections. In the Braccesi Field, $F_{\rm X}^{\rm soft}$ is low, and consistent with 0.0 when source-maskings are applied.

However, this is due partly to the large $\Gamma^{\rm hard} \sim 1.55$ in BF when $\Gamma^{\rm hard}$ is left free. As seen in figure 7.16, $F_{\rm X}^{\rm soft}$ is not so small if $\Gamma^{\rm hard}$ is fixed to 1.44, compared with that in figure 7.12. Therefore, $F_{\rm X}^{soft}$ is affected by the hard component to some considerable degree. Then, how about the opposite direction? Does mis-modeling of the soft component affects the fitting parameters of $PL^{\rm hard}$? This is probably negligible, we believe. As described in §6.3, $\Gamma^{\rm hard}$ is affected only by ~ 0.015 whether we choose the power-law model or Raymond-Smith model as the soft component. The absorption column difference of $N_{\rm H} = 4 \times 10^{20}$ cm^{-2} affects $\Gamma^{\rm hard}$ by similar level, although it affects $F_{\rm X}^{\rm soft}$ by a factor 1.6. In figure 7.18, we plotted $F_{\rm X}^{\rm hard}$ against the parameters of $PL^{\rm hard}$. These distributions are scattered and particular correlations are not seen.

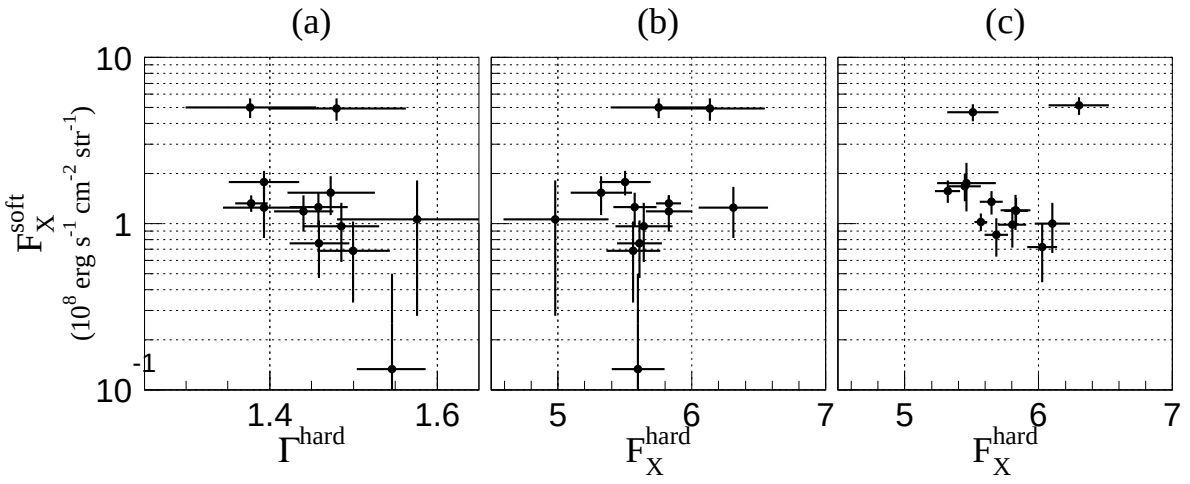

Figure 7.18: $F_{\rm X}^{\rm hard}$ of each sample field plotted against (a) $\Gamma^{\rm hard}$, (b) $F_{\rm X}^{\rm hard}$ with $\Gamma^{\rm hard}$ left free, and (c) $F_{\rm X}^{\rm hard}$ with $\Gamma^{\rm hard}$ fixed to 1.44. All of them are processed through the source-maskings at the threshold of 0.1. Error bars represent the 90% confidence levels independently derived for $F_{\rm X}^{\rm hard}$, $\Gamma^{\rm hard}$, and $F_{\rm X}^{\rm hard}$.

7.5 Average CXB spectra excluding point sources

In this section, we return to the average CXB spectrum of the whole LSS, and examine its behavior by applying the source-maskings. We also created the CXB spectrum of the best statistics (total CXB spectrum) by summing up the SA57, LSS, Draco, NEP, QSF3, ZSYS, and BF spectra, after processed through the source-maskings at the threshold of 0.1. However, this total CXB spectrum is quite biased to the SA57 field which have comparable exposure with the whole LSS. Therefore, we only utilize it to examine the possible spectral features in the CXB spectra. We also remark that the integration time of the total CXB (1,437 ks) has already exceeded that of the night-earth data (1,202 ks), which we utilize to estimate RNXB (ref. §4.4.4). Therefore, the statistical error of each spectrum bin in the total CXB spectrum is dominated by RNXB, especially in higher energy bands.

In table 7.5, we summarize the fitting results for the average CXB spectra of the

Table 7.5: ($PL^{\rm hard}$+$PL^{\rm soft}$) fits to the 0.6–10 keV spectrum of the total CXB (SA57+LSS+Draco+NEP+QSF3+ZSYS+BF) and the whole LSS. All errors represent 90% confidence levels.

Name	Mask$^{\diamondsuit}$	Exp.†	Area‡	$\chi^{2\sharp}$	$\Gamma^{\rm hard}$	$F_{\rm X}^{\rm hard\triangleleft}$	$\Gamma^{\rm soft}$	$F_{\rm X}^{\rm soft*}$
ALL*	0.10	1,436,959	9.19	104.7	1.439 ± 0.017	5.85 ± 0.07	6.3 ± 0.6	1.34 ± 0.23
				105.5	1.432 ± 0.013	5.86 ± 0.07	6.0 fix	1.23 ± 0.10
				106.6	1.44 fix	5.82 ± 0.03	6.0 fix	1.19 ± 0.08
LSS*	None	515,392	7.22	105.7	1.486 ± 0.021	6.14 ± 0.09	6.4 ± 0.8	1.40 ± 0.14
				106.5	1.479 ± 0.021	6.14 ± 0.02	6.0 fix	1.27 ± 0.14
				122.4	1.44 fix	6.33 ± 0.04	6.0 fix	1.49 ± 0.11
	0.10	515,392	5.24	102.0	1.465 ± 0.027	5.66 ± 0.10	6.5 ± 1.1	1.19 ± 0.16
				102.5	1.458 ± 0.020	5.68 ± 0.09	6.0 fix	1.06 ± 0.16
				104.7	1.44 fix	5.75 ± 0.05	6.0 fix	1.15 ± 0.12
	0.06	515,392	3.90	101.8	1.481 ± 0.039	5.22 ± 0.11	5.7 ± 1.5	0.84 ± 0.33
				101.9	1.486 ± 0.023	5.22 ± 0.10	6.0 fix	0.89 ± 0.18
				112.7	1.44 fix	5.39 ± 0.05	6.0 fix	1.11 ± 0.14

$^{\diamondsuit}$ Source-masking threshold on M^{FLAT}.

† Total exposure time (s).

‡ Integration area (deg^2) on the sky.

$^{\sharp}$ Degrees of free are 100, 101, and 102, respectively, coresponding to the fixed parameters.

$^{\triangleleft}$ Flux of $PL^{\rm hard}$ (10^{-8} erg s^{-1} cm^{-2} str^{-1}) in the 2–10 keV energy band.

* Flux of $PL^{\rm soft}$ (10^{-8} erg s^{-1} cm^{-2} str^{-1}) in the 0.5–2 keV energy band.

* Absorption columns are fixed to 2.0×10^{20} cm^{-2} for ALL and 1.1×10^{20} cm^{-2} for LSS.

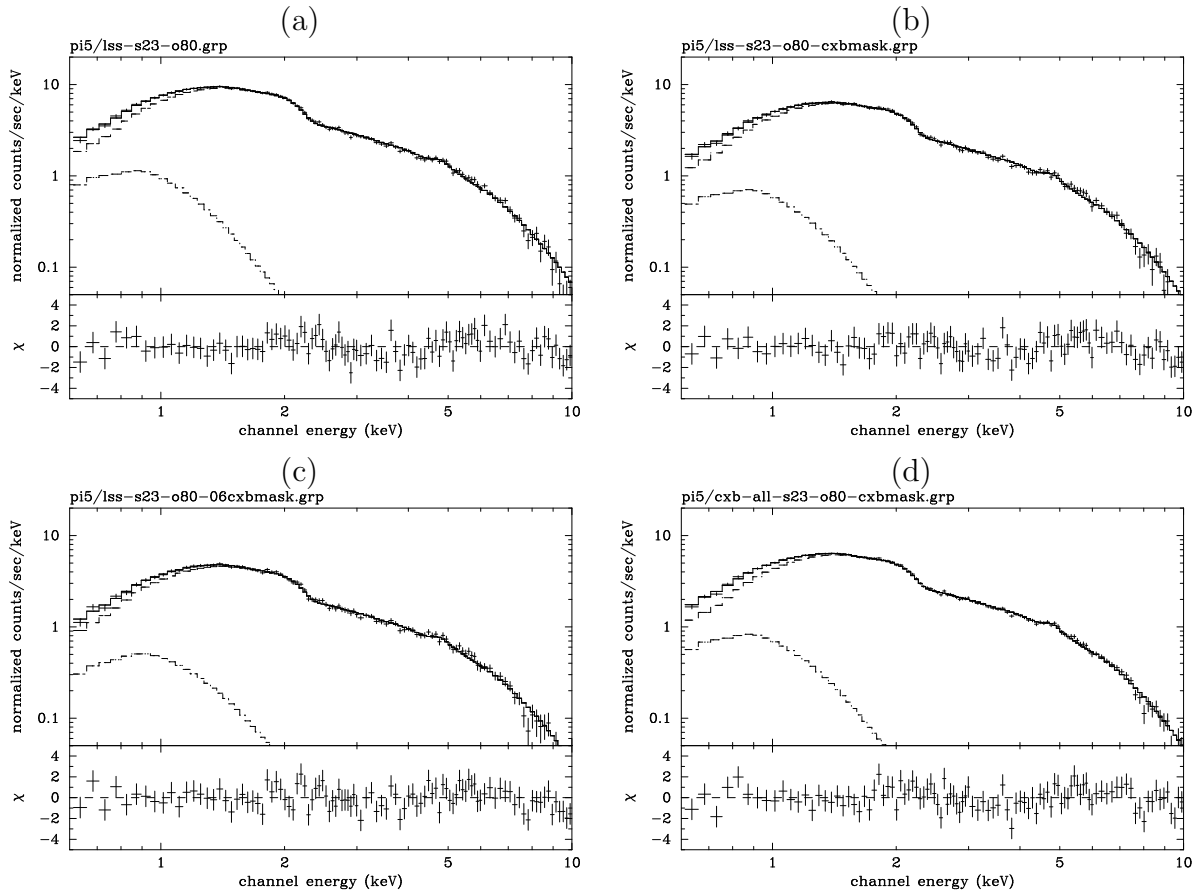

Figure 7.19: Average CXB spectra for (a) LSS with no source-masking, (b) LSS processed through source-masking at the threshold of 0.1, (c) LSS processed through source-masking at the threshold of 0.06, (d) ALL (SA57+LSS+Draco+NEP+QSF3+ZSYS+BF) processed through source-masking at the threshold of 0.10, fitted with the absorbed power-law model in the 0.6–10 keV energy band. The Galactic absorptions are fixed as given in table 7.5, and $\Gamma^{\rm soft}$ are left free. Upper panels show GIS2+3 spectrum (corosses) and the best fit model (solid line). Lower panels show residuals plotted in the unit of σ.

whole LSS at three levels of the source-maskings (no source-mask, threshold 1.0 and 0.06) under three fitting conditions (all free, $\Gamma^{soft} = 6.0$, and $\Gamma^{hard} = 1.44$), together with those of the total CXB spectrum. Each spectrum is shown in figure 7.5. All three models are acceptable for all three (LSS) plus one (ALL) spectra at the 90% confidence level. This indicates that the 0.7–10 keV spectral shape of the average CXB is little modified by the source-elimination brighter than $\sim 2 \times 10^{-13}$ erg s^{-1} cm^{-2} (2–10 keV). The resolved fractions of the CXB into discrete sources, i.e. decreasing fractions of $F_{\rm X}^{\rm hard}$, are 7.5% and 15% corresponding to the processed source-masking threshold of 0.10 and 0.06, respectively. In order to visualize the changes of $F_{\rm X}^{\rm hard}$, we plot the confidence contour of $\Gamma^{\rm hard}$ vs. $F_{\rm X}^{\rm hard}$ for each CXB spectrum on the same plane in figure 7.20. In chapter 8, we will discuss this fraction from the view of the $\log N$-$\log S$ relation (ref. 2.3). The decreasing fractions of $F_{\rm X}^{\rm soft}$ are 23% and 24%, respectively. Although these fractions

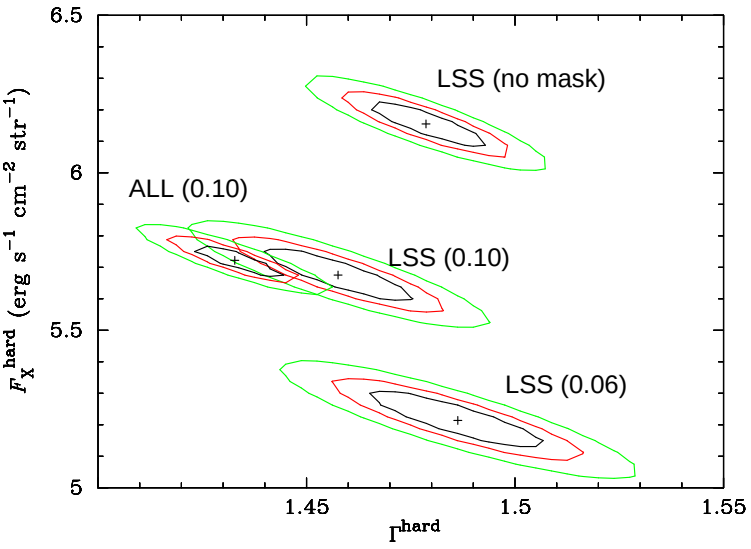

Figure 7.20: Confidence contour of $\Gamma^{\rm hard}$ vs. $F_{\rm X}^{\rm hard}$, for the spectra shown in figure 7.19. The Galactic absorptions are fixed as given in table 7.5, and $\Gamma^{\rm soft}$ are fixed to 6.0. Contours (from inner to outer) represent 68, 90 and 99% confidence levels, and crosses show the best fit position.

are larger than that of $F_{\rm X}^{\rm hard}$, this is due mainly to the bright soft sources in d-LSS (e.g. NGC 5098).

Even summing up all the CXB spectra in our sample fields, the $PL^{\rm hard}$+$PL^{\rm soft}$ model has been acceptable as given in table 7.5; i.e. any other component is not required to explain the CXB spectrum in the 0.7–10 keV energy band. This very flatness of the average CXB spectrum is a remarkable fact. In figre 7.19d, there appears a possible edge-like structure $\sim$ 8 keV, which is due probably to a little over-subtraction of RNXB which contains the 8.04 keV instrumental Cu-K line. We note again that the statistical errors of the estimated RNXB spectrum are dominant in fitting the total CXB spectrum.

Chapter 8

Discussion and conclusion

8.1 Average CXB spectrum

8.1.1 Summary of the observation

In chapter 6, we have studied the average CXB spectrum in the LSS field including point sources. The background (= RNXB; residual non X-ray background) spectrum to be substracted, and the detector response to be convolved to the model were created as described in chapter 4. The 0.6–10 keV CXB spectrum in the LSS field has been successfully fitted with a model consisting of an absorbed ($N_{\rm H} = 1.1 \times 10^{20}$ cm^{-2}) hard power-law model ($PL^{\rm hard}$) of $\Gamma^{\rm hard} \sim 1.5$, plus a soft component expressed by either a steep power-law model ($PL^{\rm soft}$) of $\Gamma^{\rm soft} \sim 6$ or a low-temperature Raymond-Smith model of $kT \sim 0.3$ keV. The soft component is statistically significant only when the data below $\sim$ 1 keV is included. Thus, the spectrum is consistent with a single power law above $\sim$ 1.2 keV. In §6.4, we conducted detailed investigations on the systematic errors using the $PL^{\rm hard} + PL^{\rm soft}$ model, and determined the error regions of the model parameters as:

$$\begin{aligned} \Gamma^{\rm hard} &= 1.486 \quad \pm 0.021 \quad \pm 0.040 \\ F_{\rm X}^{\rm hard} &= 6.14 \quad \pm 0.08 \quad \pm 0.92 \quad (10^{-8} \text{ erg s}^{-1} \text{ cm}^{-2} \text{ str}^{-1};\ \text{2–10 keV}) \\ F_{\rm X}^{\rm soft} &= 1.40 \quad \pm 0.27 \quad \pm 0.22 \quad (10^{-8} \text{ erg s}^{-1} \text{ cm}^{-2} \text{ str}^{-1};\ \text{0.5–2 keV}), \end{aligned} \tag{8.1}$$

where the former error represents the 90% confidence level statistical erorr and the latter represents the systematic errors. The systematic error of $F_{\rm X}^{\rm hard}$ represents the absolute flux uncertainty ($\sim$ 15%), but the relative flux uncertainty is 3%.

In chapter 7, we have developed the method of eliminating point sources brighter than a fixed threshold intensity (source-masking). Utilizing the source-maskings, we created the average CXB spectra in LSS excluding point sources brighter than $\sim 2\times10^{-13}$ erg s^{-1} cm^{-2} (threshold = 0.10) or $\sim 1.2\times10^{-13}$ erg s^{-1} cm^{-2} (threshold = 0.06) in §7.5. We conducted the $PL^{\rm hard} + PL^{\rm soft}$ fit to these spectra with the detector responses corrected for the decrease in the integration region. We could not find any significant spectral changes on

the average CXB spectrum in LSS, although $F_{\rm X}^{\rm hard}$ decreased by 9.2±1.5% and 14.8±1.6% corresponding to the source-masking threshold of 0.10 and 0.06, respectively. We also created the total CXB spectrum, which is the best-statistics CXB spectrum we can obtain, by summing up the spectra in our 10 sample fields after processed through the source-maskings at the threshold of 0.10. Even for this total CXB spectrum, the $PL^{\rm hard} + PL^{\rm soft}$ model was fully acceptable and we could not find any spectral features in the average CXB spectrum. Again, the spectrum above $\sim$ 1.2 keV was essentially consistent with a single power-law.

8.1.2 Comparison with previous observations

In the 3–10 keV energy band, the CXB spectrum has been expressed in a power-law model of $\Gamma = 1.4$ or a thermal bremsstrahlung model of $kT = 40$ keV, as reviewed in §2.1. On the other hand, ROSAT reported steeper ($\Gamma \sim 2.1$) slope in the 0.5–2 keV energy band, yet it may be quite isotropic. In the present thesis, we have obtained much better-quality 0.7–10 keV CXB spectrum in both statistics and energy resolution, owing to the ASCA XRT+GIS.

To make a comparison, we plot the unfolded 0.6–10 keV energy spectra of the average CXB in LSS including point sources, together with those obtained with HEAO-1 A2, Einstein, ROSAT, and ASCA SIS. Although our results show a little steeper photon index of $\Gamma^{\rm hard} \sim 1.49$, it is probably consistent with HEAO-1 A2 results of $\Gamma \sim 1.4$, considering our systematic errors (~ 0.04), the possible field-to-field variation (~ 0.06), and that the Crab photon index obtained with the XRT+GIS seems to be steeper by ~ 0.06 than the generally suggested values (§4.2.5). The absolute flux of the CXB is also consistent with HEAO-1 A2, whose error region of the power-law normalization is 8–11 keV cm^{-2} s^{-1} str^{-1} keV^{-1}.

Our results indicate that $PL^{\rm hard}$ is dominant down to $\sim$ 1.2 keV. Below $\sim$ 1.2 keV, the very steep component of $\Gamma \sim 6$ appears, although its level varies from field to field. Our unfolded spectra somewhat depend on the choice between the power-law or Raymond-Smith model as the soft-component, which is an artifact caused by the process of unfolding. We can constrain almost nothing below $\sim$ 0.7 keV with the ASCA XRT+GIS.

Naturally, comparion between the GIS and the ROSAT PSPC results are of significant interest and of great importance. In figure 8.1, our unfolded spectrum appears roughly consistent with the ROSAT PSPC result, in such a way that the ROSAT slope of $\Gamma \sim 2.1$ is well reproduced by the combination of $\Gamma^{\rm hard} \sim 1.4$ and $\Gamma^{\rm soft} \sim 6$ components. It is however very difficult and misleading to compare these unfolded spectra, because they are affected by the effects so called "obliging"; i.e. the unfolded spectrum tends to obey

the particular model used for the specral deconvolution. Accordingly we make comparion in space of the observed quantities. To do this, we fitted our entire LSS spectrum with a model consisting of two power-laws and a soft Raymond-Smith component. We fixed the second power-law slope to $\Gamma = 2.1$ and the RS temperature to 0.3 keV, both indicated by the ROSAT spectrum. We left the other model paramters all free. We have then found that our spectrum does not require the $\Gamma = 2.1$ component, and the 90% upper limit on its contribution at 1 keV is only 32% of the total flux. We varied the second power-law slope in the range 1.7–2.5, but the conclusion remained essentially unchanged. This indicates that the CXB spectrum obtained with the GIS is actually composed of the hard power-law of $\Gamma \sim 1.4$ and the very steep (probably Galactic) component. Perhaps the sharp spectral break produced by these two distinct components could not be resolved by the ROSAT PSPC, because of the insufficient spectral resolution ($\Delta E/E \simeq 0.45\,E^{-0.5}$). We do not think that this discrepancy is due to the difference in the observed fields between ASCA and ROSAT, since our spectra in most of the sample fields have been fitted well with the two component model.

In figure 8.1, our GIS results are slightly inconsistent with those obtained with the ASCA SIS by Gendreau et al. (1995); note that it is much less dangerous to compare these two in the unfolded form, because the two ASCA instruments have much higher energy resolution than the ROSAT PSPC. The discrepancy is found on the following two points. One is that the GIS slope appears to be steeper than the SIS one, which is fixed to 1.4, by ~ 0.1; this may well be explained by the fact that the SIS results are based on the older version XRT ray-tracing program, which has already been confirmed to give a flatter photon index by $\Gamma \sim 0.1$, and that the SIS low-energy response is subject to a larger uncertainty than the GIS. The other discrepancy is the considerably higher level of the soft comonent indicated by the GIS spectrum, which appears to be significant even considering the mutual instrumetal calibration differences. Given that the soft component exhibit a signficant field-to-field variation, this may be attributed to the difference in the observed field; our sample field is LSS, whereas that of the ASCA SIS is the Lynx Field, Lockman Hole, QSF3, NEP, and Draco Field. To show typical field-to-field variation, in figure 8.2, we plotted the unfolded CXB spectrum from the XRT+GIS, for the LSS, NEP, and ZSYS fields, separately. The spectrum in the ZSYS field well agrees with the SIS spectrum below ~ 2 keV.

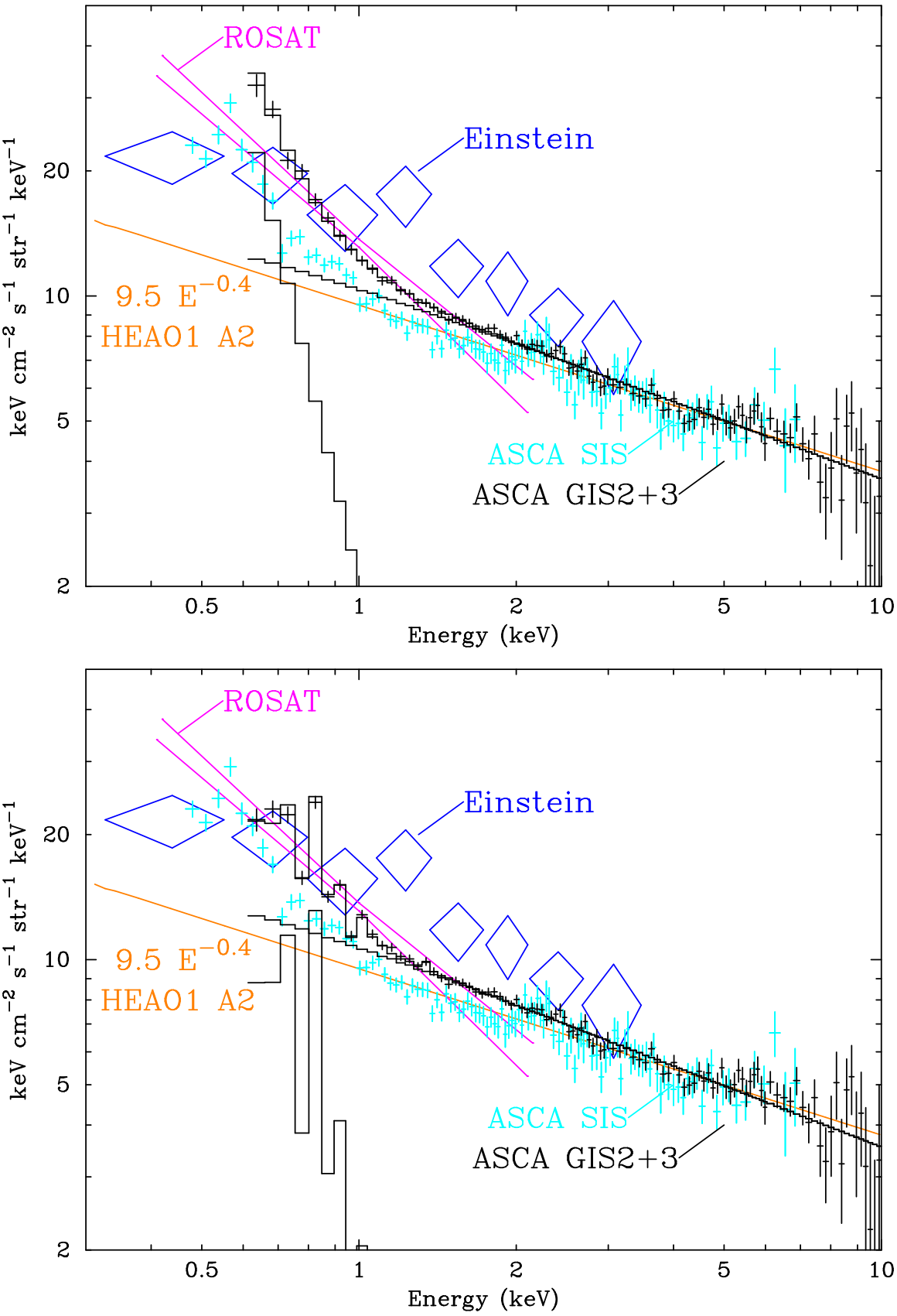

Figure 8.1: Unfolded 0.6–10 keV energy spectra of the average CXB in LSS including point sources. Thick lines and crosses in upper (lower) panel represent the best fit $PL^{\rm soft} + PL^{\rm hard}$ ($RS+PL^{\rm hard}$) model shown in figure 6.5a (figure 6.5b), respectively. Hard- and soft-components are also shown individually in thick lines. Results from ROSAT PSPC (Hasinger 1992), Einstein IPC (Wu et al. 1991), HEAO-1 A2 (Marshall et al. 1980), and ASCA SIS (Gendreau et al. 1995) are overlaied.

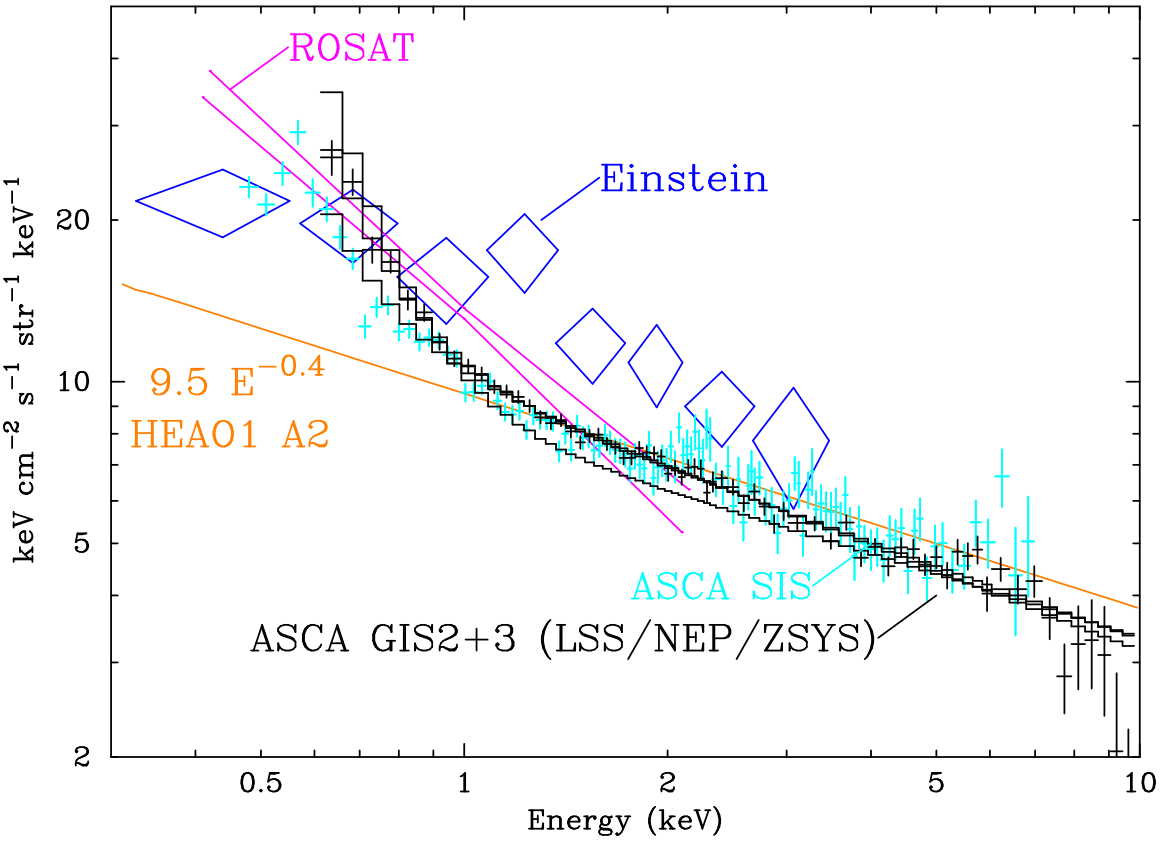

Figure 8.2: Same as upper panel of figure 8.1, except that three GIS spectra in LSS, NEP, and ZSYS after processed through the source-masking at the threshold of 0.10 are instead plotted, separately.

8.1.3 Effects of discrete sources

By applying the source-maskings, we have observed $9.2 \pm 1.5\%$ and $14.8 \pm 1.6\%$ decreases of $F_{\rm X}^{\rm hard}$ in the LSS field, corresponding to the source-masking threshold of 0.10 and 0.06, respectively. We examine these values from the viewpoint of the $\log N$-$\log S$ relation. From the $\log N$-$\log S$ relation, we can estimate the decrease of the CXB flux when we removed the contributions of discrete sources brighter than a certain level. In figure 8.3, we show the $\log N$-$\log S$ relation in the 2–10 keV energy band measured with previous X-ray observations (HEAO-1 A2, Ginga, and ASCA). Although ROSAT reported the deviation from the Euclidian slope below $S \sim 10^{-14}$ erg s^{-1} cm^{-2} (ref. §2.3), most previous results show that the $\log N$-$\log S$ relation above $S \sim 10^{-13}$ erg s^{-1} cm^{-2} is consistent with the Euclidian universe. If we denote $S_{100\%}$ as the source flux where the extension of the Euclidian $\log N$-$\log S$ relation crosses the 100% CXB limit, the fractional contribution to the CXB of discrete sources which is brighter than S is calculated by $\sqrt{S_{100\%}/S}$.

Considering that $S_{100\%}$ derived from the figure 8.3 is $\sim 8 \times 10^{-15}$ and that our source-masking threshold of 0.10 roughly corresponds to 2×10^{-13} erg s^{-2} cm^{-2} (ref. §7.3), the decreases by source-maskings at the threshold of 0.10 and 0.06 are estimated to be 20.0% and 25.8%, respectively. Thus, the observed decreases are much less than these values. This is probably explained by two reasons; that we cannot remove the source flux entering to the f.o.v. as the stray light, and that the brightest discrete soruce we have eliminated in LSS is $2\text{–}3 \times 10^{-12}$ erg s^{-1} cm^{-2}. We can estimate the fraction of the CXB photons which really come from the corresponding sky area within 20 mm centered on the optical axis to be 65% (figure 4.14b), and the fractional contribution of discrete sources brighter than 3×10^{-12} erg s^{-1} cm^{-2} to be 5.2%. Therefore, the expected decrease of the CXB flux is $0.65 \times (20.0 - 5.2) = 9.6\%$ for the source-masking threshold 0.10, and $0.65 \times (25.8 - 5.2) = 13.4\%$ for the source-masking threshold 0.06. These values are consistent with the observed ones.

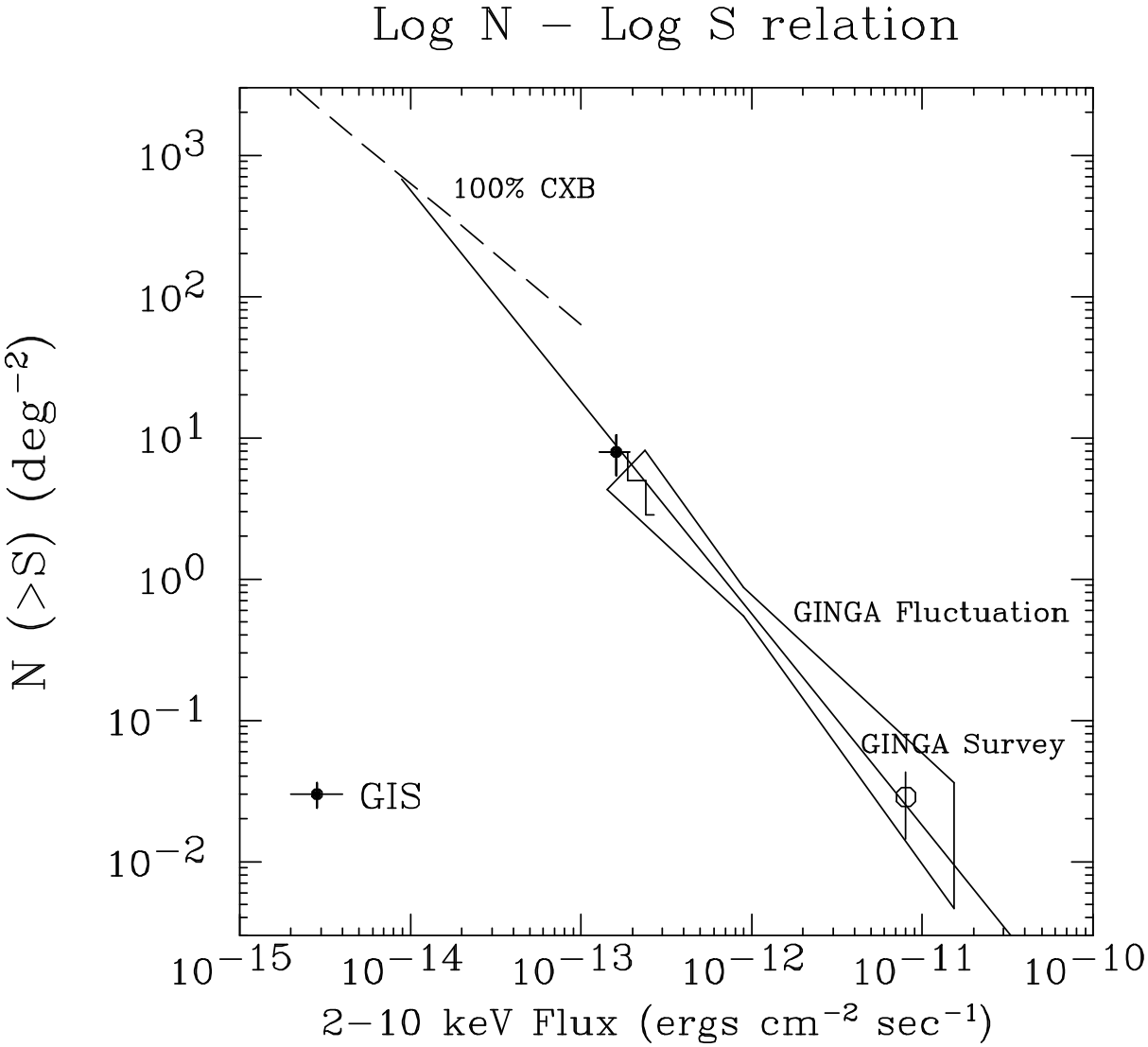

Figure 8.3: The $\log N$-$\log S$ relation in the 2–10 keV energy band. Solid line with a slope of -1.5 represents the extension of the HEAO-1 A2 result expressed in equation 2.5. Dashed line with a slope of -1.0 represents the 100% CXB limit, assuming the CXB intensity as 6.2×10^{-8} erg s^{-1} cm^{-2} str^{-2} (2–10 keV). The 90% confidence contour from Ginga fluctuation analysis (Hayashida 1990), the point from Ginga source survey (Kondo 1991), and the preliminary results from ASCA Large Sky Survey (Ueda, private communication) are overlaid. Photon index of 1.7 is assumed to calculate the flux. This figure is kindly provided by Y. Ueda.

8.1.4 Constraints on the AGN mixture models of the CXB

As reviewed in §2.3.3, it has been suggested that the flat spectrum of the CXB, i.e. $\Gamma \sim 1.4$ in the 2–10 keV energy band, could be explained by the superposition of absorbed sources at different redshifts. The main candidates of the absorbed sources are Seyfert 2 galaxies and similar objects. So far, a number of models are presented to explain the CXB by mixing the Seyfert 1 and Seyfert 2 galaxies (AGN mixure model). For example, we show the calculations by Matt and Fabian (1994) in figure 8.5.

On the other hand, we have determined the CXB spectrum in the $\sim$ 1–10 keV energy band to be almost featureless and well expressed by a single power-law. In figure 8.4, we show our total CXB spectrum plotted in the same fashion as figure 8.5. Comparing these figures, we can immediately reject the models A1, A10, and A16. Taking into account the iron line emissions (dashed lines), the model A17 would be also rejected. When absorbed spectra are subjected to a redshift of $z = 2$–3, a sharp feature by the iron K-edge or the iron line emission appears in the 1–3 keV energy band, as seen in figure 8.5. According to our accurate measurements of the CXB spectrum in the 1–3 keV energy band, the AGN mixure models require more carefull fine-tuning of the parameters.

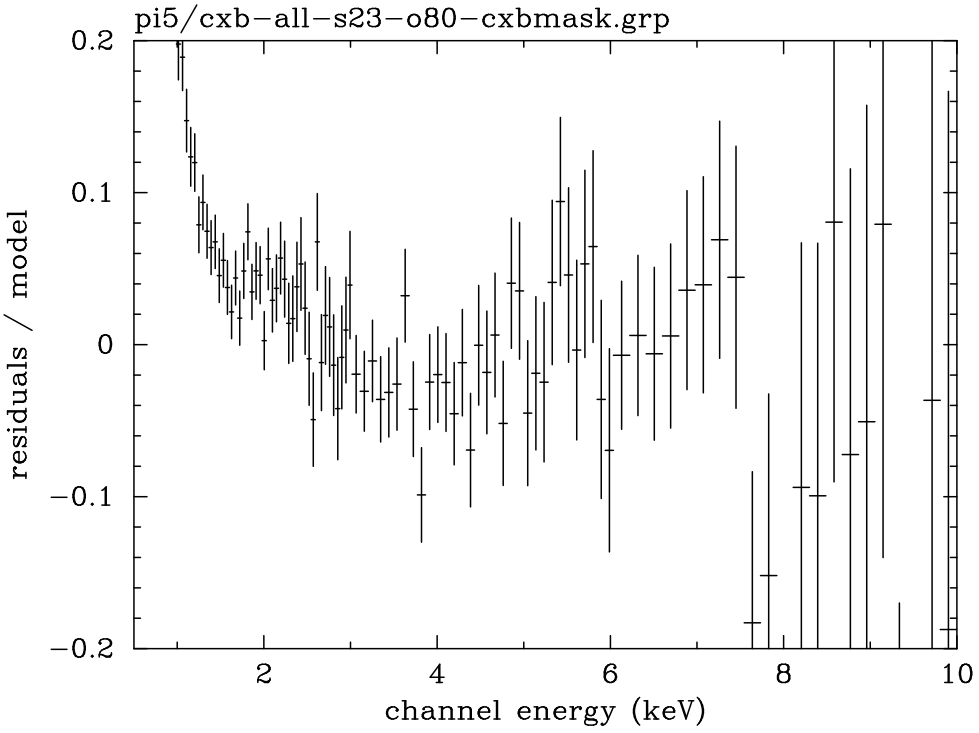

Figure 8.4: The fractional residuals, i.e. (Data − Model) / Model, of the total CXB spectrum shown in figure 7.19d to a power-law of $\Gamma = 1.4$. The data excess just below $\sim$ 2 keV is due partly to the energy resolution ($\sim$ 20% FWHM at 1 keV) of the GIS.

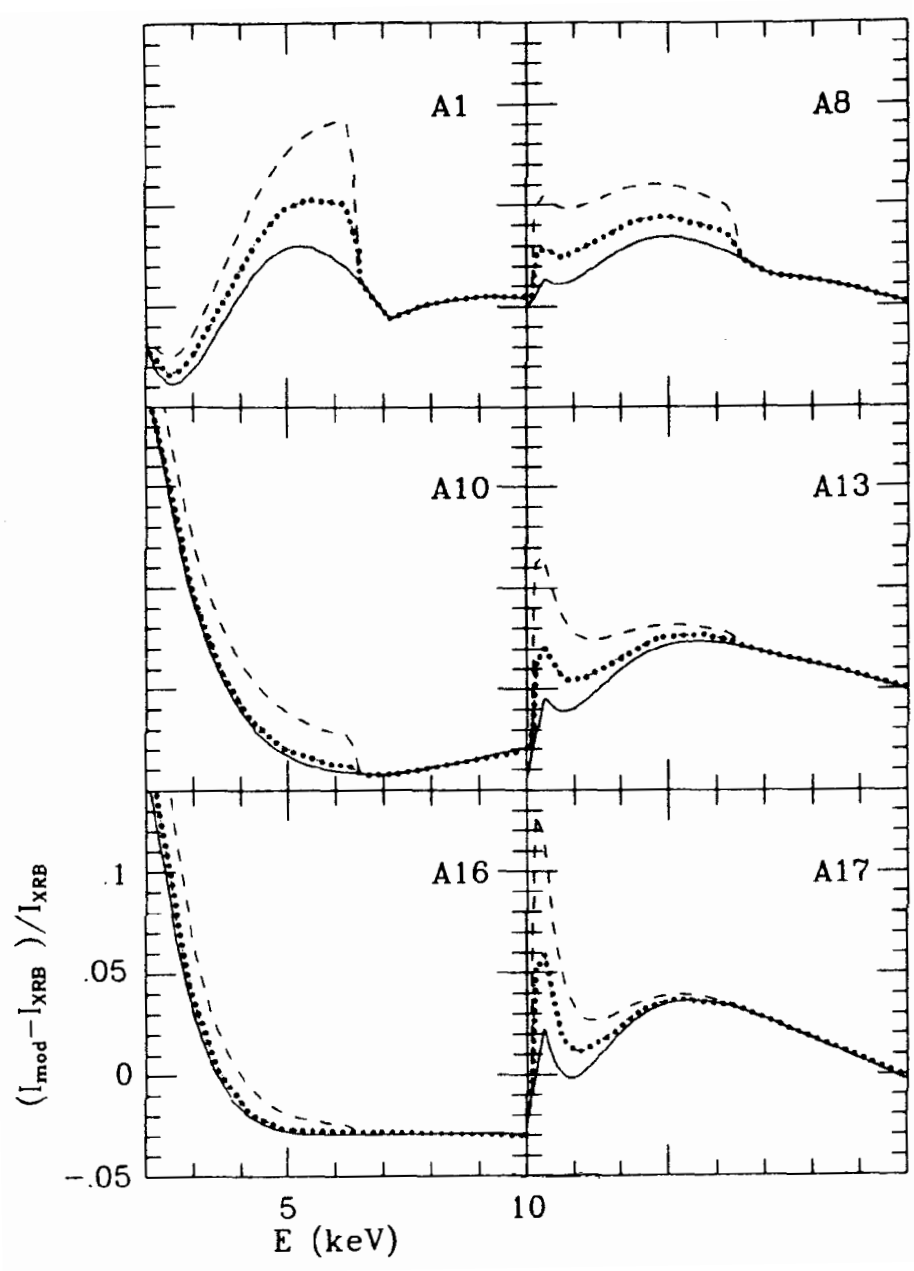

Figure 8.5: The fractional residuals of various Seyfert 1 and Seyfert 2 mixture 2–10 keV CXB spectra to a power-law of $\Gamma = 1.4$, adopted from Matt and Fabian (1994). The solid lines show the model without no line emission. The dotted lines include the iron line emission from the intervening matter, while the dashed lines show the further intrinsic line emission. The fraction of Seyfert 2 galaxies is ranging 0.6–0.8. Seyfert 1 (unabsorbed) and Seyfert 2 (absorbed) are assumed to have the same intrinsic spectrum and evolve in the same way, in terms of the unified model of the AGN (e.g. Antonucci & Miller 1985). The model A1 is the unevolved model, while the evolution of the volume emissivity as $(1+z)^{2.5}$, $(1+z)^{4.5}$ and $(1+z)^{6}$ are assumed for A8/A10, A13/A16, and A17, respectively. The difference between A8 (A13) and A10 (A16) is the lower-limit $N_{\rm H1}$ of the intrinsic absorption; $N_{\rm H1} \sim 10^{23}$ cm^{-2} for A8, A13, and A17, while $N_{\rm H1} = 10^{24}$ cm^{-2} for A13 and A16.

8.2 Field to field fluctuation of the CXB

8.2.1 Summary of the observation

In chapter 7, we have investigated the field-to-field variation of the CXB properties in 13 sample fields each covering the $\sim$ 1–2 deg^2 sky, utilizing the method as we have done to study the average CXB spectrum.

From the spectral fitting of individual fields, the field-to-field rms variation of the 2–10 keV CXB intensity ($F_{\rm X}^{\rm hard}$) was derived to be $\pm$3.4% rms, after processed through the source-maskings at the threshold of 0.10. This level of the CXB intensity fluctuation is consistent with being constant within the systematic errors. Therefore, the intrinsic rms fluctuation of the 2–10 keV CXB brightness should be less than 9.2% (90% confidence level) on the $\sim 1^\circ$ angular scale, when we remove discrete X-ray sources with 2–10 keV fluxes exceeding $\sim 2 \times 10^{-13}$ erg s^{-1} cm^{-2}. The field-to-field variation of $\Gamma^{\rm hard} \sim 0.05$ is likely to be real but marginal, considering the systematic errors. The 0.5–2 keV flux of the soft component ($F_{\rm X}^{\rm soft}$) varies significantly from field to field, which is consistent with the general belief that the X-ray background below $\sim$ 2 keV is anisotropic, due to the Galactic contributions.

We have also examined the field-to-field variation of the CXB brightness by determining the CXB base level (= α) observed with the XRT+GIS. This CXB base level α varies only 2% rms from field to field, which implies that the CXB intensity is isotropic by $\sim$ 2% rms at the 1–2 deg^2 scale, if $\sim$ 12% of the CXB is resolved by ASCA. This result is consistent with the fluctuation of $F_{\rm X}^{\rm hard}$, within the uncertainties of $F_{\rm X}^{\rm hard}$ and α determinations. In particular, the fluctuation of $F_{\rm X}^{\rm hard} \sim 2.8\%$ gets close to that of $\alpha \sim 2.0\%$, when $\Gamma^{\rm hard}$ is fixed to the mean slope of 1.44 at the source-masking threshold of 0.06. It is probably because the determination of $F_{\rm X}^{\rm hard}$ is more weighted on the region where exposure is deep, that the fluctuation of $F_{\rm X}^{\rm hard}$ tends to be larger than that of α. This effect is explained by the larger Ω_e (effective beam size) for α (ref. appendix H).

8.2.2 Comparison with previous measurements

In table 8.1, we summarize previous measurements of the CXB isotropy in the 2–10 keV energy band, as well as our present work. Our distinctive features are much smaller S_c and Ω_e than those of Ginga LAC by about one order of magnitude, although our data sample (= 10) is much smaller than those of HEAO-1 A2 (= 698) or Ginga LAC (= 151). Here, S_c (erg s^{-1} cm^{-2}) represents the upper cut-off flux of the discrete sources in the detector f.o.v., and Ω_e (deg^2) represents the effective beam size (or effective solid angle) of the detector when observing the Euclidian sky (see appendix H for their definitions).

Table 8.1: Summary of the previous results and the present work (ASCA XRT+GIS)

Instrument	HEAO-1 A2[†]	Ginga LAC[‡]	ASCA XRT+GIS
Data	698 sample	151 sample	10 sample
Effective Area	530 cm^2	4,000 cm^2	200 cm^2
Energy Band	2.5–46 keV	2–10 keV	0.6–10 keV
f.o.v.	$3^\circ \times 3^\circ$ with 6° scan	$1^\circ \times 2^\circ$ pointing	$40'$ diameter $\sim 3'$ imaging
Ω_e [a]	15.8 deg^2	1.3 deg^2	0.14 deg^2 / 1 pointing
S_c [b] (erg s^{-1} cm^{-2})	8×10^{-11}	6×10^{-12}	2×10^{-13}
I_{CXB} [c]	13.3 c/s	15–16 c/s	0.25 c/s/GIS2+3
I_{BGD} [d]	3.4 c/s	50–100 c/s	0.12 c/s/GIS2+3
σ_{stat} [e]	0.18 c/s	0.11 c/s	0.003 c/s/GIS2+3
σ_{BGD} [f]	0.28 c/s	0.152 c/s	0.004 c/s/GIS2+3
σ_{CXB} [g]	0.16 c/s	0.9 c/s	$\lesssim$ 0.01 c/s/GIS2+3
σ_{CXB}/I_{CXB}	2.8%	$\sim$ 6%	$\lesssim$ 3.4%

[†] These values are from Shafer (1983). [‡] These values are from Hayashida (1990).

[a] Effective beam size of the detector. See appendix H.

[b] Upper cut-off of the 2–10 keV flux from discrete sources in the f.o.v. See appendix H.

[c] Average CXB counting rate.

[d] Typical intrinsic background (= RNXB) counting rate.

[e] Typical statistical 1σ error to the observed (= CXB+RNXB) counting rate.

[f] Typical 1σ error of the I_{BGD} estimation.

[g] Observed CXB fluctuation, i.e. excess variance of $P(D)$ distribution after subtracting σ_{stat} and σ_{BGD}.

In figure 8.6, we plot the positions of these measurements on the Ω_e-S_c plane. Therefore, we have observed the CXB on smaller scales, with much fainter objects. Such small S_c and Ω_e are mostly owing to the imaging capability of the XRT+GIS and the procedure of the source-masking. In addition, as given in table 8.1, the very low counting rate of the intrinsic background (= RNXB) makes our result reliable.

The value of $\Omega_e = 0.14$ deg^2 for the GIS applies only to one sensor and one pointing without source-masking. We roughly estimate the actual Ω_e for our CXB observations in table 8.2, by multiplying 0.41 to each integration area. This value of 0.41 is the ratio of $\Omega_e = 0.14$ deg^2 to the geometrical integration area of 0.34 deg^2 on the sky corresponding to the 20 mm radius of one GIS f.o.v. As described in appendix H, there is a relation of $(\sigma_{CXB}/I_{CXB}) \propto \Omega_e^{-0.5}\ S_c^{0.25}$, where (σ_{CXB}/I_{CXB}) is the fractional CXB fluctuation due to the statistical fluctuation of the discrete source number in the f.o.v. If we take $\Omega_e = 0.5$ deg^2 as a typical effective solid angle of our observations, we can predict the CXB fluctuation with the XRT+GIS utilizing the HEAO-1 A2 values, as

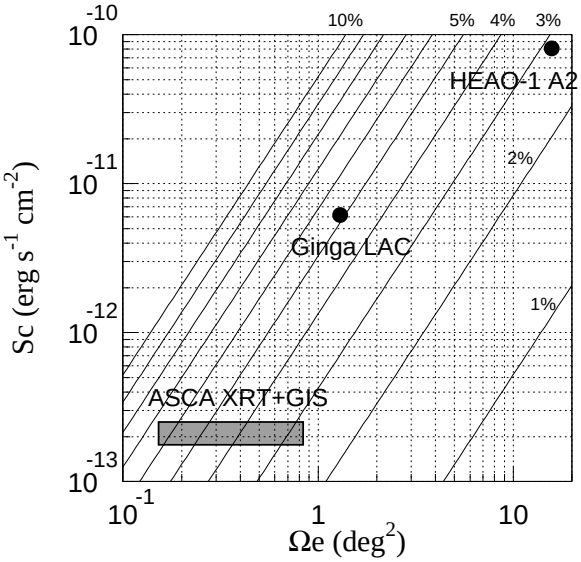

Figure 8.6: Positions of the HEAO-1 A2, Ginga LAC, and ASCA XRT+GIS on the Ω_e-S_c plane. Contours labeled 1%, 2%, ..., 10% represents the expected fractional CXB fluctuation, i.e., σ_{CXB}/I_{CXB}.

Table 8.2: Rough estimations of the effective beam size Ω_e (deg^2) for each CXB observation

ID	Name	No-Mask†	0.10†	0.06†	ID	Name	No-Mask†	0.10†	0.06†
–	LSS	2.94	2.13	1.59	7	NEP	0.24	0.17	0.14
1	SA57	0.28	0.24	0.19	8	QSF3	0.18	0.14	0.11
2	a-LSS	0.85	0.70	0.53	9	ZSYS	0.68	0.47	0.36
3	b-LSS	0.95	0.73	0.55	10	BF	0.60	0.33	0.22
4	c-LSS	0.92	0.77	0.60	11	Jupiter	0.16	0.11	0.06
5	d-LSS	0.89	0.53	0.39	12	Arp 220	0.16	0.15	0.09
6	Draco	0.29	0.26	0.22	13	3C368	0.16	0.13	0.05

† Threshold level of the source-maskings on M^{FLAT}.

$2.8 \times (15.8/0.5)^{0.5} \times (8 \times 10^{-11}/2 \times 10^{-13})^{-0.25} = 3.5\%$, which is fully consistent with our result. This prediction assumes the Euclidian $\log N$-$\log S$ relation with the same normalization on the whole sky, i.e., discrete X-ray sources are distributing uniformly in the whole Euclidian universe. Therefore, this fact, that our CXB fluctuation is consistent with the extension of the HEAO-1 A2 result, implies not only the spatial isotropy of the $\log N$-$\log S$ relation but also that the Euclidian $\log N$-$\log S$ relation extends at least to our S_c flux of $\sim 2 \times 10^{-13}$ erg s^{-1} cm^{-2}. This supports the $\log N$-$\log S$ relation derived from the Ginga fluctuation analysis (Hayashida 1989) and the direct $\log N$-$\log S$ measurement by the ASCA Large Sky Survey (Ueda 1996), which are shown in figure 8.3.

We note here that the calculations conducted above fully takes into account the effects of stray-lights. As described in §H.2, contribution of the stray-lights to Ω_e is expected to be less than 10% of the total Ω_e. This is because the low transmission region in the

f.o.v. produces insignificant source-confusion noise, as expressed by equation (H.5). In other words, there must exist quite bright sources in such region in order to generate a detectable fluctuation, while such bright sources are rare. On the other hand, the stray-lights contributes to the absolute CXB flux as much as by 35%, as mentioned in §8.1.3. Therefore, the stray-lights generally work to reduce (σ_{CXB}/I_{CXB}), although we cannot remove discrete sources from the stray-lights, which works to increase (σ_{CXB}/I_{CXB}).

Appendix A

Log of the observed fields

In table A.3, A.1, and A.2, we show pointing lists of the CXB observations utilized in the present thesis. The observation period, exposure time, Euler angles, and Galactic longitude / latitude of each pointing are given.

Table A.1: Pointing list of the LSS observations in GO-1 and GO-2

No.	Date		Exposure	Euler Angles			Gal.	
	yy/mm/dd	START – END	(sec)	ϕ	θ	ψ	l	b
lss101	93/12/26	10:22 – 17:49	4,770	197.653	59.667	330.298	69.5	84.5
lss102	93/12/26	17:50 – 22:00	4,839	197.458	59.952	330.391	68.0	84.8
lss103	93/12/26	22:00 – 01:50	7,449	197.274	60.244	330.486	66.1	85.1
lss104	93/12/27	01:50 – 10:00	11,159	197.083	60.533	330.578	64.1	85.3
lss105	94/01/04	10:32 – 15:49	3,914	197.316	59.500	330.468	72.7	84.6
lss106	94/01/04	15:50 – 20:22	6,724	197.124	59.791	330.560	71.3	84.9
lss107	94/01/04	20:22 – 02:41	9,165	196.935	60.080	330.653	69.6	85.2
lss108	94/01/05	02:41 – 13:20	5,752	196.751	60.375	330.744	67.7	85.5
lss109	94/01/05	13:21 – 17:42	6,356	197.579	59.439	330.330	71.8	84.4
lss110	94/01/05	17:42 – 23:30	9,119	197.386	59.728	330.432	70.4	84.7
lss111	94/01/05	23:30 – 10:42	8,829	197.200	60.017	330.520	68.7	85.0
lss112	94/01/06	10:43 – 16:00	5,671	197.010	60.309	330.620	66.9	85.3
lss113	94/01/06	16:01 – 20:50	8,149	197.053	59.563	330.598	73.7	84.8
lss114	94/01/06	20:50 – 04:26	10,690	196.862	59.851	330.692	72.3	85.1
lss115	94/01/07	04:26 – 15:29	6,104	196.676	60.147	330.781	70.6	85.4
lss116	94/01/07	15:30 – 19:30	6,305	196.487	60.434	330.871	68.7	85.7
lss201	94/06/16	16:36 – 04:12	7,193	198.548	59.395	150.196	70.7	84.2
lss202	94/06/17	04:12 – 07:42	3,787	198.741	59.101	150.100	72.1	83.9
lss203	94/06/17	07:42 – 10:59	5,032	198.930	58.812	150.001	73.3	83.6
lss204	94/06/17	10:59 – 15:40	3,735	199.114	58.528	149.905	74.4	83.3
lss205	94/06/17	15:40 – 04:10	9,198	199.325	58.239	149.798	75.3	82.9
lss206	94/06/18	04:11 – 07:42	4,324	198.987	58.072	149.976	77.9	83.1
lss207	94/06/18	07:43 – 12:07	2,481	198.793	58.364	150.074	77.0	83.4
lss208	94/06/18	12:07 – 17:10	8,894	198.594	58.649	150.176	76.1	83.7
lss209	94/06/18	17:10 – 04:10	6,415	198.401	58.941	150.273	75.0	84.0
lss210	94/06/19	04:10 – 08:31	5,708	198.210	59.229	150.372	73.8	84.3
lss211	94/06/27	23:12 – 04:04	4,662	198.471	59.163	150.238	72.9	84.1
lss212	94/06/28	04:05 – 08:39	5,312	198.667	58.877	150.135	74.1	83.8
lss213	94/06/28	08:39 – 13:37	7,598	198.863	58.586	150.036	75.2	83.5
lss214	94/06/28	13:37 – 00:48	6,204	199.060	58.299	149.930	76.2	83.2
lss215	94/06/29	00:49 – 05:35	4,932	199.259	58.010	149.832	77.1	82.8
lss216	94/06/29	05:36 – 10:49	6,384	198.721	58.131	150.114	78.8	83.3
lss217	94/06/29	10:51 – 20:25	8,062	198.521	58.424	150.220	78.0	83.6
lss218	94/06/29	20:26 – 02:28	1,482	198.322	58.709	150.324	77.1	83.9
lss219	94/06/30	02:28 – 07:38	5,654	198.863	58.589	150.037	75.2	83.5
lss220	94/06/30	07:38 – 13:20	6,614	197.946	59.290	150.505	74.7	84.5

Table A.2: Pointing list of the LSS observations in GO-3

No.	Date		Exposure	Euler Angles			Gal.	
	yy/mm/dd	START – END	(sec)	ϕ	θ	ψ	l	b
lss301	94/12/25	21:35 – 06:00	7,318	198.212	57.823	330.016	79.8	82.9
lss302	94/12/26	06:01 – 13:25	5,745	198.412	57.541	329.912	80.4	82.6
lss303	95/01/06	08:16 – 14:30	8,271	198.604	57.257	329.815	81.1	82.3
lss304	95/01/07	20:55 – 05:01	9,297	198.804	56.959	329.706	81.7	82.0
lss305	95/01/08	05:02 – 11:10	7,204	199.008	56.673	329.598	82.3	81.6
lss306	95/01/09	10:54 – 12:50	2,864	199.212	56.383	329.491	82.8	81.3
lss307	95/01/09	12:51 – 20:50	6,903	199.278	56.612	329.452	81.5	81.4
lss308	95/01/09	20:51 – 03:20	7,353	199.080	56.906	329.563	80.8	81.8
lss309	95/01/10	03:21 – 08:00	4,733	198.877	57.189	329.665	80.2	82.1
lss310	95/01/10	08:01 – 15:51	10,242	198.677	57.476	329.771	79.6	82.4
lss311	95/01/10	15:52 – 22:20	5,991	198.752	57.708	329.731	78.0	82.5
lss312	95/01/10	22:21 – 04:41	7,796	198.948	57.417	329.623	78.7	82.2
lss313	95/01/11	04:42 – 11:00	9,351	198.481	57.763	329.868	78.9	82.7
lss314	95/01/11	11:02 – 17:21	6,292	199.149	57.128	329.517	79.4	81.9
lss315	95/01/11	17:22 – 23:50	6,268	199.353	56.840	329.408	80.1	81.5
lss316	95/01/11	23:51 – 06:11	8,522	199.553	56.554	329.300	80.7	81.2
lss317	95/01/12	06:12 – 12:40	7,369	198.820	57.934	329.690	76.4	82.6
lss318	95/01/12	12:41 – 19:00	6,040	199.021	57.644	329.585	77.2	82.3
lss319	95/01/12	19:02 – 01:20	7,695	199.224	57.358	329.477	77.9	82.0
lss320	95/01/13	01:20 – 07:50	8,217	199.422	57.068	329.367	78.6	81.7
lss321	95/06/18	16:23 – 02:25	9,119	198.137	58.999	150.414	75.9	84.2
lss322	95/06/19	02:26 – 08:40	7,025	200.118	56.117	149.350	83.2	81.0
lss323	95/06/19	08:40 – 15:11	5,031	200.190	56.346	149.338	81.9	81.1
lss324	95/06/19	15:12 – 23:05	8,769	200.534	56.518	149.145	79.9	81.0
lss325	95/06/19	23:05 – 05:01	7,791	200.328	56.805	149.260	79.2	81.4
lss326	95/07/01	05:03 – 10:30	4,285	200.467	56.290	149.181	81.2	80.9
lss327	95/07/01	10:30 – 17:11	9,490	200.808	56.462	148.996	79.1	80.8
lss328	95/07/02	05:41 – 12:51	7,108	200.196	57.318	149.329	77.1	81.8
lss329	95/07/01	23:21 – 05:40	6,222	200.402	57.032	149.215	77.8	81.5
lss330	95/07/01	17:11 – 23:20	8,683	200.605	56.750	149.106	78.5	81.2
lss331	95/07/05	22:13 – 03:50	4,509	198.234	60.198	150.357	65.1	84.8
lss332	95/07/06	03:50 – 10:09	6,073	198.426	59.913	150.262	66.9	84.5
lss333	95/07/06	10:10 – 16:30	10,526	198.616	59.620	150.165	68.5	84.3
lss334	95/07/06	16:31 – 22:59	9,067	198.811	59.333	150.066	70.0	84.0
lss335	95/07/06	23:00 – 05:20	4,293	199.008	59.046	149.963	71.2	83.7
lss336	95/07/07	05:21 – 11:40	8,216	199.197	58.727	154.868	72.5	83.3
lss337	95/07/07	11:41 – 16:30	7,345	199.396	58.467	149.758	73.6	83.0
lss338	95/07/07	16:30 – 23:00	9,717	199.597	58.180	149.653	74.6	82.7
lss339	95/07/07	23:00 – 05:19	3,444	199.795	57.894	149.548	75.5	82.4
lss340	95/07/08	05:20 – 11:01	6,542	199.994	57.607	149.442	76.3	82.1

Table A.3: Pointing list of the observations

Name	Date		Exposure	Euler Angles			Gal.	
	yy/mm/dd	START – END	(sec)	ϕ	θ	ψ	l	b
SA57	93/12/21	10:25 – 06:50	60,759	196.872	60.660	339.983	64.4	85.5
	93/12/24	13:40 – 10:20	46,211	196.739	60.624	340.035	65.6	85.6
	93/12/28	13:20 – 10:30	95,025	197.012	60.712	339.899	63.1	85.5
	94/01/16	05:12 – 03:25	44,129	196.825	60.782	339.996	63.3	85.6
	94/01/18	03:26 – 01:00	33,820	196.923	60.553	339.949	65.3	85.4
	95/06/02	16:09 – 12:00	181,399	197.586	60.699	138.582	63.8	85.5
Draco	93/06/04	14:13 – 09:10	21,475	256.939	19.289	109.068	102.2	34.2
Field	93/06/05	09:10 – 19:01	10,715	257.587	19.196	108.476	102.3	33.9
	93/06/05	19:02 – 15:35	24,812	258.229	19.096	107.878	102.3	33.7
NEP	93/06/09	23:39 – 10:51	10,691	270.205	23.712	79.027	96.4	29.8
	93/07/20	20:08 – 05:45	16,120	270.588	23.596	117.658	96.4	29.8
	93/10/21	20:58 – 08:10	14,732	270.381	23.196	209.708	96.4	29.8
	94/03/28	08:03 – 20:50	15,235	269.426	23.603	8.028	96.4	29.8
	93/07/02	04:25 – 15:36	13,850	270.025	23.665	100.391	96.4	30.0
	93/08/16	13:44 – 00:35	16,849	270.289	23.500	139.619	96.4	30.0
	93/09/30	05:05 – 17:42	15,301	270.178	23.282	185.975	96.4	30.0
	93/11/16	10:31 – 22:00	15,656	269.593	23.155	240.536	96.4	30.0
QSF3	93/07/11	12:17 – 13:50	24,133	55.283	134.381	39.660	250.8	−52.0
	93/09/15	15:00 – 01:55	11,819	55.045	134.174	343.463	250.8	−52.0
	93/09/10	22:21 – 11:45	12,810	55.041	134.163	341.008	250.8	−52.0
	93/09/21	06:35 – 16:20	11,395	55.046	134.139	335.801	250.8	−52.0
z-system	94/08/09	05:48 – 02:20	19,028	39.629	112.886	11.419	208.6	−65.1
	94/08/10	02:20 – 07:20	24,984	39.843	113.253	11.402	209.6	−65.0
	94/08/11	07:21 – 03:55	19,733	39.550	113.854	11.149	210.8	−65.5
	95/07/28	02:01 – 22:40	23,029	40.400	113.543	16.901	210.5	−64.6
	95/07/27	04:44 – 02:00	23,119	39.609	112.481	16.711	207.6	−65.1
Braccesi	95/05/26	19:42 – 08:33	19,079	196.512	54.510	134.792	105.3	81.1
Field	95/05/28	08:35 – 15:25	26,182	194.631	54.504	124.307	115.0	81.4
	95/12/22	13:51 – 18:20	34,292	195.192	54.201	331.569	108.7	81.0
	95/12/21	09:05 – 13:50	35,185	194.572	54.497	331.848	111.4	81.4
Jupiter	93/06/06	15:44 – 18:50	20,389	185.203	90.575	156.169	286.2	61.2
Arp 220	93/07/26	13:39 – 15:10	23,039	233.934	66.525	154.961	36.5	53.1
3C368	93/09/12	16:38 – 18:10	19,934	271.456	78.944	174.006	37.6	15.3

Appendix B

Contour-map images of the observed fields

We show the counting rate contour-map images $M^{CCF}(SKYX, SKYY)$ in the 0.7–7 keV energy band and the exposure time gray scale map $M^{EXP}(SKYX, SKYY)$ of the CXB observations in figure B.1–B.10. We smoothed the GIS2 and GIS3 images of each pointing independently with the XRT+GIS PSF, and summed them up on the sky. RNXB are not subtracted. See §5.3.2, for detailed handling of observed images.

Contour levels are $(5, 10, ..., 95, 100) \times 10^{-6}$ c s^{-1} pixel^{-1}. Coordinates superposed on the images are J2000. IPC sources and QSOs catalogued in Veron-Cetty and Veron (1993) are also plotted by filled circles and triangles, respectively.

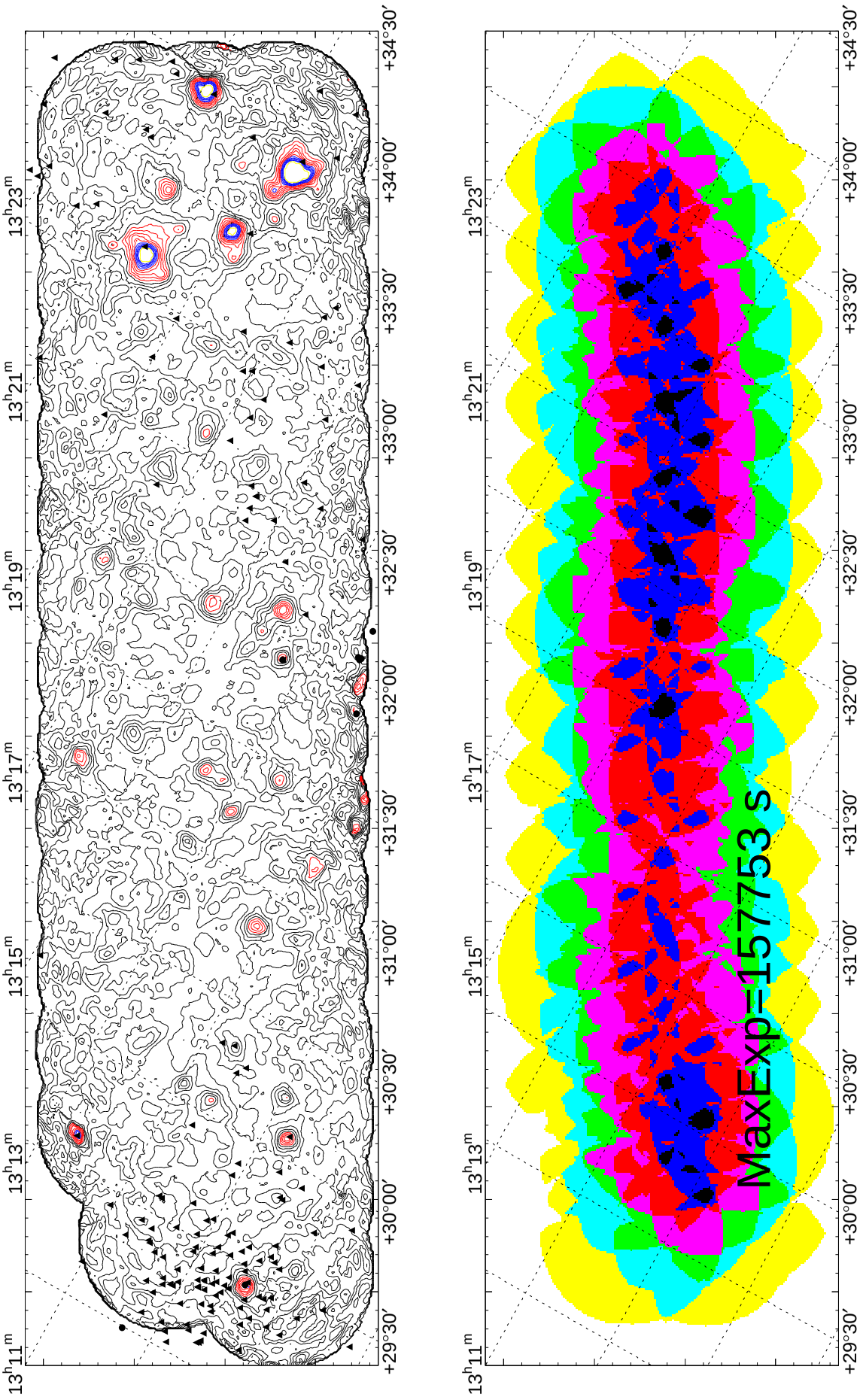

Figure B.1: LSS

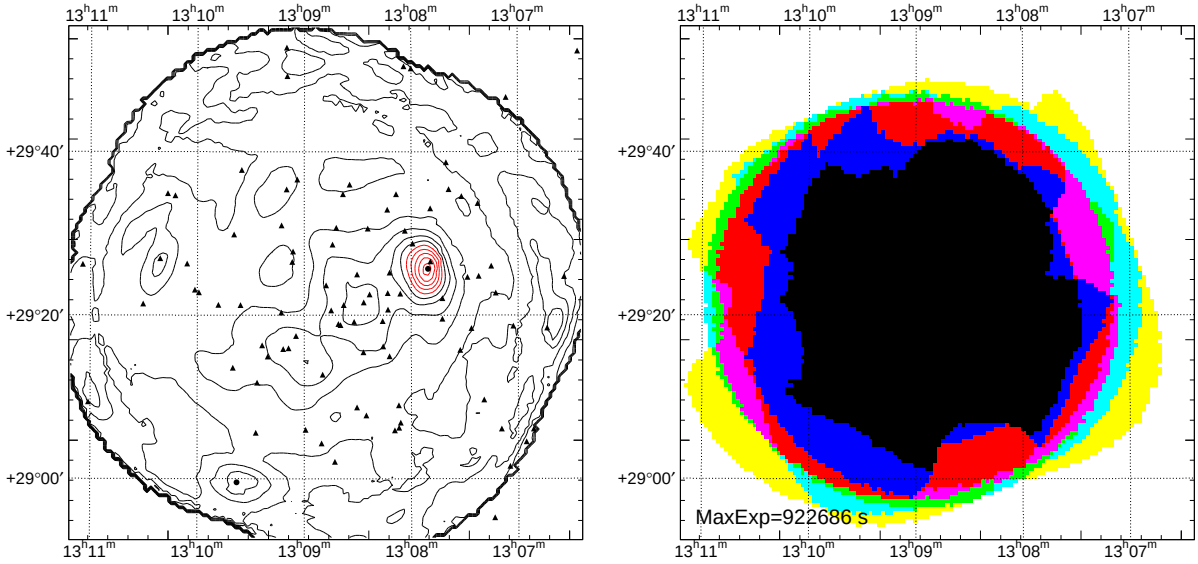

Figure B.2: SA57

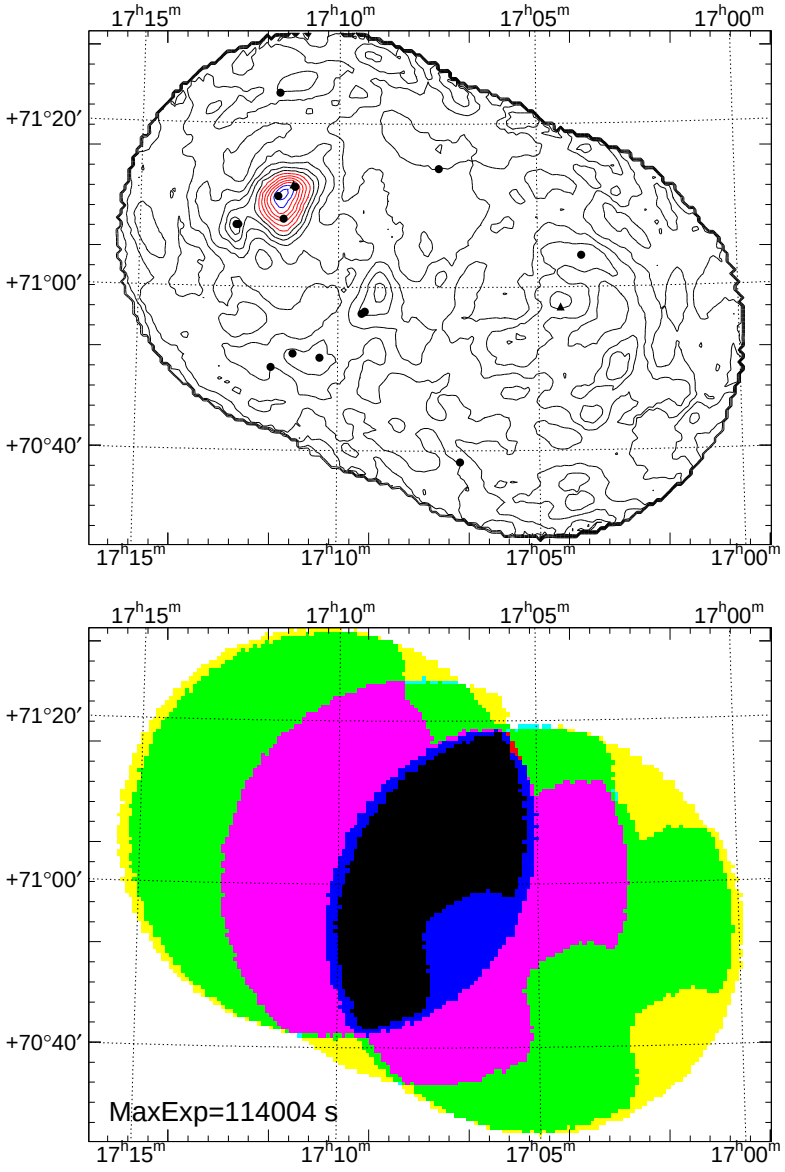

Figure B.3: Draco Field

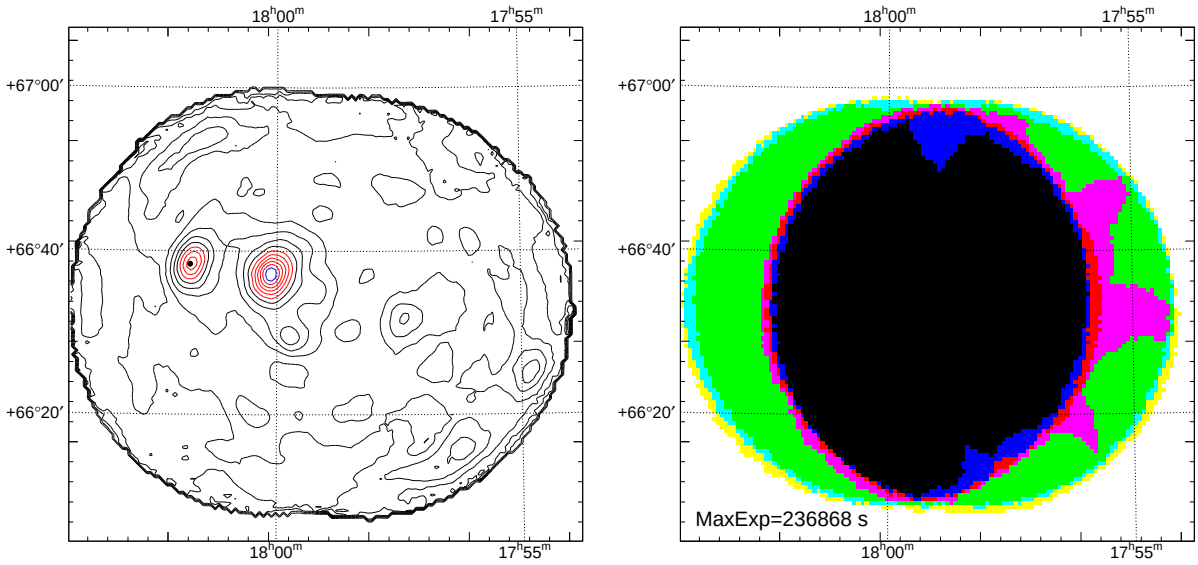

Figure B.4: NEP

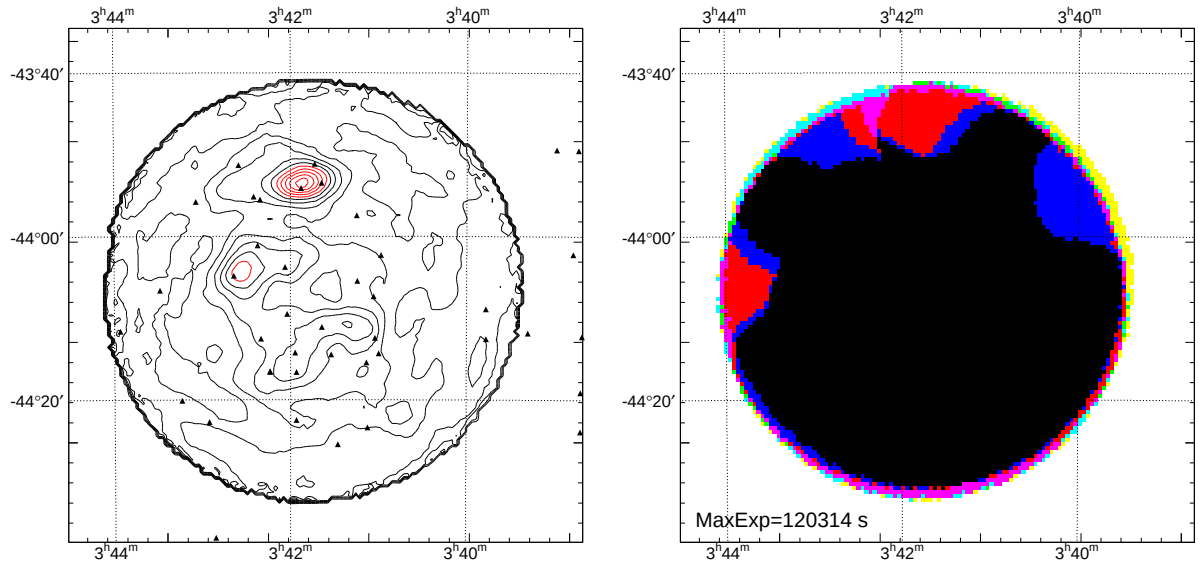

Figure B.5: QSF3

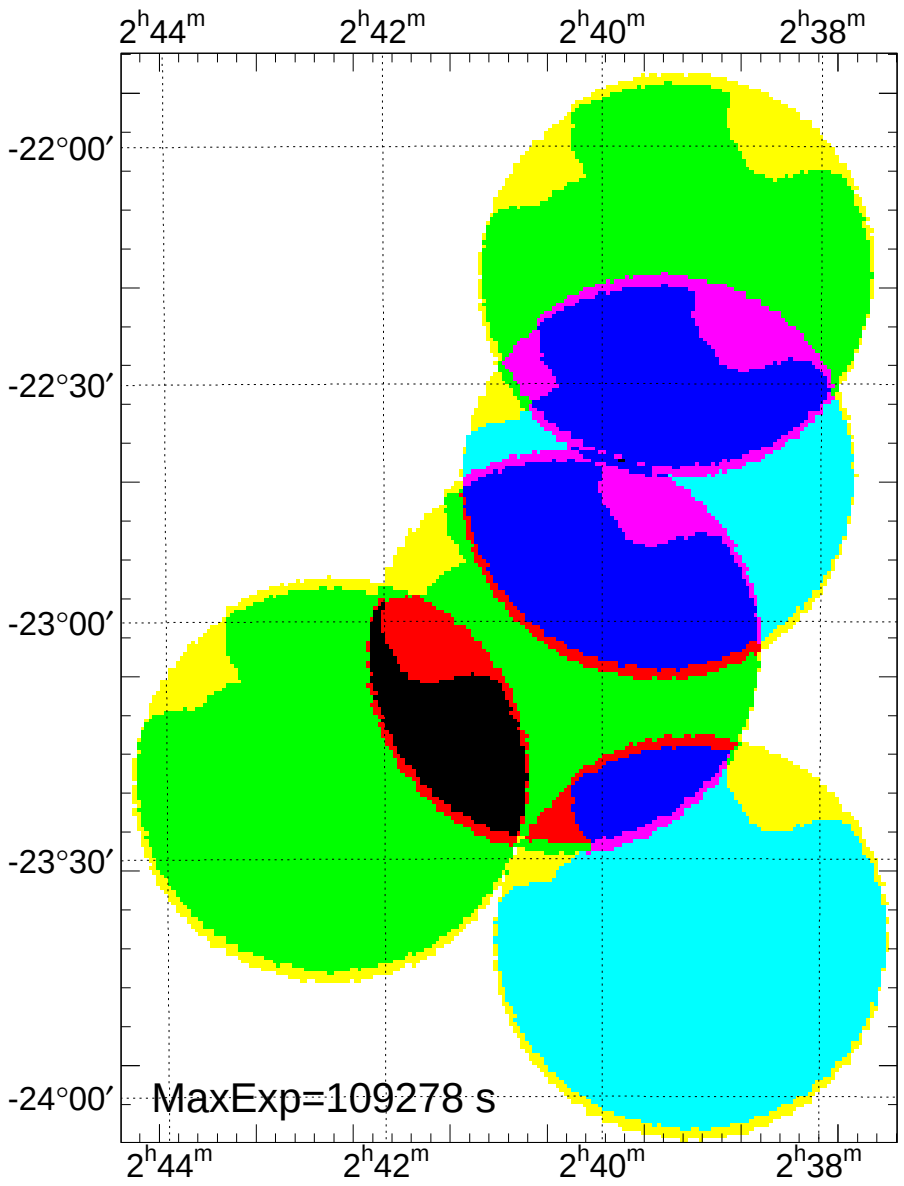

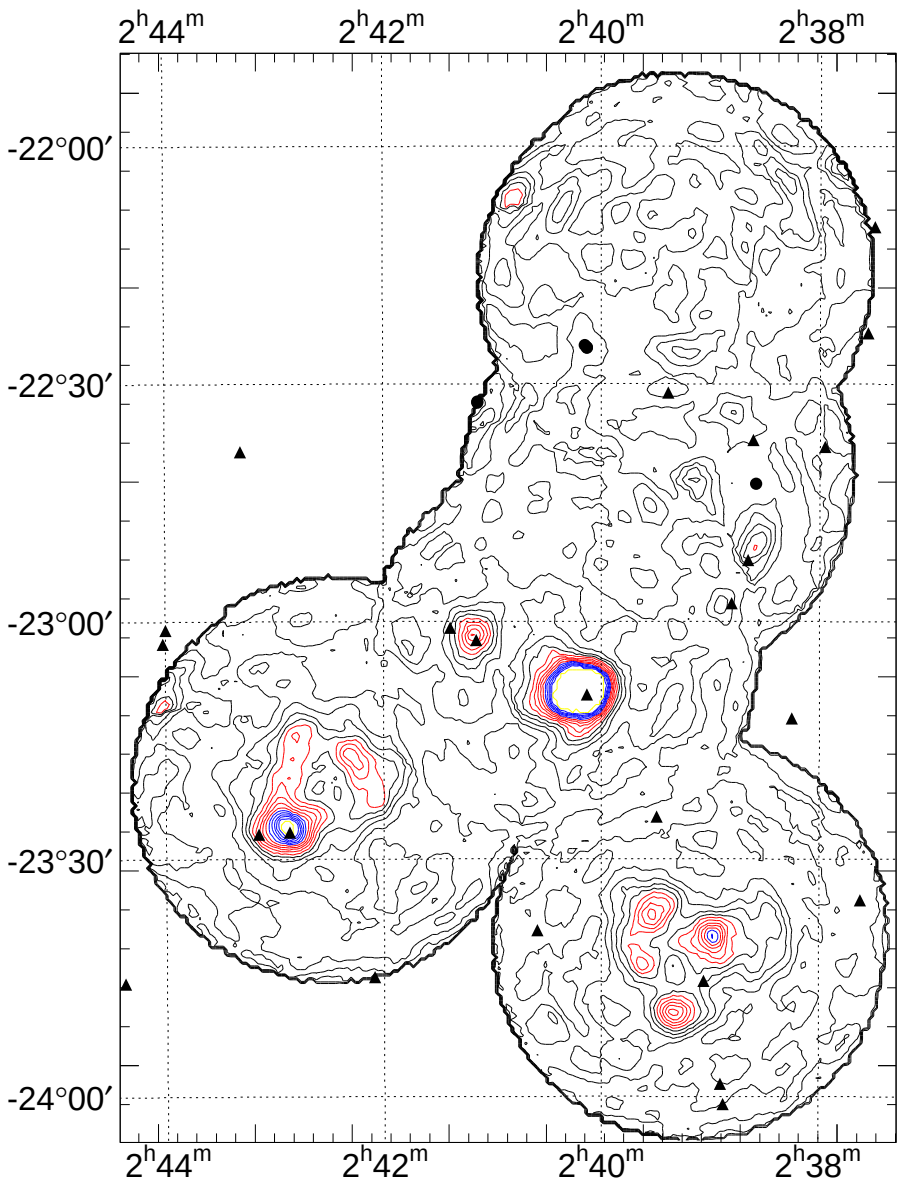

Figure B.6: z-system

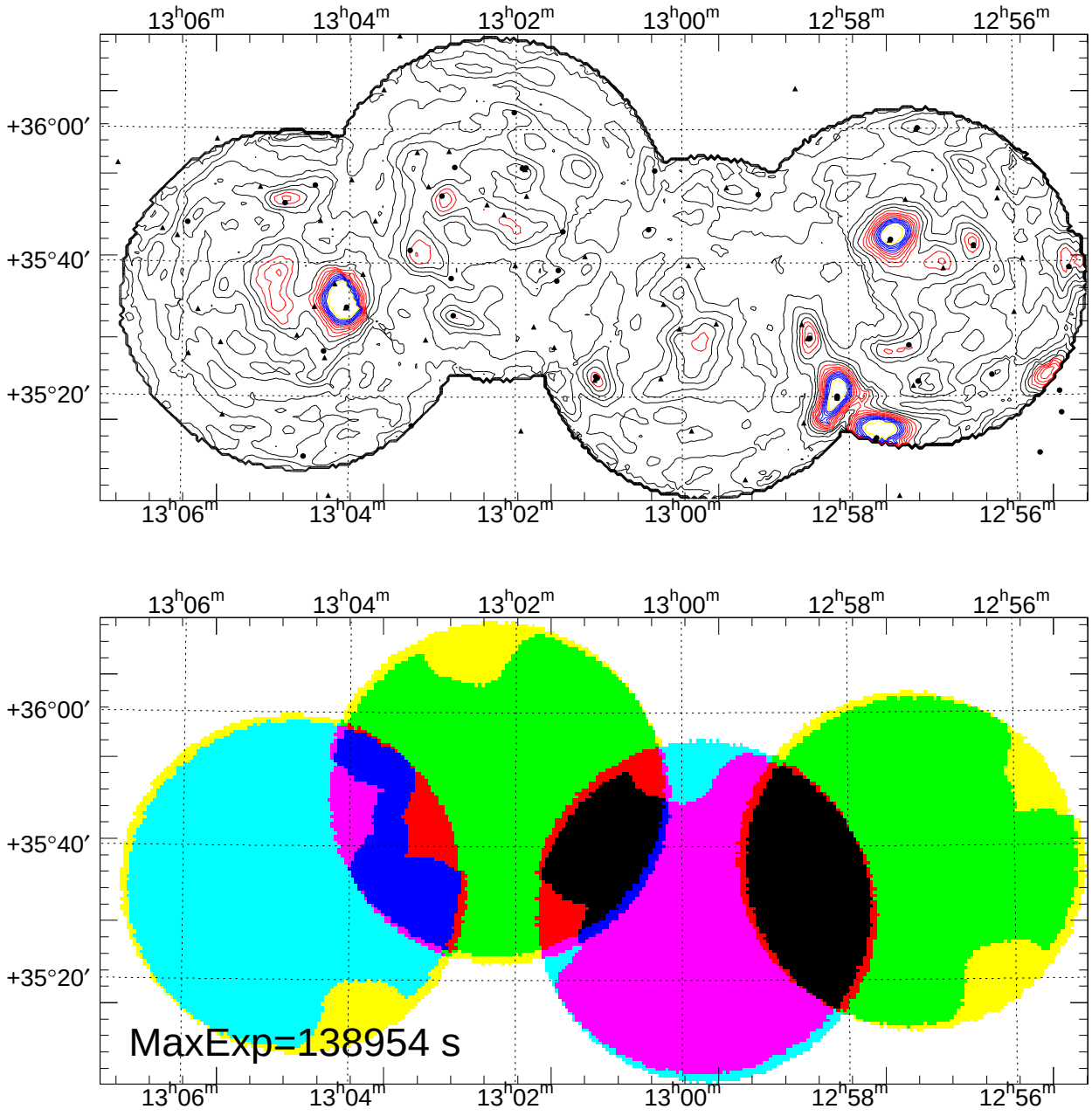

Figure B.7: Braccesi Field

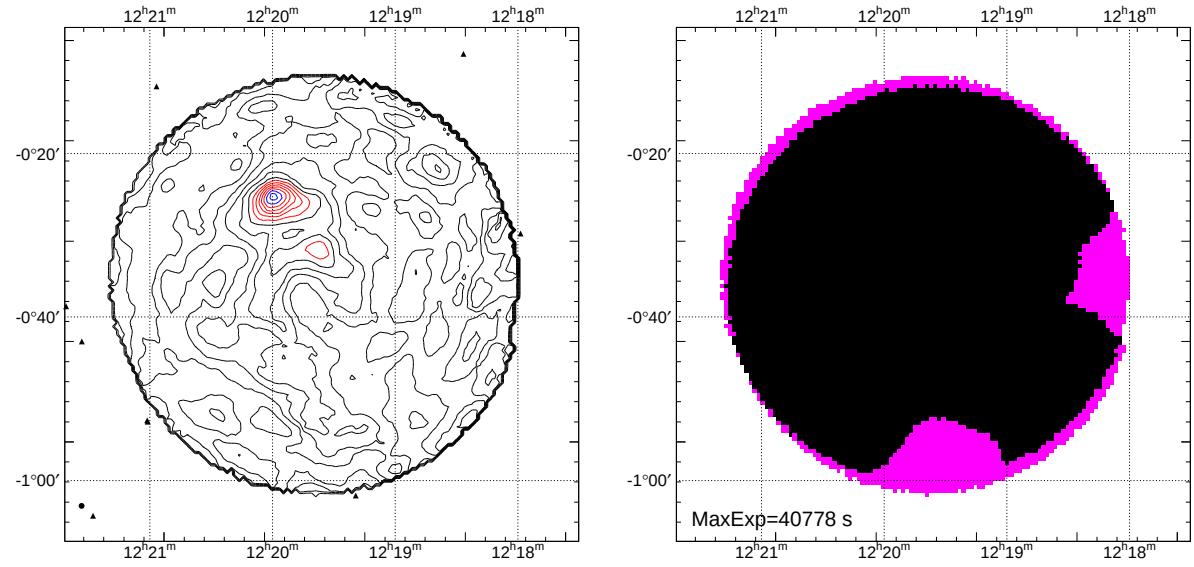

Figure B.8: Jupitar

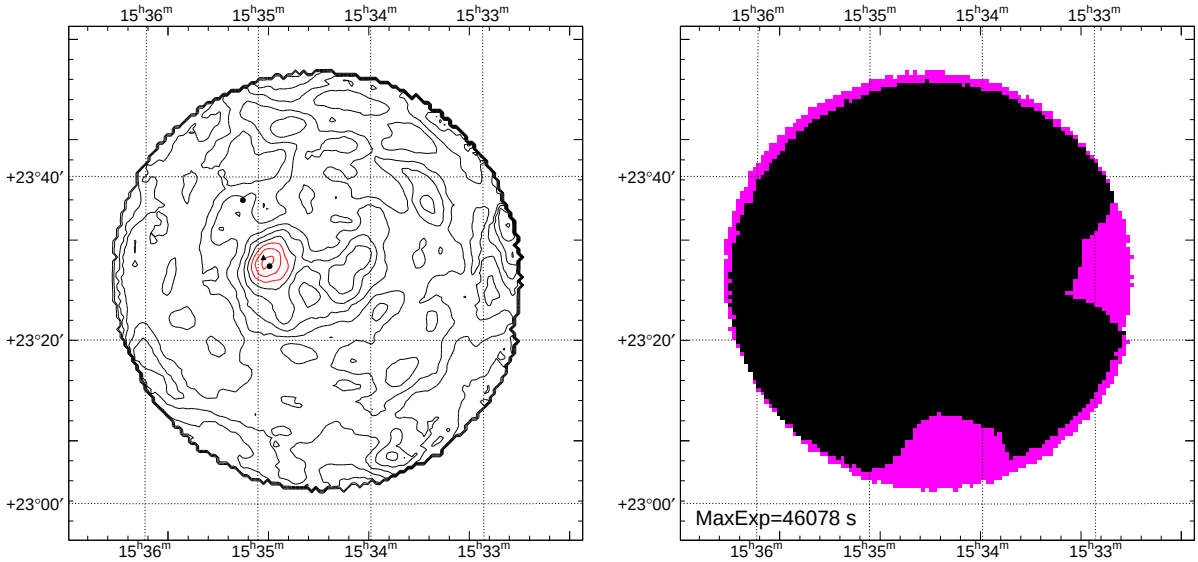

Figure B.9: Arp 220

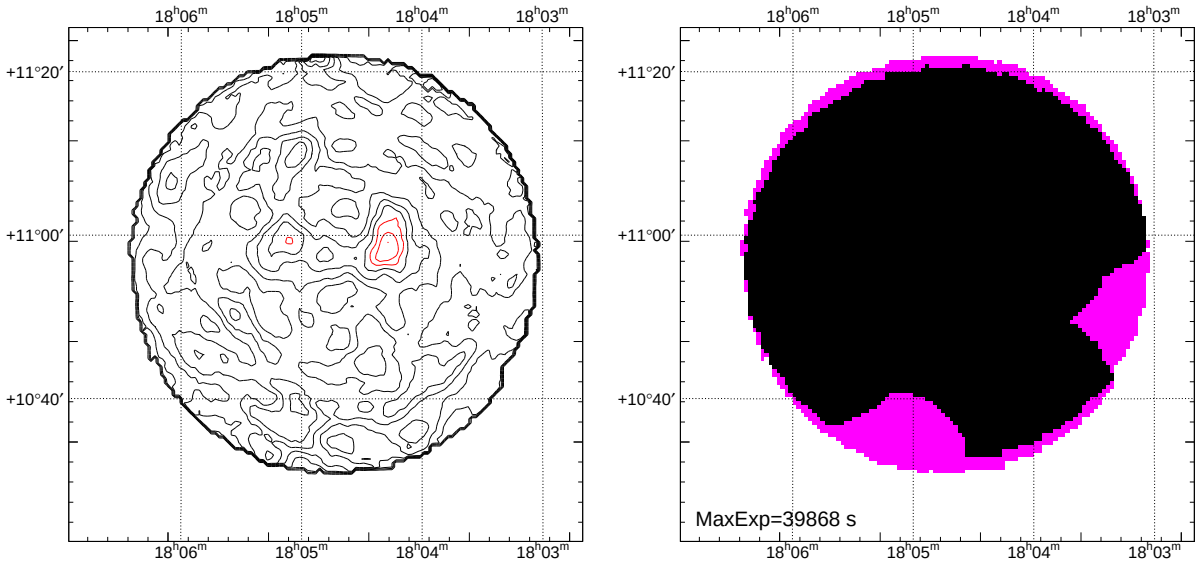

Figure B.10: 3C368

Appendix C

Flat field images and source-masks

Flat field images of the CXB observations, which are created by the method described in §7.2. The white pixel and black pixel represent -0.1 and 0.4, respectively. Source-masks at the threshold of 0.1 are also accompanied with.

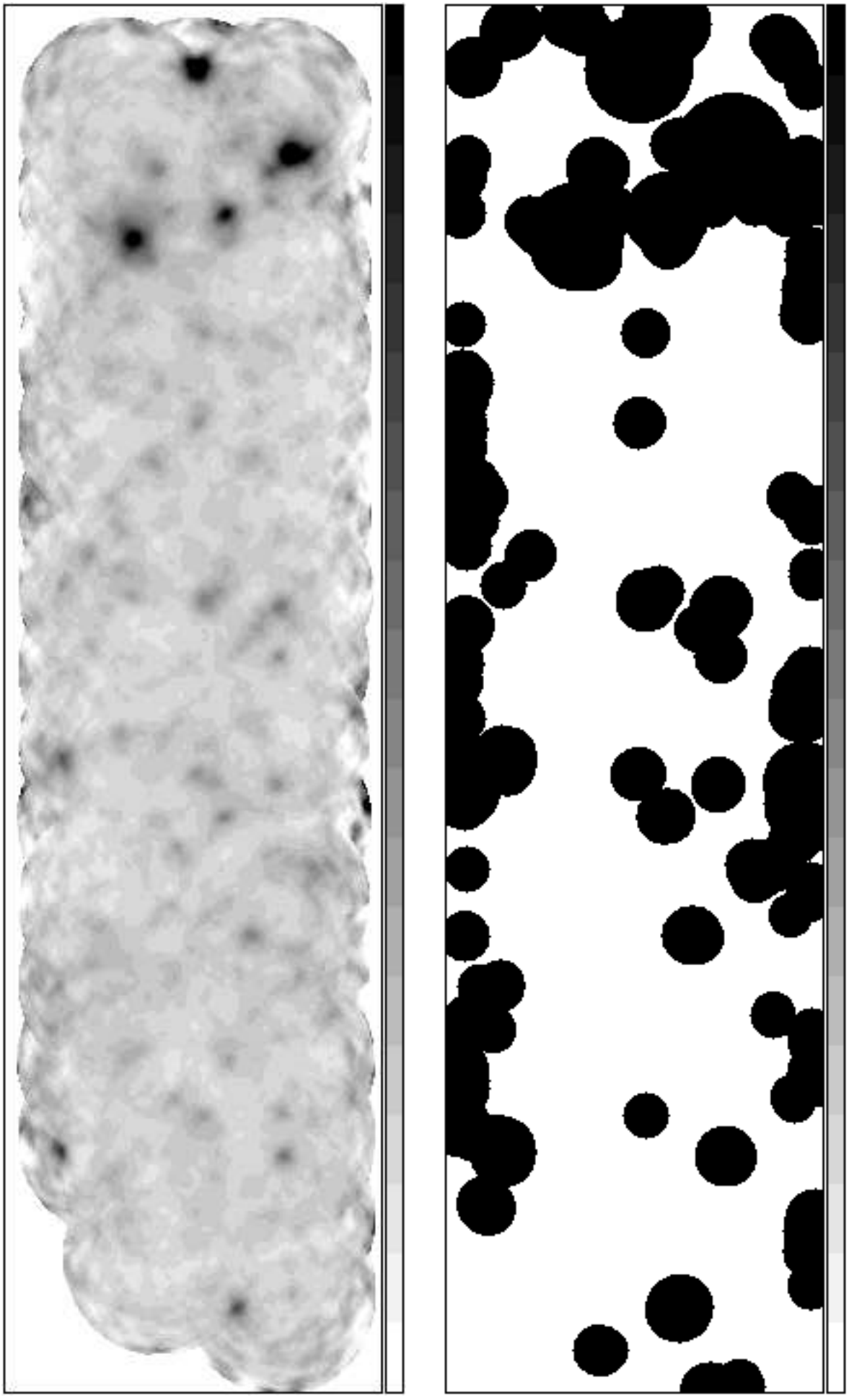

Figure C.1: LSS

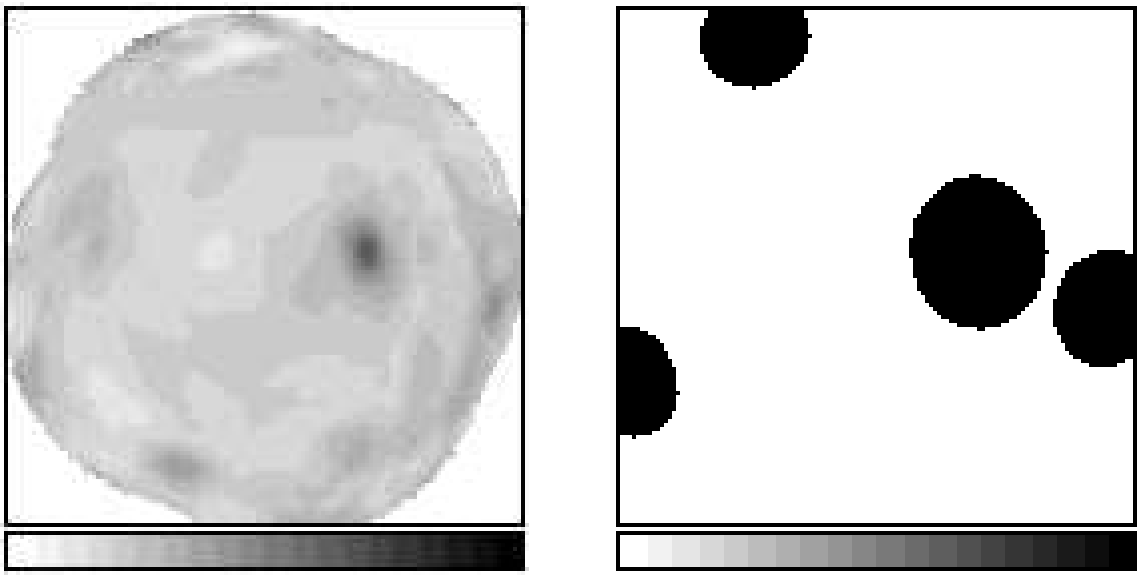

Figure C.2: SA57

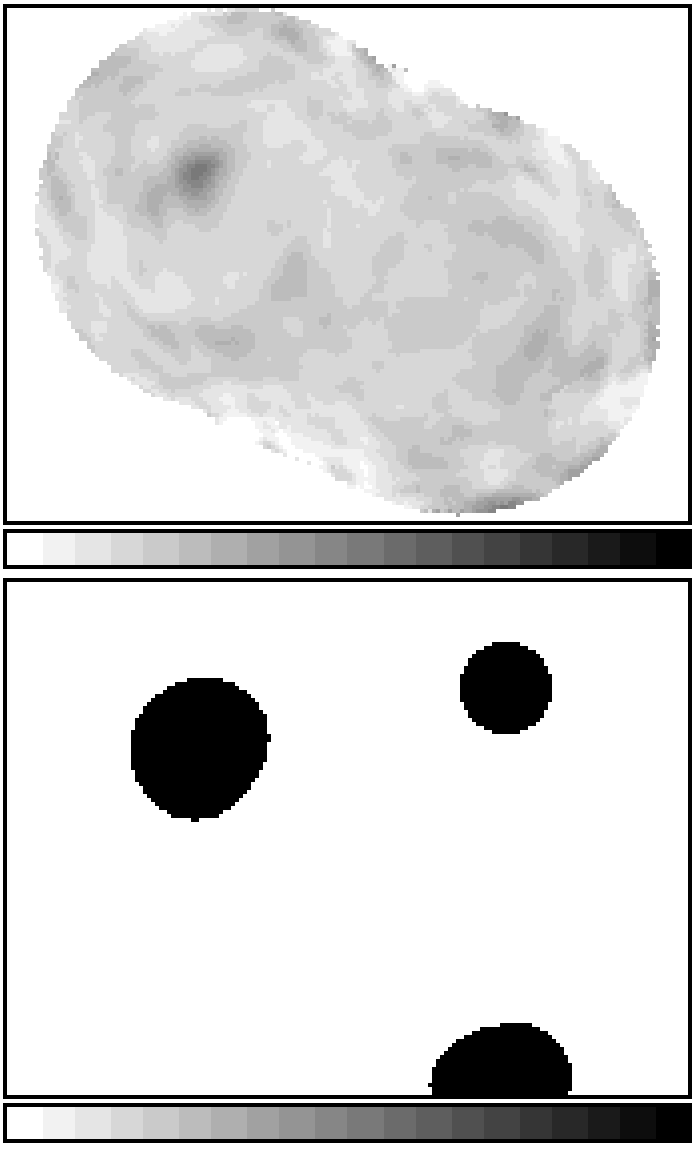

Figure C.3: Draco Field

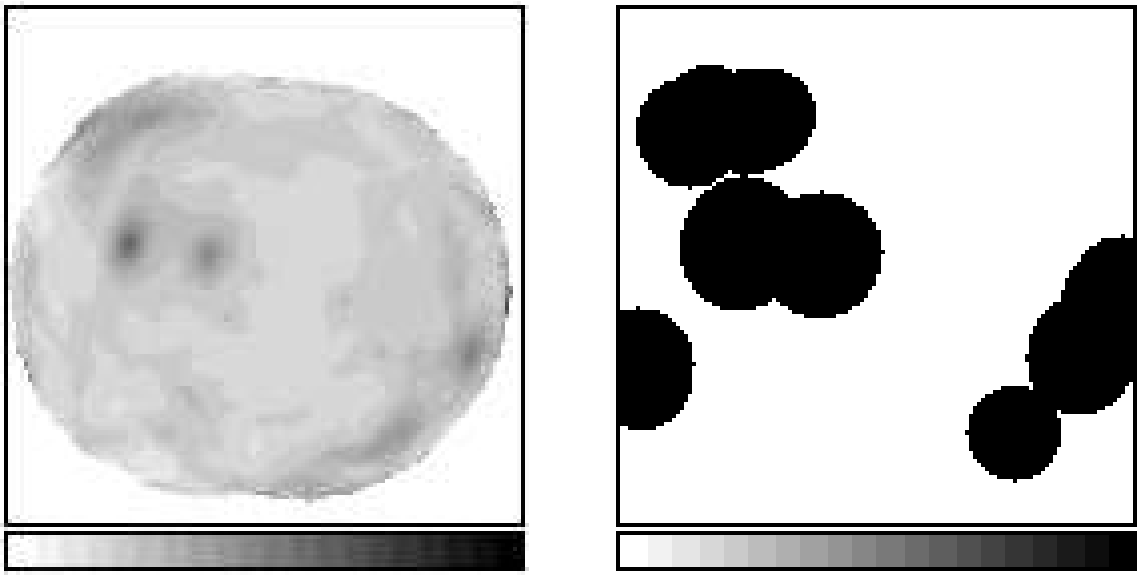

Figure C.4: NEP

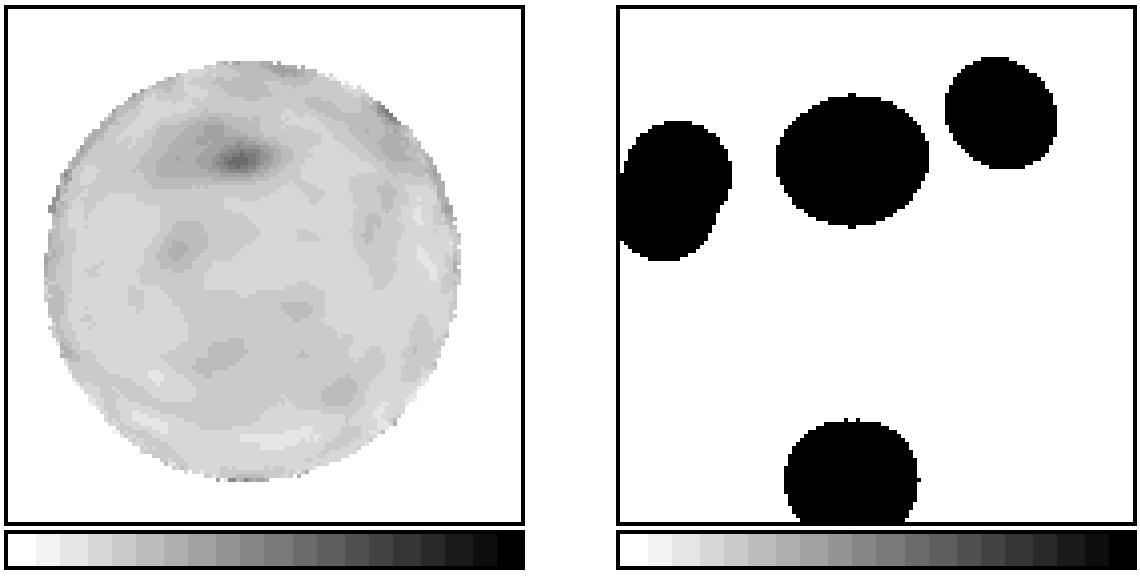

Figure C.5: QSF3

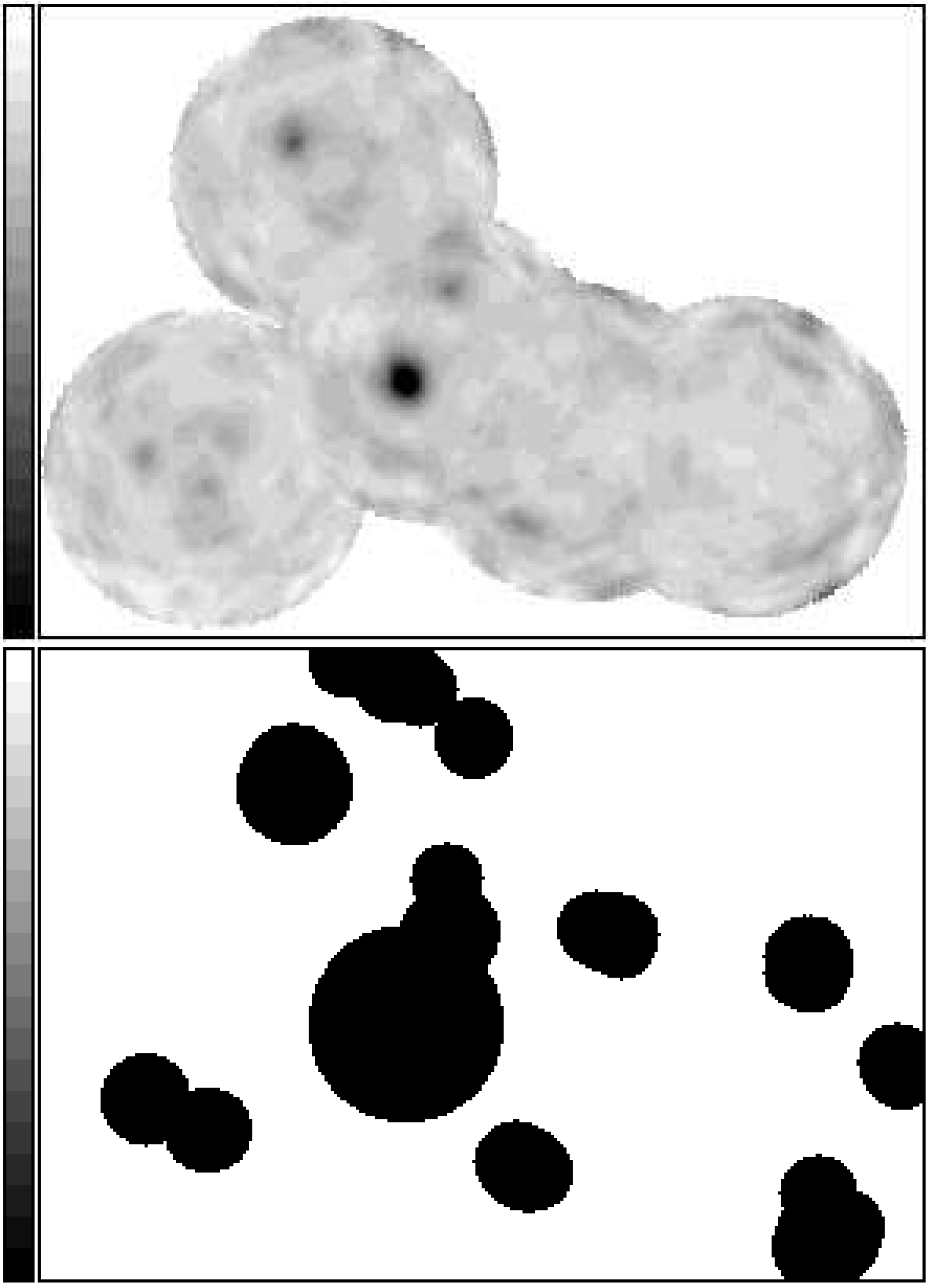

Figure C.6: z-system

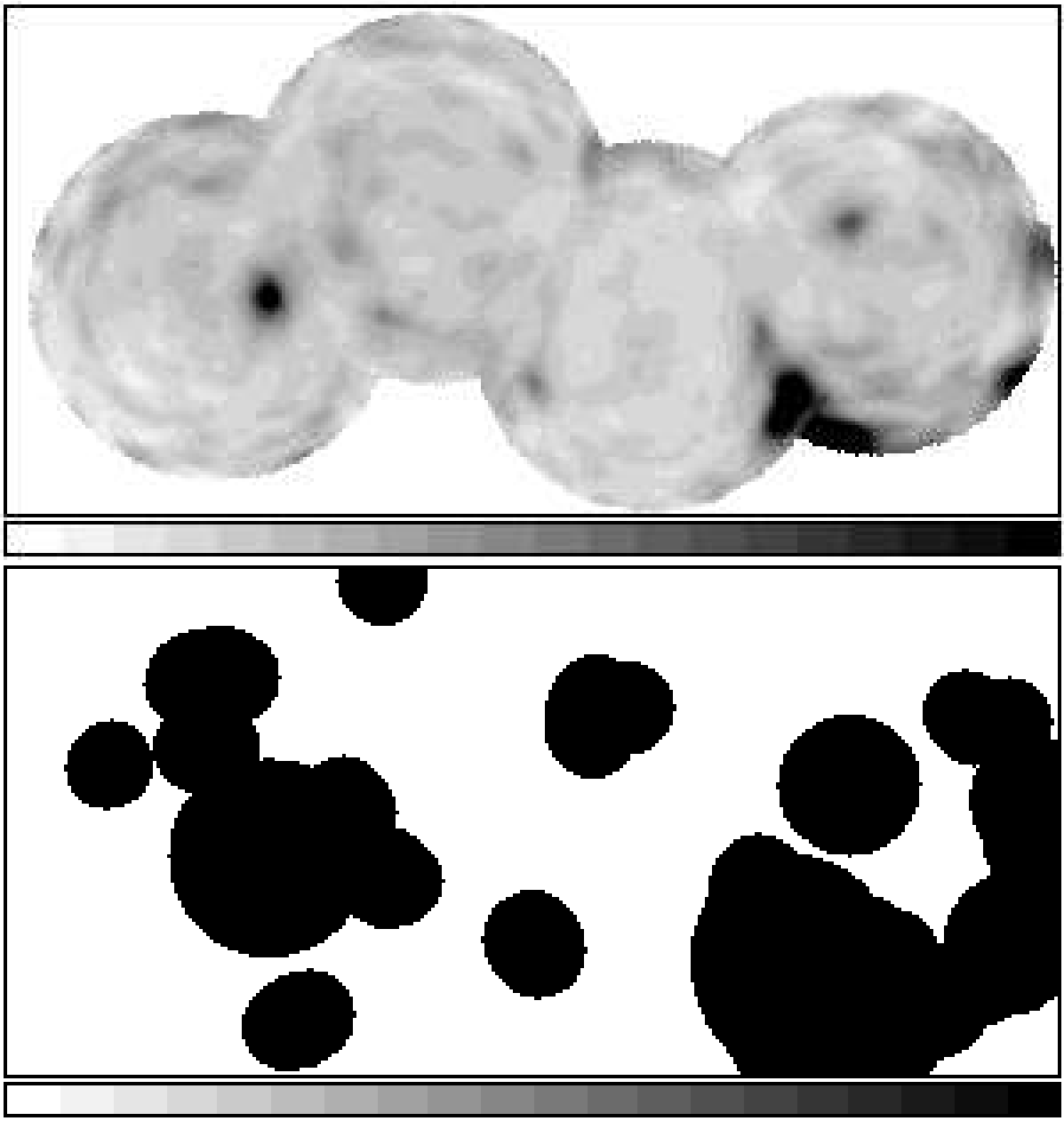

Figure C.7: Braccesi Field

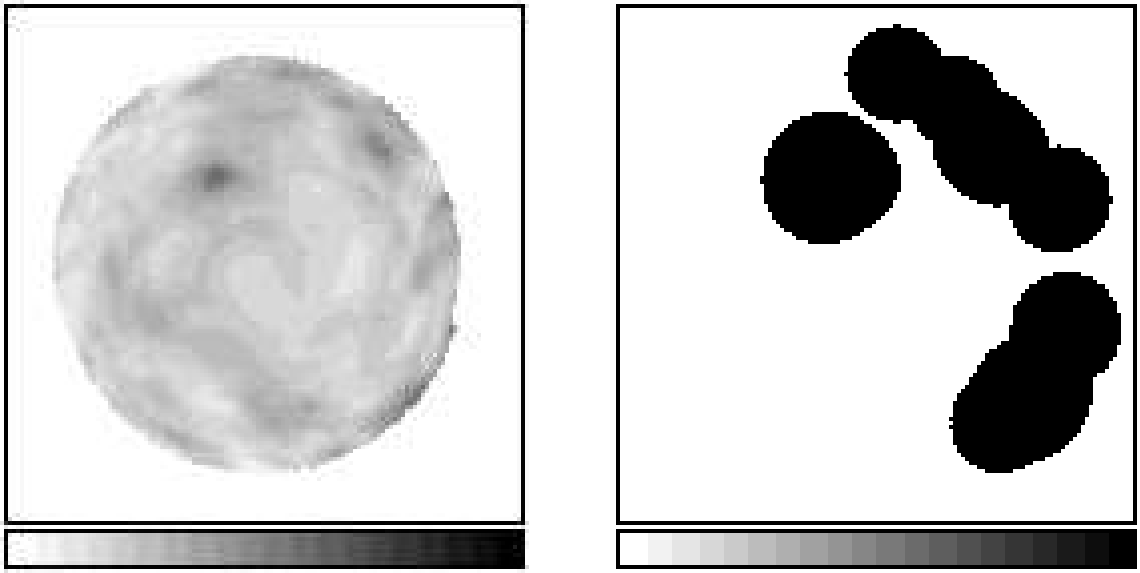

Figure C.8: Jupiter

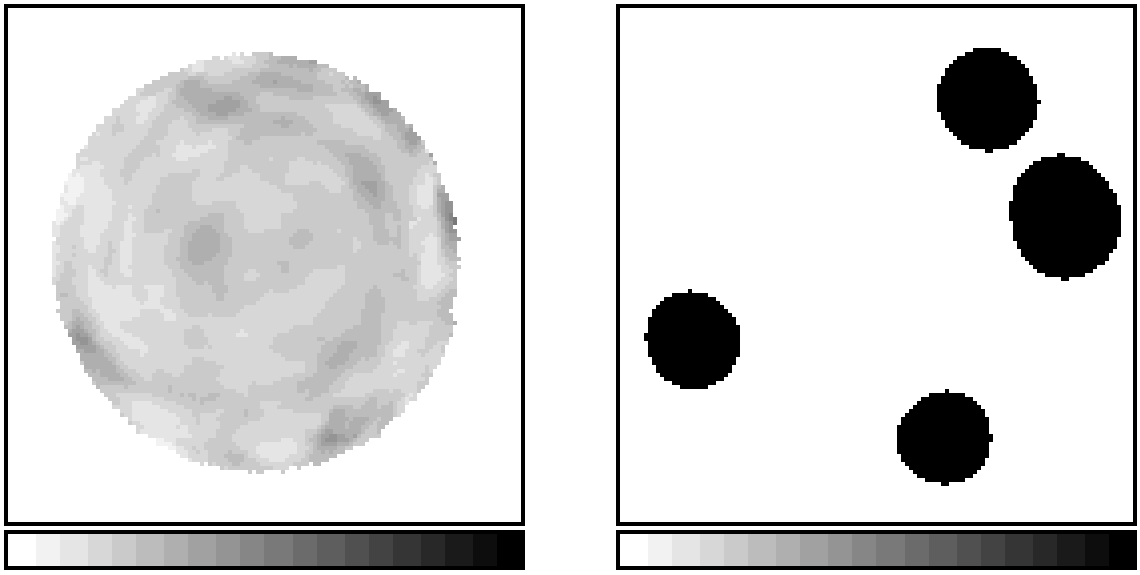

Figure C.9: Arp220

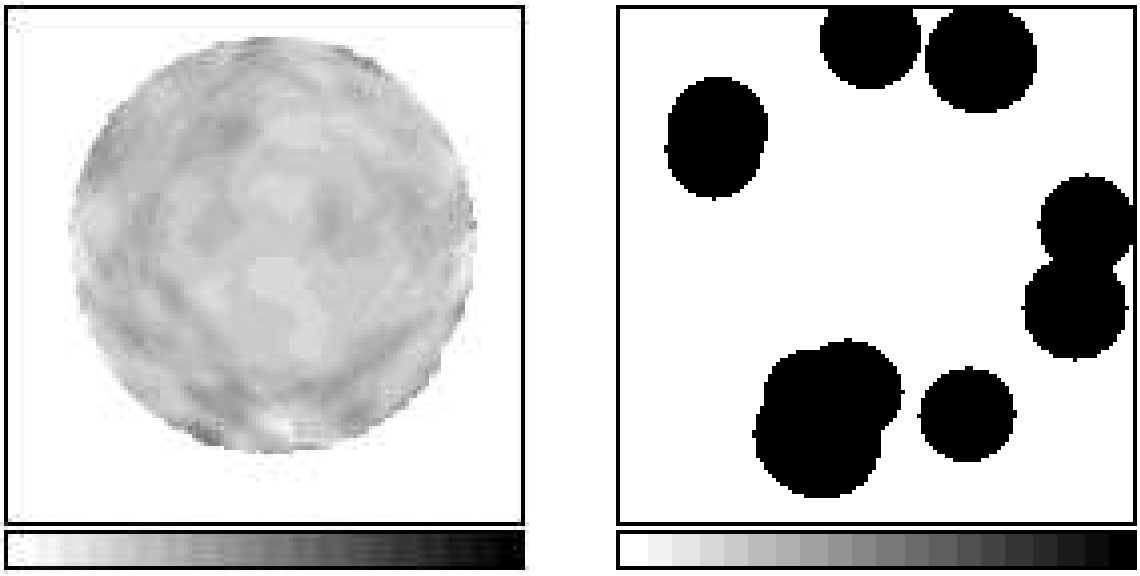

Figure C.10: 3C368

Appendix D

Spectra of the CXB observations

We show the spectra of the CXB observations fitted in the 0.6–10 keV energy band with an absorbed power-law ($PL^{\rm hard}$) plus a steep power-law model ($PL^{\rm soft}$), in figure D.1–D.13. Photon indices of $PL^{\rm soft}$ are fixed to 6.0. Absorption columns are also fixed to the values derived from Einstein On-line Service (*EINLINE*), as shown in table 7.1. Left figures show the spectra including point sources, and right figures shows the spectra processed through the source-maskings at the threshold of 0.1 on M^{FLAT} (ref. §7.2). Upper panel of each figure shows GIS2+3 spectrum (crosses), the best fit model (solid line), $PL^{\rm hard}$ (dashed line), and $PL^{\rm soft}$ (dot-dashed line). Lower panels show residuals plotted in unit of σ.

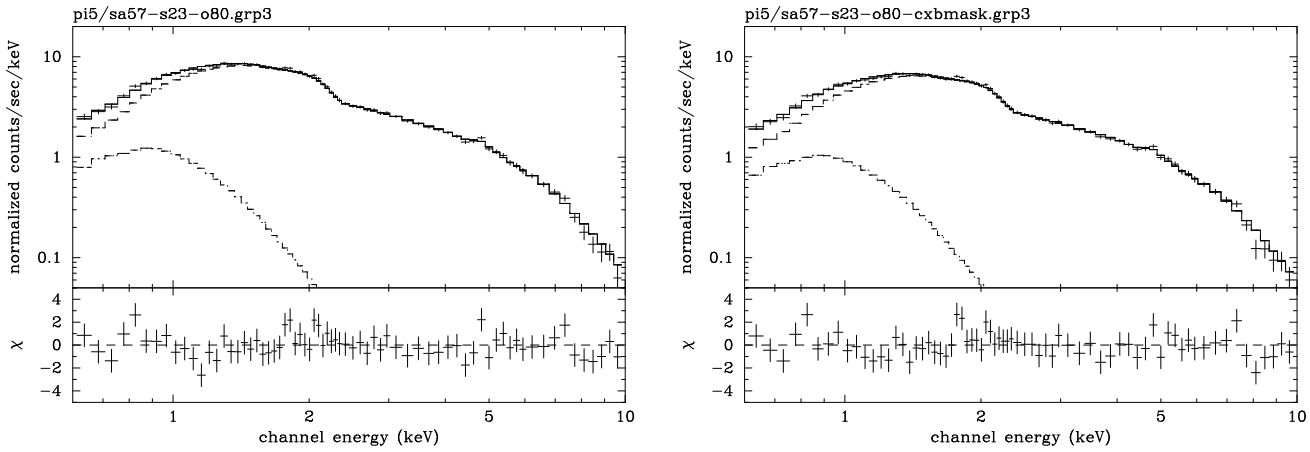

Figure D.1: SA57

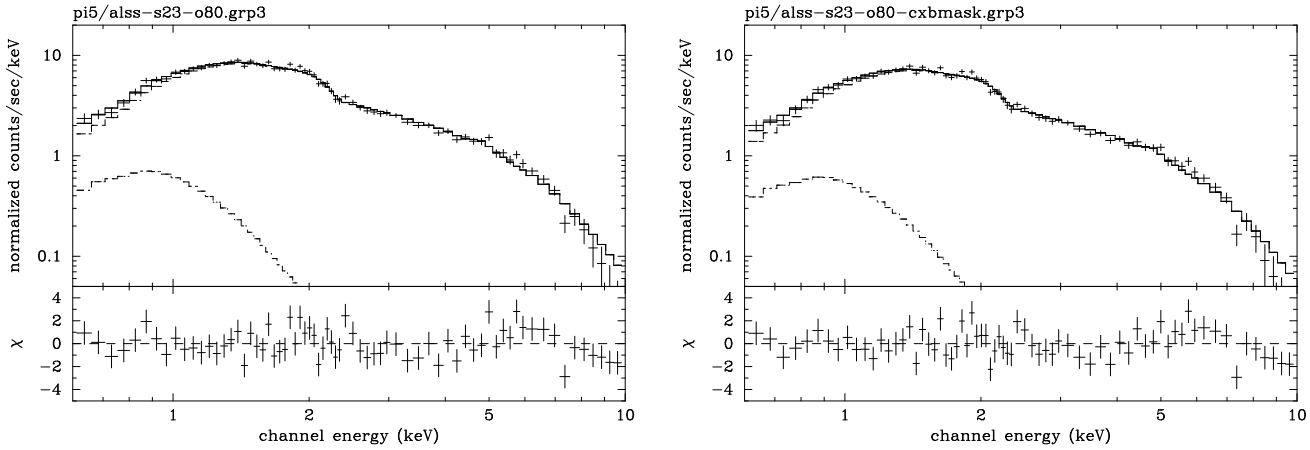

Figure D.2: a-LSS

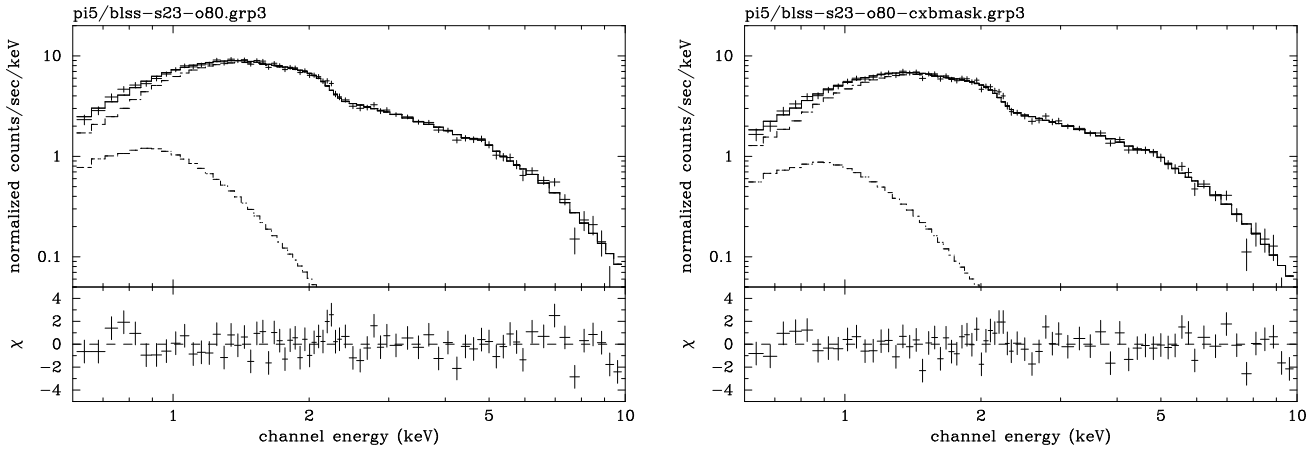

Figure D.3: b-LSS

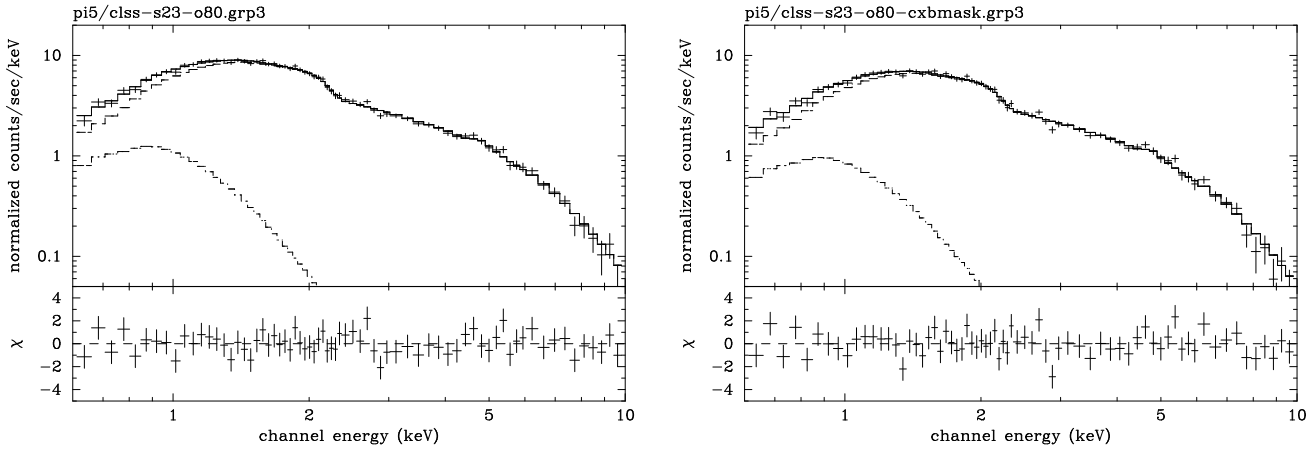

Figure D.4: c-LSS

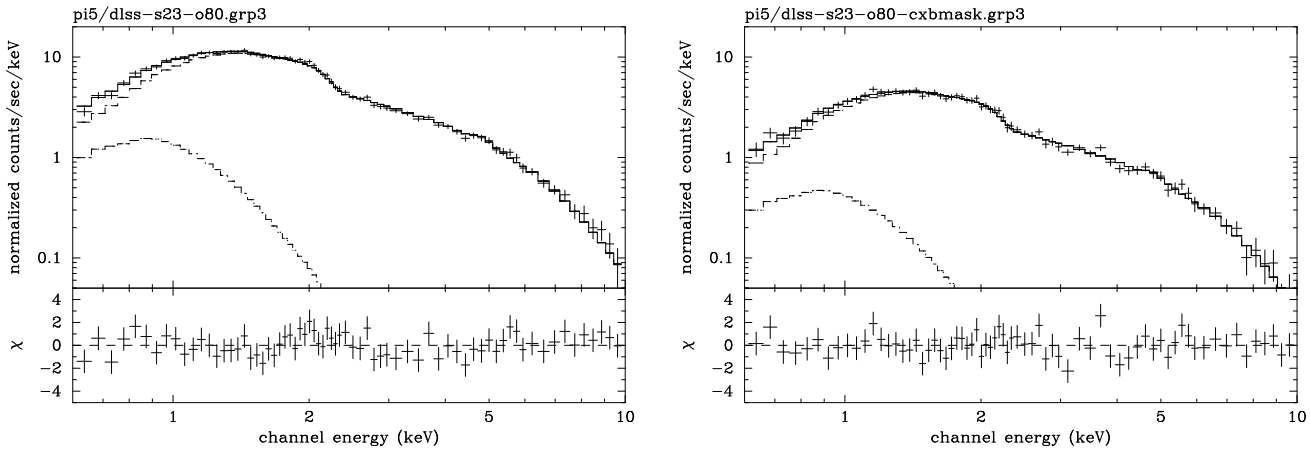

Figure D.5: d-LSS

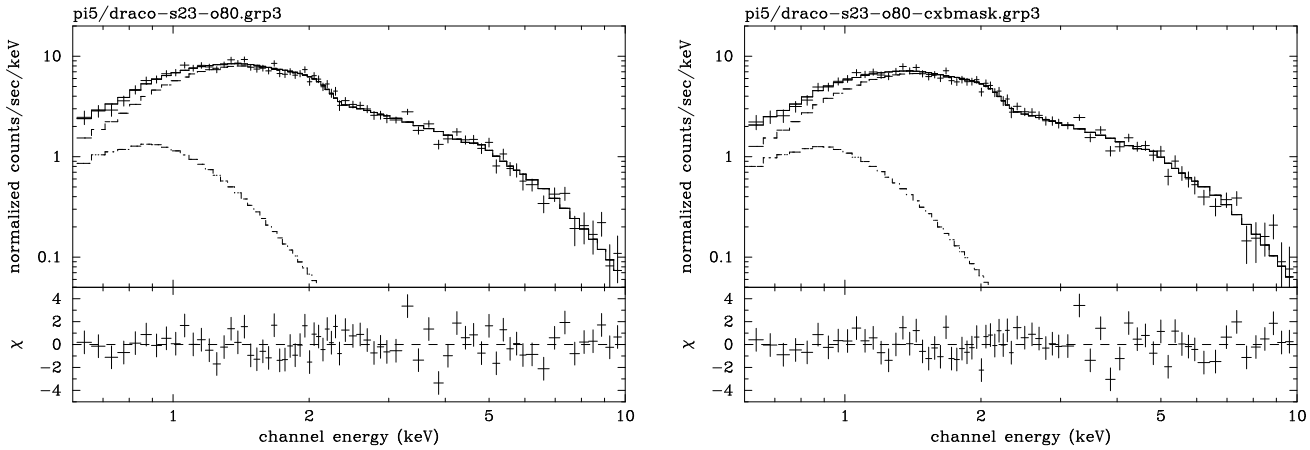

Figure D.6: Draco Field

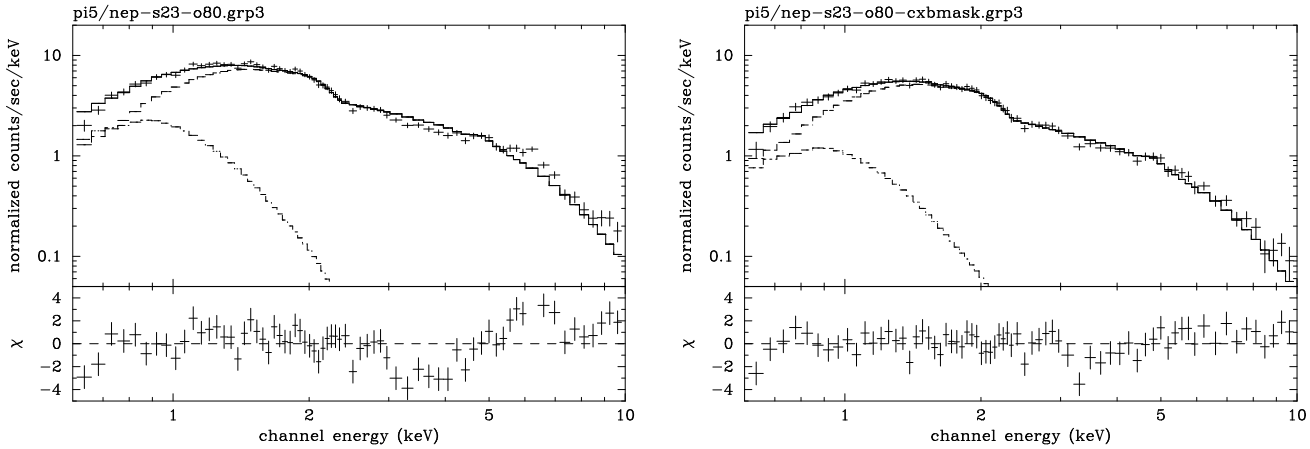

Figure D.7: NEP

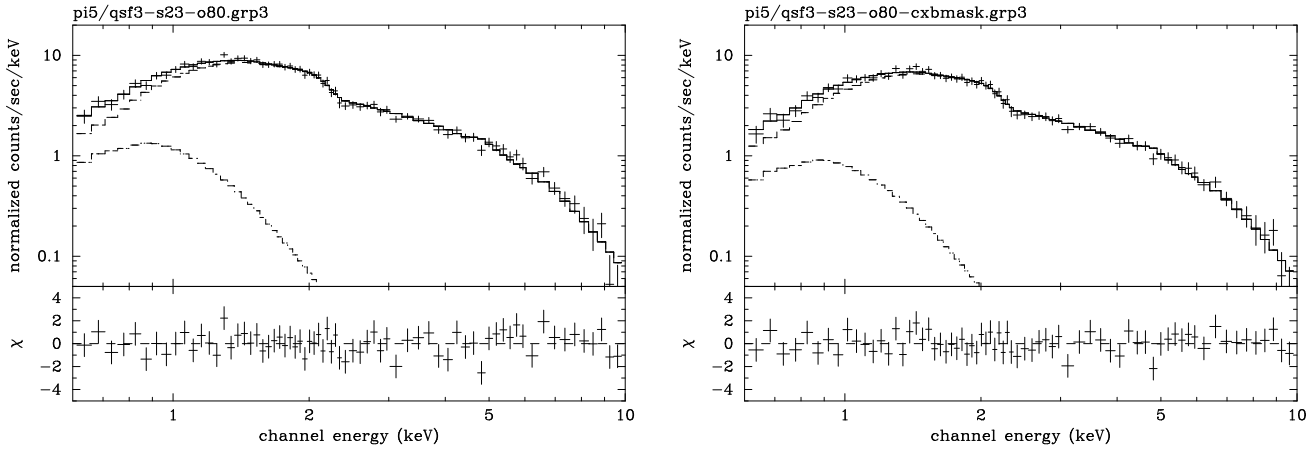

Figure D.8: QSF3

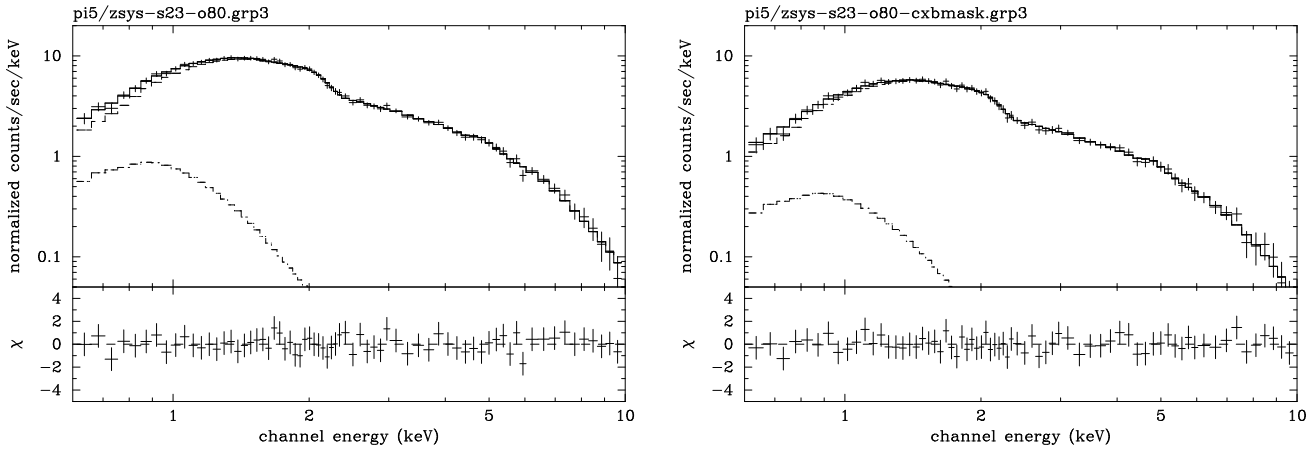

Figure D.9: z-system

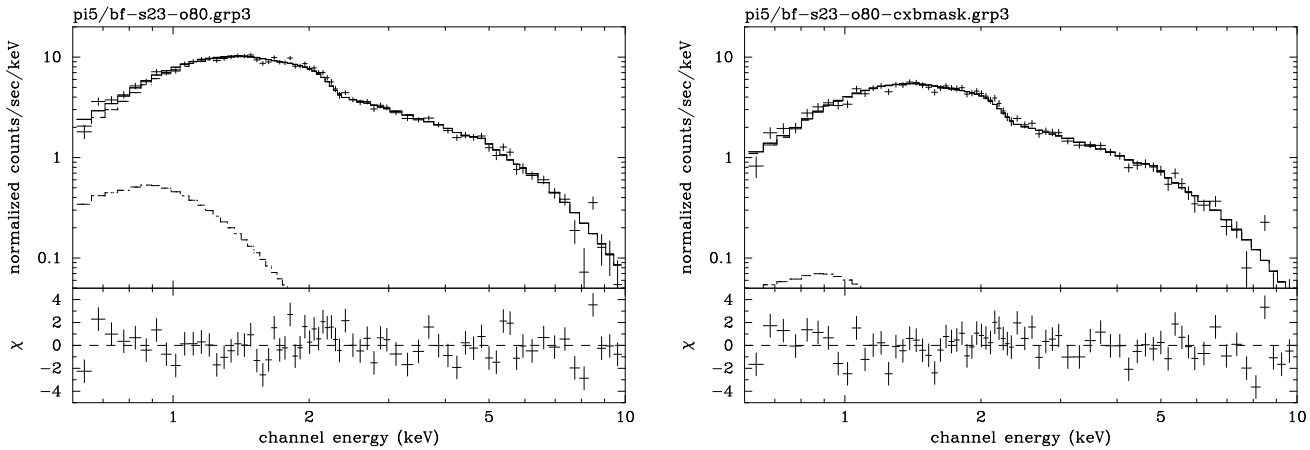

Figure D.10: Braccesi Field

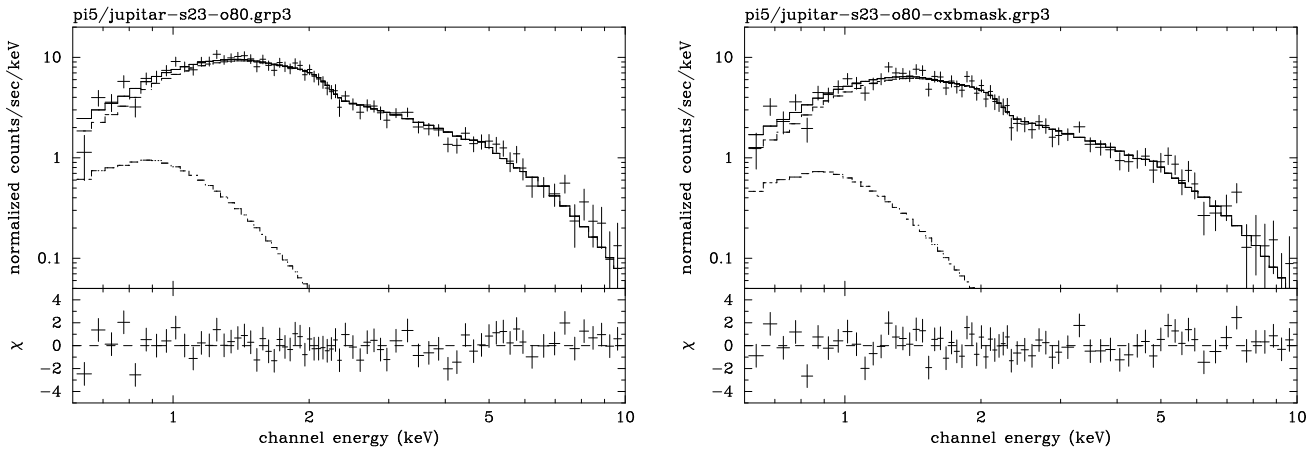

Figure D.11: Jupiter

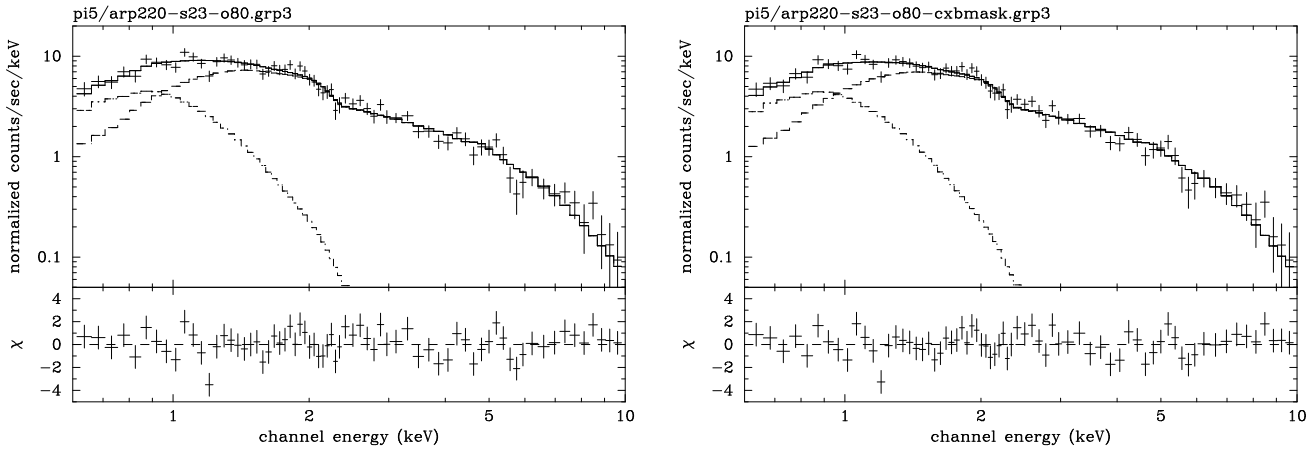

Figure D.12: Arp 220

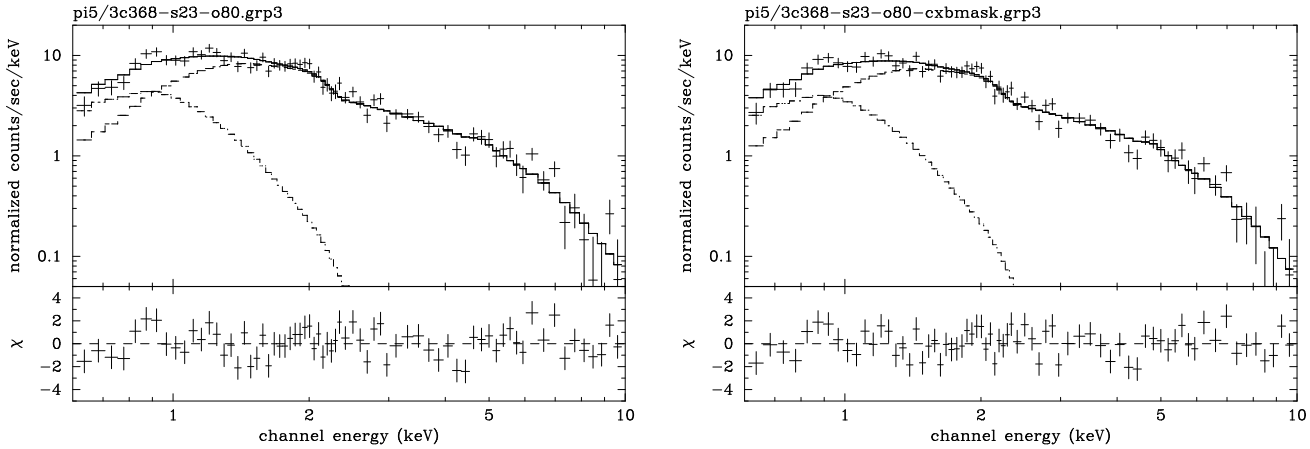

Figure D.13: 3C368

Appendix E

Fitting results processed through source-masking at the threshold of 0.06

In table E.1, we show the fitting results of each field when point sources are masked at the threshold of 0.06 on M^{FLAT}. The source-mask used for the fitting are shown in figure E.1–E.10.

Table E.1: ($PL^{\rm hard}$+$PL^{\rm soft}$) fits to the 0.6–10 keV spectrum of each field with point sources being masked at the threshold of 0.06 on M^{FLAT}. All errors are the 90% confidence level. $\Gamma^{\rm soft}$ is fixed to 6.0.

ID	Name	Exp.†	Area‡	$N_{\rm H}^{\sharp}$	χ^2/d.o.f	$\Gamma^{\rm hard}$	$F_{\rm X}^{\rm hard\triangleleft}$	$F_{\rm X}^{\rm soft*}$
1	SA57	461,343	0.48	1.0	64.4/67	1.382 ± 0.020	5.69 ± 0.09	1.21 ± 0.15
2	a-LSS	119,221	1.31	1.1	87.4/67	1.471 ± 0.041	5.28 ± 0.18	0.59 ± 0.31
3	b-LSS	130,206	1.36	1.1	77.9/67	1.481 ± 0.041	5.37 ± 0.18	1.03 ± 0.33
4	c-LSS	138,641	1.47	1.1	68.7/67	1.498 ± 0.043	4.94 ± 0.18	1.07 ± 0.32
5	d-LSS	127,324	0.95	1.1	65.4/67	1.509 ± 0.054	5.21 ± 0.23	0.78 ± 0.42
6	Draco	57,002	0.55	4.1	77.4/67	1.489 ± 0.055	5.20 ± 0.24	1.60 ± 0.42
7	NEP	118,434	0.35	4.2	70.5/67	1.406 ± 0.043	5.41 ± 0.19	1.70 ± 0.31
8	QSF3	60,157	0.26	1.7	53.5/67	1.398 ± 0.055	6.20 ± 0.28	0.99 ± 0.46
9	ZSYS	109,893	0.89	2.3	35.2/67	1.501 ± 0.050	5.28 ± 0.22	0.68 ± 0.38
10	BF	114,738	0.55	1.2	88.2/67	1.548 ± 0.045	5.31 ± 0.22	0.02 ± 0.22
11	Jupiter	20,389	0.16	2.1	63.0/67	1.616 ± 0.117	4.55 ± 0.43	0.43 ± 0.66
12	Arp 220	23,039	0.22	4.2	49.4/67	1.410 ± 0.106	4.79 ± 0.41	3.97 ± 0.78
13	3C368	19,934	0.11	9.8	82.3/67	1.494 ± 0.141	5.07 ± 0.56	4.09 ± 1.11

† Total exposure time (s).

‡ Integration area (deg^2) on the sky after applying the source maskings (threshold 0.06).

$^{\sharp}$ Absorption for $PL^{\rm hard}$ (10^{20} cm^{-2}) from Einstein On-line Service (*EINLINE*). Fixed while fitting.

$^{\triangleleft}$ Flux of $PL^{\rm hard}$ (10^{-8} erg s^{-1} cm^{-2} str^{-1}) in the 2–10 keV energy band.

* Flux of $PL^{\rm soft}$ (10^{-8} erg s^{-1} cm^{-2} str^{-1}) in the 0.5–2 keV energy band.

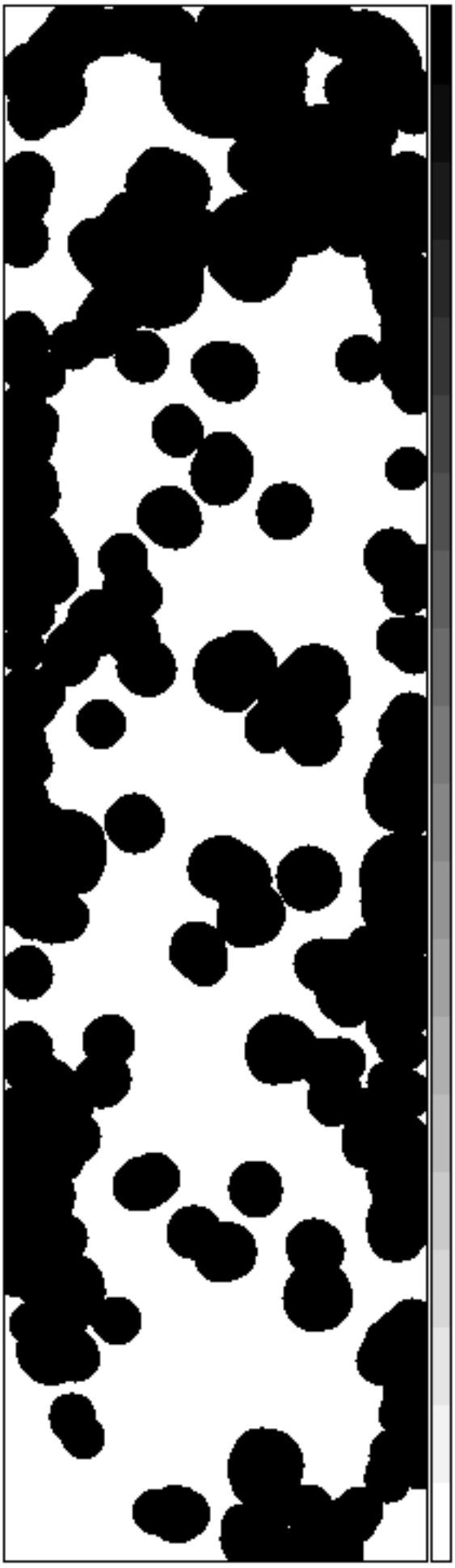

Figure E.1: LSS

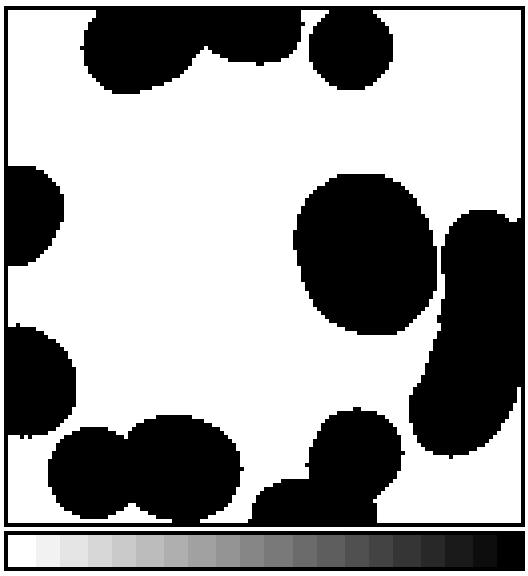

Figure E.2: SA57

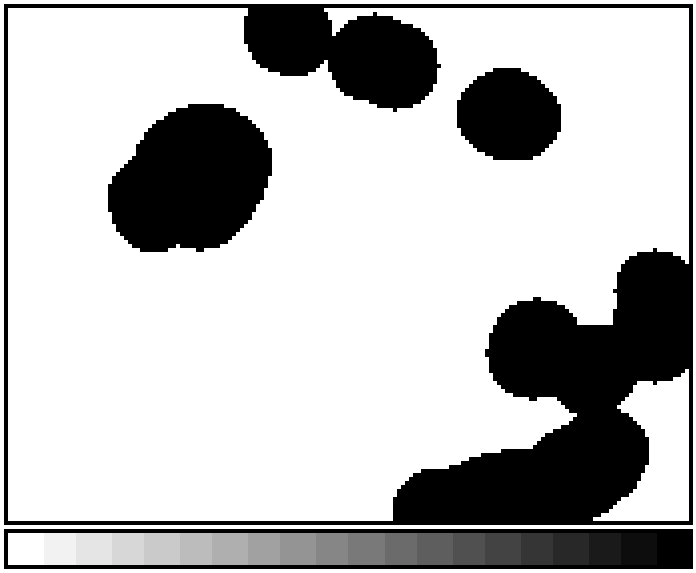

Figure E.3: Draco Field

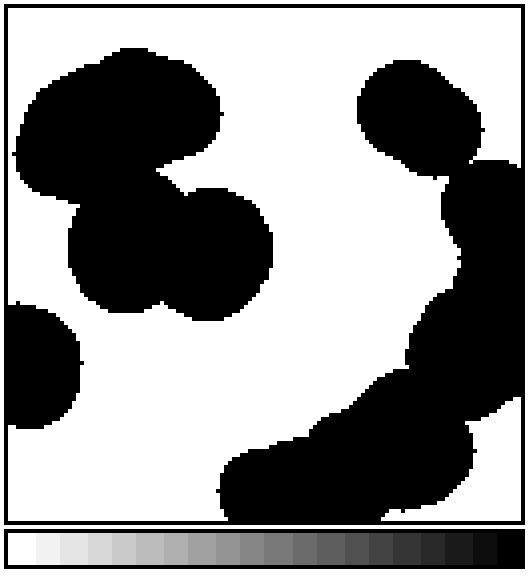

Figure E.4: NEP

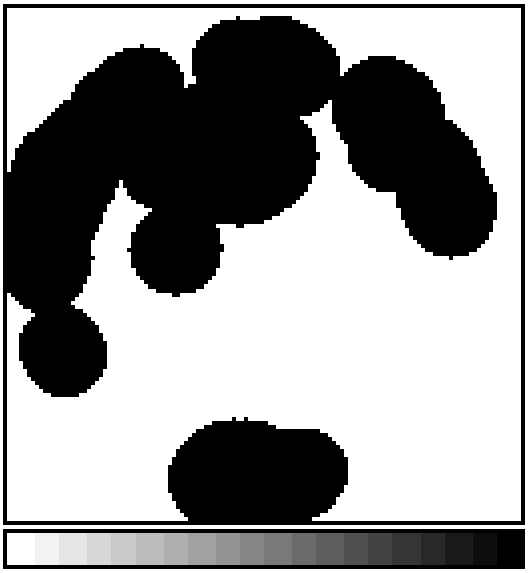

Figure E.5: QSF3

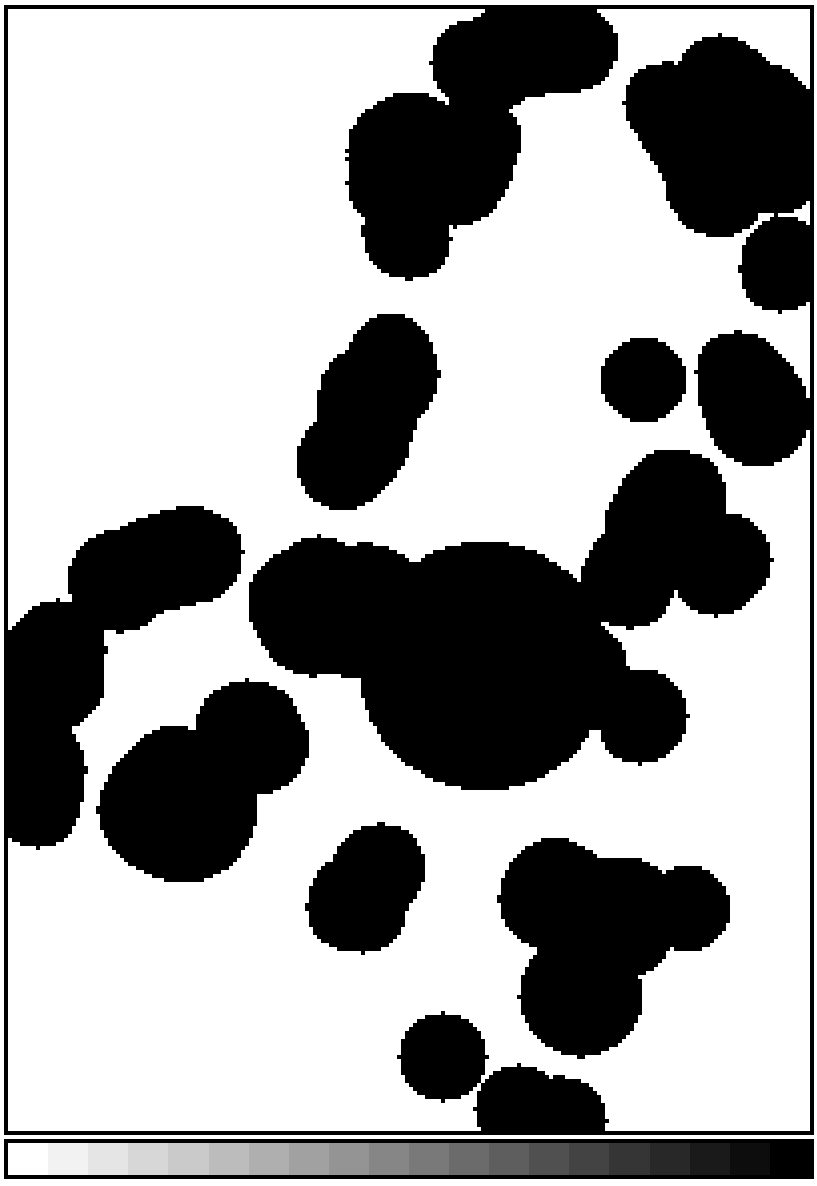

Figure E.6: z-system

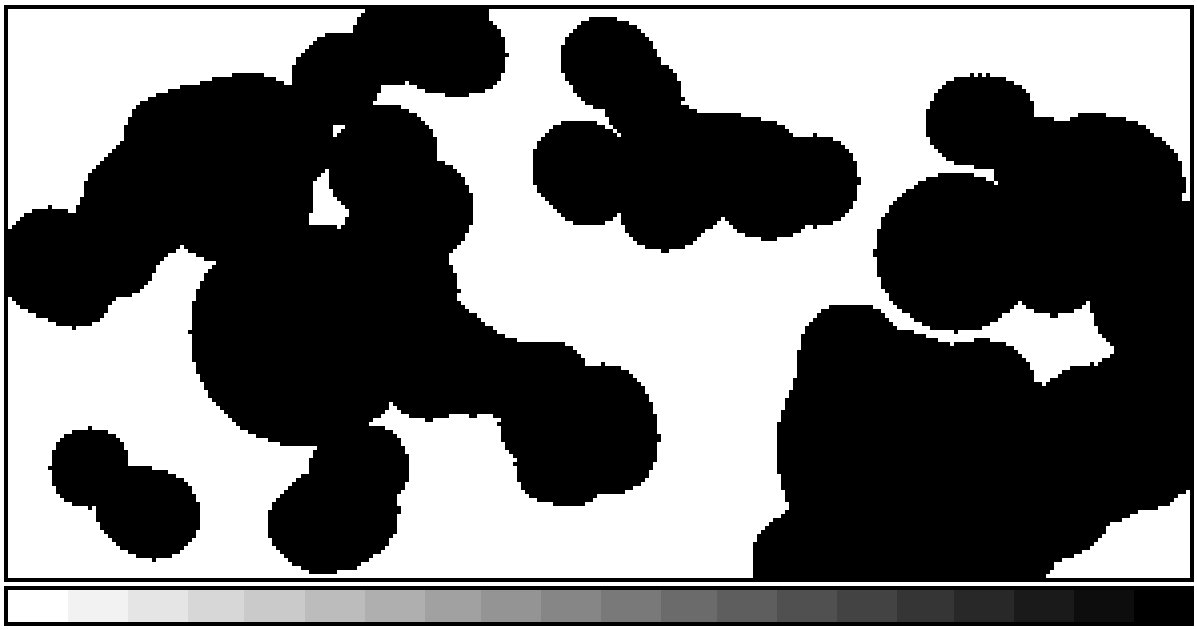

Figure E.7: Braccesi Field

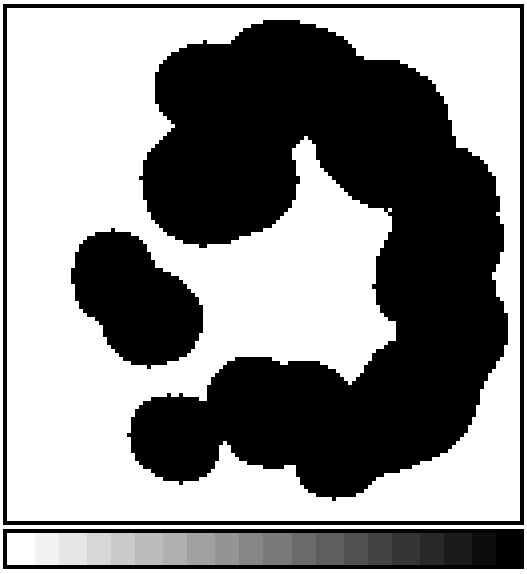

Figure E.8: Jupiter

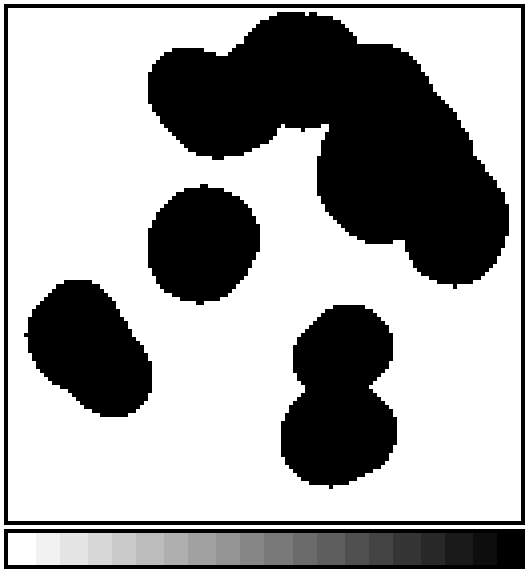

Figure E.9: Arp 220

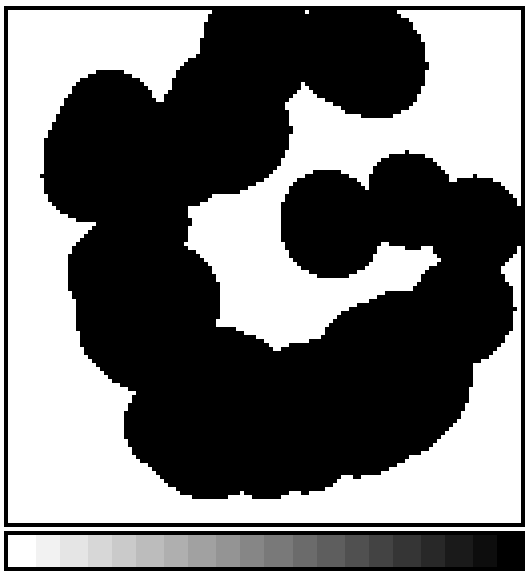

Figure E.10: 3C368

Appendix F

Hardness-map images of the observed fields

We show the hardness-map gray-scale images $M^{H/S}(SKYX, SKYY)$ in figure F.1–F.10. Black and white pixels correspond to 0.5 and 2.0, respectively. This $M^{H/S}$ has been created by calculating

$$M^{H/S}(SKYX, SKYY) = \frac{M^{FLAT}_{2\text{–}7\,\mathrm{keV}}(SKYX, SKYY) + 0.5}{M^{FLAT}_{0.7\text{–}2\,\mathrm{keV}}(SKYX, SKYY) + 0.5}, \tag{F.1}$$

where $M^{FLAT}_{2\text{–}7\,keV}$ and $M^{FLAT}_{0.7\text{–}2\,keV}$ represent the flat-field images in the 2–7 keV and 0.7–2 keV energy bands, respectively, as described in §7.2.1. The offset terms of 0.5 are chosen rather optionally to avoid dividing 0.0 by 0.0. Therefore, pixel values of $M^{H/S}$ are not necessarily proportional to the real hardness, we can see at least whether bright sources are flatter (harder) or steeper (softer) than the average CXB.

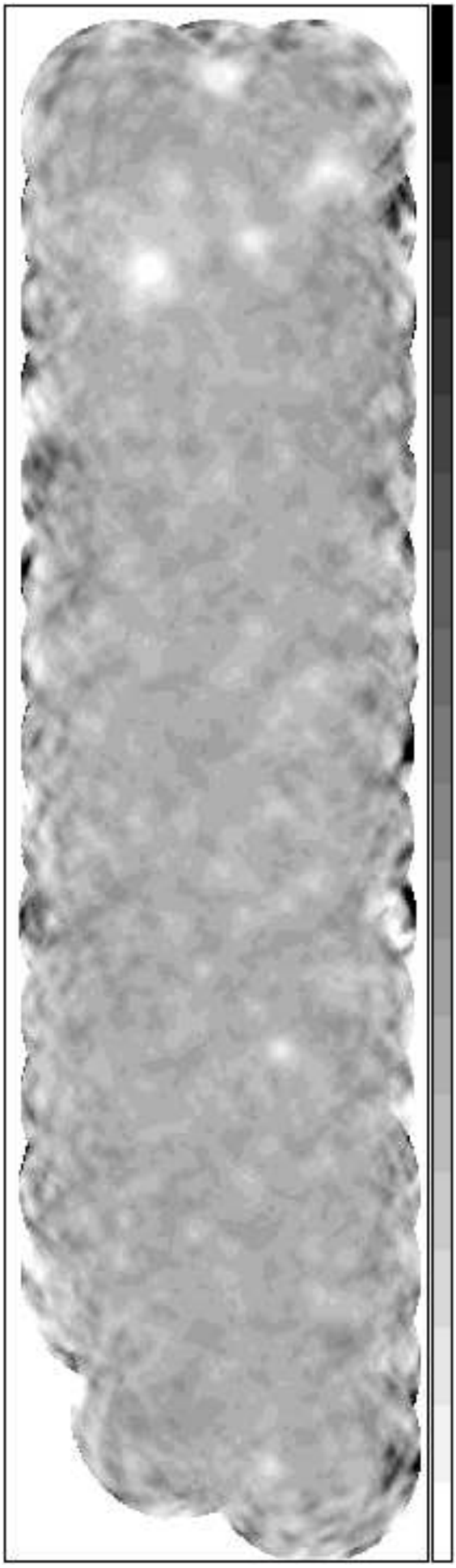

Figure F.1: LSS

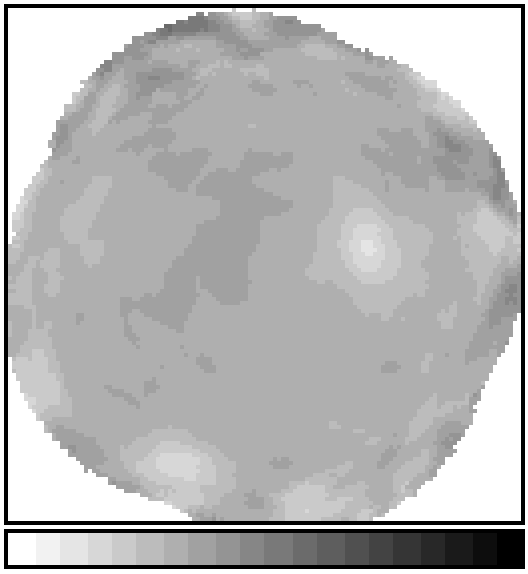

Figure F.2: SA57

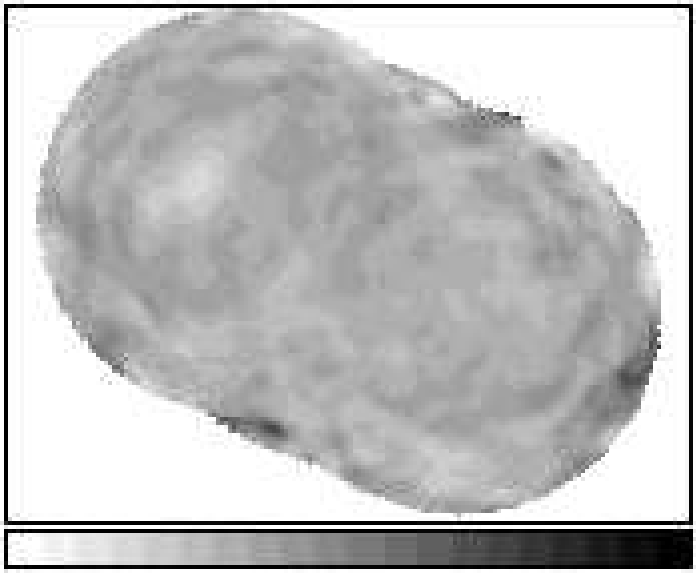

Figure F.3: Draco Field

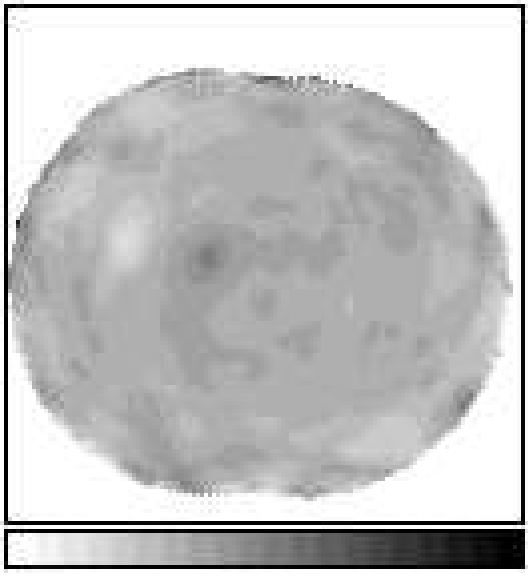

Figure F.4: NEP

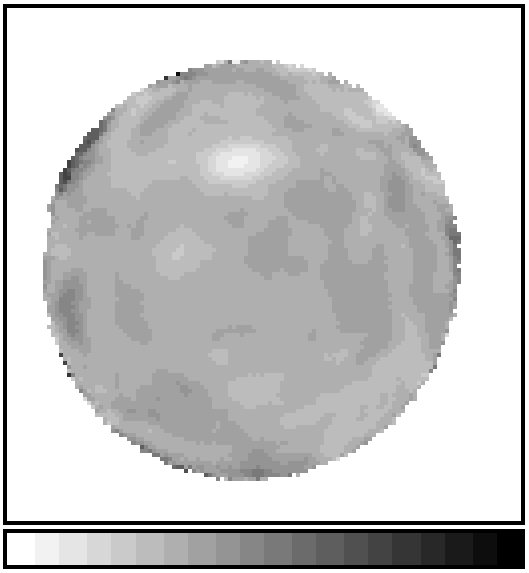

Figure F.5: QSF3

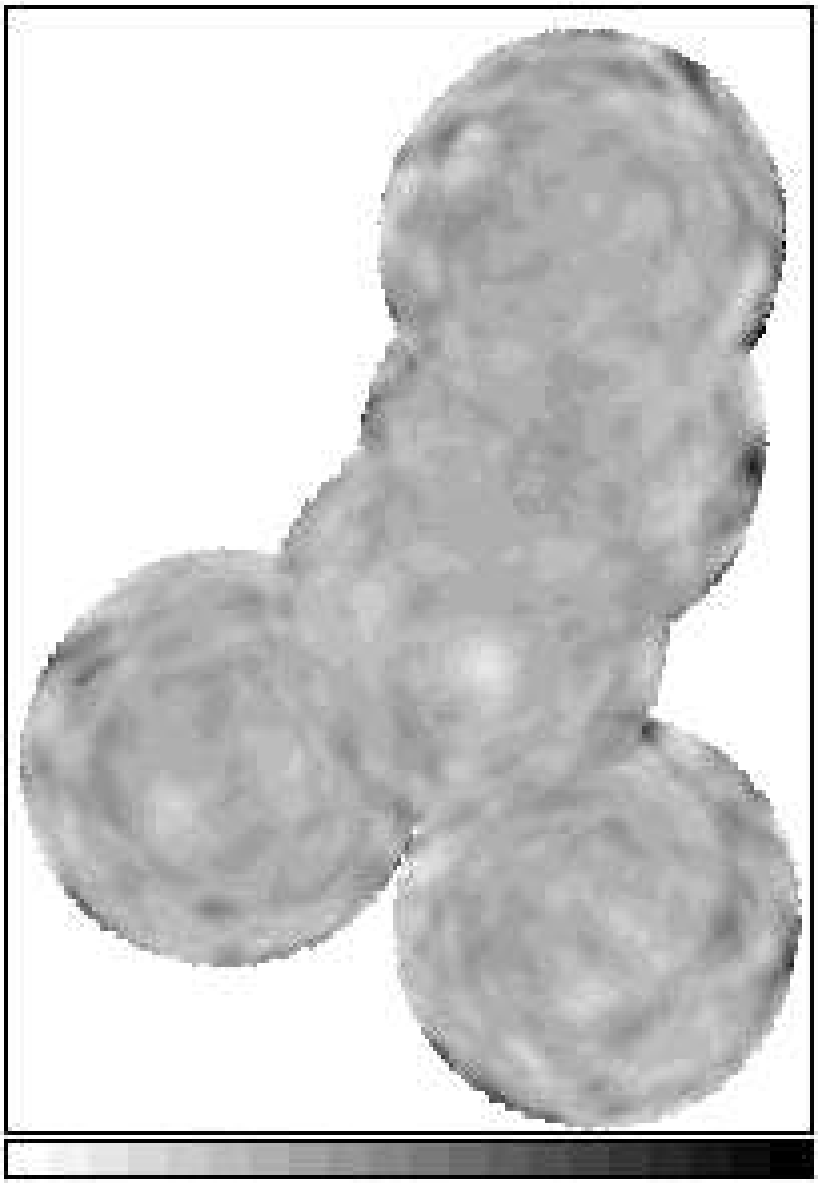

Figure F.6: z-system

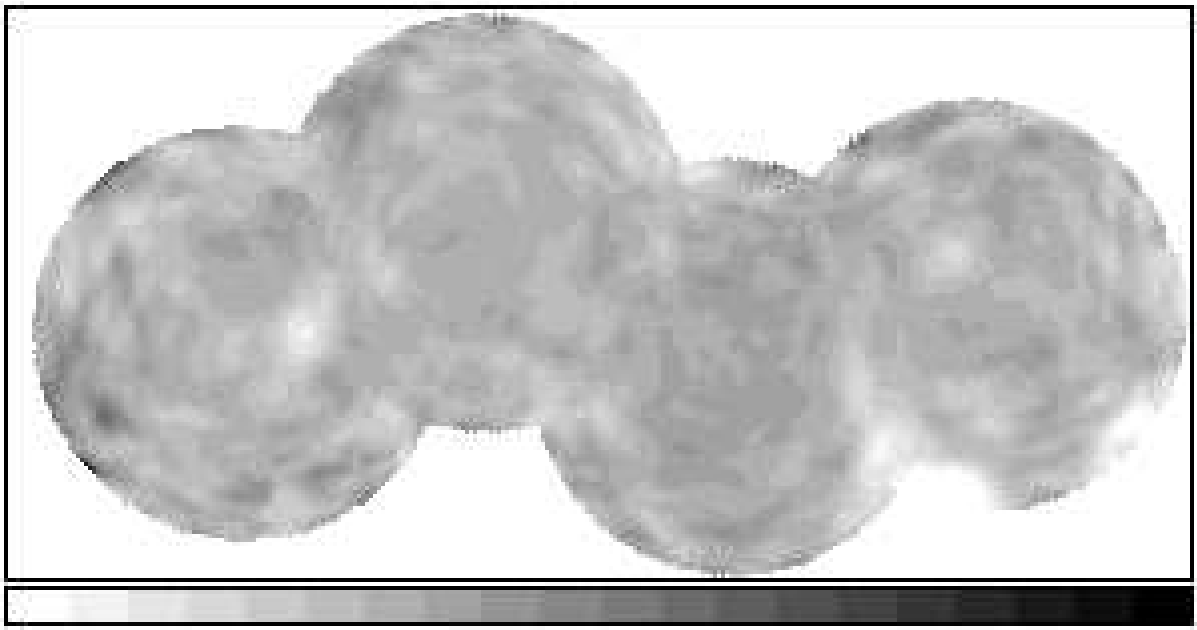

Figure F.7: Braccesi Field

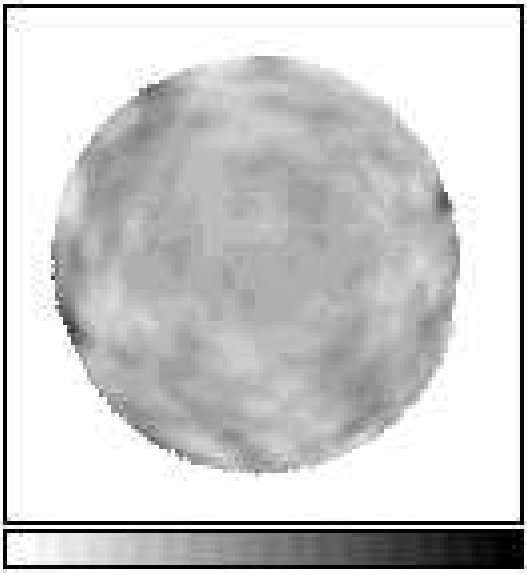

Figure F.8: Jupiter

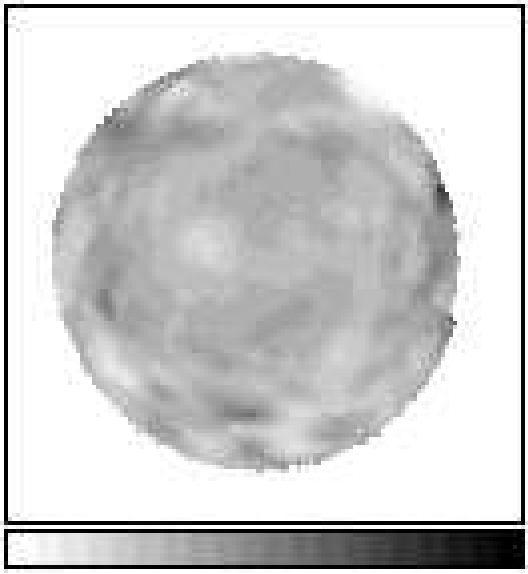

Figure F.9: Arp 220

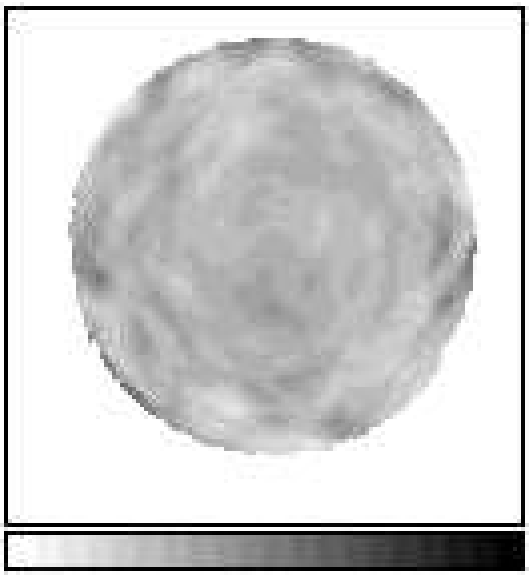

Figure F.10: 3C368

Appendix G

All-sky maps of the X-ray observations

We show all-sky maps of the previous X-ray observations in figure G.2–G.5, as well as the hydrogen column map in figure G.1. All maps are shown in the Galactic coordinate centered on the $l = 0°$, and increasing to the left. Table G.1 is the summary of the X-ray images.

Table G.1: Summary of the X-ray images in this chapter

Instrument	Energy Band	Resolution	Figure
HEAO-1 A2	2–60 keV	$3° \times 3°$	G.2
ROSAT PSPC	1/4 keV	2°	G.3a
	3/4 keV	2°	G.3b
	1.5 keV	2°	G.3c
Wisconsin survey	C-band ($\sim$ 0.16–0.284 keV)	7°	G.5a
(proportional counter)	M-band ($\sim$ 0.49–$\sim$ 1.09 keV)	7°	G.5a

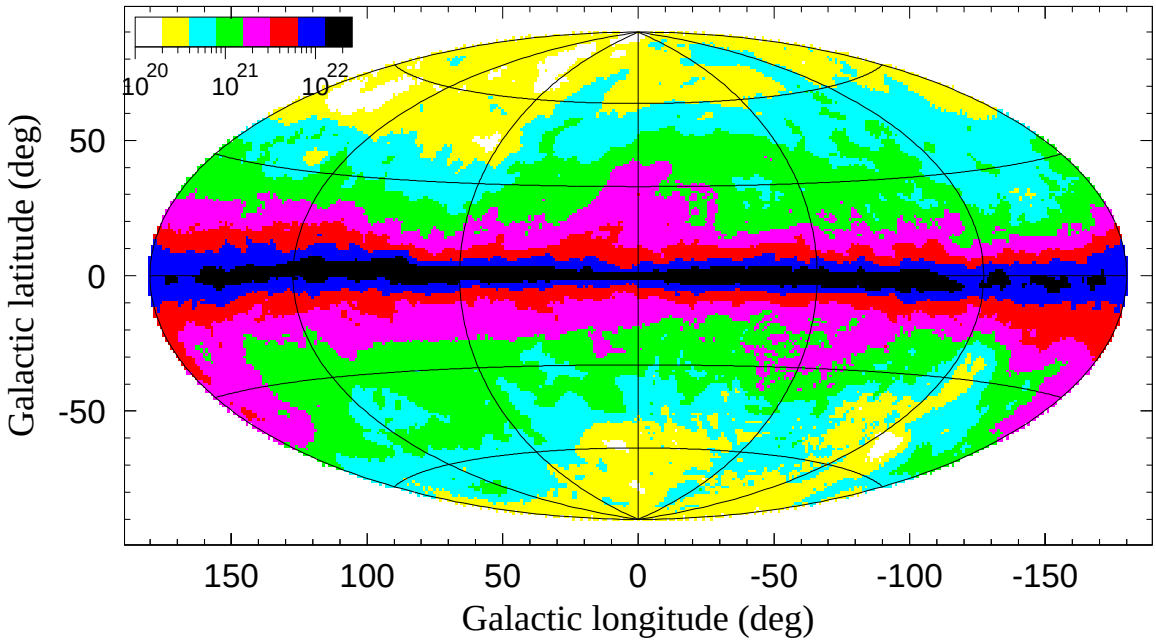

Figure G.1: Map of the total number of hydrogen atoms in different directions on the sky, adopted from the NRAO Radio CD-ROM. Seven different 21 cm HI surveys are combined, and averaged over 1 square degree intervals. Most of the arcs and circular structures outline huge regions created by supernova explosions (Dickey, and Lockman 1990).

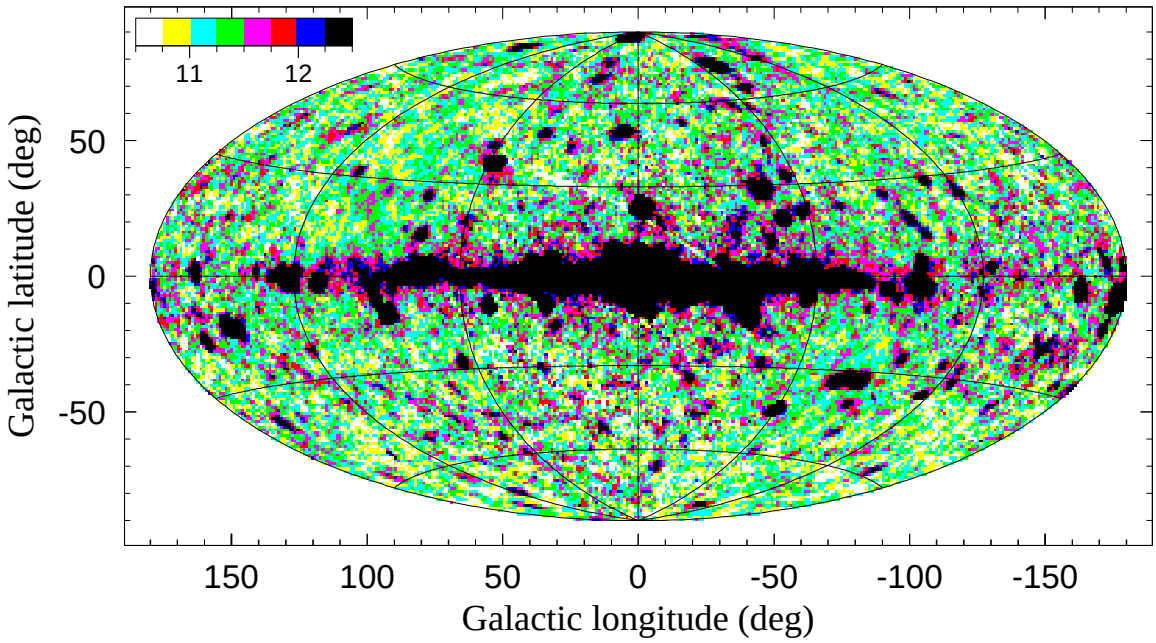

Figure G.2: The X-ray sky from HEAO-1 A2 in Galactic coordinates at 3° resolution, adopted from the WWW service of NASA/GSFC at *http://heasarc.gsfc.nasa.gov*. Bright sources and diffuse emission from the Galaxy dominate at low Galactic latitudes. Besides it, X-ray sky is dominated by the CXB, and fluctuations in the CXB are seen in at high Galactic latitude (Allen, Jahoda, and Whitlock in article Vol. 5 of Legacy, journal of the HEASARC).

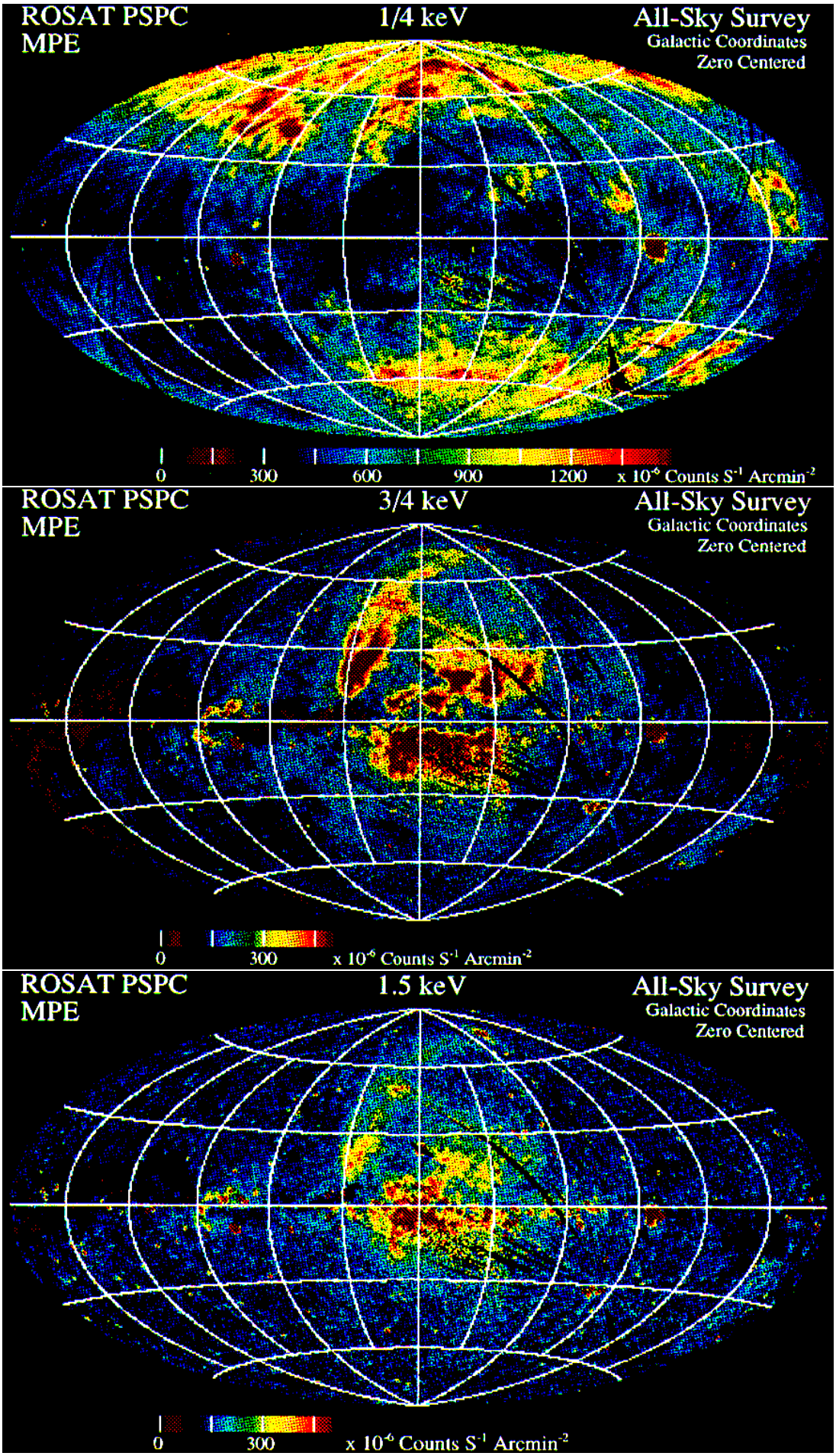

Figure G.3: ROSAT PSPC all sky survey X-ray intensity Galactic coordinates maps in (a) 0.25 keV, (b) 0.75 keV, and (c) 1.50 keV energy band, adopted from Snowden et al. (1995).

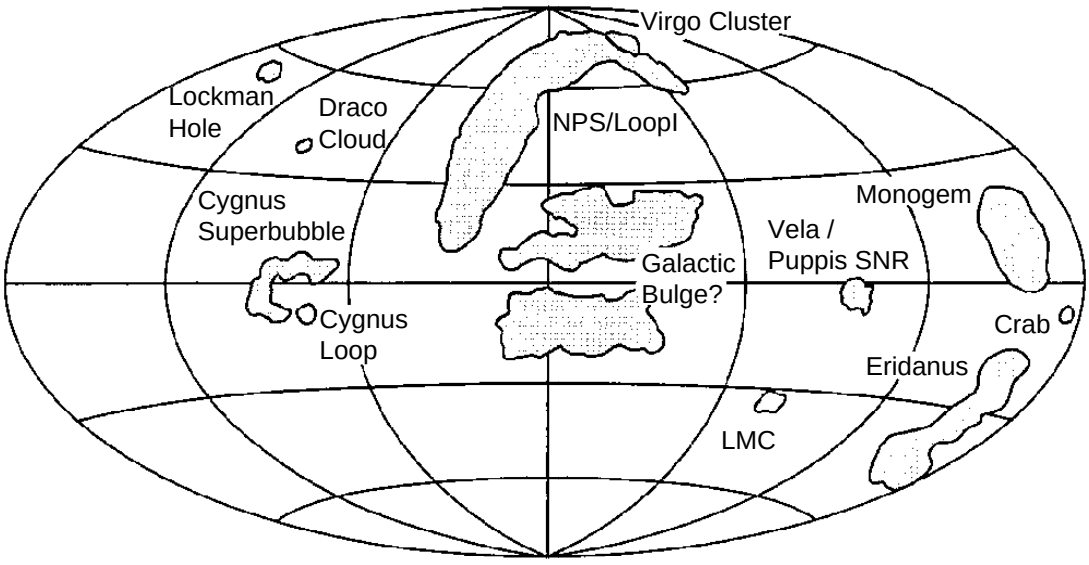

Figure G.4: Brief descriptions of the main features seen in figure G.3, adopted from the same paper.

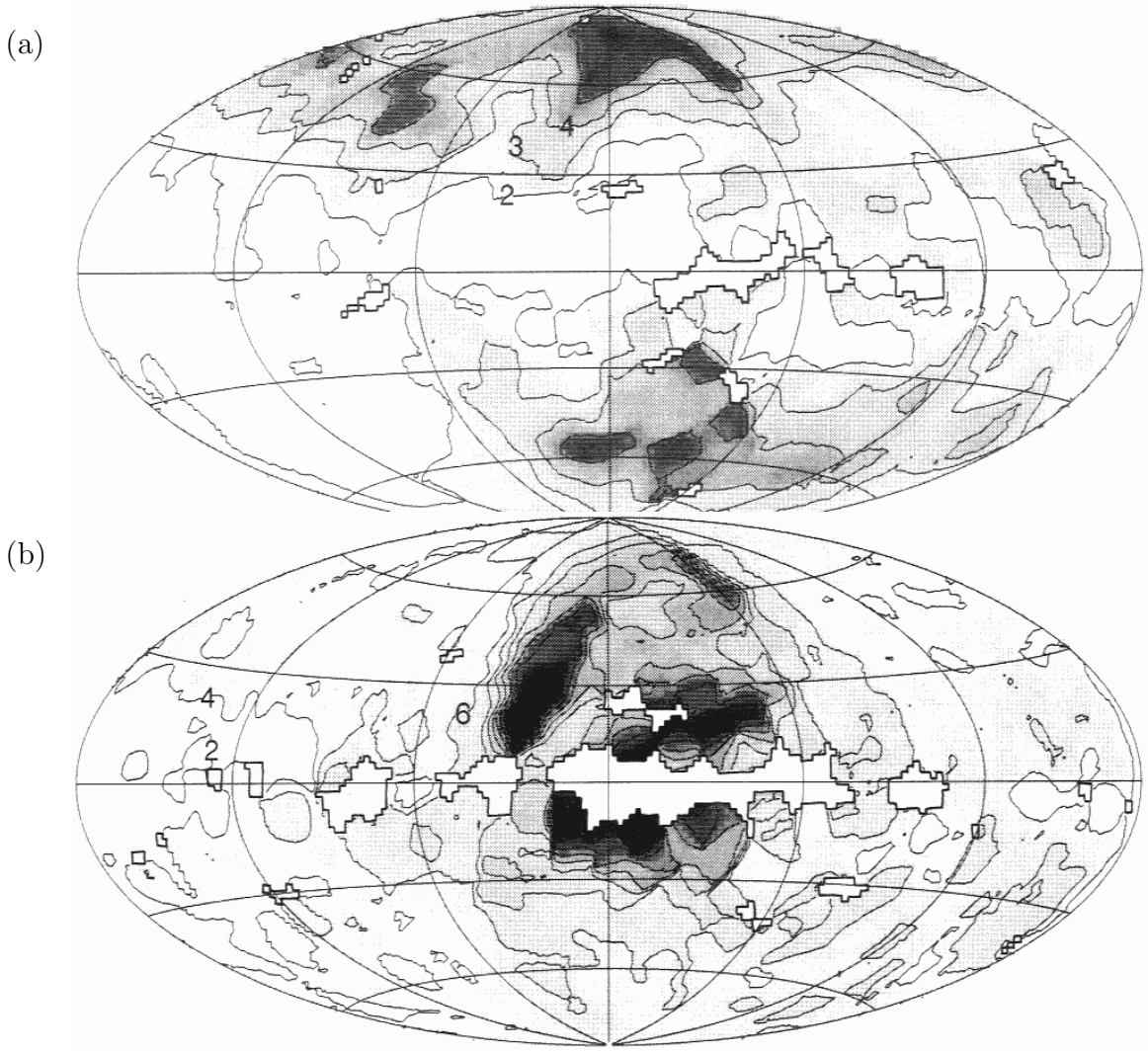

Figure G.5: (a) C-band (∼ 160–284 eV) and (b) M-band (∼ 490–∼ 1090 eV) maps from the Wisconsin sky survey (McCammon et al. 1983), adopted from the review by McCammon & Sanders (1990).

Appendix H

CXB fluctuation due to unresolved sources

H.1 Formulation of the CXB fluctuation

As describeded in §2.2, the CXB intensity observed with an instument with a finite f.o.v. fluctuates from field to field, since the number of discrete sources in the f.o.v. statistically fluctuates. Condon (1974) estimated this fluctuation level, and we below introduce her results briefly.

Let $n(S)$ denote the differential source number density with the flux S (erg cm^{-2} s^{-1}). This $n(S)$ represents the $\log N$-$\log S$ relation described in §2.2 and usually expressed by

$$n(S) = k\, S^{-\gamma} \quad (\gamma = 2.5 \ \text{ for the Euclidian universe}). \tag{H.1}$$

We next define the transmission function $f(\theta, \phi)$ for the detector, which relates the observed counting rate x (c s^{-1} cm^{-2}) for the detector to the flux S from the source locating at $\Omega = (\theta, \phi)$ on the sky as:

$$x = A\, f(\Omega)\, S, \tag{H.2}$$

where A is a constant which normalizes $f(\theta, \phi)$ to be 1.0 at the peak, i.e., $f(0, 0) = 1$. Then, the expectation $d\overline{n}(x)$ of the source number with the counting rate in the range $x \sim x + dx$ can be estimated as

$$d\overline{n}(x)\, d\Omega = n(S)\, dS\, d\Omega = n\left(\frac{x}{A\, f(\Omega)}\right) \frac{dx}{A\, f(\Omega)}\, d\Omega, \tag{H.3}$$

since $dx = A\, f(\Omega)\, d\Omega$. Assuming equation (H.1), we derive

$$d\overline{n}(x) = k\, A^{\gamma-1}\, x^{-\gamma}\, \Omega_e\, dx, \tag{H.4}$$

where

$$\Omega_e \equiv \int [\, f(\Omega)\,]^{\gamma-1} d\Omega. \tag{H.5}$$

This Ω_e is called "effective beam size" and represents the response of the detector to the source confusion.

Utilizing equation (H.4), we can calculate the expectation $\overline{D}$ of the observed counting rate D (c s^{-1} cm^{-2}) as:

$$\overline{D} = \int_{D_0}^{\infty} x\, d\overline{n} = k\, A^{\gamma-1}\, \Omega_e \int_{D_0}^{\infty} x^{-\gamma+1} dx = \frac{k\, A^{\gamma-1}\, \Omega_e}{2-\gamma}\, D_0^{2-\gamma}, \tag{H.6}$$

where D_0 is a lower cut-off of x, which is introduced to avoid the divergence of the integral. Physically, this means that the $\log N$-$\log S$ relation should flatten below some flux. Since dn should be subject to the Poisson distribution, i.e., $\delta(dn)^2 = d\overline{n}$, we can also calculate the standard deviation σ_D of the observed conting rate D as:

$$\sigma_D^2 = \int_0^{D_c} \frac{[\, x\, \delta(dn)\,]^2}{dx}\, dx = \int_0^{D_c} x^2\, d\overline{n} = \frac{kA^{\gamma-1}\Omega_e}{3-\gamma}\, D_c^{3-\gamma}, \tag{H.7}$$

where D_c is an upper cut-off of x, i.e. we discard the data brighter than D_c regarding not a blank sky. Therefore, the fraction of the CXB fluctuation is

$$\sigma_D/\overline{D} = \frac{(k\, A^{\gamma-1}\, \Omega_e\, D_c^{3-\gamma})^{1/2}\, (\, 2-\gamma)}{(3-\gamma)^{1/2}\, k\, A^{\gamma-1}\, \Omega_e\, D_0^{2-\gamma}} = \frac{2-\gamma}{\sqrt{(3-\gamma)\, k\, \Omega_e}} \left(\frac{D_c}{A}\right)^{(3-\gamma)/2} \left(\frac{D_0}{A}\right)^{\gamma-2}. \tag{H.8}$$

for the Euclidian universe, i.e., $\gamma = 2.5$, this becomes

$$\sigma_D/\overline{D} \propto \Omega_e^{-0.5}\, S_c^{0.25} \quad (S_c \equiv D_c/A). \tag{H.9}$$

H.2 Effective beam size for the XRT+GIS

Taking into account both vignetting and stray-light effects, we calculate Ω_e for the XRT+GIS when we use inside 20 mm from the optical axis as the data integration region.

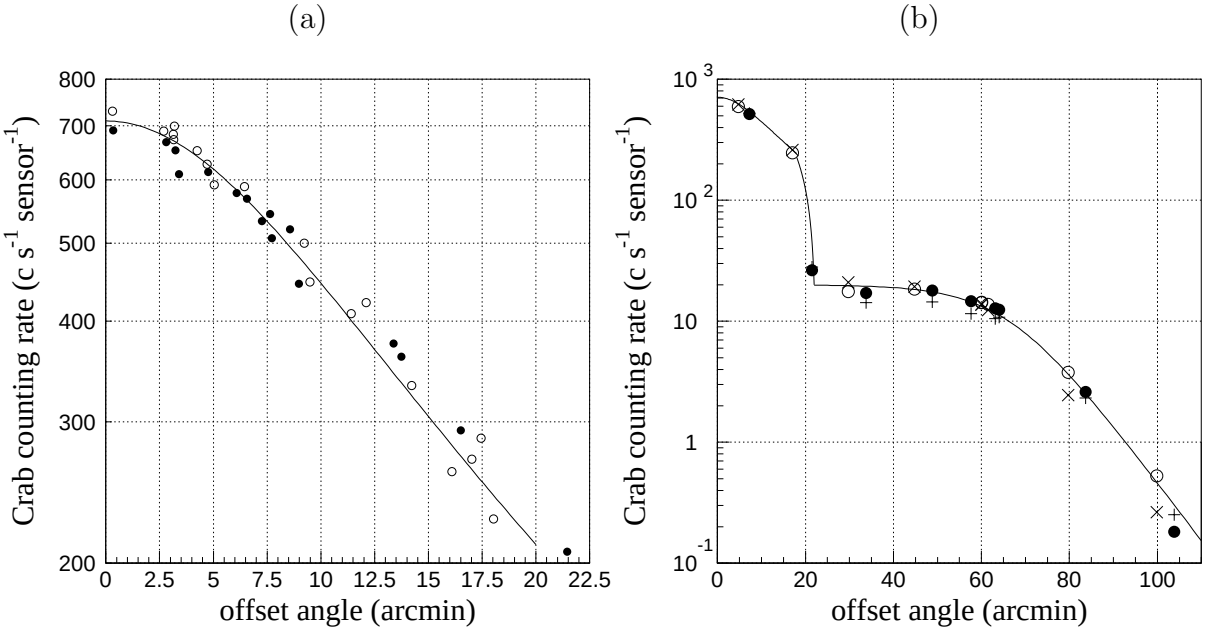

Figure H.1: (a) The observed Crab counting rate in the 0.7–10 keV energy band plotted against the offset angle from the XRT optical axis. Filled circles represent GIS2 and open circles GIS3. (b) Same as upper panel of figure 4.17a. Solid line represents equation (H.10).

Figure H.1 shows the dependence of the Crab counting rate on the offset angle θ from the XRT optical axis. As seen in the figure, we approximate the counting rate as:

$$f(\theta) = \begin{cases} \dfrac{710}{1+(x/13)^2} & \cdots\ (\theta < 18') \\ -51.6\,(\theta - 22) + 20 & \cdots\ (18' \leq \theta < 22') \\ \dfrac{20}{1 + 0.5\ \exp[(\theta - 60)/9]} & \cdots\ (22' \leq \theta) \end{cases} . \tag{H.10}$$

If we ignore the azimuth angle dependence, we can calculate Ω_e as:

$$\Omega_e = 2\pi \int_0^\infty [\, f(\theta)/f(0)\,]^{\gamma-1} \sin\theta\, d\theta. \tag{H.11}$$

In figure H.2, we show

$$\Omega_e(\theta_c) = 2\pi \int_0^{\theta_c} [\, f(\theta)/f(0)\,]^{1.5} \sin\theta\, d\theta. \tag{H.12}$$

Therefore, Ω_e for the XRT+GIS is 0.142 deg^2. Contribution of the stray light to Ω_e is ~ 0.01 deg^2 and almost negligible.

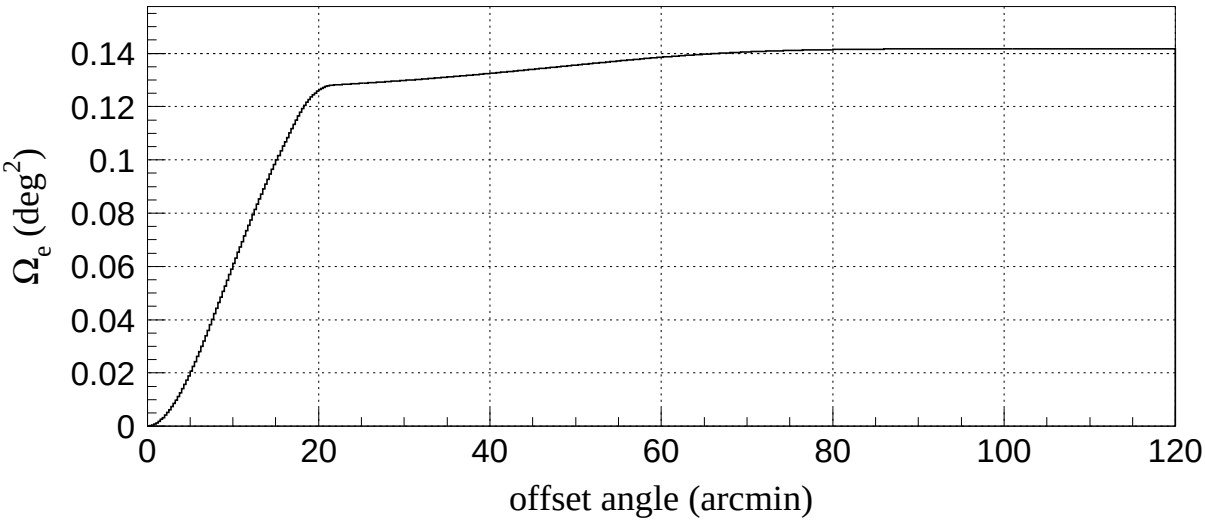

Figure H.2: Calculation of Ω_e for the XRT+GIS.

Acknowledgement

First of all, I would like to express my best gratitude to Prof. K. Makishima for his continuous guidance and hearty support for this thesis. He has also led me throughout these five years of my graduate course, and I have learned much from him. I am deeply grateful to Dr. T. Takahashi, Mr. Y. Ueda, and Mr. Y. Ogasaka, for their constructive discussions and cooperations. I also thank Prof. Y. Suto, Prof. H. Inoue, Prof. R. Mushotzky, and Dr. K. Gendreau for their valuable comments and suggestions.

The ASCA observatory was developed, launched, and operated successfully with great efforts by ASCA team members, including people at Institute of Space and Astronautical Science (ISAS), University of Tokyo, Tokyo Metropolitan University, Institute of Physical and Chemical Research (RIKEN), Nagoya University, Osaka University, Kyoto University, Iwate University, and Miyazaki University. I am indebted to the staff of the ASCA Guest Observers Facility. I owe a great deal to all the scientists and engineers who worked on the development and operation of the ASCA project.

I wish to thank all the members, past and present, of the cosmic X-ray astronomy group in the University of Tokyo, including Prof. T. Ohashi, Dr. M. Tashiro, Mr. Y. Fukazawa, Dr. T. Tsuru, Dr. M. Ishida, Dr. T. Sakao, Dr. T. Mihara, Dr. M. Inda Koide, Dr. Y. Kohmura, Dr. Y. Ikebe, Mr. S. Kamijo, Mr. H. Kaneda, Ms. K. Matsushita, Mr. T. Tamura, Ms. N. Iyomoto, Ms. E. Idesawa, Mr. T. Mizuno, and Mr. H. Obayashi. I especially thank Mr. M. Hirayama, Mr. T. Kotani, and Mr. R. Fujimoto among many people in other institutes.

I appreciate Dr. T. Kii, Dr. T. Tsuru, and Dr. N. Yamasaki who kindly agreed me to use their GO-phase data. I also appreciate the authors of XSPEC, DISPLAY45, ASCA_ANL, SimASCA, SimARF, jbldarf, XRT ray-tracing, mule, TEX, LATEX, tgif, etc.

References

[1] Antonucci, R.R.J & Miller, J.S. 1985, *Astrophys. J.*, **297**, 621.

[2] Awaki, H. *et al.* 1990, *Nature*, **346**, 544.

[3] Awaki, H. *et al.* 1991, *Publ. Astron. Soc. Japan*, **43**, 195.

[4] Awaki, H. *et al.* 1993, *Adv. Space Res.*, **13**, 221.

[5] Awaki, H. *et al.* 1994, Publ. Astron. Soc. Japan, **46**, L65.

[6] Bahcall, N.A. 1988, *Ann. Rev. Astron. Astrophys.*, **26**, 631.

[7] Bahcall, N.A. & West, M.J. 1992, *Astrophys. J.*, **392**, 419.

[8] Bolt, E. 1987, *Phys. Rep.*, **146**, 215.

[9] Boyle, B.J. *et al.* 1993, *Mon. Not. Royal Astron. Soc.*, **260**, 49.

[10] Brandbardi-Raymont, G. *et al*, 1994, *Mon. Not. R. Astron. Soc.*, **270**, 947

[11] Burke, B.E. *et al.* 1991, *IEEE Trans.* **ED-38**, 1069

[12] Burrows, D.N., & Mendenhall, J.A. 1991, *Nature*, **351**, 629.

[13] Chen, L.W. & Fabian, A.C. in preparation

[14] Condon, J. J. 1974, *Astrophys. J.*, **188**, 279

[15] Cowsik, R., & Kobetich, E.J. 1972, *Astrophys. J.*, **177**, 585.

[16] Cristiani *et al.* 1984, *Astro. Astrophys.*, **135**, 122.

[17] Dotani,T. 1995 in ASCA News No.3

[18] Ebeling, H. *et al.* 1995, in *proceedings on Röntgenstrahlung from Universe*, at Würzburg, eds. J. Trümper and U. Zimmermann, in press.

[19] Fabbiano, G. 1989, *Ann. Rev. Astron. Astrophys.*, **27**, 87.

[20] Fabbiano, G. *et al.* 1989, *Astrophys. J.*, **347**, 127.

[21] Fabian, A.C. & Balcons, X. 1992, *Ann. Rev. Astron. Astrophys.*, **30**, 429.

[22] Fabian, A.C. *et al.* 1990, *Mon. Not. Royal Astron. Soc*, **242**, 14.

[23] Fabianno, G. and Trinchieri, G. 1985, *Astrophys. J.*, **296**, 430.

[24] Fanti *et al.* 1977, *Astro. Astrophys.*, **61**, 487.

[25] Field, G.B., & Perrenod, S.C. 1977, *Astrophys. J.*, **215**, 717.

[26] Fukazawa, Y. *et al.* 1994, *Publ. Astron. Soc. Japan*, **46**, L141.

[27] Gendreau, K.C. *et al.* 1995, *Publ. Astron. Soc. Japan*, **47**, L5.

[28] Giacconi, R.H. *et al.* 1962, *Phys. Rev. Lett.*, **9**, 439.

[29] Giacconi, R.H. *et al.* 1979, *Astrophys. J. letters*, **234**, L1.

[30] Gioia, I.M. *et al.* 1984, *Astrophys. J.*, **283**, 495.

[31] Gioia, I.M. *et al.* 1990, *Astrophys. J. Suppl.*, **72**, 567.

[32] Goerigk, W. *et al.* 1983, *Astro. Astrophys.*, **120**, 63.

[33] Griffiths, R.E. and Padovani, P. 1990, *Astrophys. J.*, **360**, 483.

[34] Hamilton, T.T., & Helfand, D.J. 1987, *Astrophys. J.*, **318**, 93.

[35] Hasinger, G. 1992, in *The X-Ray Background*, eds. X. Barcons and A.C. Fabian (Cambridge University Press: Cambridge), p229.

[36] Hasinger, G. *et al.* 1991, *Astro. Astrophys.*, **246**, L2.

[37] Hasinger, G. *et al.* 1993, *Astro. Astrophys.*, **275**, 1.

[38] Hasinger, G. *et al.*, 1993, *Astron. Astrophys.*, **275**, 1

[39] Hayashida, K. 1989, *Ph. D dissertation of Univ. of Tokyo*, *ISAS RN* 466.

[40] Heiles, H. & Cleary, M.N. 1979, *AJPAS*, **47**, 1.

[41] Heisker, J. *et al.* 1989, *Astrophys. J.*, **347**, 52.

[42] Hewitt, A. & Burbidge, G. 1989, *Astrophys. J. Suppl.*, **69**, 1.

[43] Hoyle, F. 1963, *Astrophys. J.*, **137**, 993.

[44] Inoue, H. *et al.* 1979, *Astrophys. J.Letters*, **227**, L85.

[45] Iwan, D. *et al.* 1982, *Astrophys. J.*, **260**, 111.

[46] Jahoda, K. *et al.* 1991, *Astrophys. J.*, **378**, L37.

[47] Kii, T. *et al.* 1995 in *IRAS galaxies observed with ASCA*

[48] Kondo, H. 1991, *Ph. D dissertation of Univ. of Tokyo*, *ISAS RN* 494.

[49] Koo, D. C. 1986, *Astrophys. J.*, **311**, 651

[50] Koo, D. C. and Kron, R. G. 1988, *Astrophys. J.*, **325**, 92

[51] Koyama, K. 1989, *Publ. Astron. Soc. Japan*, **41**, 665.

[52] Koyama, K. *et al.* 1984, *Publ. Astron. Soc. Japan*, **36**, 659.

[53] Koyama, K. *et al.* 1986, *Publ. Astron. Soc. Japan*, **38**, 121.

[54] Koyana, K. *et al.* 1986, *Publ. Astron. Soc. Japan*, **38**, 121.

[55] Lahav, O. *et al.* 1993, *Nature*, **364**, 693.

[56] Lockman, F. J., Jahoda, K., McCammon, D. 1986, *Astrophys. J.*, **302**, 432

[57] Majewski, S. R. *et al.*, 1994, *Publ. Astron. Soc. Pscific*, **106**, 1258

[58] Makishima, K. *et al.* 1996, *Publ. Astron. Soc. Japan*, submitted

[59] Makishima, K. *et al* 1994, *Puble. Astron. Soc. Japan*, **46**, L77.

[60] Marshall, F. *et al.* 1984, *Astrophys. J.*, **283**, 50.

[61] Marshall, F. *et al.* 1980, *Astrophys. J.*, **235**, 4.

[62] Marshall, F.J. and Clark, G.W. 1984, *Astrophys. J.*, **287**, 633.

[63] Mather, J.C. *et al.* 1990, *Astrophys. J. letters*, **354**, L41.

[64] Mather, J.C. *et al.* 1994, *Astrophys. J.*, **420**, 439.

[65] Mathis, D. F. *et al.*, 1994, *Bull. American Astron. Soc.*, **185**

[66] Matt, G. and Fabian, A.C., 1994, *Mon. Not. Royal Astron. Soc.*, **267**, 187.

[67] McCammon, D. 1983, *Astrophys. J.*, **269**, 107.

[68] McCammon, D. and Sanders, W.T. 1990, *Ann. Rev. Astron. Astrophys.*, **28**, 657.

[69] McKee *et al.* 1980, *Astrophys. J.*, **242**, 843.

[70] Miyaji, T. 1995, *private commun.*

[71] Mushotzky, R.F. 1983, *Adv. Space Res.*, **3**, 10.

[72] Mushotzky, R.F. *et al.* 1978, *Astrophys. J.*, **225**, 21.

[73] Mushotzky, R.F., Done, C. and Pounds, K.A. 1993, *Annu. Rev. Astron. Astrophys.*, **31**, 717.

[74] Neuschaefer, L. W. and Windhorst, R. A. 1995, *Astrophys. J. Supple.*, **96**, 371

[75] Ogasaka, Y. 1996, Ph.D.Thesis, Gakusyuin University

[76] Ohashi, T. *et al.* 1996, *Publ. Astron. Soc. Japan*, submitted

[77] Piccinotti, G. *et al* 1982, *Astrophys. J.*, **253**, 485.

[78] Primini, F.A. *et al.* 1991, *Astrophys. J.*, **374**, 440.

[79] Protheroe, R.J. *et al.* 1980, *Mon. Notices Roy. Astron. Soc.*, **192**, 445.

[80] Roche, N. *et al.* 1995, *Mon. Not. Royal Astron. Soc.*, **273**, L15.

[81] Rothschild, R. *et al.* 1983, *AstroPhys. J.*, **269**, 423.

[82] Sandars, D.B. *et al.* 1988, *Astrophys. J*, **325**, 74.

[83] Sarazin, C.L. 1986, *Rev. Modern Phys.*, **58**, 1.

[84] Schwartz, D.A. and Gursky, H. 1974, in *X-ray Astronomy*, eds. R. Giacconi and H. Gursky (Dordrecht: Reidel).

[85] Schwartz, D.A. 1979 in *X-ray Astronomy*. Oxford: Pergamon. pp.453

[86] Serlemitsos, P. J. 1981, *NASA Tech. Mem.*, **83848**, 441

[87] Serlemitsos, P. J. 1988, *Appl. Opt.*, **27**, 1447

[88] Serlemitsos, P.J. *et al.* 1995, *Publ. Astron. Soc. Japan*, **47**, 105.

[89] Shafer, R.A. 1983, *Ph. D dissertation of Univ. of Maryland*, *NASA TM* 85029.

[90] Shafer, R.A., & Fabian, A.C. 1983 in *Early Evolution of the Universe and its Present Structure,* ed. G.O. Abell, G.Chincarini, pp.333-34. Dordrecht: Reidel

[91] Shanks, T. *et al.* 1991, *Nature*, **353**, 315.

[92] Smoot, G.F. *et al.* 1977, *Phys. Rev. Letters*, **39**, 898.

[93] Stocke, J.T. *et al.* 1991, *Astrophys. J. Suppl.*, **76**, 813.

[94] Suto, Y. *et al.* 1996, *Astrophys. J.Letters*, in press

[95] Suginohara, T. 1992, Ph.D.Thesis, University of Tokyo

[96] Tanaka, Y. and Bleeker, J.A.M. 1977, *Space Sci. Rev.*, **20**, 815.

[97] Tanaka, Y. *et al.* 1984, *Publ. Astron. Soc. Japan*, **36**, 641.

[98] Tanaka, Y. *et al.* 1994, *Publ. Astron. Soc. Japan*, **46**, L37.

[99] Tsusaka, Y. *et al*, 1995, *Appl. Opt.*, **34**, 4848

[100] Turner, T.J., & Pound, K.A. 1989, *Mon. Not. Royal Astron. Soc*, **240**, 833.

[101] Tusaka, Y. *et al.* 1995, *App.Otp*

[102] Ueda, Y. 1996, Ph.D.Thesis, University of Tokyo

[103] Warwick, R.S. *et al.* 1980, *Mon. Not. Royal Astron. Soc*, **190**, 243.

[104] Willams, O.R. *et al.* 1992, *Astrophys. J.*, **389**, 157.

[105] Windhorst, R. A., Kron, R. G., Koo, D. C. 1984, *Astron. Astrophys.*, **58**, 39

[106] Wood, *et al.* 1984, *Astrophys. J. Suppl.*, **56**, 507.

[107] Worral, D.M. *et al.* 1982, *Astrophys. J.*, **255**, 111.

[108] Wu X. *et al.* 1991, *Astrophys. J.*, **379**, 564.

[109] Yamasaki, N *et al.* 1995 in *meeting of Astronomical Society of Japan*

[110] Yamashita, A 1995 Master Thesis, University of Tokyo

[111] Yamauchi, S. and Koyama, K. 1993, *Astrophys. J.*, **404**, 620.

[112] Zeldovich, Ya. and Sunyaev, R.A. 1969, *Astrophys. Space Sci.*,**4**, 301.